UNIVERSITY OF OKLAHOMA

GRADUATE COLLEGE

DEVELOPMENT OF PATIENT-SPECIFIC SHAPE MEMORY POLYMER FOAMS FOR THE TREATMENT OF INTRACRANIAL ANEURYSMS

A DISSERTATION

SUBMITTED TO THE GRADUATE FACULTY

in partial fulfillment of the requirements for the

Degree of

DOCTOR OF PHILOSOPHY

By

SERGIO ANDRES PINEDA CASTILLO
Norman, Oklahoma
2023

Downloaded from SHAREOK. Persistent Handle URL: https://hdl.handle.net/11244/337541

DEVELOPMENT OF PATIENT-SPECIFIC SHAPE MEMORY POLYMER FOAMS FOR THE TREATMENT OF INTRACRANIAL ANEURYSMS

A DISSERTATION APPROVED FOR THE
STEPHENSON SCHOOL OF BIOMEDICAL ENGINEERING

BY THE COMMITTEE CONSISTING OF

Dr. Chung-Hao Lee, Chair

Dr. Michael S. Detamore, Co-Chair

Dr. Handan Acar

Dr. Keisha B. Walters

Dr. Andres Gonzalez

© Copyright by SERGIO ANDRES PINEDA CASTILLO 2023
All Rights Reserved.

Dedication

To Nelly, Celio, and Natalia,
who always believed.

TABLE OF CONTENTS

List of Figures xi
List of Tables xx
Acknowledgments xxi
Vita xxiv
Publications xxv
Conference Presentations xxvii
Abstract of the Dissertation xxviii
CHAPTER 1 Introduction 1
1.1 Motivation 1
1.2 Objective and Scope 1
CHAPTER 2 Literature Review 5
2.1 Brain Vasculature Anatomy and Intracranial Aneurysms 5
2.1.1 Brain Vasculature Anatomy 5
2.1.2 Intracranial Aneurysms: Definition, Incidence and Demographics 6
2.2 Unruptured Aneurysms and Treatment Options 7
2.2.1 Endovascular Embolization 9
2.3 *State-of-the-art* Endovascular Devices 10
2.3.1 Hydrogel-Coated Coils 10
2.3.2 Hydrogel/Liquid Embolic Materials 11
2.3.3 Woven EndoBridge 12
2.3.4 Flow Diversion Devices 13
2.3.5 Trellix 14
2.3.6 Summary of Current Endovascular Devices 15
2.4 Shape Memory Polymers and Their Potential as Endovascular Devices 16
2.4.1 Shape Memory Polymer Classification by Polymer Architecture 18
2.4.1.1 Physically Crosslinked Co-Polymers 18
2.4.1.2 Covalently Crosslinked Copolymers 18
2.4.2 Shape Memory Polymer Classification by Pore Fabrication Methods 19
2.4.2.1 Gas Foaming 19
2.4.2.2 Particle Leaching 20

2.4.2.3 Additive Manufacturing (3D-Printing) 21
2.4.3 Shape Memory Polymer Actuation Methods 22
2.4.3.1 Joule heating activation 22
2.4.3.2 Infrared (IR) light activation 23
2.4.3.3 Electromagnetic Activation 24
2.4.3.4 pH activation 24
2.4.4 Potential of SMPs for ICA Endovascular Therapies & Future Directions 29
2.5 Previous Work at the Biomechanics and Biomaterials Design Laboratory 30
2.5.1 Synthesis and Characterization of Pristine Polyurethane SMPs 30
2.5.2 First attempts at Fabricating Porous SMPs with Conductive Properties 31
2.5.3 ICA Fluid Dynamics 31
2.6 Concluding Remarks 31
CHAPTER 3 Design and Characterization of a Joule-Heating Activated Shape Memory Foam Using Carbon Nanotubes 33
3.1 Materials and Methods 33
3.1.1 Preparation of CNT/Porogen Solution 33
3.1.2 Preparation of CNT-infiltrated SMP foams 34
3.1.3 Attenuated Total Reflectance - Fourier Transform IR Spectroscopy 34
3.1.4 Density Measurement 35
3.1.5 Differential Scanning Calorimetry (DSC) 35
3.1.6 Resistivity Measurement 35
3.1.7 Uniaxial Mechanical Characterizations 36
3.1.8 Assessment of the Shape Recovery Time 37
3.1.9 Measurement of the Joule-Heating-Induced Heat Transfer 37
3.1.10 Fabrication of an Idealized Aneurysm Model and Occlusion Demonstration 38
3.1.11 Scanning Electron Microscopy 38
3.1.12 Statistical Analysis 39
3.2 Results 39
3.2.1 Synthesis and Characterization of CNT-Infiltrated SMP Foams 39
3.2.2 CNT-Induced Thermal and Electric Conductivities 41
3.2.3 Mechanical Characterizations of CNT-Infiltrated SMP Foams 46
3.2.4 Demonstration of the Aneurysm Occlusion Process via an Idealized Aneurysm Phantom Model 55

3.3 Discussion 56
3.3.1 Overall Findings 56
3.3.2 Study Limitations 58
3.4 Conclusion 60
CHAPTER 4 Development of A Leaching/3D-Printing Method for the Fabrication of Patient-Specific Porous SMP Foams 61
4.1 Materials and Methods 62
4.1.1 3D-printing of PVA Templates 62
4.1.2 Preparation of 3DSMP Foams 62
4.1.3 Attenuated Total Reflectance - Fourier Transform Infrared Spectroscopy (ATR-FTIR) 64
4.1.4 Scanning Electron Microscopy 65
4.1.5 Differential Scanning Calorimetry 65
4.1.6 Mechanical Characterization - Uniaxial Compressive Testing 65
4.1.7 Shape Recovery Assessments 66
4.1.8 Fabrication of a Patient-Specific Aneurysm Model and *In Vitro Proof-of-Concept* Occlusion Demonstration 67
4.1.9 Statistical Analysis 67
4.2 Results 68
4.2.1 Fabrication of 3DSMP Foams and Microstructure 68
4.2.2 Differential Scanning Calorimetry (DSC) 70
4.2.3 Attenuated Total Reflectance – Fourier Transform Infrared Spectroscopy (ATR-FTIR) Characterization 71
4.2.4 Compressive Mechanical Properties of 3DSMP Foams 72
4.2.5 Shape Recovery Properties of the 3DSMP-X Foams 73
4.2.6 Fabrication of Patient-Specific 3DSMP Foams: Demonstration of Image-Based Fabrication and Phantom Occlusion 77
4.3 Discussion 79
4.3.1 Overall Findings 79
4.3.2 Study Limitations 80
4.3.3 Future Directions 82
4.4 Conclusions 83
CHAPTER 5 Design and Characterization of a Joule-Heating-Activated Patient-Specific SMP using Polypyrrole Coating 84

5.1 Materials and Methods 84
5.1.1 Fabrication of 3DSMP Foams 84
5.1.2 Polypyrrole coating of 3DSMP Foams 85
5.1.3 Microscopy of PPy-coated 3DSMP Foams 86
5.1.4 Attenuated Total Reflectance – Fourier Transform Infrared Spectroscopy 86
5.1.5 Differential Scanning Calorimetry 86
5.1.6 Volumetric Resistivity Assessment 87
5.1.7 Assessment of Joule-Heating Behavior 88
5.1.8 Shape Recovery Analysis 89
5.2 Results 90
5.2.1 Fabrication of PPy-coated 3DSMP Foams 90
5.2.2 Microstructure of PPy-Coated 3DSMP Foams 91
5.2.3 Attenuated Total Reflectance – Fourier Transform Infrared Spectroscopy (ATR-FTIR) Characterization 95
5.2.4 Differential Scanning Calorimetry 97
5.2.5 Assessment of resistivity of PPy-Coated 3DSMP Foams 98
5.2.6 Evaluation of Joule-Heating Behaviors of PPy-Coated 3DSMP Foams 99
5.2.7 Shape Recovery using Joule-Heating 103
5.3 Discussion 106
5.3.1 PPy Coating Method Selection 106
5.3.2 Overall Findings 108
5.3.3 Study Limitations 110
5.4 Conclusion 114
CHAPTER 6 Translation of SMP-based Endovascular Devices: Elastase-induced Aneurysm Formation in New Zealand Rabbits for the Study of Pre-Clinical Effectiveness of Endovascular Devices 115
6.1 Materials and Methods 116
6.1.1 Aneurysm Formation 116
6.1.2 Assessment of Aneurysm Formation 117
6.1.3 Histology 118
6.1.4 Statistical Analysis 119
6.2 Results 119
6.2.1 Aneurysm Formation 119

6.2.2 Histological Assessment 120
6.3 Discussion 121
6.3.1 Our Approach 121
6.3.2 Applications for Endovascular Device Testing 123
6.3.3 Study Limitations 124
6.4 Conclusions 124
CHAPTER 7 Translation of SMP-based Endovascular Devices: Meta-Analysis of the Occlusion Effectiveness of Modern Endovascular Technology 125
7.1 Materials and Methods 126
7.1.1 Literature Search 126
7.1.2 Inclusion/Exclusion (I/E) Criteria for Study Screening 126
7.1.3 Data Collection 127
7.1.4 Outcomes 128
7.1.5 Statistical Analysis 128
7.2 Results 129
7.2.1 Literature Search Results and Screening 129
7.2.2 Patient and Study Demographics 130
7.2.3 Occlusion Effectiveness 132
7.2.3.1 Immediate Occlusion after Endovascular Treatment 132
7.2.3.2 Long-Term Occlusion Effectiveness of Endovascular Treatment 133
7.3 Discussion 135
7.3.1 Overall Remarks and Occlusion Effectiveness 135
7.3.2 Occlusion Efficacy of Other Devices 138
7.3.3 Implications for the Development of SMP-based Endovascular Devices 139
7.3.4 Study Limitations 140
7.4 Conclusions 141
CHAPTER 8 Conclusions and Future Work 143
8.1 Summary of Results 143
8.2 Future Directions 146
8.2.1 Material Microstructural Design for Guided Compression 146
8.2.2 Biocompatibility and Immunogenicity of SMPs 148
8.2.3 Mechanical & Microstructural Characterization of Arterial Tissues 150
8.2.4 Scaling of SMP-based Endovascular Device Production 151

8.2.5 Pre-Clinical Studies 152
APPENDIX A Nomenclature 153
APPENDIX B Synthesis of Patient-Specific Shape Memory Polymers Using a Leaching/3D-Printing Method 156
APPENDIX C PPy-Coating 168
APPENDIX D Label-Free Microstructural Characterization of Arterial Tissues Using Optical Clearing and Multiphoton Microscopy 170
APPENDIX E Meta-Analysis Protocol 174
APPENDIX F Meta-Analysis: List of Included Studies 181
References 186

List of Figures

Figure 2-1. Schematic of the Circle of Willis. Green labels indicate the posterior circulation segments and blue labels represent the posterior circulation. 6

Figure 2-2. Schematic of the two primary aneurysm treatment methods: (*left*) surgical clipping (the metal clip not drawn to scale) and (*right*) endovascular embolization using the Guglielmi detachable coils (GDCs). 8

Figure 2-3. Schematic of different state-of-the-art endovascular devices for occluding (i) "bifurcation" aneurysms (e.g., GDCs, hydrogel coils, liquid embolic devices, and woven EndoBridge—WEB); and (ii) "side-walled" aneurysms (e.g., flow diverter). . 9

Figure 2-4. Histological analysis of embolized aneurysms with bare coils vs. SMP-coated coils in a rabbit model. Staining was performed using Masson's trichrome at different timepoints (30, 60 and 180 days post-implantation) in this pre-clinical study. Scale bars = 1 mm. (Images were adapted from Herting *et al*. [21] with permission of John Wiley & Sons)..... 15

Figure 2-5. Schematic of two potential approaches to fabricate shape memory polymer (SMP)-based endovascular devices for ICA treatment: (a) SMP-coated coils; and (b) SMP coil-free foams with patient-specific geometries. 17

Figure 2-6. Methods for the fabrication of porous SMPs: CO_2 gas foaming (*left*), particle leaching (*middle*), and 3D-printing (*right*). 20

Figure 3-1. (a) Schematic of the experimental setup for measuring the volumetric resistivity of the CNT-infiltrated SMP foam. (b) Schematic of the experimental setup for shape recovery time assessment of the CNT-infiltrated SMP foam. 36

Figure 3-2. Scanning electron microscopy (SEM) images at 50X magnification: (a) the pristine

SMP foam, and (b) the CNT-infiltrated SMP foam. Scale bar = 500 μm. (c) Pore diameter fistribution of the pristine and CNT-infiltrated SMP foam. 40

Figure 3-3. (a) Photos of a pristine SMP foam (*left*) and a CNT-infiltrated SMP foam (*right*). (b) Measured density of the CNT-infiltrated foams at various CNT/POR ratios. (***denotes $p < 0.001$, and * indicates $p < 0.05$). (c) ATR-FTIR spectrum of the synthesized pristine aliphatic polyurethane SMP. 42

Figure 3-4. DSC measurements of Tg for (a) the pristine SMP at different monomer ratios (SMP11 is the target ratio in the present work), and (b) the porous CNT-infiltrated SMP foams with various CNT/POR ratios. Measurements of (c) the shape recovery time for the CNT-infiltrated SMP foams with various CNT/POR ratios, and (d) the volumetric resistivity (*** denotes $p < 0.001$, and * denotes $p < 0.05$)..... 43

Figure 3-5. (a) Minimum current required to trigger shape recovery for uniaxially-compressed CNT-infiltrated SMP foams at different CNT/POR concentrations. (b) Minimum current required to obtain 90% shape recovery in a period of ~2 min for uniaxially-compressed CNT-infiltrated SMP foams at different CNT/POR concentrations..... 46

Figure 3-6. IR thermal camera-measured heatmaps of a SMP foam (0.5% w/w CNT/POR concentration) subject to different direct currents, for evaluating its Joule-heating triggering behaviors at different time points of the applied current. 48

Figure 3-7. IR thermal camera-measured heatmaps of a SMP foam (0.75% w/w CNT/POR concentration) subject to different direct currents, for evaluating its Joule-heating triggering behaviors at different time points of the applied current. 49

Figure 3-8. IR thermal camera-measured heatmaps of a SMP foam sample (1.0% w/w CNT/POR concentration) subject to different direct currents, for evaluating its Joule-

heating triggering behaviors at different time points of the applied current..... 50

Figure 3-9. IR thermal camera-measured heatmaps of a SMP foam sample (1.25% w/w CNT/POR concentration) subject to different direct currents, for evaluating its Joule-heating triggering behaviors at different time points of the applied current..... 51

Figure 3-10. Average surface temperature as a function of time of the CNT-infiltrated SMP foams during electrical stimulation with different direct currents and various CNT/POR ratios: (a) 0.5%, (b) 0.75%, (c) 1.0%, and (d) 1.25% w/w. 53

Figure 3-11 (a) Representative results of the cyclic compression tests at Tg for (a) the pristine, and (b) the CNT-infiltrated SMP foams. (c) Cumulative stress reduction of the pristine and CNT-infiltrated SMP foams at various CNT/POR ratios after cyclic compression tests, demonstrating the stress relaxation trend (*** denotes $p < 0.001$). 54

Figure 3-12. Representative stress-strain compression curve for CNT-infiltrated SMP foams ($n = 3$) with a CNT/POR concentration of 0.75% w/w. 55

Figure 3-13. Demonstration of an idealized aneurysm phantom model occlusion using a CNT-infiltrated SMP foam (1.0% w/w CNT/POR). Heat maps indicate surface temperature of the foam during shape recovery. Shape recovery was triggered with a DC current of 1.0 A..... 56

Figure 4-1. (a) Schematics showing the steps for the fabrication of SMP foams using PVA 3D-printed templates (b) Pipeline for the production of patient specific PVA templates and phantoms from CTA imaging. The yellow arrow points at the parent vessel, which has a diameter of 2.45 mm. 3D model was enlarged twofold from its original dimensions to facilitate parent vessel access. 64

Figure 4-2. Photographs and SEM micrographs of the 3DSMP foams from the (a) top view

and (b) side view. 68

Figure 4-3. SEM micrographs of PVA templates (*top*) and 3DSMP foams (*bottom*) at different infill densities (*columns*). 69

Figure 4-4. Wall thickness measurements of PVA 3D-printed templates and the resultant 3DSMP foams after PVA leaching. (Significance levels: $*$ for $p < 0.05$, $**$ for $p < 0.01$). 70

Figure 4-5. (a) Tg measurements of solid SMP and 3DSMP. (b) Tg exponential models as a function of TEA molar ratio used to predict TEA content of 3DSMP foams with Tg ~ 41 °C. 71

Figure 4-6. (a) FTIR spectra of solid SMP and 3DSMP of the SMP-X ratio. (b) Zoomed spectra showing the modified urethane chemistry of the 3DSMP foams. 72

Figure 4-7. Representative compressive stress-strain curves of the 3DSMP foams fabricated with different infilldensities: (a) 40% (b) 50% (c) 60%. 74

Figure 4-8. Mechanical parameters derived from the stress-stretch curves of 3DSMP foams: (a) Peak stress, (b) CSR and (c) Elastic Mudulus; obtained for the *X*- (*left*) and *Z*-axis (*right*). 75

Figure 4-9. Shape recovery properties of the 3DSMP foams: Shape storage at (a) room temperature (T = 23 °C) and (b) T = –20 °C. (c) Shape recovery triggering using a heating ramp up to $T = T\text{g} + 10$°C. 76

Figure 4-10. Snapshots at different time points of the shape recovery experiment of 3DSMP specimens in a heating chamber. Insets show the temperature inside the heating chamber at each time point. 77

Figure 4-11. *Proof-of-concept* demonstration of the occlusion of aneurysm phantoms with

patient-specific image-based geometries using 3DSMP foams. Aneurysm geometries were enlarged threefold to facilitate delivery of the foam. 78

Figure 5-1. (a) Circuit diagram showing a microcontroller (MCU) sending a PWM signal to a transistor that controls electric flow through the PPy-coated 3DSMP foam. (b) Graphical representation of PWM signals at different duty cycles. 88

Figure 5-2. (a) Diagram representing the measured height of the foam during the shape recovery experiment. (b) Setup for the assessment of Joule-heating-induced shape recovery of the PPy-coated 3DSMP foams. 90

Figure 5-3. Representative photographs of the 3DSMP foams at different steps of the PPy-coating process: (*left*) pristine 3DSMP foam, (*center*) FeCl3-coated foam and (*right*) PPy-coated foam. 91

Figure 5-4. Ultramicroscope photographs of (a) pristine 3DSMP foams and (b) PPy-coated 3DSMP foams fabricated using 50% infill pattern densities. The yellow dashed box shows the area covered in (c) of the PPy-coated 3DSMP foams. (d) Edge of a PPy-coated foam demonstrating lack of PPy-coating at the contact areas with the container where polymerization was performed. 93

Figure 5-5. SEM micrographs of individual strands of 3DSMP foams: (a) Pristine 3DSMP and (b) PPy-coated 3DSMP foam. (c) Additional strand from the edge of a PPy-coated 3DSMP foam demonstrating charging (brighter edges), which is produced by (d) $FeCl_3$ crystals on the surface of the material. 94

Figure 5-6. ATR-FTIR spectrum of a PPy-coated 3DSMP foam. Labels indicate the most relevant molecular structures of the PPy-coated polyurethane material. 95

Figure 5-7. ATR-FTIR spectrum of a preliminary PPy-coated 3DSMP foam. Labels indicate

the molecular structures of the PPy that were observed in preliminary 3DSMP polyurethane foams. 96

Figure 5-8. Experimental Tg of 3DSMP-X and SMP9 ratios. Dashed lines indicated the predicted monomer ratio that yielded a $Tg \sim 41$ °C. 98

Figure 5-9. Volumetric resistivity measurements of PPy-coated 3DSMP foams coated with different $FeCl_3$ concentrations and polymerization time. 99

Figure 5-10. Representative heatmaps of a 3DSMP foam coated with PPy using a 5%w/v FeCl3 solution and 30min of polymerization time. Joule-heating was induced using a 30 VDC signal in a parallel plate setup. Thermal images were taken at different timepoints during electric stimulation. Square brackets indicate the position of the copper plates for all thermal images. 100

Figure 5-11. Representative heatmaps of a a 3DSMP foam coated with PPy using a 5%w/v FeCl3 solution and 60min of polymerization time. Joule-heating was induced using different duty cycles of a PWM 30 VDC signal at 490 Hz. Thermal images were taken after 10 s of stimulation with PWM signal. 101

Figure 5-12. Average temperature increase of the PPy-coated SMP foams after stimulation with different PWM duty cycle signals for 10 s. Results are grouped by FeCl3%w/v solution concentration: (a) 5%w/v, (b) 7.5%w/v and (c) 10%w/v. 102

Figure 5-13. Heating rate of the PPy-coated SMP foams after stimulation with different PWM duty cycle signals for 10 s. Results are grouped by FeCl3%w/v solution concentration: (a) 5%w/v, (b) 7.5%w/v and (c) 10%w/v. 103

Figure 5-14. Representative results of the shaperecovery of a PPy-coated 3DSMP foam (SMP8, FeCl3 = 7.5% ,Polymerization time = 60min) using Joule-heating at different

timepoints: (a) before applying a 30V pulse ($t = 0$s), (b) at the midpoint of the electrical pulse ($t = 5$s), (c) at the end of the pulse ($t = 10$s), and (d) cooling of the foam after the end of the pulse ($t = 20$s). (*Top row*) Top-down view of the surface temperature of the foam during shape recovery. (*Middle row*) Frontal view of the foam during shape recovery. (*Bottom row*) shows the average temperature of the foam during shape recovery. 105

Figure 5-15. Shape recovery behavior of three PPy-coated 3DSMP specimens and their surface temperature during the Joule-heating activation. 106

Figure 5-16. Representative thermographies of two PPy-coated 3DSMP foams with non-homogenous heating patterns: (a) exhibits a hotspot at one corner of the foam, and (b) exhibited a hotspot along the left side of the foam. 112

Figure 6-1. (a) Surgical setup for aneurysm formation, showing the use of the butterfly catheter. (b) Schematic of aneurysm formation via elastase injection: (b.1) healthy vascular wall with integral elastic lamina, (b.2) elastic lamina degradation induced by elastase injection and (b.3) focal dilation of the arterial wall caused by the breakdown of the elastic lamina. 118

Figure 6-2. Representative angiograms of the created aneurysms. The green arrows point towards the created aneurysms and the yellow arrow indicates the RCCA. Scale bars = 10 mm). 120

Figure 6-3. Histology slides of the created aneurysms depicting elastin degradation at (a) 2 weeks, (b) 4 weeks, and (c) 6 weeks. Red arrows indicate the portions of the non-degraded elastic lamina. Yellow arrows indicate the degradation of the elastic fibers. Scale bars = 0.5 mm. 121

Figure 7-1. Flow diagram for the screening of obtained studies. *n* represents the number of studies that were included after each phase of the screening process..... 129

Figure 7-2. LGLMM model fits for probability of RROC-I as a funcion of follow-up time for the evaluated endovascular therapy techniques. Grey shading areas represent CI 95%. 135

Figure 8-1. Compression patterns and their effects on the compressed foam geometry. Diagrams represent a cross-section of the 3DSMPs obtained using our leaching/3D-printing method. (a) represents the current infill design of the 3DSMP foams, and the dashed gray lines represent the compressed geometry exhibiting Poisson effect. (b) denotes an ideal design (not physically accurate) with a porosity gradient that allows compression to a circular cross sections (a rod-like geometry in 3D). 147

Figure 8-2. Comparison of the normalized absorbance of PrestoBlue assay on rBMSC cultured on 3DSMP, solid SMP or alone, as control ($n = 6$). 149

Figure 8-3. Representative specimens of our MPM microstructural assesssments of coronary artery tissues. Each representative autofluorescence micrograph represents a region of the left anterior descending artery and its collagen fiber architecture at the tunica adventitia. The arrows represent the longitudinal (L) and circumferential (C) directions of the tissue. Heatmaps represent the tissue-thickness-dependent fiber orientation probability. See Pineda-Castillo *et al*. [209] for more details on this study. 151

Figure B-1. Photograph of a PVA template with a 50% grid infill density. 158

Figure B-2. Photograph of a representative specimen of a PVA template infiltrated with cured SMP solution. The bulging of the SMP on the top surface (referred to as “SMP mushroom” internally) of the PVA template demonstrates proper curing. 164

Figure D-1. Photographs of coronary artery tissues in a falcon tube containing the clearining solutions and their effect in the resultant optically-cleared tissue. 172

Figure D-2. (a) Diagram representing the top and cross-sectional view of the mounting of a cleared specimen on a glass slide using double sided tape to build a BABB reservoir. (b) Photograph of a cleared specimen mounted on a glass slide. 173

List of Tables

Table 2-1. Current endovascular devices for the treatment of ICAs and their advantages and limitations. 16

Table 2-2. Summary of materials with shape memory properties, activation methods and outstanding reported features. 26

Table 4-1. Monomer molar ratios for the fabricated polyurethane 3DSMP foams. 63

Table 6-1. Geometric dimensions of the elastase-induced aneurysms in New Zealand rabbits at different time points. 119

Table 7-1. List of aneurysm locations at the Circle of Willis and their corresponding acronyms. 128

Table 7-2. Country distribution of the studies included in the meta-analysis. 130

Table 7-3. Patient demographics and meta-averages of aneurysm dimensions. 131

Table 7-4. Meta-proportions of ICA anatomic location on the circle of Willis. 131

Table 7-5. Pooled meta-proportions of RROC-I for modern endovascular devices, except flow diverters..... 133

Table 7-6. Model parameters for the LGLMM and FELM models of probability of RROC-I as a function of follow-up (FU) time for endovascular therapy techniques. OR: odds ratio. 134

Table A-1. List of abbreviations used throughout the dissertation. 153

Table F-1. List of the studies included in the meta-analysis after the screening process. ... 181

Acknowledgments

The research presented in this dissertation would not have been possible without the contributions of many people. First, I would like to thank my advisor Dr. Chung-Hao Lee. I would like to thank you for the opportunity to join this research group, for allowing me to be a part of this project and for all the endless support and mentoring over the years. My journey at the University of Oklahoma as a doctoral student was filled with exciting and challenging experiences, and your mentorship was fundamental for my professional development. I will remember my time at the Biomechanics and Biomaterials Design Laboratory (BBDL) as a ride full of adventures, ideas, discussions, and growth.

I also want to thank my doctoral committee: Dr. Michael S. Detamore, Dr. Handan Acar, Dr. Keisha B. Walters, and Dr. Andres Gonzalez. Each one of you contributed to my professional development in a unique way, and I will be forever grateful for your teachings, time, and dedication to my education. Also, I would like to thank other faculty: Dr. Tingting Gu, for all your dedication and passion for confocal microscopy, Dr. Preston Larson, for your kindness and dedication to scanning electron microscopy, Dr. Brian Grady, for your mentorship with polymer science, Dr. Ingo Schlupp, for the passion for statistics that you passed on to me, among many other faculty members.

The BBDL was also a place of friendship. Here, I was able to collaborate, discuss research, and grow with my PhD brothers: Colton Ross, Dr. Devin Laurence, Luke Hudson and Ryan Bodlak. You have been a source of inspiration, friendship, and support that I will cherish forever. My learnings and memories from each of you have been a fundamental part of my

professional and personal development. I would also like to thank many researchers that have passed through our lab, including Santiago Aparicio, Keely Laurence, Launy Ohanina, Tanner Cabaniss, Marwan Hashem, Madison Burns, Aryn Stiles, Lauren Thoendel, Elizabeth Bradshaw, Evan Jones, Michael Barber, and so many other great members of the BBDL. Also, I would like to extend my gratitude to fellow doctoral researchers and friends at the Stephenson School of Biomedical Engineering: Rana Ajeeb, Boushra Ajeeb, and Vinit Sheth. You provided me with friendship and support at different times of my doctoral program, and I will always be thankful to have shared this adventurous ride with you.

I would also like to express my deep gratitude towards the Colombian Student Association (COLSA) at OU. COLSA has been a home away from home, a small piece of my country in Oklahoma. Specially, I would like to thank Yoana Walschap and Dr. Andres Gonzalez, who continuously devote their lives and energy to our members and Colombian culture. At COLSA, I have built many friendships that have supported me and have made these years easier and happier: Valentina Ricaurte (and Magdalena), Andrea Tavera, Angela Tavera, Pedro Sánchez, Camila Quintero, and Nicole Molina. I will be forever thankful for all the great memories that we built together.

I would also like to express my eternal gratitude to my best friends: Libia Barandica, Juan Pablo Bedoya, Johana Albarracin and Cristian Bernal. You are the family that I chose. You have provided me with the most unconditional support and love. Even from the thousands of kilometers that separate us, I have always felt your company and support during these years.

I would also like to thank my family in Oklahoma: Alejandro, Luis Alberto, Amelia, Adriana, Javier, Christian and Sarah. You have been my greatest source of support in Oklahoma, and I will always be thankful for introducing me to this *Sooner* family and for everything that you have done for me.

Lastly, and most importantly, I would like to thank my parents Celio Pineda and Nelly Castillo, and my sister, Dr. Natalia Pineda. You inspire me every day with your love, passion, and determination. Thank you for giving me the support and inspiration to dream and to live my life to the fullest. I dedicate this dissertation to you, to our family and to all the great things that we have done and will do together.

Thank you.

Vita

2012-2018	B.S., Biomedical Engineering, Universidad Manuela Beltrán (UMB) *Thesis: "Synthesis and characterization of chitosan/polyvinyl alcohol scaffolds via freeze-drying for bone regeneration"*
2018	First *first-author* publication in MDPI Molecules
2018-2019	Clinical Data Manager, Merck & Co, Bogotá, Colombia
2019-2023	Research Assistant, Biomechanics and Biomaterials Design Laboratory, University of Oklahoma (OU)
2019-2023	OU Graduate College Alumni Fellowship
2021	Featured Cover Art, Advanced Engineering Materials
2022	Approval of Doctor of Philosophy Candidacy
2022	OU Graduate College Dissertation Excellence Award
2023	3-minute Thesis® Competition Finalist

Publications

2023

Pineda-Castillo SA, Cabaniss TL, Jones ER, Thoendel LR, Lee H, Bohnstedt BN, Liu Y, Lee C-H "Development of a Polypyrrole-Coated Shape Memory Polymer Device for the Treatment of Intracranial Aneurysms" *In preparation,* 2023.

Pineda-Castillo SA, Jones ER, Thoendel LR, Cabaniss TL, Lee H, Bohnstedt BN, Liu Y, Lee C-H "Are Coils Still the Gold Standard for Endovascular Therapy of Unruptured Saccular Aneurysms? – A Comprehensive Meta-Analysis" *In preparation,* 2023.

Pineda-Castillo SA, Cabaniss TL, Aboukeila H, Grady B, Lee H, Bohnstedt BN, Liu Y, Lee C-H "Towards the Development of A Patient-Specific Endovascular Device for Intracranial Aneurysm Therapeutics Using a 3D-Printing/Leaching Method" *Submitted to Advanced Healthcare Materials,* 2023.

Pineda-Castillo SA, Acar H, Detamore MS, Holzapfel GA, Lee C-H "Smooth Muscle Cell Phenotype Modulation: A Key Component for the Translation of Tissue-Engineered Vascular Grafts" *Tissue Engineering Part B,* 2023.

2022

Pineda-Castillo SA, Stiles AM, Bohnstedt BN, Lee H, Liu Y, Lee C-H, "Shape Memory Polymer-Based Endovascular Devices: Design Criteria and Future Perspective" *Polymers*, 14(13), 2526, 2022.

Pineda-Castillo SA, Aparicio-Ruiz S, Burns MM, Laurence DW, Bradshaw E, Gu T, Holzapfel GA, Lee C-H, "Linking the Region-Specific Tissue Microstructure to the Biaxial Mechanical Properties of the Porcine Left Anterior Descending Artery" *Acta Biomaterialia*, 15, 295-309, 2022.

2021

Pineda-Castillo, S, Laurence, KA, Homburg, H, Fung, K-M, Bohnstedt, BN, and Lee, C-H, "A Protocol for the Reduction of Applied Torque On Parent Vessel During Elastase-Induced Aneurysm Formation Using Rabbit Animal Models" *bioRxiv* (*preprint*), 2021**.**

Pineda-Castillo SA, Luo J, Lee H, Bohnstedt BN, Liu Y, Lee C-H, "Effects of Carbon

Nanotube Infiltration on a Shape Memory Polymer-Based Device for Brain Aneurysm Therapeutics: Design and Characterization of a Joule-Heating Triggering Mechanism" *Advanced Engineering Materials – Featured in Issue Cover*, 14(13), 2100322, 2022.

2018

Pineda-Castillo SA, Bernal-Ballén A, Bernal-López C, Segura-Puello H, Nieto-Mosquera D, Villamil-Ballesteros A, Muñoz-Forero D, Munster L, "Synthesis and Characterization of Poly(Vinyl Alcohol)-Chitosan-Hydroxyapatite Scaffolds: A Promising Alternative for Bone Tissue Regeneration" *MDPI Molecules*, 23(10), 2412, 2022.

Conference Presentations

2023

Pineda-Castillo SA, Cabaniss T, Bohnstedt BN, Lee C-H, "Shifting the Endovascular Paradigm: Patient-Specific Treatment of Intracranial Aneurysms Using Shape Memory Polymers and Additive Manufacturing" (*Oral presentation*) Summer Biomechanics, Bioengineering and Biotransport Conference (SB3C), June 4-8, 2023.

2022

Pineda-Castillo SA, Aparicio-Ruiz S, Lee C-H, "Investigation of the Regional Variations in the Mechanical Properties and Microstructure of Porcine Left Anterior Descending Artery" (*Oral presentation*) Summer Biomechanics, Bioengineering and Biotransport Conference (SB3C), June 20-23, 2022.

2021

Pineda-Castillo SA, Aparicio-Ruiz S, Lee C-H, "Regional Microstructural and Mechanical Properties of Porcine Left Anterior Descending Artery" (*Poster*) Biomedical Engineering Society Annual Meeting, October 6-9, 2021.

Pineda-Castillo SA, Bohnstedt BN, Liu Y, Lee C-H, "Carbon Nanotube Infiltration Effects in Thermal Properties of Shape Memory Polymer Foams – Design of a Triggering Mechanism for Endovascular Devices" (*Poster*) Summer Biomechanics, Bioengineering and Biotransport Conference (SB3C), June 14-18, 2021

2020

Pineda-Castillo SA, Luo J, Bohnstedt BN, Liu Y, Lee C-H, "Shape Memory Polymer Foam with Tunable Properties for Treatment of Intracranial Aneurysm." (*Peer-reviewed paper*), International Mechanical Engineering Congress and Exposition (IMECE2020) Virtual meeting, November 16-19, 2020

Abstract of the Dissertation

DEVELOPMENT OF PATIENT-SPECIFIC SHAPE MEMORY POLYMER FOAMS FOR THE TREATMENT OF INTRACRANIAL ANEURYSMS

by

Sergio Andres Pineda Castillo

Doctor of Philosophy in Biomedical Engineering

University of Oklahoma, Norman, OK, 2023

Dr. Chung-Hao Lee, Chair

The objectives of this research include: (1) designing an electrically conductive shape memory polymer (SMP) material, (2) developing a method for the systematic fabrication of SMPs with complex three-dimensional geometries based on computerized angiography tomography (CTA) of human patients, and (3) establishing translation strategies for a SMP-based endovascular device for the treatment of unruptured saccular intracranial aneurysms (ICA).

We first characterized the thermomechanical properties of a porous polyurethane SMP that was infiltrated with carbon nanotubes (CNT) to induce electric conductivity in the polymeric matrix. The CNT-infiltrated SMP foams were characterized using materials science techniques that include: (i) differential scanning calorimetry (DSC) to determine the effect of CNT-infiltration on the thermal properties of the material; (ii) scanning electron microscopy (SEM) to characterize the pore morphology and interconnectivity, and (iii) uniaxial compressive testing, to characterize the effect of CNT-infiltration in the cyclic mechanical properties of the material. Then, we demonstrated the use of a CNT-infiltrated SMP foam to occlude an idealized aneurysm phantom. From these experiments, we determined that CNT-infiltrated SMP materials have the potential to be used as ICA embolic devices. However, these materials were subject to several limitations that make their translation difficult, including poor mechanical properties under cyclic compression, and a relatively high electric resistivity, that requires high currents to trigger shape recovery of the SMP.

Based on the observed limitations of the CNT-infiltrated SMP material, we further performed two studies to improve the performance of our polyurethane formulation to be used as an embolic device for ICA endovascular therapy. First, we developed a method for the manufacturing of SMPs with complex 3D geometries. Due to the high degree of chemical crosslinking present in our SMP formulation, traditional 3D-printing techniques are not compatible with our material. Therefore, we developed a technique that combines leaching and 3D-printing for the fabrication of SMP foams based on CTA-informed ICA geometries. First, we fabricated polyvinyl alcohol (PVA) templates with custom pore geometries and densities. Then, we used these templates to fabricate our SMP material. By means of washing out the

PVA after SMP curing, we obtained 3DSMP foams that mimicked the PVA template geometry. We also explored the effect of PVA leaching on the thermomechanical properties of the material. We found, from DSC, that the PVA leaching process induced a reduction in the glass transition temperature of the material (T_g), due to the chemical modification of the urethane groups. In addition, we found that the 3DSMP foams exhibited anisotropic mechanical properties and long-term shape recovery storage. Finally, we demonstrated the use of this manufacturing process to synthesize *patient-specific* 3DSMP foams. Using *in vitro* aneurysm models, we demonstrated that these personalized foams had the potential to provide complete ICA occlusion immediately after treatment.

Building on our knowledge on the fabrication of 3DSMP foams using a leaching/3D-printing method, we aimed to induce conductivity on the 3D matrices. To do this, we performed *in situ* polymerization of polypyrrole (PPy), a well-described biocompatible conductive polymer, on the surface of the foams. We also modified our leaching/3D-printing method to prevent the reduction of the T_g of the material. The coating of the 3DSMP foam resulted in the induction of excellent electric conductivity on the polyurethane material. We observed that the material exhibited significantly lower resistivities than the previously developed CNT-infiltrated SMPs. This allowed the 3DSMP foams to undergo the Joule-heating process at low voltages and reach temperatures above T_g in less than 10 seconds. In addition, we developed a system to control the maximum temperature reached by the foams using pulsed electrical signals. Further, the PPy-coated 3DSMP foams underwent recovery behaviors as a response to electric stimuli. These characterizations showed the potential of the PPy-coated 3DSMP material for the development of a novel endovascular device for the treatment of unruptured saccular ICAs.

In addition to the development of the material properties and functionality as an endovascular device, we also focused on planning translational research that facilitates the application of the proposed SMP-based endovascular device in the clinic. To achieve this, we first established an animal model for the testing of our embolic device *in vivo* prior to clinical trial studies. This animal model involves the creation of saccular aneurysms in New Zealand rabbits. Aneurysms were surgically created at the right common carotid artery by temporarily ligating the artery and then allowing an elastase solution to degrade the elastic lamina of the vascular wall. This weakening of the wall induced the bulging of the artery. In this work, we explored the stability of the aneurysms at different periods and assessed the histological structure of the aneurysms. This animal model will serve as a means to test the *in vivo* biocompatibility and endovascular occlusion effectiveness of our PPy-coated 3DSMP foam in the future.

These future studies will be comparing the immediate and long-term occlusion effectiveness between our SMP-based device and a "*gold standard*" device that is currently available in the market. This comparison will demonstrate the potential superior effectiveness of our individualized treatment approach. However, selecting the *gold standard* as the control group is a challenging decision, due to the great diversity of modern endovascular devices for the treatment of unruptured saccular ICAs. Therefore, we performed a *first-of-its-kind* meta-analysis of the immediate (day 0) and long-term (post-implantation)occlusion effectiveness of modern endovascular devices. We thus performed a systematic search of studies that characterized the complete occlusion degree of ICAs of endovascular devices. Our results suggested that the most prominent endovascular devices of modern times (Guglielmi

detachable coils (GDCs), flow diverters and the Woven EndoBridge) exhibit similar long-term efficacy in ICA treatment. In addition, we further showed that the immediate occlusion probability of the GDCs is the highest among the compared devices. Therefore, we selected coiling techniques as the *gold standard* for the *in vivo* assessment of endovascular embolization efficacy of our SMP-based device.

CHAPTER 1 Introduction

1.1 Motivation

Intracranial aneurysms (ICAs) are focal dilations of the brain arterial wall with relative risk of rupture. This event leads to subarachnoid hemorrhage (SAH), which can lead to death or long-term disability. Surgeons have aimed at treating ICAs since 1933, when Norman Dott surgically treated an ICA for the first time [1]. Ever since, techniques and devices have emerged for the treatment of ICAs. In 1991, Guglielmi *et al*. revolutionized the field of ICA therapeutics with the invention of the Guglielmi detachable coil (GDC), a device that allowed endovascular embolization of the ICA using a minimally invasive approach [2, 3].

Despite the invention of GDCs and its improved iterations and novel endovascular device, ICA recurrence is still a major issue than can lead to retreatment or ICA rupture. While aneurysm recurrence is related to several risk factors associated with initial treatment, the most prominent predictor for aneurysm recurrence is whether complete aneurysm occlusion is achieved immediately after treatment [4]. Therefore, the development of endovascular therapies that guarantee complete occlusion immediately after treatment is of paramount importance for the long-term prevention of ICA recurrence and retreatment.

1.2 Objective and Scope

The objective of this dissertation is three-fold: (i), to develop a coil-free endovascular device based on polyurethane shape memory polymers (SMPs); (ii) to design a method for the fabrication of individualized SMP-based endovascular devices using medical imaging data of ICAs, and (iii) to establish experimental strategies for the translation of the SMP-based

endovascular device. These developments are summarized as follows:

(1) *Design and characterization of carbon nanotube-infiltrated porous SMPs*

In this work, we took our first attempt at the fabrication of SMPs with a functional triggering mechanism. We infiltrated carbon nanotubes (CNTs) in the polymeric matrix by using a sugar-leaching method to fabricate porous SMPs. We characterized the thermomechanical properties of the material to determine the effects of CNT infiltration in SMP's properties. Then, we used the CNT-infiltrated porous SMP to demonstrate the occlusion of idealized aneurysm models.

(2) *Development of a leaching/3D-printing method for the fabrication of patient-specific SMP foams*

Based on the observed limitations of the sugar leaching method, we further developed a manufacturing process that allows for the fabrication of complex 3D porous geometries of SMPs. We developed a facile technique that uses polyvinyl alcohol (PVA) water-soluble templates for customizable SMP fabrication. Then, we used microscopy to demonstrate the potential of the SMPs to replace the inner microstructure of PVA templates with controllable resolution. Finally, we used this method to fabricate porous SMPs with patient-specific geometries for *in vitro proof-of-concept* of ICA occlusion.

(3) *Use of polypyrrole as a triggering mechanism for shape recovery of the 3DSMP foams*

Due to the limitations of CNTs in the design of a conductive SMP material, we introduced an *in situ* polymerization method to coat 3DSMP foams with polypyrrole

(PPy), a biocompatible conductive polymer. We employed thermal analysis techniques to assess the induced Joule-heating behaviors on the foam, and its potential to trigger shape recovery of the material. In addition, we applied pulse-width-modulated electrical signals to control the heat release of the PPy-coated 3DSMP foams. With this development, we overcame the limitations of our previous attempts of obtaining an electrically triggered SMP.

(4) *Establishing an animal model for the in vivo testing of SMP-based endovascular devices*

Translation of SMP-based devices requires careful *in vivo* testing prior to its assessment in clinical settings. Therefore, we established an animal model for the testing of safety and efficacy of our SMP-based endovascular devices. We adapted New Zealand male rabbits for the modeling of saccular aneurysms. We performed right common carotid artery ligation and elastase washing to degrade the vascular wall. This induces the degradation of the elastic lamina and the subsequent protrusion of a saccular aneurysm. We also provided new insights into the surgical procedure required to create reproducible aneurysms in this rabbit model.

(5) *Meta-analysis of modern endovascular therapy long-term efficacy*

The pre-clinical assessment of our SMP-based device requires that we assess the immediate occlusion effectiveness of our SMP embolic device and compare it to the "*gold standard*" in ICA endovascular therapy. Traditionally, the GDCs have been considered the *gold standard* for this type of assessments. However, due to the

emergence of novel endovascular devices for the treatment of saccular unruptured ICAs, we performed a meta-analysis of the reported immediate occlusion rates of several modern endovascular devices to determine the validity of this assumption. Using long-term data available in the literature and meta-regressions, we compare the efficacy of the most prominent endovascular devices and select one for the pre-clinical *in vivo* testing of our SMP-based device.

The remainder of this dissertation is organized as follows. Chapter 2 provides a literature review of brain vasculature, ICA incidence and risk factors, *state-of-the-art* endovascular devices for ICA therapy and the use of SMPs as embolic devices. In Chapter 3, we explore the use of CNTs to induce Joule-heating behaviors in SMP foams. The limitations from Chapter 3 are then addressed by Chapter 4, where we explore the use of a leaching-3D-printing method for the fabrication of patient-specific SMP foams, and in Chapter 5, where we use PPy as an alternative for the induction of Joule-heating behaviors in 3DSMP foams. Chapter 6 describes our approach to the establishment of a New Zealand rabbit animal model of saccular aneurysms. Then, Chapter 7 describes a meta-analysis of the reported immediate occlusion rates of modern endovascular devices; information that will be used to guide our future *in vivo* testing of the SMP devices. Finally, concluding remarks and future research strategies for the translation of SMP-based devices are provided in Chapter 8.

CHAPTER 2 Literature Review

2.1 Brain Vasculature Anatomy and Intracranial Aneurysms

2.1.1 Brain Vasculature Anatomy

Brain irrigation initiates at the left atrium, where oxygenated blood is ejected into the ascending aorta. As blood travels along the aortic arch, it first circulates to the brachiocephalic trunk, which branches into the subclavian artery and the right common carotid artery (RCCA). The left common carotid artery (LCCA) emerges directly from the aortic arch. Both CCAs ascend to the head and neck and then traverse the carotid sheath, where they bifurcate into the external and internal carotid arteries (ECA and ICaA, respectively) at the level of the fourth cervical vertebra (C4). The ECAs supply blood to the neck, face, and scalp, while the ICaAs travel across the carotid canal of the temporal bone (base of the skull) to enter the cranial cavity, where they anastomose with the vertebral arteries (the VAs) to form the circle of Willis (**Figure 2-1**) [5]. The VAs emerge from the subclavian arteries at the root of the neck, and travel through the foramina transversaria of the sixth cervical vertebra upwards to the first cervical vertebra. Then, they traverse the foramen transversarium of the atlas vertebra, the foramen magnum, and the dura mater to reach the cranial cavity. Inside the cranium, they anastomose with the branches of the ICaAs. Due to its complex anatomical structure (**Figure 2-1**), the Circle of Willis harbors more than 85% of intracranial aneurysms [6].

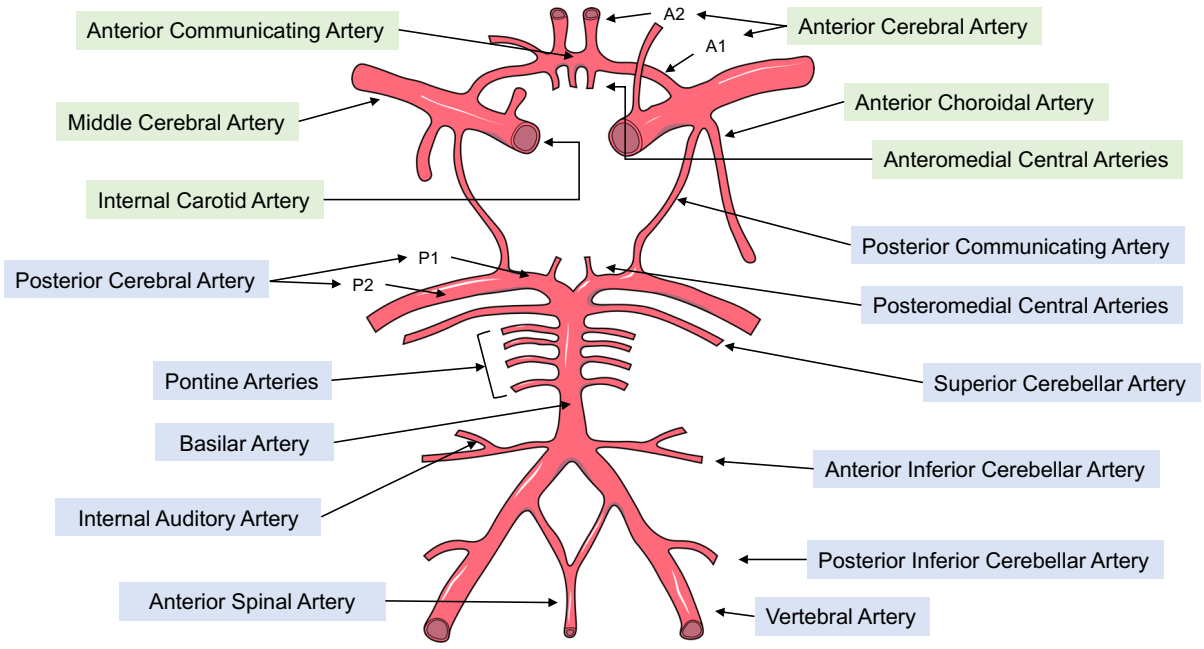


Figure 2-1. Schematic of the Circle of Willis. Green labels indicate the posterior circulation segments and blue labels represent the posterior circulation.

2.1.2 Intracranial Aneurysms: Definition, Incidence and Demographics

Intracranial aneurysms (ICA) are focal dilations of the vascular wall of intracranial arteries. ICAs predominantly emerge at the Circle of Willis and are described to occur due to a combination of factors that include hypertension, high wall shear stress, and collagen and elastin degradation in the vascular wall [7]. Specifically, aneurysm formation begins with the degradation of the elastic lamina of the arterial wall [8], which leads to the bulging of the wall, the initiation of inflammatory processes, and the stabilization of the aneurysm [9]. However, this dilation of the wall is at a relatively high risk of rupture, which makes ICAs the main cause of subarachnoid hemorrhage (SAH): a bleeding in the space between the arachnoid membrane and the pia mater that can lead to moderate-to-severe brain damage, long-term morbidity, and/or mortality [6, 10, 11].

Unruptured ICAs affect 3-5% of the general worldwide population, but the incidence can vary regionally, with countries such as Japan and Finland exhibiting incidences as high as 21.5 and 27.9 per 100,000 person-years, respectively. They are in particular prevalent at ages of 40-65 years old [12] and most remain asymptomatic. However, 3-50 in every 100,000 ICAs will eventually rupture. The risk of ICA rupture is associated with multiple factors, including aneurysm size, location, sex, hypertension, and smoking history [12, 13]. This rupture risk can potentially be mitigated by timely ICA diagnosis and prophylactic therapy.

2.2 Unruptured Aneurysms and Treatment Options

Current treatment of unruptured aneurysms involves microsurgical clip ligation or endovascular embolization. In microsurgical clipping, neurosurgeons first perform a craniotomy. Then, they use a metallic clip to tighten the aneurysm neck to completely prevent the intra-aneurysmal flow (**Figure 2-2**). Due to its high invasiveness, microsurgical clipping poses higher procedural risks and may not be suitable for elder patients. On the other hand, endovascular embolization serves as a minimally invasive approach. In endovascular embolization, surgeons deliver platinum coils (or other embolic devices) to the aneurysm sac to minimize the intra-aneurysmal flow (**Figure 2-2**). Overall, endovascular therapies have better clinical outcomes and are associated with reduced treatment-related mortality [14-16]. Despite this short-term therapeutic advantage, endovascular embolization therapies more frequently require a second procedure (i.e., re-operation) than microsurgical clipping, according to the randomized, multicenter Phase III International Subarachnoid Aneurysm Trial (ISAT) [17]. The unsatisfactory long-term outcome of endovascular embolization is an emerging clinical issue that arises from aneurysm recurrence, where the aneurysm sac grows

and the neck becomes incompletely occluded due to the gradual coil compaction over time and the resulting increased residual flow within the aneurysm sac [4].

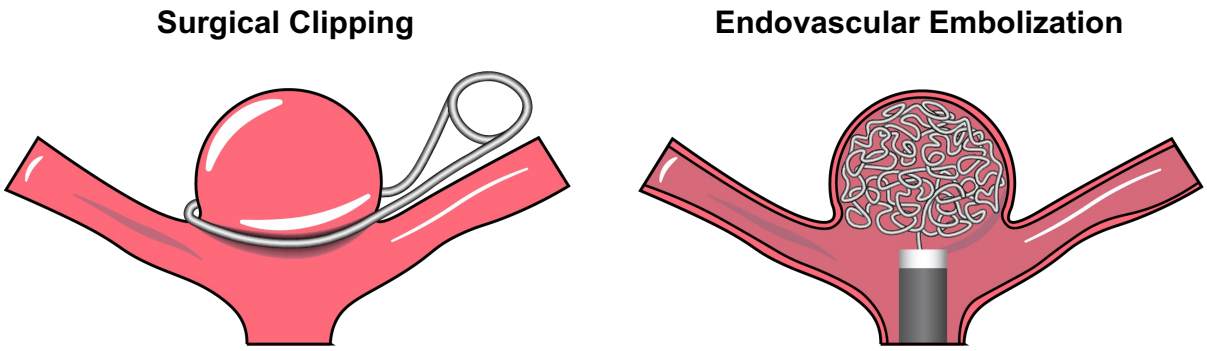


Figure 2-2. Schematic of the two primary aneurysm treatment methods: (*left*) surgical clipping (the metal clip not drawn to scale) and (*right*) endovascular embolization using the Guglielmi detachable coils (GDCs).

The remainder of this chapter is as follows. We will first discuss the *state-of-the-art* endovascular devices for ICA endovascular embolization, their mechanisms of action, and their advantages and limitations. Then, we will present our approach for the development of SMP-based endovascular devices and the status of SMP research: materials, polymeric architectures, chemical features, activation methods, and the recent efforts for the clinical translation of SMP-based endovascular devices for ICA treatment. Finally, we will conclude this literature review with remarks on the developments in our group prior to this dissertation.

2.2.1 Endovascular Embolization

Endovascular devices for ICA treatment were first developed by Guglielmi *et al*. [2, 3, 18] in 1990, where soft and thin platinum wires, called Guglielmi detachable coils (GDCs), were wrapped inside the aneurysm sac to prevent the intra-aneurysmal blood flow (**Figure 2-3**). In addition, the GDCs were designed with the capacity to induce thrombogenesis, a process where platelets accumulate on the surface of the coil using electrical stimuli. These devices revolutionized the treatment of ICAs, owing to their minimally invasive approach using catheter-guided delivery. Ever since the first introduction of this technology, it has become the *gold standard* for the treatment of saccular ICAs.

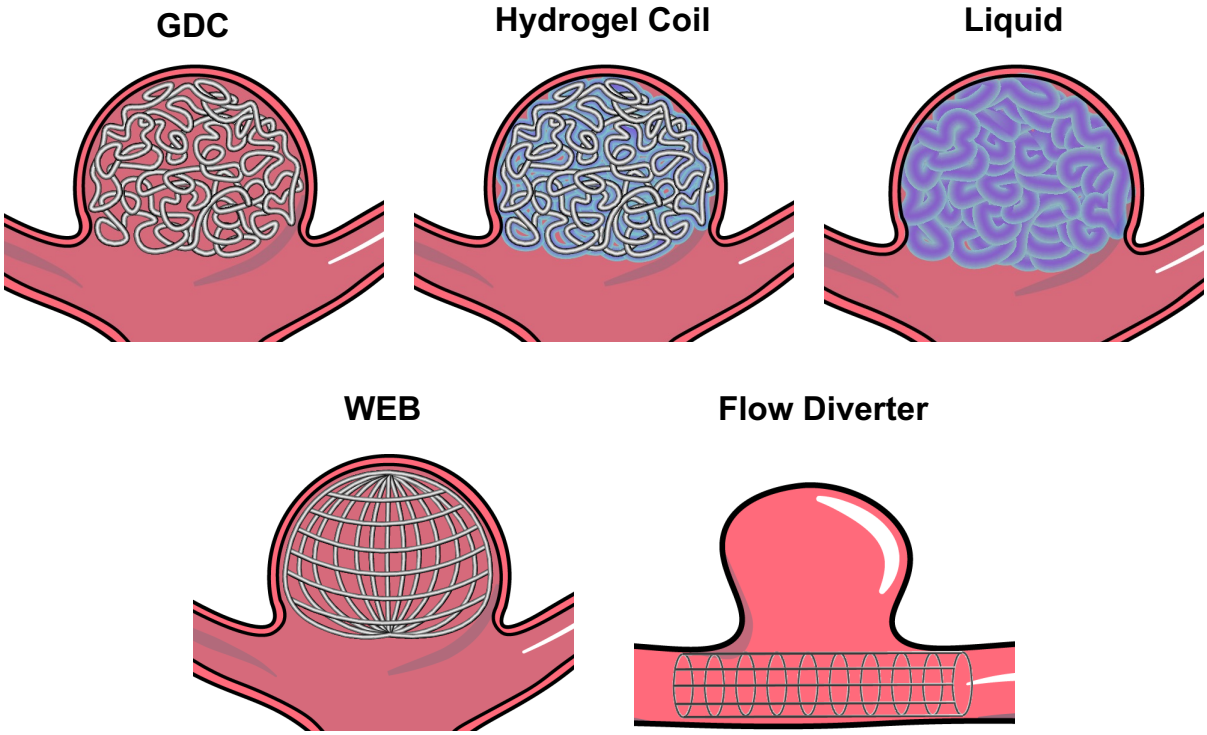


Figure 2-3. Schematic of different state-of-the-art endovascular devices for occluding (i) "bifurcation" aneurysms (e.g., GDCs, hydrogel coils, liquid embolic devices, and woven EndoBridge—WEB); and (ii) "side-walled" aneurysms (e.g., flow diverter).

The GDC-based therapies have been further improved by the inclusion of assisting devices. For example, treatment of wide-neck ICAs was not possible with GDCs alone, as coils might migrate into the bloodstream in the parent artery. This limitation was later overcome by integrating wire-meshed stents or balloons to mechanically support the implanted coils [19]. In addition, coatings for coils, such as hydrogel or porous polymers, have also been developed to increase the packing density – another challenge in the conventional endovascular coil embolization (i.e., bare coils) [20, 21]. In the following, we will present an overview of the most prominent developments of various endovascular devices for ICA embolization, as well as their limitations.

2.3 *State-of-the-art* Endovascular Devices

2.3.1 Hydrogel-Coated Coils

The GDCs frequently face limitations in packing density, due to the non-homogeneous spatial distribution of the coil inside the aneurysm [22]. To address this, the coating of coils has been designed to reduce the gaps between coil wrappings. Hydrogel-coated coils are the most predominant designs for this approach (**Figure 2-3**). For example, the HydroCoil endovascular system has been extensively studied for its application in ICA treatment. This device aims to increase the volumetric filling of the aneurysm using a hydrogel that swells in contact with water. The HydroCoil endovascular aneurysm occlusion and packing study (HELPS) compared their performance to bare GDCs, where they found that the major aneurysm recurrence was reduced with the use of the hydrogel-coated coil, but other clinical outcomes had similar performance to the control group (i.e., bare GDCs) [23, 24]. This led to the subsequent development of the HydroSoft, a more advanced hydrogel-based coil, where the

hydrogel was used as the inner core of the device. The HydroSoft aimed to reduce the limitations of the HydroCoil that introduced coil stiffness and a highly sensitive time restriction for its delivery. Guo *et al.* compared the use of these two devices and found that the HydroSoft coils had lower rates of neck remnant than the HydroCoil [25]. The German-French Randomized Endovascular Aneurysm Trial (GREAT) also tested the HydroSoft device and compared it to bare GDCs [26]. This multicenter study found that composite angiographic and clinical outcomes were improved in the HydroSoft group, while adverse and serious adverse events occurred at similar rates in both groups. However, other clinical trials, like the Patients Prone to Recurrence After Endovascular Treatment (PRET) trial, have demonstrated that hydrogel-coated coils do not provide improved clinical outcomes when compared to bare coils [27]. Overall, meta-analysis of the performance of hydrogel coils have demonstrated that the second-generation hydrogel coils (HydroSoft) might improve residual aneurysm and midterm recurrence, but do not exhibit any other significant differences to traditional GDC coiling [28].

2.3.2 Hydrogel/Liquid Embolic Materials

As another ICA treatment technique, coil-free materials have been developed to occlude ICAs and, potentially, result in a higher rate of complete occlusion. Materials with induced *in situ* polymerization have been used for these applications (**Figure 2-3**). For example, Poupart *et al.* designed a liquid polyethylene glycol dimethacrylate (PEGDMA) precursor with the potential to be delivered to an in-vitro aneurysm model and to be photopolymerized using ultraviolet (UV) light *in situ*. This material exhibits great potential for its *in vitro* application, due to its ease-of-use and low erosion rates [29, 30]. However, *in vivo* testing and evaluation are yet to be performed to understand the complete potential of this device.

Another liquid embolic material with great potential for translation is Onyx. This material is a copolymer of ethylene and vinyl alcohol dissolved in dimethyl sulfoxide (DMSO). When in contact with other liquids, DMSO rapidly phase separates from the co-polymer and induces *in situ* solidification. This mechanism allows for the delivery of the embolic material at the aneurysm lumen. Early in-vivo testing of the Onyx device in swine models demonstrated that occlusion with the material alone was effective, despite long delivery times (~ 40 min) and potential migration of the material into the parent artery [31]. Onyx has been translated into clinical use, where excellent occlusion rates have been reported [32]. Nonetheless, complications, such as mass effect, DMSO toxicity, and off-target embolization have been reported [33].

2.3.3 Woven EndoBridge

The treatment of wide-necked bifurcation intracranial aneurysms (WNBIAs) can be difficult if performed with traditional endovascular devices. The WEB device is a nitinol mesh oblate spheroid device that is expanded inside the aneurysm space and is specifically designed for WNBIAs (**Figure 2-3**) [34]. Several clinical studies have been performed for testing the WEB device in ruptured and unruptured, bifurcation ICAs [35-38], where it has been demonstrated that the WEB can provide technically straightforward occlusion of WNBIAs. Further, the WEB provides the great advantage of not requiring anti-platelet therapy post-implantation, while maintaining acceptable rates of immediate occlusion (~ 80%) [39, 40]. Overall, the WEB provides great improvement in the treatment of WNBIAs, making it a great candidate for its expansion into other types of ICAs. However, aneurysm recurrence is still a challenge and re-treatment is oftentimes required.

2.3.4 Flow Diversion Devices

Flow diversion is a technique that aims at preventing intra-aneurysmal flow using a fine mesh that resembles a stent (**Figure 2-3**). This mechanism is described to induce the formation of a neoendothelium and, ultimately, completely stop the blood flow into the aneurysm space [41]. In addition, flow diverters are targeted for the treatment of side-walled aneurysms, where the use of other embolic devices can be technically difficult. The first flow diverter device, named the Pipeline Embolization Device, was introduced in 2008. Its current iteration – the Pipeline Flex – recently received FDA approval in 2021 with improved surface technology for the prevention of thrombogenesis. Outcomes of this device, and other versions of flow diverters, have demonstrated its safe use [42]. Complete aneurysm occlusion has been achieved in ~ 80% of the patients treated with this device [42-44], and similar rates have been reported for other flow diversion devices, such as the Flow-Redirection Endoluminal Device (FRED) (82.5%) [45], the Tubridge (75.3%) [46, 47], and the p64 flow modulation device (80.2%) [48]. However, flow diverters cannot be used for other aneurysms geometries. Also, the mechanism for ICA embolization is not immediate, as it relies on the progressive clotting of blood within the aneurysm. For example, the FRED device exhibits complete occlusion rates of 20% at 90 days of follow up, which increased to 82.5% at 180 days, 91.3% at 1 year, and 95.3% at >1 year post-implantation. This implies that the aneurysm sac is subjected to residual flow, increasing the risk of rupture.

2.3.5 Trellix

TrelliX is another alternative to coated coils, which has a similar approach to the hydrogel coils. Trellix coils are coated with a polyurethane (PU) SMP foam, which allows the device to occupy 2.5 times more volume than the bare GDCs after its activation [49] (**Figure 2-5**). Expansion of the foam can be triggered after aneurysm coiling, which is hypothesized to increase packing density and prevent aneurysm recurrence. In addition, the polymer formulation of this device has been reported to promote aneurysm healing through neoendothelium formation and increased collagen deposition on the surface of the material [21, 50, 51] (**Figure 2-4**). These devices have also been reported to have acceptable occlusion rates in *in vivo* rabbit animal models, where progressive occlusion was observed [21]. Recently, results for the first clinical trial using TrelliX (NCT03988062) were reported [52]. Echeverria *et al*. reported the 1-year follow-up of their clinical study where they report to not have any cases of recurrence (in a total of 9 patients), and 5 cases of complete occlusion. Future more complete follow-ups will provide more information about the long-term effectiveness of the TrelliX coils.

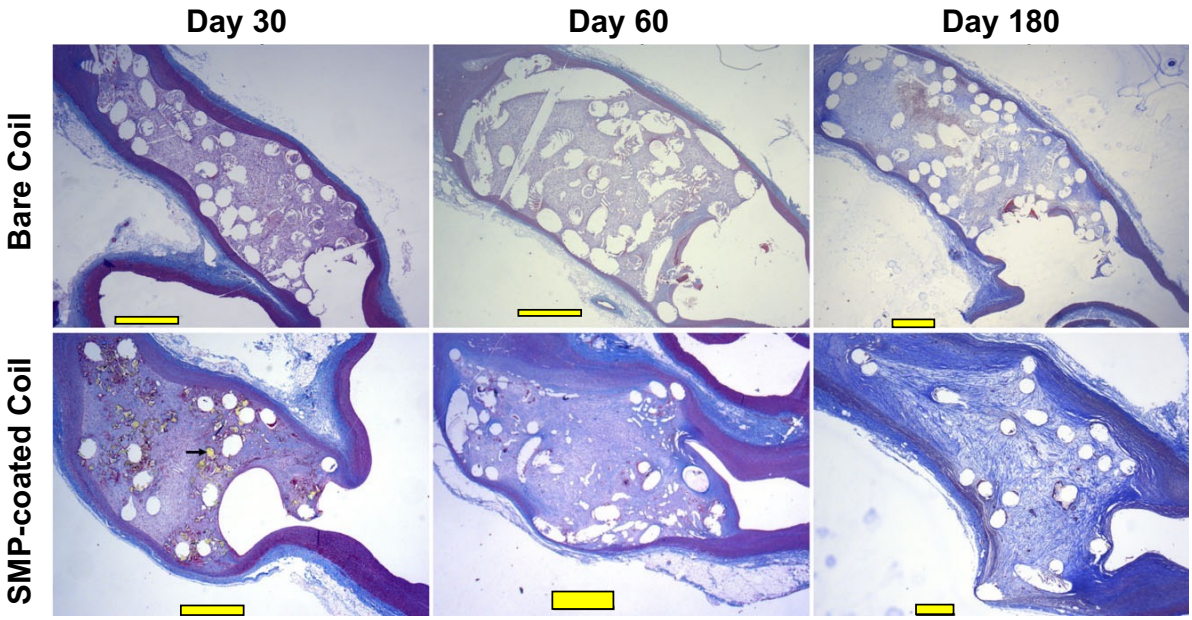


Figure 2-4. Histological analysis of embolized aneurysms with bare coils vs. SMP-coated coils in a rabbit model. Staining was performed using Masson's trichrome at different timepoints (30, 60 and 180 days post-implantation) in this pre-clinical study. Scale bars = 1 mm. (Images were adapted from Herting *et al*. [21] with permission of John Wiley & Sons).

2.3.6 Summary of Current Endovascular Devices

The *state-of-the-art* technology for the treatment of ICAs has allowed to expand the range of aneurysm types that can be treated with endovascular approaches. However, endovascular devices still face limitations related to incomplete occlusion, mass effect, device migration, among others. **Table 2-1** summarizes the advantages and limitations of the endovascular devices described previously.

Table 2-1. Current endovascular devices for the treatment of ICAs and their advantages and limitations.

Device	Advantages	Limitations/Complications
GDCs (Bare coils)	Gold standard for ICA endovascular treatment	Complete occlusion of 49–65%, high recurrence (44% in 5–6 years) and assisting devices required for the treatment of wide-necked ICAs
Hydrogel coils	Higher packing for improved aneurysm sac filling	Recurrence and complete occlusion are not better than GDCs
Liquid embolic devices	Potential higher packing and maximized aneurysm sac filling	High potential for device migration and FDA approval not granted yet
WEB	Designed for wide-necked aneurysms without assisting device	Limited occlusion, prone to compression in large ICAs, and very high recurrence (~72%)
Flow diverter	Can treat complex ICA geometry and ideal for side-walled ICAs	Limited geometries can be treated, high delayed rupture and prone to immediate failure
TrelliX	Improved packing density	Not approved by the FDA yet (in clinical trial—NCT03988062)

2.4 Shape Memory Polymers and Their Potential as Endovascular Devices

Based on the limitations presented in the previous section of this review, we have proposed a novel approach for the development of endovascular devices for ICA therapy. Our approach involves the use of shape memory polymers (SMPs) for the development of individualized coil-free embolic devices. SMPs are the materials with the capacity to undergo thermo-mechanical changes in response to different stimuli. These polymer materials can be fabricated in a "home" configuration, where the material is rigid and not deformable. Then, by introducing

an external stimulus, the material can become flexible and be deformed to a "reprogrammed" configuration. With a second stimulus, the material can undergo shape recovery to the original (home) geometry. This unique feature poses great opportunities for designing responsive materials that enable personalized endovascular ICA treatment. For example, the TrelliX device uses an SMP coating to occupy the gaps between coils (**Figure 2-5a**). On the other hand, we propose to use of SMPs as a coil-free alternative for patient-specific treatment of ICAs (**Figure 2-5b**).

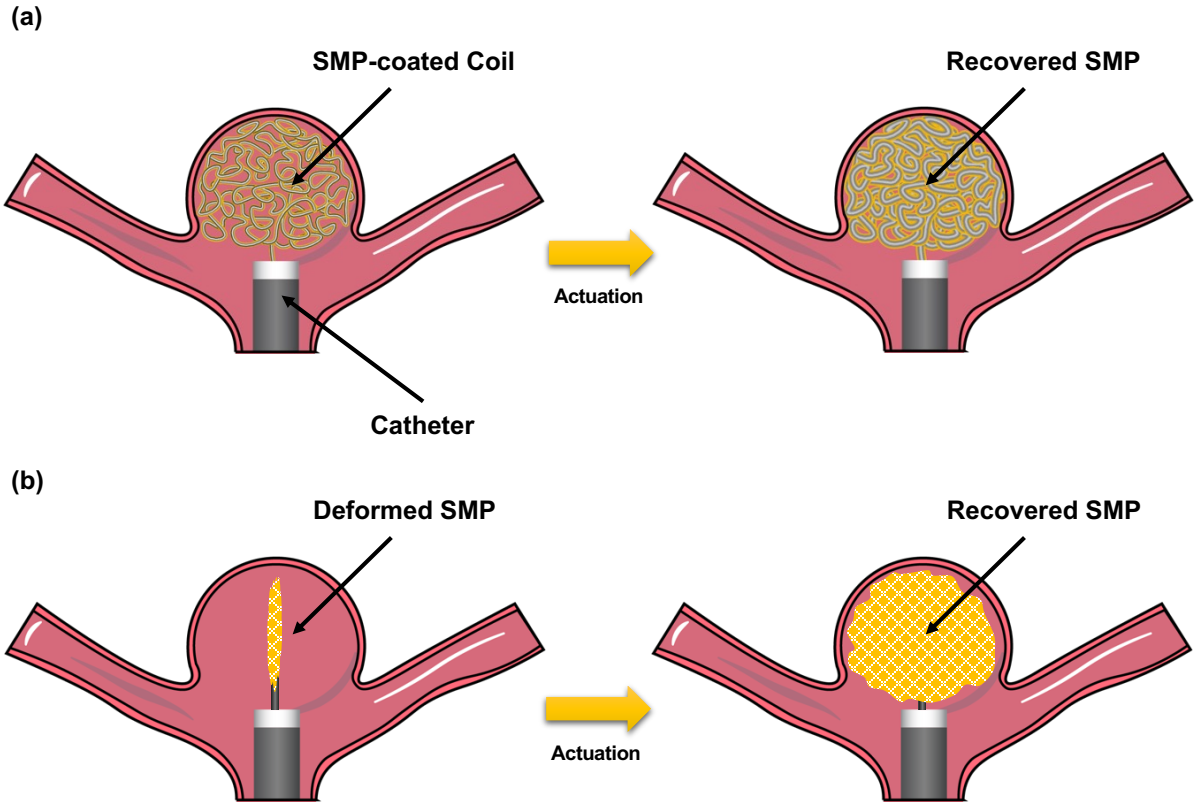


Figure 2-5. Schematic of two potential approaches to fabricate shape memory polymer (SMP)-based endovascular devices for ICA treatment: (a) SMP-coated coils; and (b) SMP coil-free foams with patient-specific geometries.

2.4.1 Shape Memory Polymer Classification by Polymer Architecture

SMPs can be fabricated with different architectures that govern their shape recovery behavior. Specifically, the type of crosslinking between polymeric chains will define their transition temperature (T_{trans}) [53].

2.4.1.1 Physically Crosslinked Co-Polymers

Physically crosslinked SMPs are linear co-polymers that consist of soft and hard segments. In this type of SMPs, a deformable/rubbery state is achieved by increasing the material's temperature (T) above its glass transition temperature (T_g) (i.e., $T_{\text{trans}} = T_g$). When $T < T_g$, the permanent/glassy state of the material is achieved through the weak interactions between the hard segments (e.g., van der Waals forces, dipole–dipole interactions or hydrogen bonding) [53, 54]. The most common example of a physically crosslinked SMP is amorphous polyurethane, which is generally synthesized through polymerization of a diisocyanates as hard segments, and polyols as soft segments. Other examples include polyesterurethanes and polyetheresterurethanes [53, 55, 56].

2.4.1.2 Covalently Crosslinked Copolymers

Covalent crosslinking of SMPs can be achieved using monomers that induce crosslinking of elongated chains or by post-processing [53]. The crosslinking can provide additional phases to the material, as well as the control over mechanical properties by altering crosslink degree. Due to the rigidity of these bonds, covalently crosslinked SMPs cannot be extruded as traditional 3D-printing filaments, limiting their processing into specific geometries [57]. Some examples of this type of SMPs include glassy thermosets (e.g., epoxy SMPs [58]), and

semicrystaline rubbers like polyethylene [54, 59].

2.4.2 Shape Memory Polymer Classification by Pore Fabrication Methods

Traditional and coated GDCs, as well as the WEB device, are transported through a microcatheter and are coiled within the aneurysm. Currently, SMP-based endovascular devices are under development so they can be utilized in a similar manner. SMP design for endovascular devices can follow two major approaches: (i) SMP-coated coils, like Trellix [21, 50], and (ii) coil-free SMPs foams (the approach proposed in this dissertation) [60-62]. SMP-coated coils have a similar goal to the hydrogel coils: to increase the packing density by augmenting the volume of the coil. On the other hand, coil-free SMPs aim to be customized to the patient-specific aneurysm geometry to achieve long-lasting complete occlusion. Both approaches require a high compressibility of the material, which can be achieved through pore formation. In this subsection, we will review some existing methods for the fabrication of highly porous SMPs.

2.4.2.1 Gas Foaming

Gas foaming is a process where the decomposition of a compound, known as blowing agent, yields the production of gas and the formation of bubbles in the polymeric solution [63] (**Figure 2-6**). Other types of blowing agents include physical and biological agents. Physical foam formation can be realized through shaking, whipping, and other mechanical methods. In contrast, biological agents frequently rely on gas-producing species like yeast [64]. For the fabrication of highly porous foams, excess isocyanate solutions in conjunction with commercial blowing agents can be utilized for polyurethane SMPs. For example, Singhal *at*

al. used Enovate, a hydrofluorocarbon, for the fabrication of porous SMPs [65]. This blowing agent has been extensively applied for foam creation, although environmental agencies have recommended against its use [66, 67]. Other methods applicable to SMP foam fabrication include CO_2 [68], diionized water [69], microwaving [70], among others.

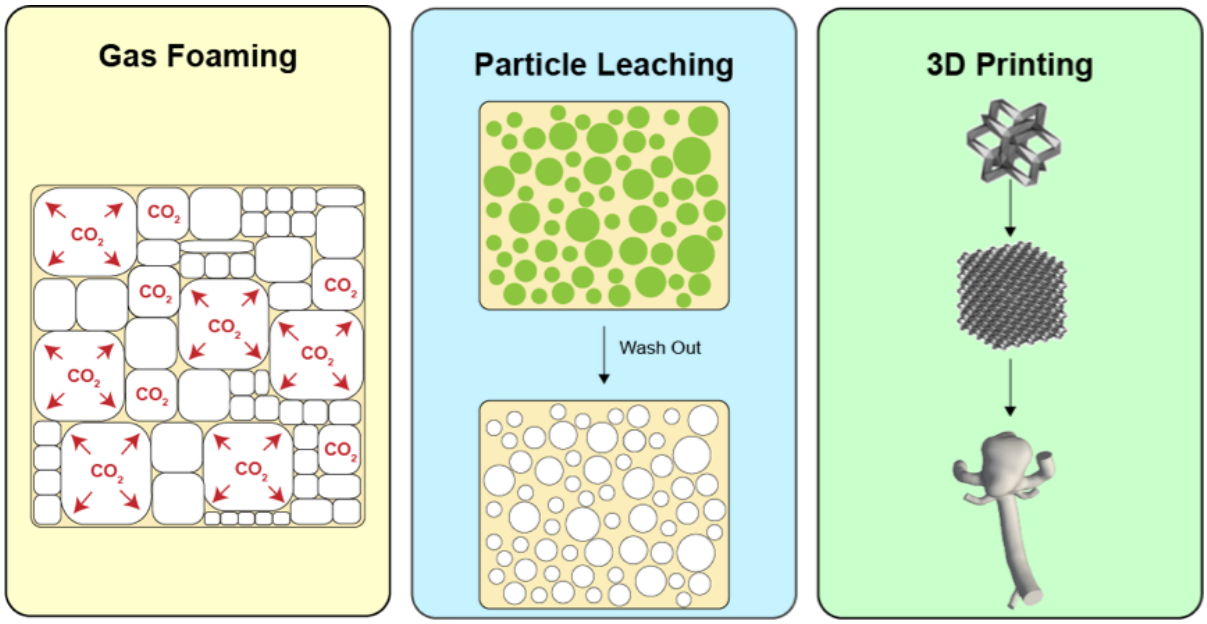


Figure 2-6. Methods for the fabrication of porous SMPs: CO_2 gas foaming (*left*), particle leaching (*middle*), and 3D-printing (*right*).

2.4.2.2 Particle Leaching

Solid particle leaching uses water-soluble particles for the fabrication of pores in SMPs. Leaching agents, typically particles of a given grain size and geometry, are dispersed in polymeric solutions before the curing of the SMP. After curing, particles are dissolved from the matrix by a solvent, leaving gaps in the polymeric structure (**Figure 2-6**). This method provides high tunability of the cell/pore shape and size, which depend on the choice of particles. Common leaching agents that have been used in the literature include sodium

chloride [71, 72], sugar [61, 62], gelatin [73], etc. In our lab, we leached polyurethane SMPs using sugar particles and demonstrated its use to obtain highly compressible SMP foams with pore geometries that mimic the sugar crystal morphology [61, 62].

2.4.2.3 Additive Manufacturing (3D-Printing)

3D-printing can be performed via different methods, where fused deposition modeling (FDM) is the most popular. 3D-printing provides a great opportunity to fabricate the patient-specific geometries for SMP-based endovascular devices (**Figure 2-6**). Using the aneurysm geometry from patient imaging data (e.g., magnetic resonance or computed-tomography imaging), patient-specific aneurysm geometry could be printed using FDM to obtain a porous endovascular device. FDM has been utilized for the printing of materials with shape memory capacities, including the use of polylactic acid (PLA) [74-76], polyurethane [77-79], polycyclooctene (PCO) [80], polyvinyl alcohol (PVA) [81], among others [82].

For example, Langford *et al.* used PLA to design a highly compressible scaffold with shape memory properties. They developed a 3D geometry based on origami tessellations, allowing for the fine control of the direction of compression and the shape recovery of the material. In addition, they designed the core of the material to have trabeculae and mimic the bone macrostructure, which can be used for bone tissue engineering applications [74]. A different approach for guided compression was developed by Mehrpouya *et al.*, where a honeycomb structure was used to print PLA-guided SMPs [75]. These designs are promising approach for the design of personalized endovascular devices tailored to patient-specific ICA geometries. Other examples for 3D-printed SMPs include stents [76] and wearable devices [78].

2.4.3 Shape Memory Polymer Actuation Methods

The shape recovery of SMPs can be triggered by different mechanisms, including pH [83], humidity [84], light triggering [85], magnetic activation [86], and resistive heating (i.e., Joule heating) [87]. The choice of actuation mechanism for shape recovery is a fundamental design criterion for the development of endovascular devices. In theory, when an SMP-based device is transported via the microcatheter to the aneurysm sac, it should be able to maintain its compressed/deformed configuration until the shape recovery has been triggered by the activation mechanism. In this subsection, we will present some of the most used methods for shape recovery actuation.

2.4.3.1 Joule heating activation

Joule heating is a process by which a material emits heat when electrical current flows through it. Therefore, this mechanism can provide a highly controllable trigger for the shape recovery in SMPs. However, most SMP materials are not conductive, which creates the necessity of incorporating additives that induce conductivity. Current developments for electrically triggered SMPs include the use of carbon nanotubes (CNTs), carbon black, polypyrrole (PPy) coating, and nanoparticles [88].

On the other hand, PPy is another alternative for the induction of conductivity. Typically, PPy is used as a coating of the SMP materials, and its polymerization is performed *in situ*. For example, Sahoo *et al.* immersed SMP films in a pyrrole aqueous solution and then transferred the films to a separate $FeCl_3$ solution. This produced a thin layer of PPy on the surface of the

SMP films and provided the material the capacity to shape recovery under electrical stimulation. As the accompanied by product, PPy coating induced an increased T_g [87]. Additionally, modifications to the PPy polymerization have also been studied. For example, Zhang *et al.* immersed PLA electrospun SMPs in a $FeCl_3$ solution and then evaporated pyrrole onto the surface of the material. This coating induced a slight decrease in T_g and minimal changes in the material's mechanical properties (e.g., Young's modulus and the ultimate tensile strength) [56]. Similar results have been observed in other studies with PPy coating [89, 90].

Overall, material modification for the induction of conductivity needs careful design. While conductivity can be achieved using additives and coatings, the thermo-mechanical properties of the SMPs may also be undesirably affected by these processes.

2.4.3.2 Infrared (IR) light activation

Infrared light can be absorbed by SMP materials, which will then be transformed into heat. This activation method avoids the infiltration of the material with other additives and prevents involuntary stimulation of the vascular tissue. Leng *et al.* induced the recovery of a polystyrene/polyvinyl SMP using an IR laser, although their material did not fully recover in the whole process due to the slow temperature gain [91]. A similar problem was observed by Baer *et al.*: they used a polyurethane SMP to fabricate a vascular stent with photothermal actuation [85]. Shape recovery of the stent was triggered within a mock artery model with active flow using an 810 nm diode laser. They observed that the shape recovery of SMP was successfully triggered in the artery phantom (without flow) and complete recovery was achieved in ~7 min (that is much longer than the GDC delivery time: 1-2 min). However, when

flow was applied to the artery phantom, the convective cooling prevented triggering of the stent [85]. Overall, IR photothermal activation has great potential for its application in SMP endovascular devices, but further research is required to improve the heating rates.

2.4.3.3 Electromagnetic Activation

The activation of shape recovery through remote signals can aid in the ease of delivery of endovascular devices. Based on this, several efforts have been made to fabricate SMPs sensitive to electromagnetic waves. For example, Schmidt fabricated biodegradable SMPs using oligo(e-caprolactone)dimethacrylates and butylacrylate (BA), which were infiltrated with Fe_3O_4 nanoparticles ($d \approx 11$ nm). These nanoparticles can transform electromagnetic radiation (radio waves of $\lambda = 300$ kHz, power of 5.0 kW) into heat that triggered the shape recovery of the SMP [92]. Similar designs have been made with carbon black, nickel [93], and CNTs [94].

2.4.3.4 pH activation

pH-activated SMPs have been developed to avoid the heating of SMP devices or elements in the bloodstream of the parent artery. Using the well-described pH of blood, SMPs can be activated when in presence of the fluid. Han *et al.* developed a β-cyclodextrin-modified alginate/diethylenetriamine-modified alginate (β-CDAlg/DETA-Alg) SMP with high deformability at pH = 7. They demonstrated that the material conserved the deformed configuration when aqueous solution pH was changed to 11.5. Then, shape recovery was triggered by transferring the material to the original solution [83]. Another use of alginate-based pH-activated SMPs was studied by Meng *et al.*, where they fabricated a phenylboronic-

acid-grafte alginate/PVA hydrogel. The material was deformed and activated at pH 6 and it was also sensitive to glucose [95]. Another approach for pH-induced behaviors was demonstrated by Lu *et al.*, where they fabricated a pH-activated SMP with self-healing capacity using four-armed poly(ethylene glycol) (PEG) with dopamine end groups loaded with Fe^{3+} ions. This material uses a pH sensitive reversible mono-, bis- and tris-catechol–Fe^{3+} coordination as a switch for shape recovery and self-healing. By setting the solution pH to 9, the material exhibited excellent shape recovery behaviors and self-healing after an induced wound [96]. Similar behaviors and mechanisms have been developed for water activated SMPs [97, 98]. pH-activated SMPs have a great potential to be used as endovascular devices due to the absence of heating elements for shape recovery, making devices safer and simple for delivery.

Overall, the research of SMPs is an evolving field with novel materials and synthesis methods constantly emerging. For the most current developments, we present a summary of all the materials and activation methods pertinent to this review in **Table 2-2**.

Table 2-2. Summary of materials with shape memory properties, activation methods and outstanding reported features.

SMP Material	**Activation Method**	**Features**	**Ref.**
Butadiene–styrene tri-block copolymer/PCL	Heat/water	Polymer blend with elastomeric and shape memory properties.	[99]
Norland Optical Adhesive 63 (propietary)	Heat	T_g gradients have been reported.	[100]
Silsesquioxane nanoparticles/PLA	Heat	Long-term (>1 year) shape storage.	[101]
PCL-coated Fe_3O_4/oligo(PCL) DMA/BA	Electromagnetism	Remote activation without reaching temperatures higher than T_g.	[92]
Perfluorosulphonic acid ionomer	Heat	Multi-shape memory effect with distinctive thermal states.	[102]
Phenylboronic-acid-grafted alginate/PVA	pH	Stable shape storage at specific pH and sugar contents.	[95]
PU/carbon nanopowder	Joule heating	Carbon powder provides conductivity for electrical actuation.	[103, 104]

Table 2-2. (*continued*) Summary of materials with shape memory properties, activation methods and outstanding reported features

Poly(propylene sebacate)	Heat	Ecologically sustainable material.	[105]
Polydopamine/PCL	Heat	Great thermal conductivity.	[106]
PLA/PPy	Joule heating	Polypyrrole provides conductivity for electrical triggering of shape recovery. PLA is biodegradable.	[56]
Polylactide-co-poly(glycolide-co-caprolactone)	Heat	Highly biodegradable.	[107]
Polymethyl metracrylate/PEG	Heat	Multi-shape memory effect with distinctive thermal states.	[108]
Polystyrene	Heat/IR light	IR activation provides a contactless actuation method (less invasive). Material can also be applied in catheter design. Self-healing properties.	[91, 109]
Polystyrene/carbonanotubes	Electromagnetism	Microwave activation provides a minimally invasive actuation method.	[94]
Polystyrene/copolyester particulates	Heat	Self-healing properties.	[110]

Table 2-2. (*continued*) Summary of materials with shape memory properties, activation methods and outstanding reported features

PU	Moisture/pH/IR Light	Extensively applied for *in vitro* and *in vivo* occlusion of aneurysms. Used in stent design. Facile control of T_g. Responsive to moisture, IR light, pH, and heat. Multi-shape memory effect.	[60, 85, 97, 98, 111-114]
PU/CNT	Heat/Joule heating	CNTs provide conductivity for electrical triggering of shape recovery.	[62, 115]
PU/PEG	Heat	Multi-shape memory effect. Facile T_g tuning.	[116]
PU/PPy	Joule heating	Polypyrrole provides conductivity for electrical triggering of shape recovery. PLA is biodegradable.	[87, 89, 90]
Silver nanowire/PET	Heat	Reported for the design of light-emitting diodes.	[117]
SiO_2/PCL	Heat	SiO_2 macroparticles provide improved mechanical properties (high strain). Biodegradable.	[118]
Tert-BA/di(ethylene glycol) diacrylate	Heat	It can be fabricated with stereolithography techniques.	[119]
β-CDAlg/DETA-Alg	pH	pH-induced recovery. Biodegradable and biocompatible.	[96]

2.4.4 Potential of SMPs for ICA Endovascular Therapies & Future Directions

Current developments have allowed the expansion of endovascular therapy to a wider spectrum of aneurysm morphologies, including giant, wide-necked, and fusiform aneurysms. However, most endovascular devices still face limitations with suboptimal outcome (i.e., high recurrence rates). As discussed in Section 2.3, complete occlusion of aneurysms is only achieved in ~ 80% of the treated cases. This incomplete occlusion allows residual flow to further promote aneurysm recurrence [120, 121]. In fact, several coated coil devices have been designed to increase the packing density. However, it has been demonstrated that the most influential risk factor for aneurysm recurrence is the residual flow, rather than the packing density [4]. Therefore, it is of paramount importance that novel developments of endovascular therapies are aimed at reducing residual flow while increasing complete occlusion rates. The fabrication of a porous patient-specific SMP is a very promising alternative for the next generation of endovascular devices. In theory, aneurysm specific SMPs could completely occlude the aneurysm space and promote vascular healing. The latter can be induced by the biocompatibility and cellular adherence properties of the material. Most importantly, aneurysm healing can also be improved through advanced surface modification.

We also envision that the next generation of SMP-based endovascular devices will need to address several limitations of these materials before they can be translated into the clinic. For example, SMPs are very sensitive to environmental conditions and the shape recovery properties can be easily affected by environmental humidity, oxidation, and heat [103, 104, 122-124]. This implies that the storage conditions for SMPs need to be carefully investigated. In addition, the storage of the material also needs to guarantee sustained sterility. SMP

sterilization is a controversial topic, as methods that are applied to other medical devices might not be readily suitable for this type of material. For example, autoclaving or plasma sterilization of polyurethane SMPs can be detrimental to its mechanical properties and shape memory/recovery features by significantly changing T_g [125, 126]. Finally, the activation methods for SMP recovery are still a matter of debate, due to the potential use of heat sources for shape recovery. Alternatives, such as pH activation, will aid in the advancement of safe shape recovery triggering.

2.5 Previous Work at the Biomechanics and Biomaterials Design Laboratory

As described across this chapter, our approach (and the focus of this dissertation) is to develop patient-specific SMP foams for the treatment of ICAs, more specifically, unruptured saccular ICAs. To achieve this, our group started developing these materials from its basic chemical formulation. The following have been the efforts performed by our group prior to the development of this dissertation.

2.5.1 Synthesis and Characterization of Pristine Polyurethane SMPs

In a work led by Robert Kunkel, our group studied the synthesis of polyurethane using a formulation based on hexamethylene diisocyanate (HDI) as a hard segment, and triethanolamine (TEA) as soft segment. The urethane linking was catalyzed by N,N,N0,N0-tetrakis (hydroxypropyl) ethylenediamine (HPED). These three reagents (referred to as "monomers" in the rest of this dissertation) produced highly chemically crosslinked polyurethane, and its thermomechanical properties depend on the molar ratio at which the

monomers are used. Our group investigated the effects of different monomer ratios, which were named SMP1-12, where SMP1 a TEA/HDI molar ratio of 0, and SMP12 a TEA/HDI molar ratio of 0.667. The results from the study shed light on the T_g of the different SMP monomer ratios, their mechanical properties and shape recovery behaviors [60, 127].

2.5.2 First attempts at Fabricating Porous SMPs with Conductive Properties

In a preliminary study led by Wang *et al*., our grouped used the HDI:HPED:TEA polyurethane formulation for the fabrication of porous foams. To achieve this, the polyurethane solution was poured over a sugar cube, which was used as a leaching agent. This method produced highly porous foams with great compressibility. In addition, preliminary experiments were also performed to design a method for CNT infiltration in the porous foams [128].

2.5.3 ICA Fluid Dynamics

In a thesis written by Ryan Bodklak, our lab studied the blood flow dynamics in ICAs using simulations. To do this, aneurysm geometries were constructed using anonymized patient imaging data (IRB #7932) from computerized tomography angiography. In total, six aneurysm geometries were obtained by using image segmentation techniques, and they were used for computational fluid dynamics analysis, under different simulation conditions. The geometries produced in this M.S. thesis [129] are utilized in this dissertation in Chapter 4 and Chapter 5.

2.6 Concluding Remarks

The literature review presented in this chapter summarizes key concepts for ICA therapy, including brain vasculature anatomy, and ICA risk factors and demographics. Also, we present

a brief description of the *state-of-the-art* endovascular devices that are modernly utilized to treat unruptured saccular ICAs, including GDCs, WEB, flow diverters, among other emerging technologies. Then, we presented our approach, which involves the use of SMPs to develop coil-free endovascular devices. This led to a brief description of polyurethane chemistry and shape recovery behaviors, methods for its fabrication as porous matrices, and different actuation methods for shape recovery. Finally, we summarized the previous research efforts performed by our lab prior to the development of this dissertation, which were instrumental to its completion and the advancement of our long-term goal of designing a Joule-heating-activated SMP-based endovascular device for the treatment of unruptured saccular ICAs.

CHAPTER 3 Design and Characterization of a Joule-Heating Activated Shape Memory Foam Using Carbon Nanotubes

This chapter presents our first effort in obtaining a Joule-heating activated SMP porous material. First, we used the methods previously developed by our group to the fabricate CNT-infiltrated porous SMPs (Section 3.1.1). Then, we explored the effect of different CNT concentrations on the material's thermomechanical properties using different material characterization techniques (Sections 3.2.1-3.2.3). The chapter is then concluded with the demonstration of Joule-heating activated shape recovery using an idealized aneurysm *in vitro* model. The results of these characterizations are then discussed to summarize the advantages and limitations of CNT infiltration for the design of our SMP-based device. Our findings established the basic properties of our material that aid in the further development of the SMP-based device.

3.1 Materials and Methods

3.1.1 Preparation of CNT/Porogen Solution

Multi-walled carbon nanotubes (Sigma Aldrich, USA) were evenly distributed in 30 mL of ethanol using an ultrasonic processor (Sonics, Vibra-Cell 505, USA) at 28% amplitude in a pulse mode (5 s on and 2 s off) for 10 min. Pure cane sugar (Florida Crystals Inc., USA) was used as the porogen (POR) for leaching of the polymeric structure. POR was introduced to the CNT/ethanol solution at various CNT/POR weight ratios (0.5, 0.75, 1.0, 1.25% w/w). The CNT/POR/ethanol solution was then sonicated in an ultrasonic water bath (Cole-Parmer, USA) for 24 h to evenly distribute the CNTs and POR crystals. Finally, the ethanol was dried out in

a vacuum oven at 60 °C for 24 h, leaving a dry mixture of evenly distributed CNT and POR.

3.1.2 Preparation of CNT-infiltrated SMP foams

Aliphatic polyurethane SMPs were synthesized using (i) hexamethylene diisocyanate (HDI, ≥98.0%, Sigma-Aldrich) as hard segment, (ii) N,N,N0,N0-tetrakis (hydroxypropyl) ethylenediamine (HPED, ≥98.0%, Alfa Aesar) as catalyst , and (iii) Triethanolamine (TEA, ≥ 99.0%, Sigma-Aldrich) as soft segment, at a molar ratio of 1:0.05:0.6 to obtain a T_g of ~34°C [60, 128]. Monomers were mixed using a magnetic stirrer in a nitrogen-protected environment until the monomer solution turned clear. Then, the solution was evenly poured onto 30×30×10 mm sugar blocks (that were made using pure sugar and various CNT/POR mixtures). The uncured SMP solutions were kept at –14 °C in vacuum for 24 h to prevent curing and to allow complete penetration into the template. Then, the specimens were cured at 60 °C for 1h and 130 °C for an additional hour under a nitrogen-rich environment using a vacuum oven (BOV-20, Being Instrument, USA). The cured blocks were immersed in deionized water and sonicated at room temperature (Branson 1800, Branson Ultrasonics Corporation, USA) for 24 h to dissolve sugar templates and wash out non-infiltrated CNTs. Finally, the CNT-infiltrated SMP foams were dried out in a vacuum oven at 60 °C until mass measurements stabilized (indicating no further water evaporation), stored in a desiccator in vacuum and wrapped in moisture-absorbent tissues before testing.

3.1.3 Attenuated Total Reflectance - Fourier Transform IR Spectroscopy

The pristine SMP foams were characterized with attenuated total reflectance – Fourier transform IR spectroscopy (ATR-FTIR) as a quality check to ensure the proper synthesis of

aliphatic polyurethane SMPs. ATR-FTIR spectrum was obtained with a spectrometer (Nicolet iS50R, Thermo Scientific, USA) with a L-alanine doped triglycine sulfate (DTGS) and mercury cadmium telluride (MCT) detector. Spectrum analysis was performed using the Bio-rad spectroscopy software and an in-house MATLAB program (Mathworks, USA).

3.1.4 Density Measurement

A pycnometer (AccuPyc II 340 Micromerimetrics, USA) was used to measure the density of solid SMP samples of 10×10×10 mm ($n = 6$). Mass was measured as the difference between the samples in the testing cup (filled up to 2/3 of the volume) and the cup mass. Volume was determined by gas displacement measured by the device.

3.1.5 Differential Scanning Calorimetry (DSC)

DSC was performed (Q1000 TA Instruments, USA) to determine the T_g of the synthesized CNT-infiltrated SMP foams ($n = 3$). Samples were tested with two heating/cooling cycles at a range of –10 °C to 80 °C at a 5 °C/min heating rate and 50 °C/min cooling rate with isothermal stabilization at the end of each cycle for 5 min. T_g was measured from the second heating cycle using the TA Universal Analysis tool.

3.1.6 Resistivity Measurement

Volumetric resistivity was measured using the procedure described by Leng *et. al* [130]. The CNT-infiltrated SMP foam cuboids ($n = 3$) in 10×10×10 mm were placed in a uniaxial mechanical testing system (Instron 5969, USA), where the compression plates were lined with the copper tape. The specimens were pressed at a 1 mN force to ensure proper contact between

the conductive materials (**Figure 3-1a**). Copper plates were then connected to a multi-meter to measure the resistivity. Next, volumetric resistivity ρ was calculated by:

$$\rho = \frac{RA}{L} \tag{3.1}$$

where R is the measured resistivity from the multi-meter, A is the cross-sectional area of the foam specimen, and L is the distance between the two plates of the compression testing system. The pristine SMP foams were not evaluated in this experiment as they are nearly electrically non-conductive.

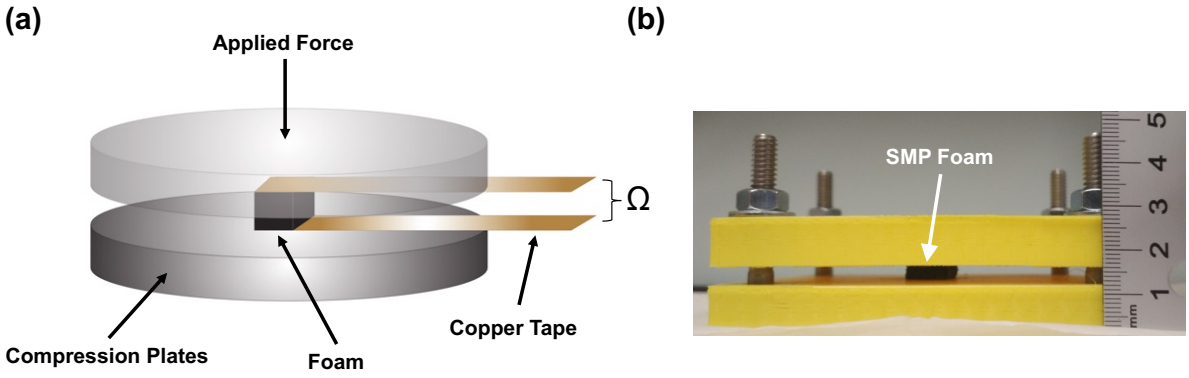


Figure 3-1. (a) Schematic of the experimental setup for measuring the volumetric resistivity of the CNT-infiltrated SMP foam. (b) Schematic of the experimental setup for shape recovery time assessment of the CNT-infiltrated SMP foam.

3.1.7 Uniaxial Mechanical Characterizations

Compression tests were performed up to 90% strain, per the device's load cell capacity, on each of the CNT-infiltrated SMP foams (of four different CNT concentrations) and the pristine SMP foam. Samples of ~ 10×10×10 mm ($n = 3$, per foam type) were tested at room temperature (20 °C) and at $T_g + 5$ °C (39 °C), after a pre-heating period of 1 h at 39 °C in a vacuum oven (BEING Instruments BOV-20). The tests were conducted in a mechanical testing

system (Instron 5969) at 2 mm/min compression rate up to a 90 % strain. In addition, *cyclic* compression tests (10 cycles) at a 2 mm/min compressive/decompressive rate were performed, targeting a 60% cyclic strain at T_g and $T_g + 5$ °C.Stress-strain curves were obtained by the testing system, and the mechanical behaviors were analyzed.

3.1.8 Assessment of the Shape Recovery Time

Cuboidal CNT-infiltrated SMP foams ($n = 3$) were kept above T_g (50 °C) for 1 h in a vacuum oven (BEING Instruments BOV-20) to ensure all samples were at the rubber-elastic state. Samples were then compressed to a ~60% strain and cooled down while pressed on a cooling plate (Biobase BK-CPI, China) at –20 °C for 5 min (**Figure 3-1b**). Shape recovery was then triggered by placing the sample on a hot plate (IKA C-MAG HS7, Wilmington, North Carolina) at temperature above T_g (39 °C). Shape recovery was measured as the time from contact with the plate to ~90% length recovery.

3.1.9 Measurement of the Joule-Heating-Induced Heat Transfer

The minimal current required for triggering the shape recovery was measured by increasing the direct current (at 0.01 A increments) applied to foams (10×10×10 mm, $n = 3$) under a parallel-plate setup. The same method was performed to obtain the required current to obtain ~90% shape recovery within 2 min. Measurements from these minimal current requirements were used to establish a direct electrical current range for introducing the required heat release for working with the synthesized CNT-infiltrated SMP foams. The Joule-heating profiles were obtained by applying direct electrical current to measure the temperature on the surface of the uncompressed CNT-infiltrated foams with dimensions relevant to the potential application

(5×5×5 mm) for 120 s. Temperature was measured by busing an infrared thermal camera (FLIR ETS320, USA) along the course of the application of direct current. Note that a combination of the setups in **Figure 3-1a** and **Figure 3-1b** was used in this experiment.

3.1.10 Fabrication of an Idealized Aneurysm Model and Occlusion Demonstration

An aneurysm phantom model was fabricated using Sylgard 184 (DOW, USA). The Sylgard solution was then poured over a 3D-printed model (CR-10s, Creality, China) of an idealized aneurysm in a Y-shaped arterial bifurcation (vessel diameter, 3 mm; aneurysm diameter, 7 mm) [131]. The synthesized model was kept in vacuum to degas the material for 24 h until the curing was complete. Then, a 1.0% w/w CNT/POR SMP foam was manually trimmed to fit the spherical shape of the aneurysm model. The CNT-infiltrated foam was kept in a vacuum oven at 39 °C for 1 h prior to being compressed uniaxially and delivered with a mock catheter to the aneurysm model. A direct current of 1.0 A was applied with two parallel copper strips to trigger shape recovery. Surface temperature of the foam measured using an infrared thermal camera (FLIR ETS320, USA).

3.1.11 Scanning Electron Microscopy

The pristine and CNT-infiltrated SMP foams were sputter-coated using gold-palladium prior to imaging. The porous structure of the specimens was characterized using an scanning electron microscope (JEOL, JSM-840, USA) with an accelerating voltage of 20 kV and a working distance of 8 mm. The foam's pore size was measured using the ImageJ software [132].

3.1.12 Statistical Analysis

All the measurements are expressed as mean $\pm$ standard error of the mean. Normality of the data was evaluated utilizing Shapiro-Wilk test: $p < 0.05$ was deemed not normally distributed. Comparisons of the measurements between different CNT/POR ratios were then determined by performing the appropriate tests: ANOVA and *post-hoc* Tukey-HSD for data in normal distribution; Kruskal-Wallis and *post-hoc* pairwise Wilcoxon rank sum test for non-normally distributed data. Differences between groups were considered as significant when $p < 0.05$. All the statistical assessments were performed on R v3.6.1 (The R Foundation for Statistical Computing, Austria).

3.2 Results

3.2.1 Synthesis and Characterization of CNT-Infiltrated SMP Foams

Pristine (i.e., without an addition of CNTs) and CNT-infiltrated SMP foams were synthesized by a sugar-leaching method at four different CNT-to-Porogen (CNT/POR) ratios (0.5, 0.75, 1.0, and 1.25% w/w). Interconnected porous structures were obtained in 30×30×10 mm cubic specimens, as shown in **Figure 3-3a**. The synthesized CNT-infiltrated and pristine SMP foams were cut into the specific dimensions for each of the subsequent experiments and stored in vacuum before testing.

First, the porous structure of the synthesized SMP foams was found to be consistent with our previous investigations [60, 128, 133] where the pore size of the foams, as determined from the scanning electron microscopy (SEM) images (**Figure 3-2a-b**), followed a non-normal distribution. The average pore diameter was not significantly altered by the CNT infiltration

process (Mann-Whitney U-test: $p = 0.53$, (**Figure 3-2c**). However, a significant increase in density was found as the CNT concentration increased (Kruskal-Wallis test: $p < 0.05$), i.e., from 0.332 ± 0.002 g/cm^3 for the 0.5% CNT/POR samples to 0.379 ± 0.002 g/cm^3 for the 0.75% CNT/POR samples (pairwise Wilcoxon test: $p < 0.01$), while the measured density did not increase significantly between the 1.0% and the 1.25% CNT/POR ratios (pairwise Wilcoxon test: $p = 0.81$, **Figure 3-3b**).

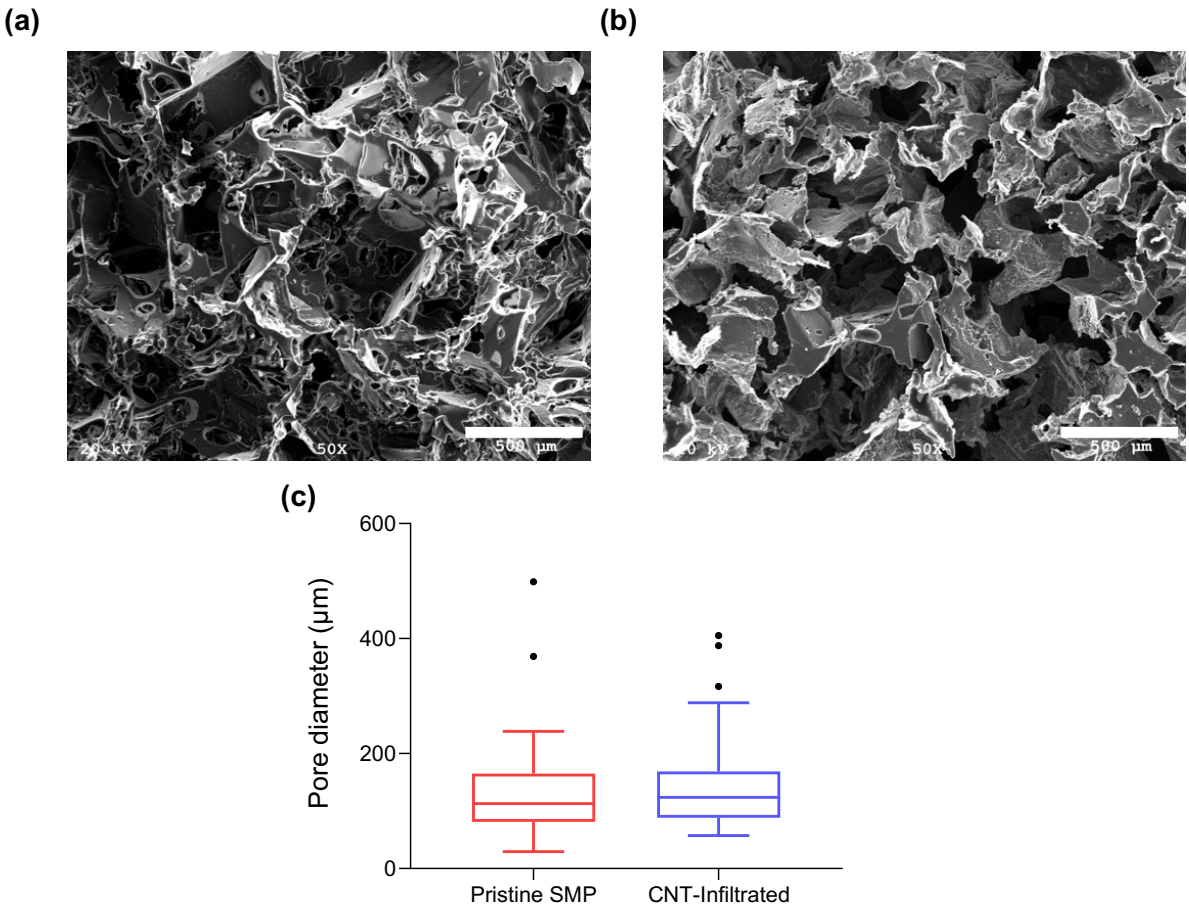


Figure 3-2. Scanning electron microscopy (SEM) images at 50X magnification: (a) the pristine SMP foam, and (b) the CNT-infiltrated SMP foam. Scale bar = 500 µm. (c) Pore diameter fistribution of the pristine and CNT-infiltrated SMP foam.

Next, ATR-FTIR spectroscopy was used to confirm the proper synthesis of the aliphatic polyurethane SMP. The ATR-FTIR spectrum exhibits local maxima at 1687 and 3330 cm^{-1}, which correspond to the C=O stretch of amides and the -NH stretch of aromatic primary amines,[123, 134-138] respectively (**Figure 3-3**). Other relevant peaks are associated with ether bonds (1049, 1137, and 1240 cm^{-1})[134, 135], hydroxyl bend and stretch (584.8 and 1459 cm^{-1}) [134], symmetric and asymmetric methylene stretch 2858 cm^{-1} and 2935 cm^{-1}) [134, 135], and aromatic primary amines (3570 cm^{-1}) [123, 134-138]. From the ATR-FTIR spectrum analysis, we were able to confirm the synthesis of our aliphatic polyurethane SMP samples.

3.2.2 CNT-Induced Thermal and Electric Conductivities

The electrical and thermomechanical properties of the CNT-infiltrated SMP foams were next analyzed and compared to those of the pristine SMP foams. Specifically, we examined the effects of the CNT infiltration process on the thermomechanical properties of the synthesized SMP specimens. Our previous studies in the thermomechanical properties of aliphatic polyurethane SMPs were performed for *non-porous* specimens [127]. Thus, we first used differential scanning calorimetry (DSC) to determine how the sugar leaching and CNT infiltration processes influence the material's T_g. The measured T_g of the pristine sugar-leached SMP foams was found to be significantly lower than the glass transition temperature of solid pristine SMPs (Mann-Whitney *U*-test: $p = 0.02$, **Figure 3-4a**), together with the finding of a reduction in T_g as the CNT/POR concentration increased (**Figure 3-4**).

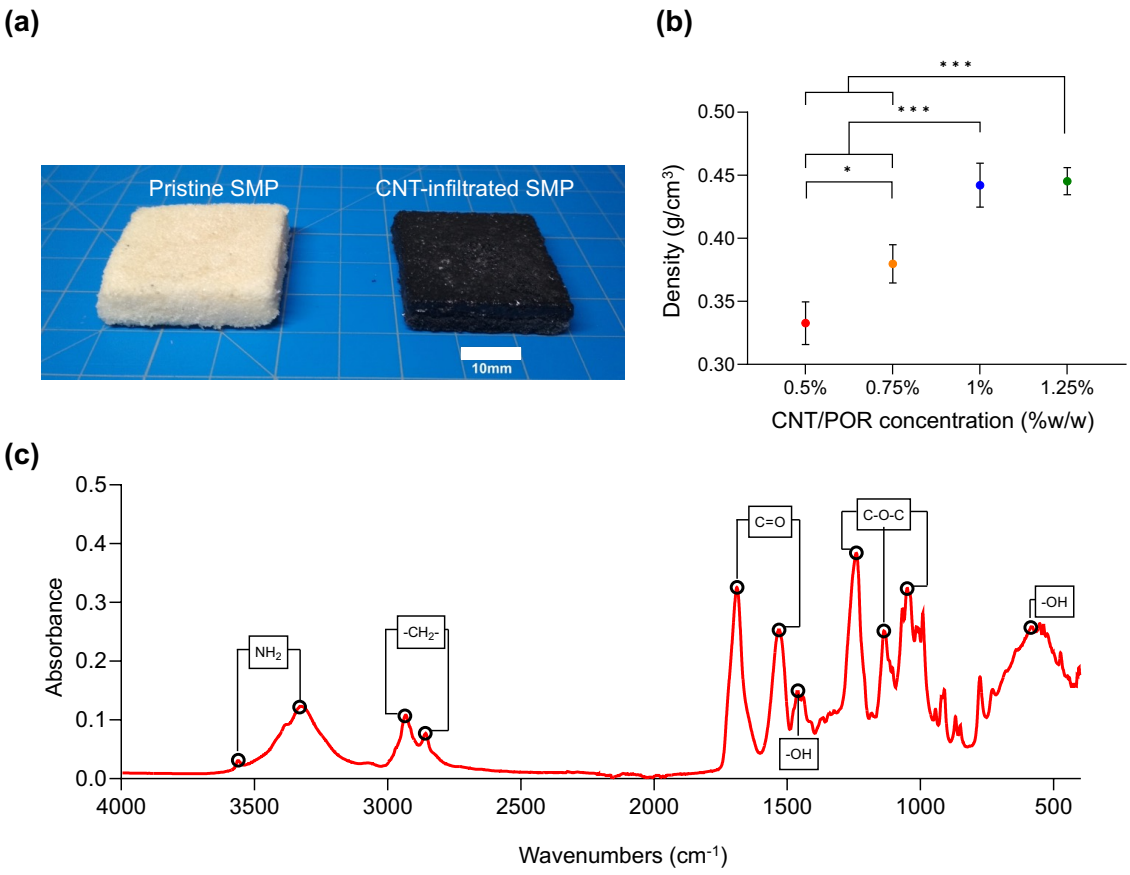


Figure 3-3. (a) Photos of a pristine SMP foam (*left*) and a CNT-infiltrated SMP foam (*right*). (b) Measured density of the CNT-infiltrated foams at various CNT/POR ratios. (***denotes $p < 0.001$, and * indicates $p < 0.05$). (c) ATR-FTIR spectrum of the synthesized pristine aliphatic polyurethane SMP.

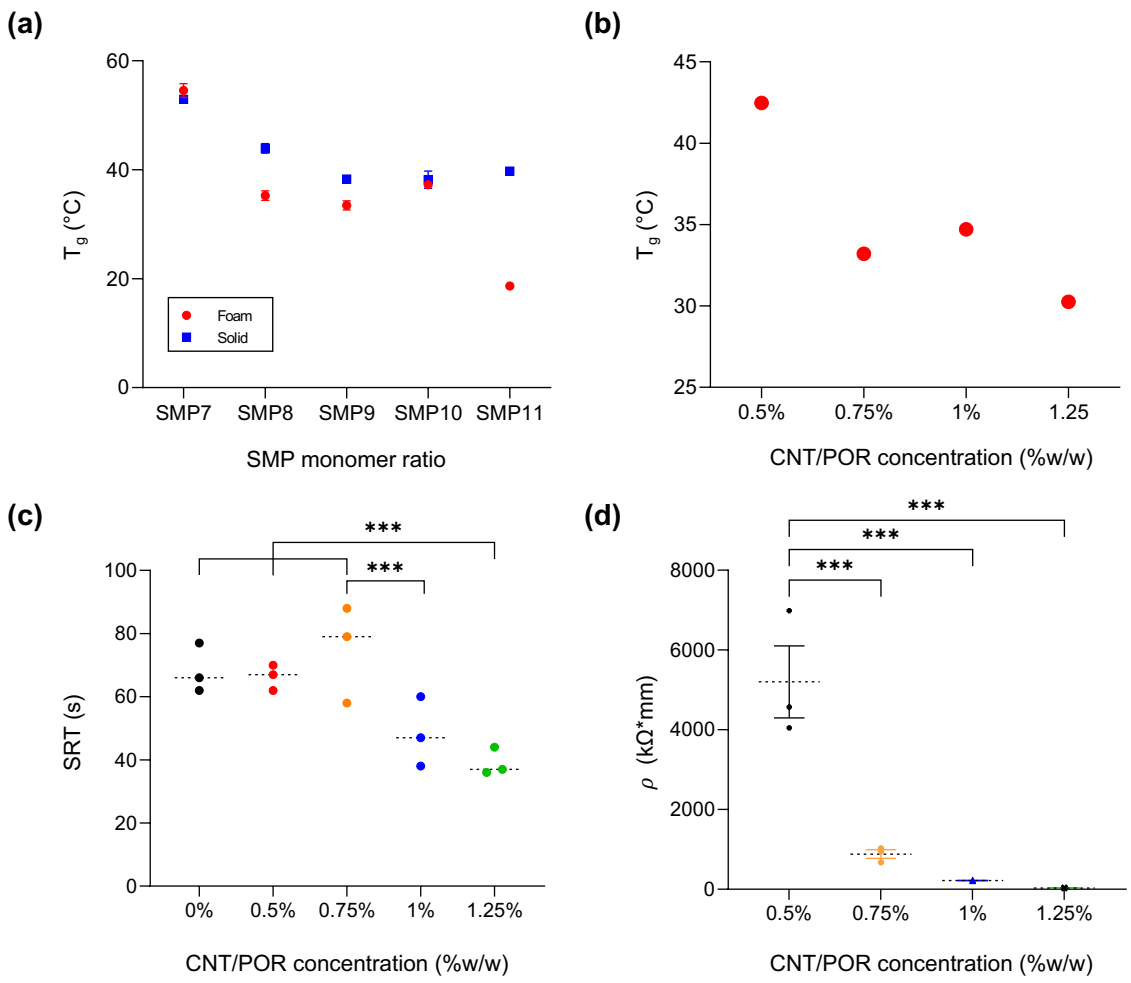


Figure 3-4. DSC measurements of T_g for (a) the pristine SMP at different monomer ratios (SMP11 is the target ratio in the present work), and (b) the porous CNT-infiltrated SMP foams with various CNT/POR ratios. Measurements of (c) the shape recovery time for the CNT-infiltrated SMP foams with various CNT/POR ratios, and (d) the volumetric resistivity (*** denotes $p < 0.001$, and * denotes $p < 0.05$).

Based on these results and considering the potential artifacts of the porosity on the DSC measurements [139], we further performed a shape recovery test (i.e., transition from the compressed/glassy state to the relaxed/rubbery states) to confirm the potential reduction in the material's T_g. This test was performed to record the shape recovery time by: (i) heating the uncompressed foams to 50 °C, (ii) uniaxially compressing the specimens using parallel plates (See Section 3.1.8), (iii) cooling the foams in a freezer (–14 °C) for 5 mins, and (iv) placing the specimens on a heating plate at 50 °C (way above T_g to obtain rapid transitions between thermomechanical states). The time required for ~90% recovery of the original height of the specimens was recorded. We observed that the specimens successfully recovered their shape after contact with the heating plate, and that the time from contact to ~90% recovery was inversely proportional to the CNT/POR ratio (**Figure 3-4c**). These results indicate that the CNT infiltration process might reduce the amount of heat needed to trigger shape recovery (i.e., a reduction in T_g was further evidenced with this shape recovery experiment). The observed reduction in T_g may be attributed to the loosened hard segments of the polymeric matrix, which can decrease motility of polymeric chains [138, 140]

In addition to the investigation of the effects of CNT infiltration on the thermal properties of the SMP samples, we also examined the Joule-heating behaviors of the CNT-infiltrated SMP foams. First, the resistivity of cuboidal specimens was measured by using a parallel plate setup (See Section 3.1.6). The addition of CNTs was found to allow electrical flow through the polyurethane SMP foams (**Figure 2-2d**). Specifically, the CNT/POR concentration was found to have a significant effect on the volumetric resistivity of the material, i.e., a reduced resistivity with an increasing CNT/POR ratio (Kruskal-Wallis test, $p < 0.05$), and the 0.5%

CNT/POR samples exhibiting a significantly higher resistivity than all other CNT/POR ratios (pairwise Wilcoxon tests, $p < 0.05$). In addition, a negative trend was observed, but the differences were not found to be statistically significant between 0.75%, 1.0%, and 1.25% CNT/POR ratios (pairwise Wilcoxon tests: $p > 0.05$). These results suggest that the CNT infiltration process promotes a higher electrical flow in the SMP material, enabling heat transfer via a Joule-heating mechanism.

A Joule-heating-activated shape recovery test was performed to establish the minimal direct current for triggering the shape recovery (**Figure 3-5a**) and the minimal current to obtain ~90% recovery of the CNT-infiltrated SMP foams after uniaxial compression in a period ≤2 min (**Figure 3-5b**). Direct current (0.5, 0.75, 1.0, 1.25 A) was applied to 5×5×5 mm uncompressed specimens between two parallel conductive plates, and the surface temperature of the specimens was monitored by using an infrared thermal camera (ETS 320, FLIR Systems). In general, the surface temperature of the CNT-infiltrated foams increased as direct current was applied. We noted that the foams gained more heat at the interface between the copper plate and the foam, which might be caused by the limited contact between the plates and the porous surfaces of the foam, leading to a high contact resistance, and by a significant dissimilarity in the thermoconductive properties of the two materials (**Figure 3-6**) [141]. Moreover, the heat flow through the foam was not uniform, with hot spots observed at varying points of the specimens. This may be due to a non-uniform dispersion of CNTs in the synthesized SMP foam. Nevertheless, after 60 s of electrical stimulation, the foam specimens reached a state where the surface temperature was evenly distributed. This Joule-heating behavior was observed in all the CNT/POR ratios (**Figure 3-7 –** 0). Additionally, the heating rate of the

CNT-infiltrated foams was directly related to both the applied current and the CNT concentration (**Figure 3-10**). Specifically, at a 0.5 A current, only the 1.25% CNT/POR foams were observed to heat up to a temperature level greater than T_g (34 °C) after 60 s of stimulation, whereas larger currents allowed the SMP foams to reach this temperature faster. Finally, the average surface temperature of the CNT-infiltrated SMP foams increased at a faster rate with an increasing CNT/POR ratio.

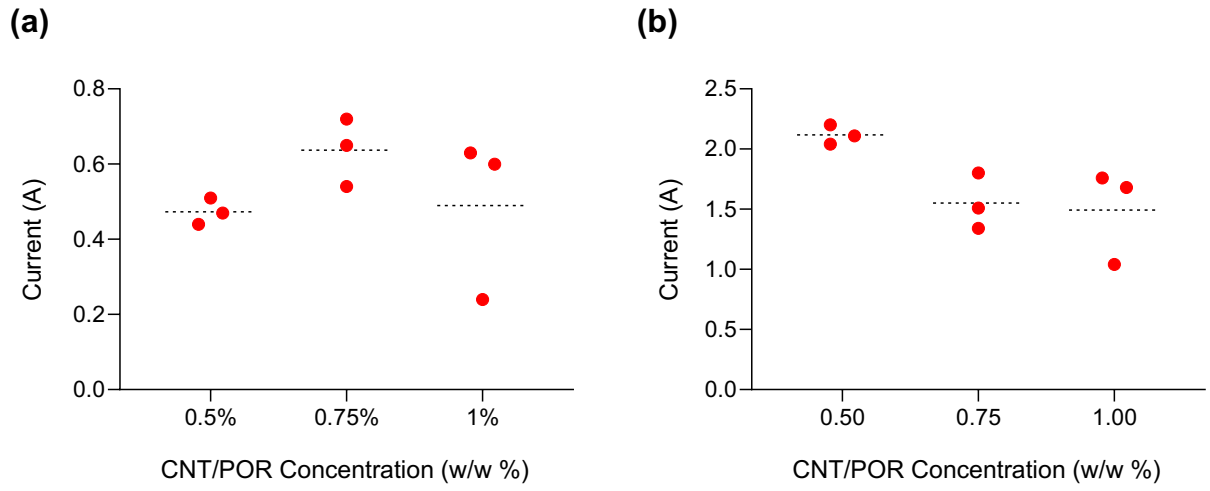


Figure 3-5. (a) Minimum current required to trigger shape recovery for uniaxially-compressed CNT-infiltrated SMP foams at different CNT/POR concentrations. (b) Minimum current required to obtain 90% shape recovery in a period of ~2 min for uniaxially-compressed CNT-infiltrated SMP foams at different CNT/POR concentrations.

3.2.3 Mechanical Characterizations of CNT-Infiltrated SMP Foams

To determine the effects of CNT infiltration on the mechanical behaviors of the SMP foams, we performed uniaxial mechanical characterization of the specimens. First, uniaxial compressive testing was performed up to 90% strain both at room temperature and above T_g (39 °C). The stress-strain curves exhibited two distinct regimes: (i) a low-stress region up to

~60% strain corresponding to the buckling of the pores in the matrix that is consistent with the observations from the previous studies [142-144], and (ii) a high-stress region, where the pores in the matrix are completely compressed in a post-buckling state and further deformation results in an abrupt increase in the elastic modulus (**Figure 3-12**). When the CNT-infiltrated SMP foams were compressed at room temperature, the specimens were found to be significantly stiffer than those being tested above T_g (Student's *t*-test, $p < 0.05$), indicating a configurational transformation between the glassy and the rubbery states of the foam. However, no significant differences were found in the uniaxial compressive behaviors with varied CNT concentrations.

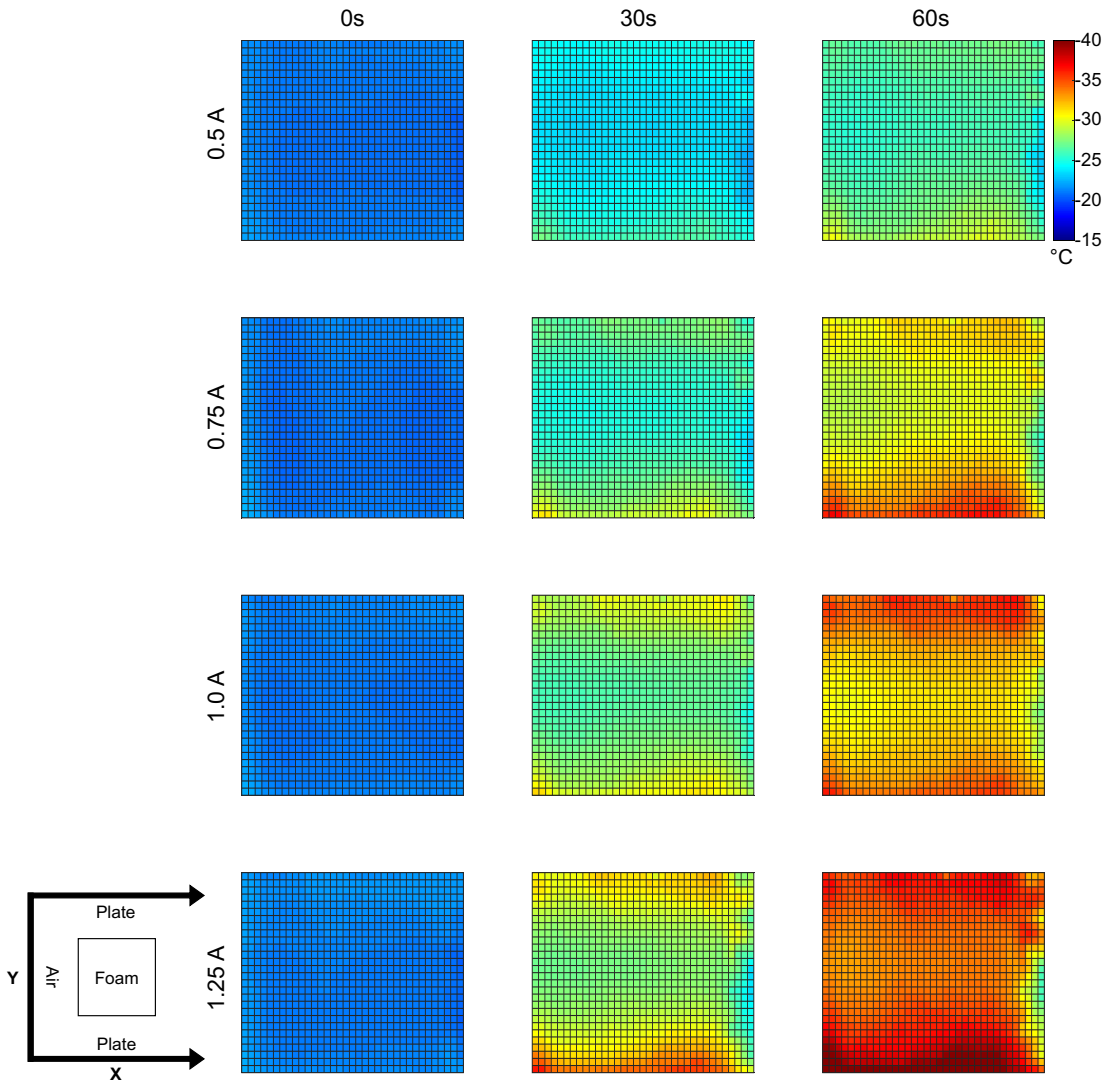


Figure 3-6. IR thermal camera-measured heatmaps of a SMP foam (0.5% w/w CNT/POR concentration) subject to different direct currents, for evaluating its Joule-heating triggering behaviors at different time points of the applied current.

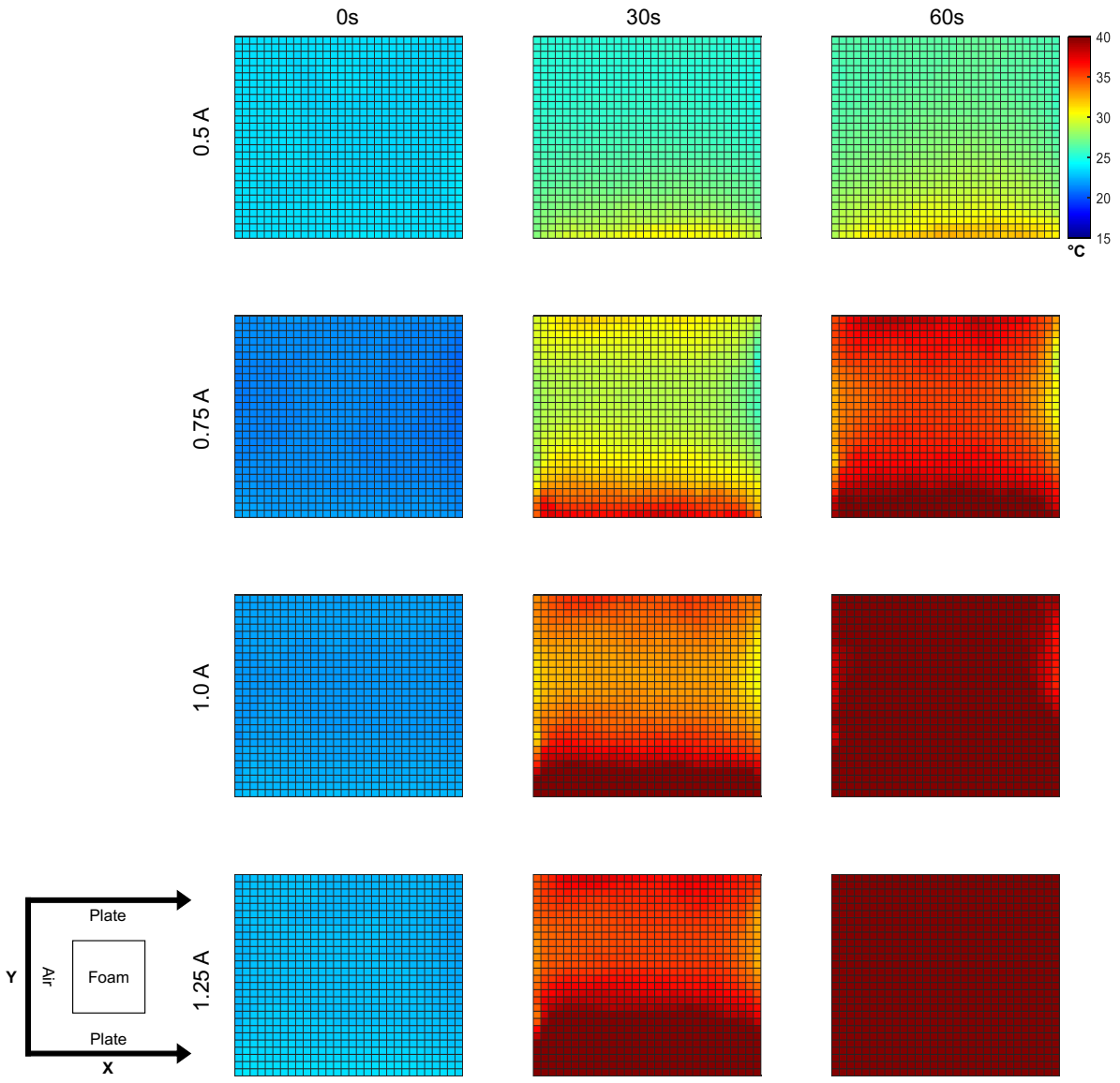


Figure 3-7. IR thermal camera-measured heatmaps of a SMP foam (0.75% w/w CNT/POR concentration) subject to different direct currents, for evaluating its Joule-heating triggering behaviors at different time points of the applied current.

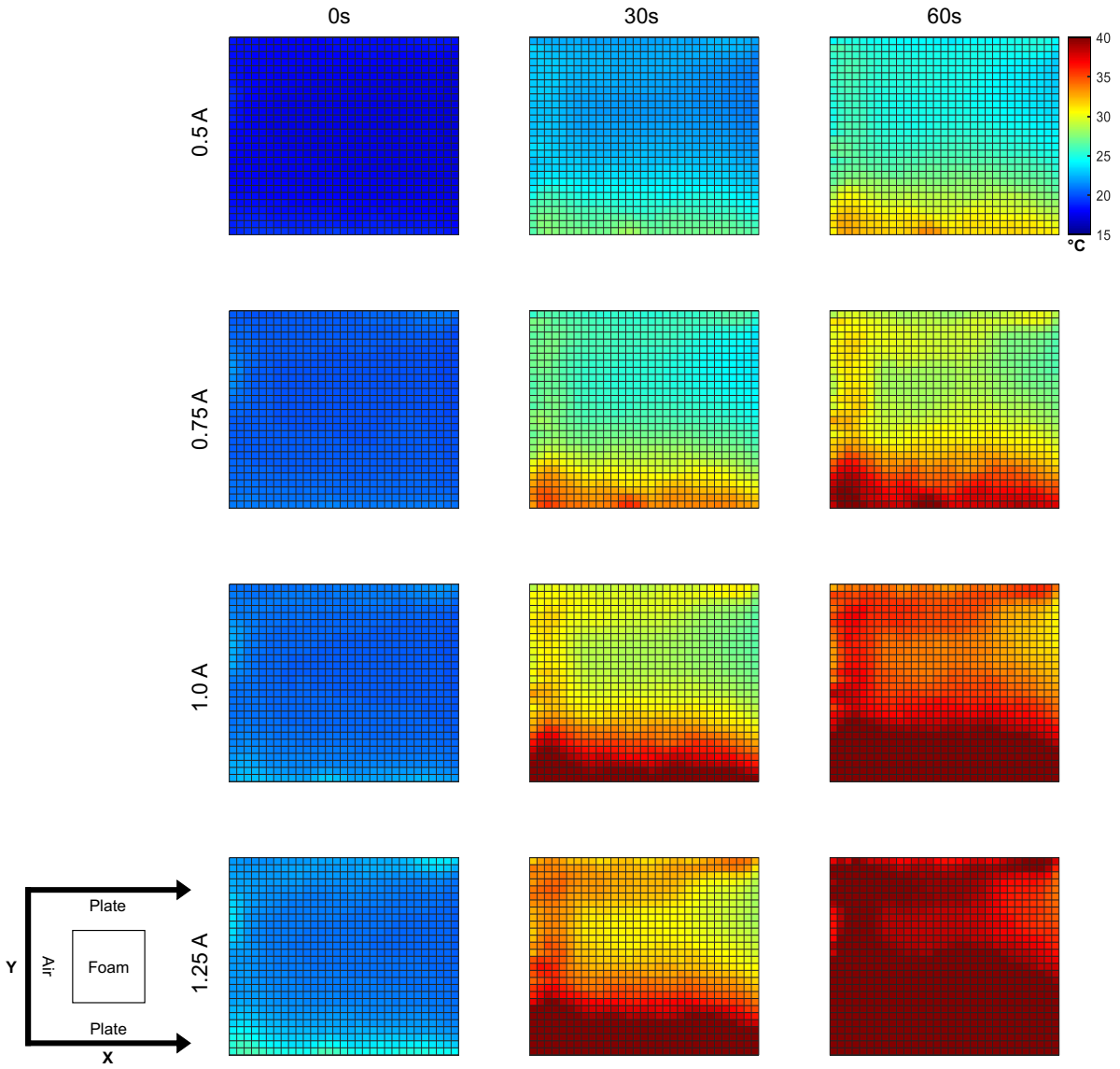


Figure 3-8. IR thermal camera-measured heatmaps of a SMP foam sample (1.0% w/w CNT/POR concentration) subject to different direct currents, for evaluating its Joule-heating triggering behaviors at different time points of the applied current.

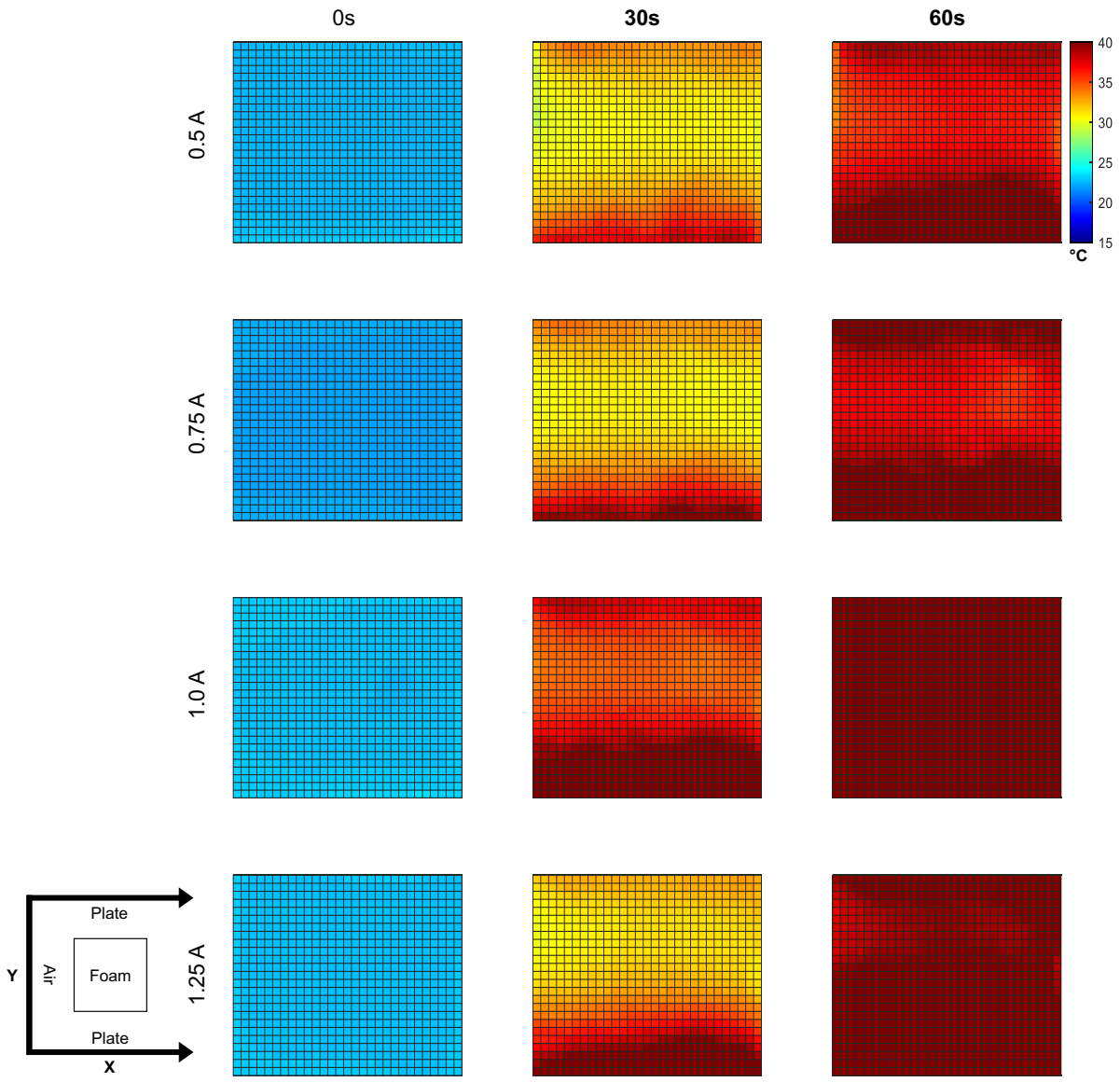


Figure 3-9. IR thermal camera-measured heatmaps of a SMP foam sample (1.25% w/w CNT/POR concentration) subject to different direct currents, for evaluating its Joule-heating triggering behaviors at different time points of the applied current.

We further investigated the characteristic hysteresis and the stress reduction of the SMP foams under cyclic compressive loading. Cyclic compression tests were performed at the low-stress region (up to 60% strain) to avoid plastic deformations at the high-stress region. The pristine SMP specimens exhibited a highly elastic behavior with undiscernible relaxation at the end of ten loading/unloading cycles (**Figure 3-11**). In contrast, the CNT-infiltrated SMP foams exhibited wider hysteresis loops than the pristine SMPs (**Figure 3-11**). Moreover, the cumulative stress reduction at 60% strain for the pristine SMP was close to zero, whereas larger cumulative stress reduction was observed for the CNT-infiltrated samples with an increasing CNT concentration (**Figure 3-11**). Specifically, specimens with the 0.5% CNT/POR ratio had an average stress reduction of $26.80 \pm 0.14\%$, which was significantly higher than the pristine SMPs ($p < 0.05$). These thermomechanical results suggest that cyclic stresses on the CNT-infiltrated SMP specimens result in the plastic deformation of the polymeric matrix, i.e., excessive stresses cause damage to the polymeric structure. The potential damage to the CNT-infiltrated SMP foams was evidenced by the loss of their shape recovery capacity after 10 cycles of repetitive compression, while the pristine SMP foams were able to recover to their initial (uncompressed) configuration.

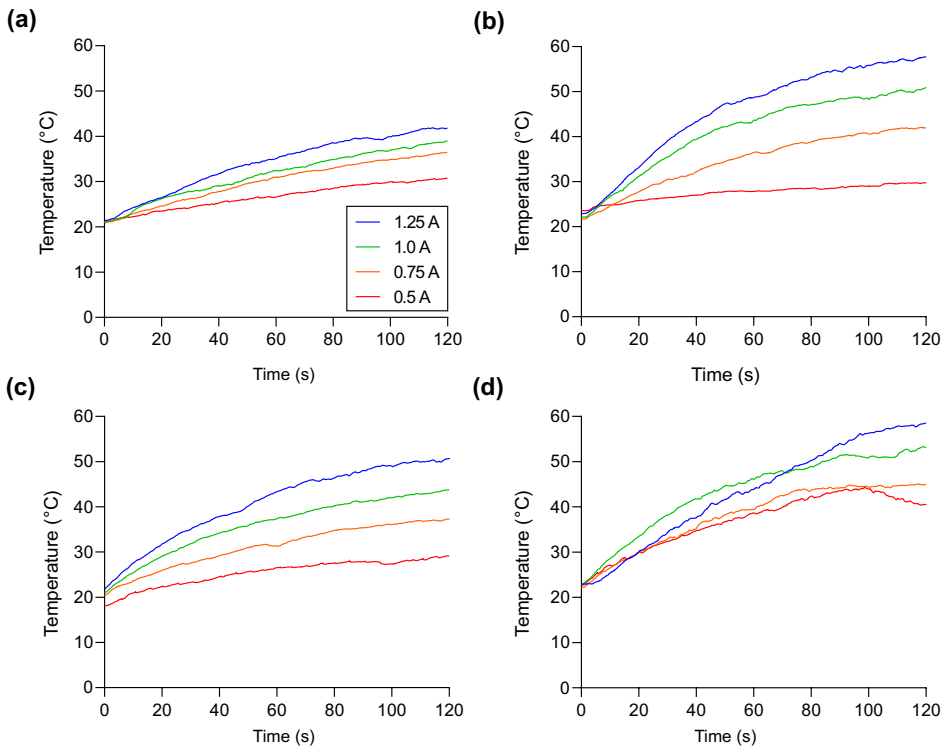


Figure 3-10. Average surface temperature as a function of time of the CNT-infiltrated SMP foams during electrical stimulation with different direct currents and various CNT/POR ratios: (a) 0.5%, (b) 0.75%, (c) 1.0%, and (d) 1.25% w/w.

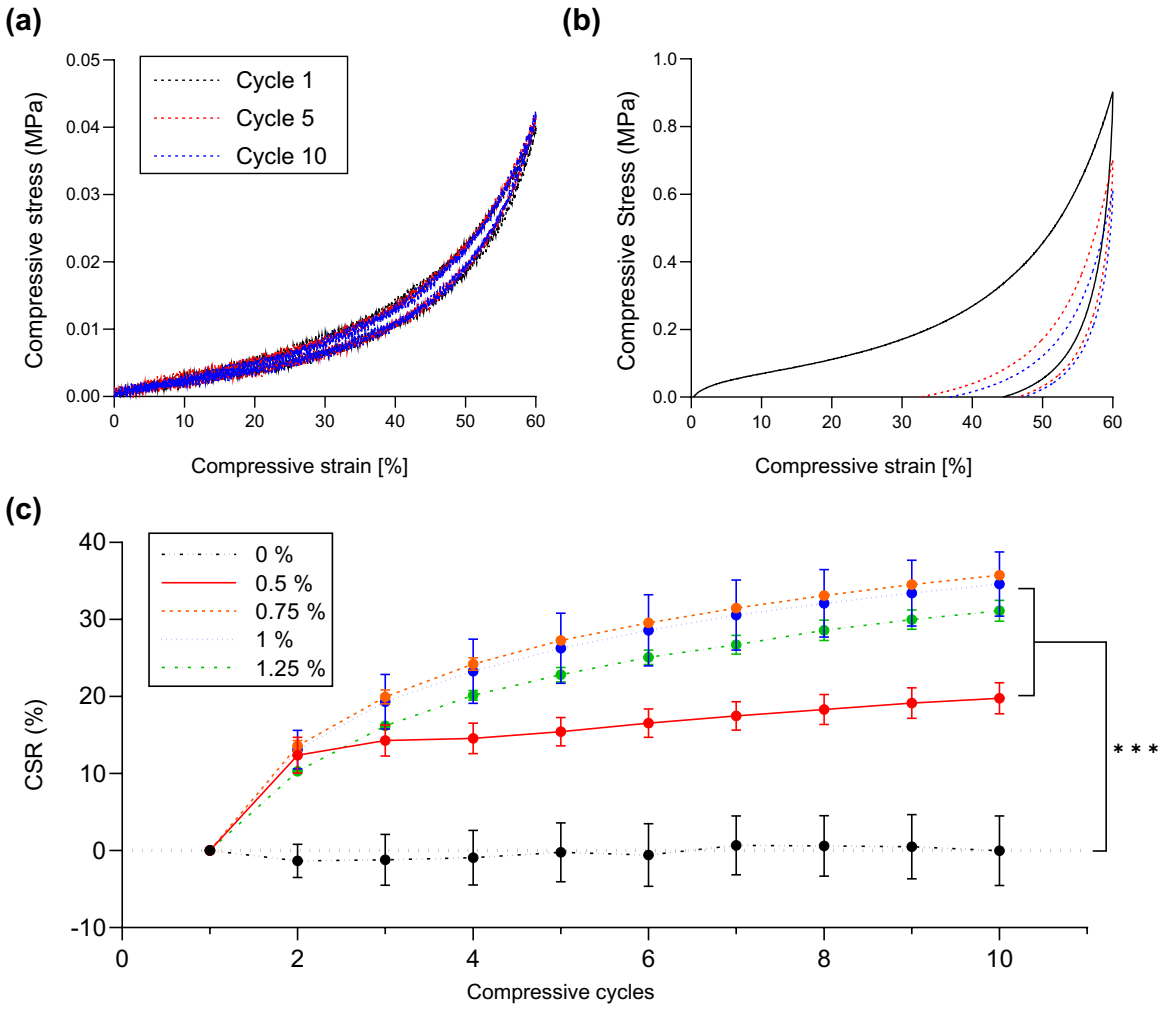


Figure 3-11 (a) Representative results of the cyclic compression tests at T_g for (a) the pristine, and (b) the CNT-infiltrated SMP foams. (c) Cumulative stress reduction of the pristine and CNT-infiltrated SMP foams at various CNT/POR ratios after cyclic compression tests, demonstrating the stress relaxation trend (*** denotes $p < 0.001$).

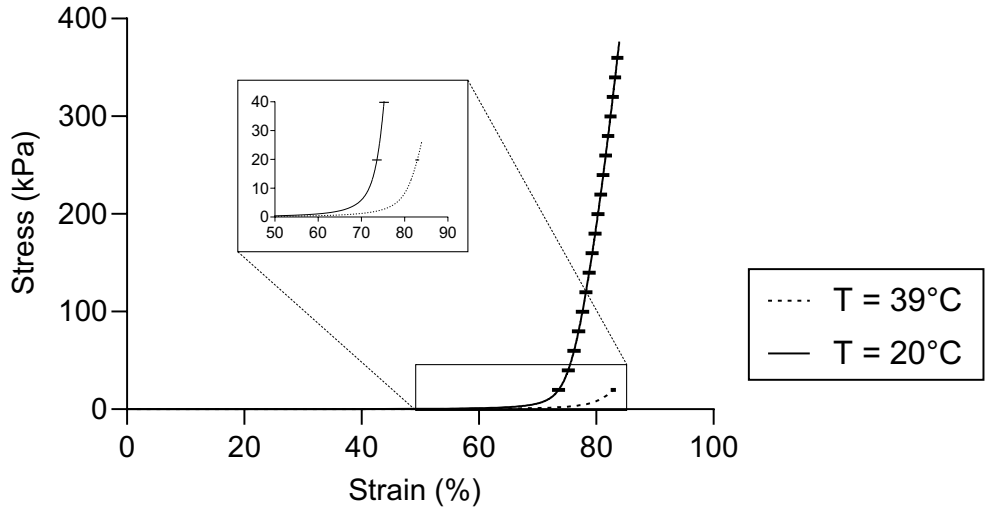


Figure 3-12. Representative stress-strain compression curve for CNT-infiltrated SMP foams ($n = 3$) with a CNT/POR concentration of 0.75% w/w.

3.2.4 Demonstration of the Aneurysm Occlusion Process via an Idealized Aneurysm Phantom Model

To examine the potential of our CNT-infiltrated SMP foam to be used as an embolic device, we simulated the occlusion of an idealized aneurysm using the proposed Joule-heating triggering mechanism. First, we designed an idealized aneurysm model that simulated a saccular aneurysm with anatomically relevant dimensions. Specifically, the model included a Y-shaped vessel bifurcation of 3 mm in diameter, to mimic the average intracranial vessel dimensions[131, 145], and a spherical chamber of 7.5 mm in diameter, representing a medium-sized saccular aneurysm[146, 147], located at the bifurcation point of the vessel (**Figure 3-13a**). Then, a CNT-infiltrated SMP foam, that was manually trimmed to fit the spherical aneurysm chamber, was heated above its T_g (39 °C), compressed uniaxially and transported to the saccular space of the aneurysm model. Finally, an electrical pulse of 1.0 A was applied to

the foam using parallel copper strips to induce Joule-heating on the surface of the material, which triggered shape recovery and occluded the model in less than 1 minute (**Figure 3-13b-c**), while maintaining safe temperatures for surgical implantation (<40 °C), demonstrating the potential of the synthesized CNT-infiltrated material to occlude an aneurysm in an anatomically-relevant environment.

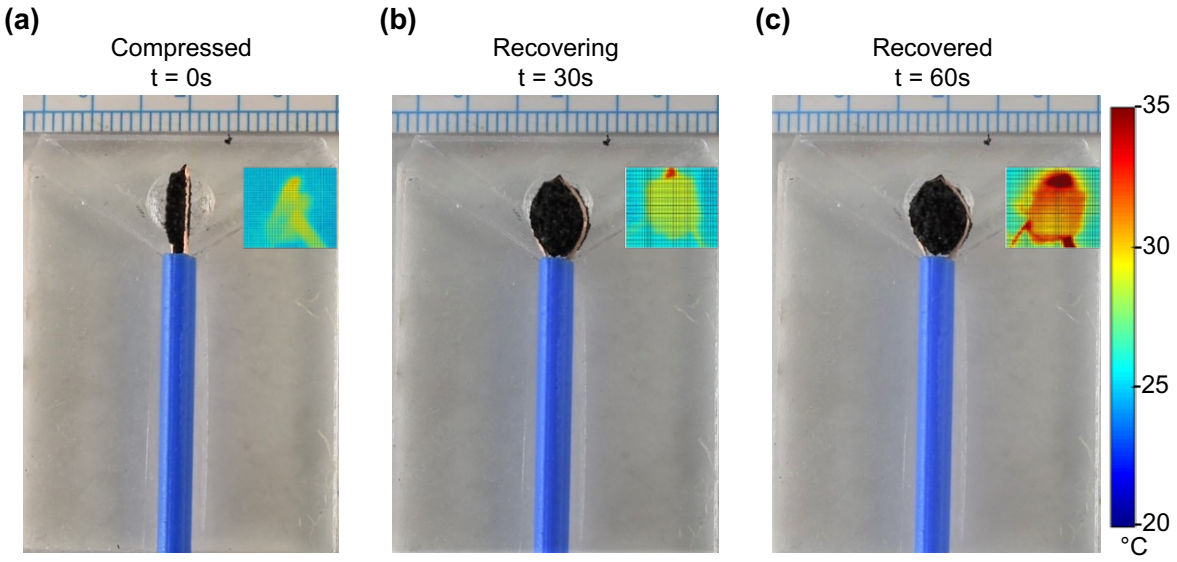


Figure 3-13. Demonstration of an idealized aneurysm phantom model occlusion using a CNT-infiltrated SMP foam (1.0% w/w CNT/POR). Heat maps indicate surface temperature of the foam during shape recovery. Shape recovery was triggered with a DC current of 1.0 A.

3.3 Discussion

3.3.1 Overall Findings

This study aimed to characterize the electrical, thermal, mechanical, and shape recovery properties of a CNT-infiltrated SMP-based embolic device. CNTs were dispersed within the SMP polymeric matrix using a sugar-leaching method to induce conductivity to the material,

enabling a shape recovery triggering mechanism via Joule-heating. We showed that this mechanism allowed the SMP polymeric matrix to trigger shape recovery, as a response to an electrical stimulus. Overall, CNT-infiltration provided control over the shape recovery processes and aneurysm occlusion of the SMP-based endovascular device. Collectively, our findings allowed us to determine that the CNT-infiltrated SMP foam has the potential to be used in a surgical setting as an embolic material for brain aneurysm treatment.

Specifically, our experiments suggested that: (i) CNT-infiltration did not significantly alter the porosity of the SMP foams (**Figure 3-2**); (ii) T_g of the sugar-leached porous SMP foams is significantly reduced compared to the solid SMP (**Figure 3-4a**); (iii) T_g, the shape recovery time, and the volumetric resistivity of the CNT-infiltrated SMP foams are inversely proportional to the CNT/POR ratios (**Figure 3-4b-c**); (iv) CNT infiltration into the SMP polymeric matrix enables heat transfer via the Joule-heating mechanism when direct current is applied to the specimens using parallel copper plates (**Figure 3-6** and **Figure 3-7-9**); (v) their heating rate is directly proportional to the CNT/POR ratio and the applied DC current (**Figure 3-10**); and (vi) significant cumulative stress reduction was evidenced after 10 compressive cycles in the CNT-infiltrated foams, whereas pristine SMP foams exhibited negligible relaxation **Figure 3-11**.

In addition to these findings, we successfully demonstrated that an anatomically relevant *in vitro* aneurysm model can be occluded using a CNT-infiltrated SMP foam through a Joule-heating triggering mechanism (**Figure 3-13**). This proof-of-concept experiment demonstrated the capability of our material to fully recover its custom shape and occlude its target aneurysm

space, indicating that our material has the potential to be used as an embolic device for *patient-specific* brain aneurysm treatment.

3.3.2 Study Limitations

To apply SMP materials to endovascular treatment of brain aneurysms, fine tuning of the T_g is paramount to obtain more precise shape recovery processes. Our results indicate that the sugar leaching process and CNT-infiltration induce significant shifting of the T_g. Future studies will address this limitation and will study the interactions between the monomer ratio and the CNT concentration to obtain a more controllable and reproducible T_g.

Moreover, our thermal assessments allowed the observation of the "*hotspots*" where the material exhibited higher heating rates than the rest of the surface of the material. This observation differed in each specimen and type of foam (**Figure 3-6-9**), indicating that random CNT clusters might have been formed during the dispersion of the CNTs and the synthesis of the foam. Additionally, the clustering of CNTs might have also had a detrimental effect in the compressive properties of the CNT-infiltrated SMP foams. Due to the rigid nature of CNTs, compressive deformation might have led to microstructural changes and breakage in the polymeric matrix, leading to the observed loss of longer-term shape recovery capacity and the cumulative stress reduction in our uniaxial cyclic compressive tests. Future studies will be focused on the design of the CNT dispersion methods that produce a more homogeneous dispersion of the carbon nanotubes in the polymeric matrix, which might improve both the thermal and mechanical properties of the material [148].

Thermal assessments of the material also allowed us to observe a high contact resistance between the copper plate and the porous surface of the foam, which was evidenced by a faster heating rate at the interface between the foam and the copper plates (**Figure 3-6**). This problem has been observed in other SMP applications. For example, Lu *et al.* observed a similar behavior when using carbon fibers to apply direct currents to an SMP-based composite. This was addressed by improving the interfacial conductivity of their system via coating the fibers with silver nanoparticles. This nanoparticle coating provided a more uniform heat distribution and shorter shape recovery times [141]. Similar approaches can be utilized in our flat copper plate system to reduce the dissimilarity of the two materials and reduce the contact resistance at the interface. An approach of this kind will also reduce the average temperature of the foam during Joule-heating processes, providing safer conditions for endovascular implantation of the embolic device.

Furthermore, the presented *in vitro* aneurysm model serves as a proof-of-concept demonstration of the embolic capacity of the CNT-infiltrated SMP foam in a controlled environment with anatomically relevant dimensions. However, this model is limited by an idealized geometry of the brain aneurysm, which might differ from clinically observed geometries. Future studies will be designed to demonstrate the occlusion of image-based aneurysm geometries to provide a more clinically accurate occlusion process [149, 150]. In addition, a flow-loop system will be utilized to provide a pulsatile flow environment to our future imaged-based models, which will also allow to investigate the effects of SMP-based aneurysm occlusion in the fluid hemodynamics of the treated vessel[151-153]. This will also be assisted by testing the capacity of our CNT-infiltrated SMP material to induce

electrothrombosis, a well-known property of current coil-based endovascular devices that utilizes electric currents to induce blood constituent deposition on the surface of the material [3, 154] Then, the biocompatibility of the CNT-infiltrated material will be tested [155], and potential issues will be addressed with surface modification methods [156].

3.4 Conclusion

We have demonstrated the effects of CNT infiltration on the thermal, electrical, mechanical, and shape recovery properties of an aliphatic polyurethane SMP-based porous material. Our results indicate that CNT infiltration is a promising technique for the design of a Joule-heating mechanism for shape recovery triggering of an SMP-based embolic device. Further, we demonstrated the potential of CNTs to induce conductivity and to control the shape recovery time of the SMP foam. Despite the limitations of CNT infiltration, the findings in this study contribute into the development of electrically activated shape memory polymers for biomedical devices, as well as for the applications outside the biomedical field, such as fillers, textiles, automotive materials and a wide range of industrial applications.

CHAPTER 4 Development of A Leaching/3D-Printing Method for the Fabrication of Patient-Specific Porous SMP Foams

Based on the limitations that were discovered in the study presented in Chapter 3, we designed strategies to improve the fabrication of porous SMP constructs. In this chapter, we present our novel method for the manufacturing of *patient-specific* SMP foams. This method involves a combination of the previously described leaching method with traditional additive manufacturing (i.e. 3D-printing) techniques. Using fused deposition modeling (FDM) of a biocompatible polyvinyl alcohol (PVA) filament, we fabricated 3D templates with complex geometries and pore designs. Here, we first summarize this technique for the fabrication of cubic and image-based foams (Section 4.1.1 and 4.1.2). Next, we present our assessment of the microstructure of the PVA templates and the resultant 3DSMP foams using microscopy methods (Section 4.2.1). Then, we present material characterizations that shed light on the effect of the fabrication process on the thermomechanical properties of the polyurethane foams (Sections 4.2.2-4.2.4). Finally, we present characterizations on the shape recovery behavior of the 3DSMP foams. This chapter is then concluded with our presentation of the application of this method for the fabrication of image-based *patient-specific* 3DSMP foams for the occlusion of *in vitro* aneurysm models. The findings of this chapter provide an important advance in our goal to develop an individualized endovascular device for ICA therapy.

4.1 Materials and Methods

4.1.1 3D-printing of PVA Templates

Sacrificial templates were 3D-printed using a PVA filament (MatterHackers, d = 1.75 mm) in a commercial 3D-printer (Creality CR-10S, China). Templates were fabricated in two different geometries: (i) cubic specimens (10×10×10 mm) for material characterization, and (ii) two patient-specific aneurysm geometries. Cubic specimens were designed using CAD software (Solidworks, Dessault Systems, USA) and exported to a 3D-printing slicing software for infill design (Cura, Ultimaker, Netherlands). Here, templates were fabricated with a grid infill pattern at different densities (40%, 50% and 60%). Top and bottom layers of the print were removed to expose the print infill for SMP solution infiltration. Additionally, two outer walls were printed around the infill structure to aid in the removal of excess cured SMP. Secondly, patient-specific geometries were designed using computed tomography angiography (CTA) images of human ICAs obtained at the University of Oklahoma's Health Science Center (IRB #7932). The CTA images were segmented using Amira (Thermofisher & Zuse Institute Berlin), surface smoothing was performed using Meshmixer (Autodesk, San Rafael, CA), and subsequently 3D-modeled for printing in SolidWorks.[129] Furthermore, a rigorous calibration protocol was performed to determine the optimal printing parameters that provided great surface quality and dimensional accuracy for each type of geometry.

4.1.2 Preparation of 3DSMP Foams

Polyurethane SMP solution was synthesized using hexamethylene diisocyanate (HDI, ≥98.0%, Sigma-Aldrich) as the hard segment, N,N,N0,N0-tetrakis (hydroxypropyl) ethylenediamine (HPED, ≥98.0%, Alfa Aesar) as the catalyst, and Triethanolamine (TEA,

≥99.0%, Sigma-Aldrich) as soft segment. HDI, HPED and TEA were mixed at different molar ratios (**Table 4-1**), as described previously [60], using a magnetic stirrer in a nitrogen-protected environment until the monomer solution turned clear. Then, the solution was evenly poured onto 10×10×10 mm PVA 3D-printed templates. The uncured SMP solutions were maintained at −20 °C in a vacuum container for 1 h to slow the curing and to allow complete infiltration of the solution into the template. Then, the specimens were cured at 70 °C for 1 h and 100 °C for an additional hour each under a nitrogen-rich environment using a vacuum oven (BOV-20, Being Instrument, USA). The cured blocks were next immersed in a water bath sonicator (Branson 1800, Branson Ultrasonics Corporation, USA) and sonicated at 50 °C for 24 h to dissolve the PVA templates and residuals. Finally, the 3D foams (3DSMP) were dried in a vacuum oven at 60 °C until mass measurements stabilized (indicating no further water evaporation). The fabricated specimens were stored in a desiccator in vacuum to preserve thermal properties of the material.

Table 4-1. Monomer molar ratios for the fabricated polyurethane 3DSMP foams.

SMP Ratio	HDI	HPED	TEA
SMP5	1	0.35	0.19
SMP6	1	0.3	0.26
SMP7	1	0.25	0.33
SMP8	1	0.2	0.4

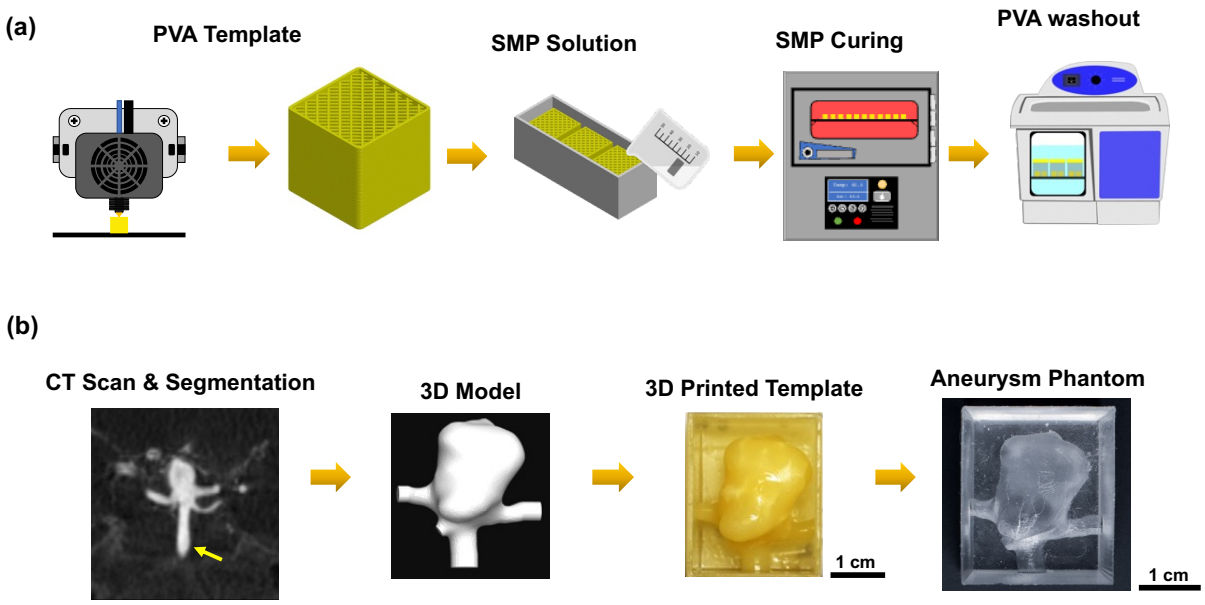


Figure 4-1. (a) Schematics showing the steps for the fabrication of SMP foams using PVA 3D-printed templates (b) Pipeline for the production of patient specific PVA templates and phantoms from CTA imaging. The yellow arrow points at the parent vessel, which has a diameter of 2.45 mm. 3D model was enlarged twofold from its original dimensions to facilitate parent vessel access.

4.1.3 Attenuated Total Reflectance - Fourier Transform Infrared Spectroscopy (ATR-FTIR)

3DSMP foams were characterized with ATR-FTIR to verify that polyurethane synthesis was not altered by the 3D-printing process. ATR-FTIR spectrum was obtained with a spectrometer (Nicolet iS50R, Thermo Scientific, USA) with a *L*-alanine doped triglycine sulfate (DTGS) and mercury cadmium telluride (MCT) detector. The 3DSMP foams were compared to solid polyurethane specimens to analyze differences in the morphology/intensity of characteristic polyurethane peaks. Spectrum analysis was performed using an in-house MATLAB program (Mathworks, USA).

4.1.4 Scanning Electron Microscopy

Micrographs of the 3DSMP specimens were obtained to characterize the architecture of the foams. The specimens were imaged in a field-emission environmental scanning electron microscope (Thermo Quattro S, Thermofisher, USA) at an accelerating voltage of 20 kV. Architectural features, such as pore size, distance between lattices and fiber thickness, were measured using ImageJ Fiji (National Institutes of Health, USA) [132].

4.1.5 Differential Scanning Calorimetry

DSC was performed to determine the effect of the PVA-leaching process in the T_g of the synthesized 3DSMP foams. The specimens ($n = 3$) at the monomer ratios described in **Table 4-1** were subjected to DSC testing. Experimental groups included the 3DSMP specimens and solid SMP specimens, as control. Specimens were tested in a DSC device (DSC2500, TA Instruments, USA) with three heating/cooling cycles at a range of –20 °C to 120 °C at a 5 °C/min heating rate and 10 °C/min cooling rate. The T_g was measured from the second heating cycle using the TA Instruments Trios software v5.1.1.45672. The obtained T_g measurements were used to obtain two-parameter exponential models in MATLAB of the leached and solid specimens. Using the predicted values of the models, a monomer ratio with $T_g \approx 41$°C was formulated. The resultant SMP ratio was named SMP-X and tested in DSC to verify T_g.

4.1.6 Mechanical Characterization - Uniaxial Compressive Testing

Using a monomer ratio with $T_g \approx 41$ °C, 3DSMP foams ($n = 6$) were subjected to cyclic compressive mechanical testing. Compressive deformation was applied to the specimens using

a plate mechanical tester (Instron 5969, USA) at a compressive rate of 4 mm/min up to a compressive strain of 80%. Specimens were kept in a heating chamber at $T = T_g + 10$ °C during mechanical testing. Mechanical parameters were calculated and processed in MATLAB R2022a (Mathworks, USA): (i) peak stress was defined as the measured stress at 80% strain; (ii) cumulative stress relaxation (CSR) was quantified as the percent reduction of peak stress at each compression cycle; and, lastly, (iii) the elastic modulus was calculated as the slope of the linear fit obtained from the data points up 60% strain of the stress-stretch curve.

4.1.7 Shape Recovery Assessments

The SMP-X specimens ($n = 3$) were heated in a vacuum oven (BOV-20, Being Instrument, USA) at $T = T_g + 10$ °C to induce the rubbery state of the SMP. Specimens were then compressed to 0.8 strain with fixed plates and cooled down to –20 °C to fix the programmed geometry. Then, the compression plates were released and shape recovery was tracked using a digital camera (Nikon d5600: 50 mm lens, 23.5×15.6 mm CMOS sensor, Japan) under three different thermal conditions (i) room temperature ($T = 23$ °C), (ii) freezing conditions ($T = -20$ °C), and (iii) a thermal ramp from room temperature to $T = T_g + 10$ °C. Shape recovery was measured using equation (4.1):

$$SR\% = \frac{h_{(t)} - h_c}{h_o - h_c} \times 100 \tag{4.1}$$

where $SR\%$ is the shape recovery percentage, $h_{(t)}$ is the height of the foam at a given time t, h_c is the height of the compressed foam, and h_o is the original (pre-compression) height of the foam.

4.1.8 Fabrication of a Patient-Specific Aneurysm Model and *In Vitro Proof-of-Concept* Occlusion Demonstration

Aneurysm geometries were obtained from human CTA images and 3D-printed using PVA water-soluble filament, as described above. Polydimethylsiloxane (PDMS, Sylgard 184, DOW, USA) solution was poured on the mold, degassed using a vacuum pump, and cured at 70 °C for 1 h in a vacuum oven. Then, PVA was washed out in a water bath and sonicated at 50 °C. Finally, the aneurysm phantoms were dried at 60 °C for 3 h. The 3DSMP foams with patient-specific geometries were transported into the aneurysm phantom and occlusion was monitored using a digital camera.

4.1.9 Statistical Analysis

Quantitative measurements were expressed as mean $\pm$ standard error of the mean. Normality was tested using the Shapiro-Wilk test and Q-Q plots. For one-factor designs, one-way ANOVA or Kruskal-Wallis were used to test differences between groups. For two-factor designs, two-way ANOVA or aligned-rank transform tests were applied [157]. Pair-wise comparisons were performed using Tukey-HSD test. Differences between groups were deemed significant when $p < 0.05$. Statistical tests were performed in Prism v9.5.1. (GraphPad Software, USA).

4.2 Results

4.2.1 Fabrication of 3DSMP Foams and Microstructure

The 3DSMP foams were fabricated with a method that combines 3D-printing and leaching. Briefly, PVA cubes were printed using a grid infill pattern (**Figure 4-1**) and were used as templates for SMP synthesis. Uncured SMP solution was poured on the PVA templates and was cured until it became solid using different thermal stages in a nitrogen-rich environment (see Section 4.1.2 and Appendix B for further detail). The PVA filament template was leached in a water bath using sonication, leaving polyurethane 3D foams that mimicked the infill microstructure of the original print (**Figure 4-2a.1** and **Figure 4-2b.1**). SEM micrographs demonstrated that the SMP solution cured around the PVA infill filaments (**Figure 4-2a.2** and **Figure 4-2a.3**), allowing the replication of the pattern and creating microchannels after sonication and washout (**Figure 4-2b.2** and **Figure 4-2b.3**).

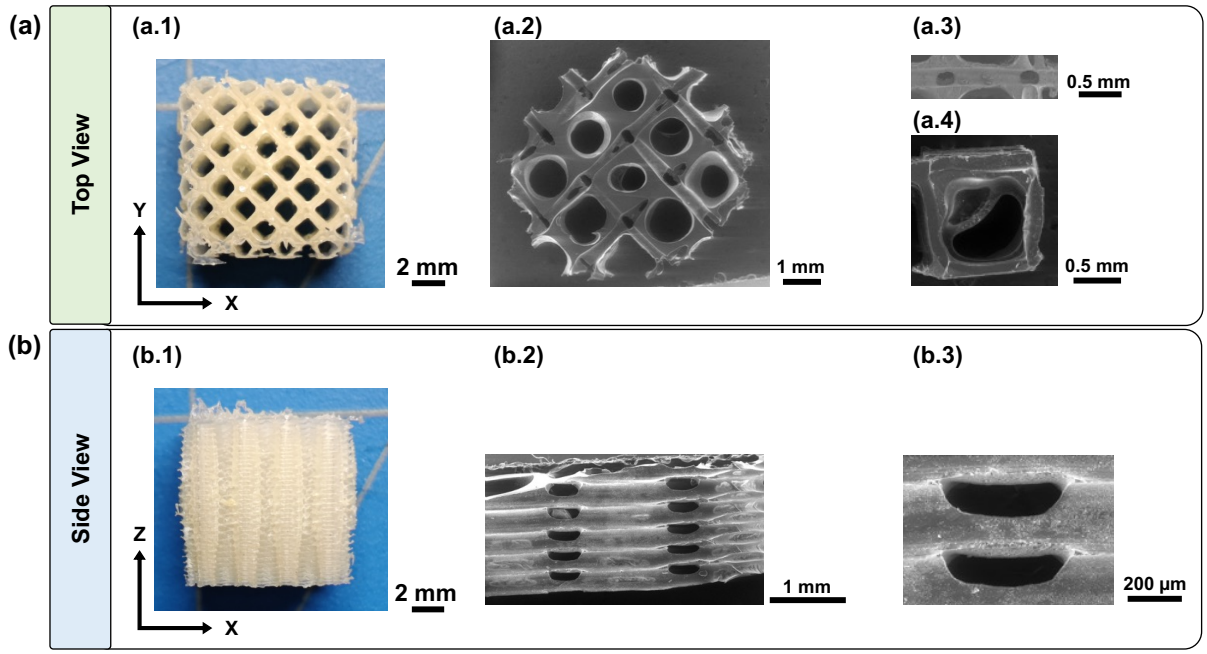


Figure 4-2. Photographs and SEM micrographs of the 3DSMP foams from the (a) top view and (b) side view.

To evaluatethe overall microstructure of the foams, we further fabricated 3DSMP foams using PVA templates with different infill densities to control porosity. The PVA templates had an average wall thickness of 0.402 ± 0.007 mm, 0.382 ± 0.005 mm, and 0.449 ± 0.009 mm for the 40%, 50% and 60% infill densities, respectively (**Figure 4-3**). These template structures yielded 3DSMP foams with consistently increased wall thickness: 0.465 ± 0.019 mm for the 40%, and 0.434 ± 0.012 mm for the 50% infill densities (**Figure 4-4**, $p < 0.05$), but with no significant change in the 60% templates (0.438 ± 0.008 mm, **Figure 4-4**, $p > 0.05$). The different infill densities allowed to obtain 3DSMPs with different porosities. Overall, 3DSMP foams accurately mimicked the PVA template with minor defects, which included increased surface roughness and randomly clogged pores (not shown).

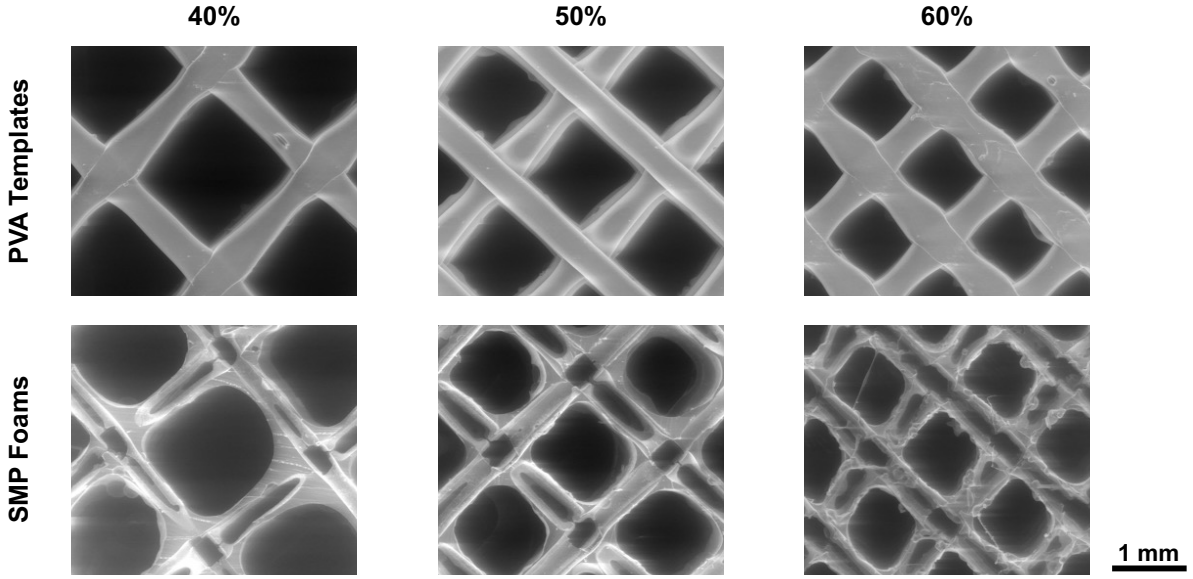


Figure 4-3. SEM micrographs of PVA templates (*top*) and 3DSMP foams (*bottom*) at different infill densities (*columns*).

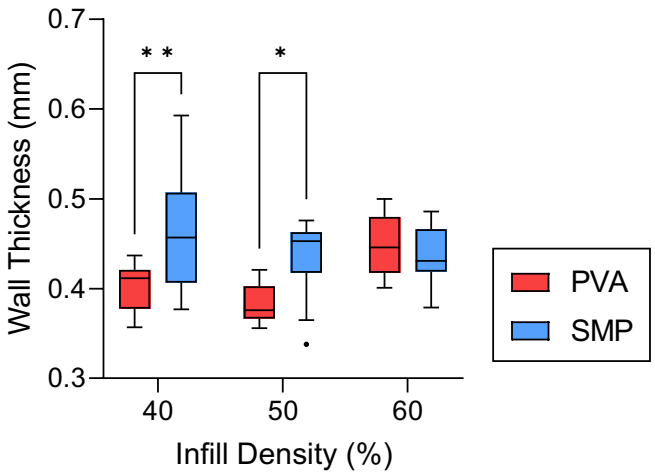


Figure 4-4. Wall thickness measurements of PVA 3D-printed templates and the resultant 3DSMP foams after PVA leaching. (Significance levels: $*$ for $p < 0.05$, $**$ for $p < 0.01$).

4.2.2 Differential Scanning Calorimetry (DSC)

DSC was performed to determine the effect of the PVA-leaching process in the T_g, of the material. 3DSMP foams were fabricated using different monomer molar ratios (**Table 4-1**), as described previously [60]. First, we observed that controlling the monomer molar ratios allowed for the control of the resultant T_g, of the material, where an increased concentration of TEA lead to a decrease in T_g, (**Figure 4-5a**). Further, we observed that the T_g, of the 3DSMP foams was significantly lower than their solid counterparts (**Figure 4-5a**), indicating that our PVA-leaching method had an effect on the thermal behavior of the resultant polyurethane matrices. Using the measured T_g, from the solid and 3D foams, we performed a 2-term exponential regression for each type of material using the TEA molar ratio as a predictor for the T_g. Using the predicted values for these models, we fabricated a new molar ratio (named SMP-X) with a TEA molar ratio with a predicted $T_g \approx 41$ °C (**Figure 4-5b**). Experimental

testing of the SMP-X ratio (TEA molar ratio of ≈ 0.22) demonstrated that our model accurately predicted the T_g, of the 3DSMP foams. This monomer ratio was used for the subsequent testing of the shape recovery and mechanical properties of the 3DSMP material, as well as the *in vitro* aneurysm embolization demonstration experiment.

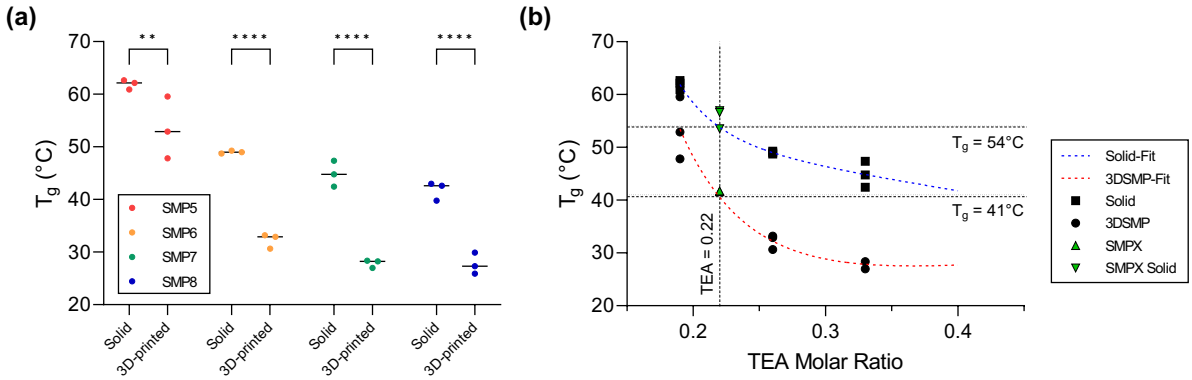


Figure 4-5. (a) T_g measurements of solid SMP and 3DSMP. (b) T_g exponential models as a function of TEA molar ratio used to predict TEA content of 3DSMP foams with T_g ~ 41 °C.

4.2.3 Attenuated Total Reflectance – Fourier Transform Infrared Spectroscopy (ATR-FTIR) Characterization

We performed ATR-FTIR to verify the chemical integrity of the material after the indirect 3D-printing process. We previously characterized the ATR-FTIR spectrum of our SMP material (See Section 3.1.3) [62], which is characterized by peaks at: (i) 1683 cm^{-1}, related to urethane carbonyl C=O stretching, (ii) 1542 cm^{-1}, associated with urethane C−N−H deformation vibrations, (iii) 1246 cm^{-1} related to C−N stretching vibrations, (iv) 1142 cm^{-1}, related to C−O−C stretching vibrations, and (v) 3306 cm^{-1}, corresponding to N-H stretching vibrations (**Figure 4-6a**) [134, 158]. This spectrum is characteristic of highly cross-linked polyurethanes, as described by Stern [158]. However, 3DSMP foams exhibited some marked differences in

their FTIR spectrum. Namely, we observed the appearance of a peak at 1616 cm^{-1} (**Figure 4-6b**), adjacent to the 1683 cm^{-1} peak, which can be observed in linear polyurethanes [158]. In addition, we observed more prominent peaks at 3327 cm^{-1}, related to O−H vibrations, and peaks at 1046 cm^{-1} and 1142 cm^{-1} associated with C−O hydroxyl stretching. These changes in the FTIR spectrum might be associated with urethane links formed by PVA and HDI during the SMP solution curing, yielding portions of the material with linear polyurethane segments.

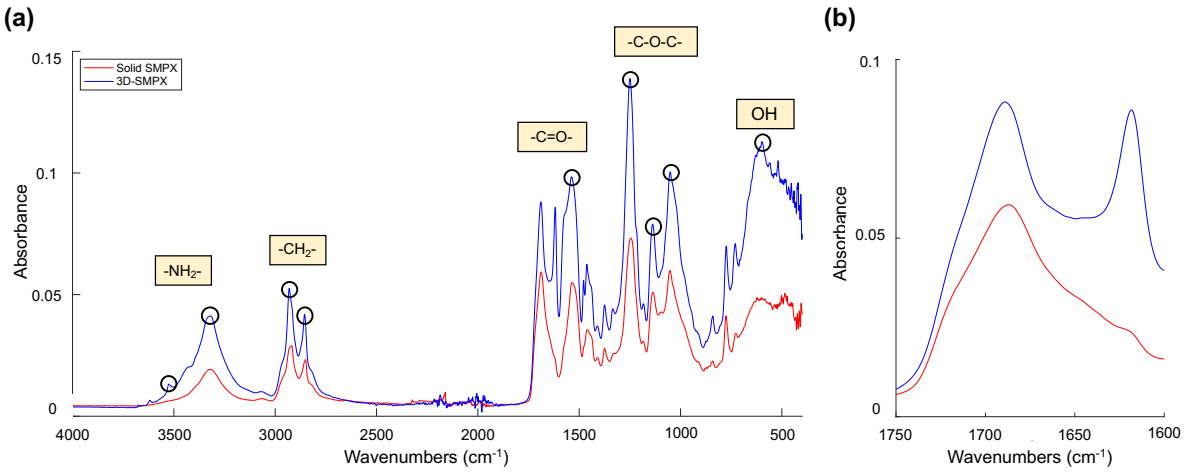


Figure 4-6. (a) FTIR spectra of solid SMP and 3DSMP of the SMP-X ratio. (b) Zoomed spectra showing the modified urethane chemistry of the 3DSMP foams.

4.2.4 Compressive Mechanical Properties of 3DSMP Foams

The mechanical properties of the 3DSMP foams were characterized using a compressive mechanical tester. We fabricated specimens with the SMP-X monomer ratio (1:0.32:0.22 HDI:HPED:TEA) using PVA templates with a grid infill pattern (**Figure 4-2**) at different infill densities (40%, 50% and 60%, **Figure 4-3**). We tested the compressive behavior of the material along the *X*- and *Z*-axis to study the effect of the different infill patterns on the

overall behavior of the foams. First, we observed that the foams' stress-strain curves exhibited a non-linear behavior for both axes of compression (**Figure 4-7**). Specifically, we observed that both axes exhibited a semi-linear behavior up to ~60% strain; then, stress increased exponentially. We also observed an anisotropic behavior, where the *Z*-axis was stiffer than the *X*-axis (**Figure 4-7a-c**), due to the higher material density in the *Z*-axis, which is caused by the short separation between printed lattices (**Figure 4-2b.2**). In addition, we observed that overall mechanical properties of the material also depended on the infill density and compressive direction (**Figure 4-8**). Namely, peak stress at ~90% compressive strain long the *X*-axis was homogenous across infill densities with an average of 0.92 ± 0.11 MPa ($p > 0.05$, **Figure 4-8a**); however, peak stress along the *Z*-axis was lower in the 40% infill density group than in the other groups, albeit with no significance (1.44 ± 0.18 MPa vs. 3.48 ± 0.61 MPa, $p = 0.15$, **Figure 4-8a**). Peak stress measurements decreased with cyclic compression, indicating plastic deformation of the foams. This cumulative stress reduction (CSR) was not dependent on infill density nor compressive direction; CSR for both directions was $-13.10 \pm 3.23\%$ ($p > 0.05$, **Figure 4-8b**). Finally, the average elastic modulus for the X-axis was 0.08 ± 0.01 MPa with no significant differences between infill density groups (**Figure 4-8c**). For the *Z*-axis, the average elastic modulus for the 60% infill density group was significantly higher than for the other groups (0.22 ± 0.02 vs 0.14 ± 0.01, $p < 0.01$, **Figure 4-8c**). Overall, the *Z*-axis exhibited a higher elastic modulus mean than the *X*-axis ($p < 0.01$).

4.2.5 Shape Recovery Properties of the 3DSMP-X Foams

As demonstrated in DSC (see Section 4.2.2), our material exhibited glass transitions which allow for the shape reprogramming and recovery. To characterize this behavior, we performed

experiments that provided an insight into the capacity of the material to store its deformed geometry and its subsequent shape recovery. We fabricated 3DSMP cubes, which were first heated above their T_g (i.e., $T = T_g + 10°C$.), compressed them uniaxially, and induced shape storage by cooling the material below T_g. Then, we measured shape recovery under different thermal conditions: (i) at room temperature (T = 23 °C), we observed that the material was able to maintain shape recovery rates <5% for an average of 53 s and that after 10 min the average shape recovery was 55% (**Figure 4-9a**); (ii) in a −20 °C freezer, we observed that the 3DSMP cubes maintained their deformed configuration, exhibiting an average of 0.68% shape recovery after 4 days of storage in freezing conditions (**Figure 4-9b**); (iii) lastly, we triggered shape recovery with a heating ramp up to $T = T_g + 10°C$ (**Figure 4-10**). We observed that >95% shape recovery was accomplished in an average of 70 s (**Figure 4-9c**).

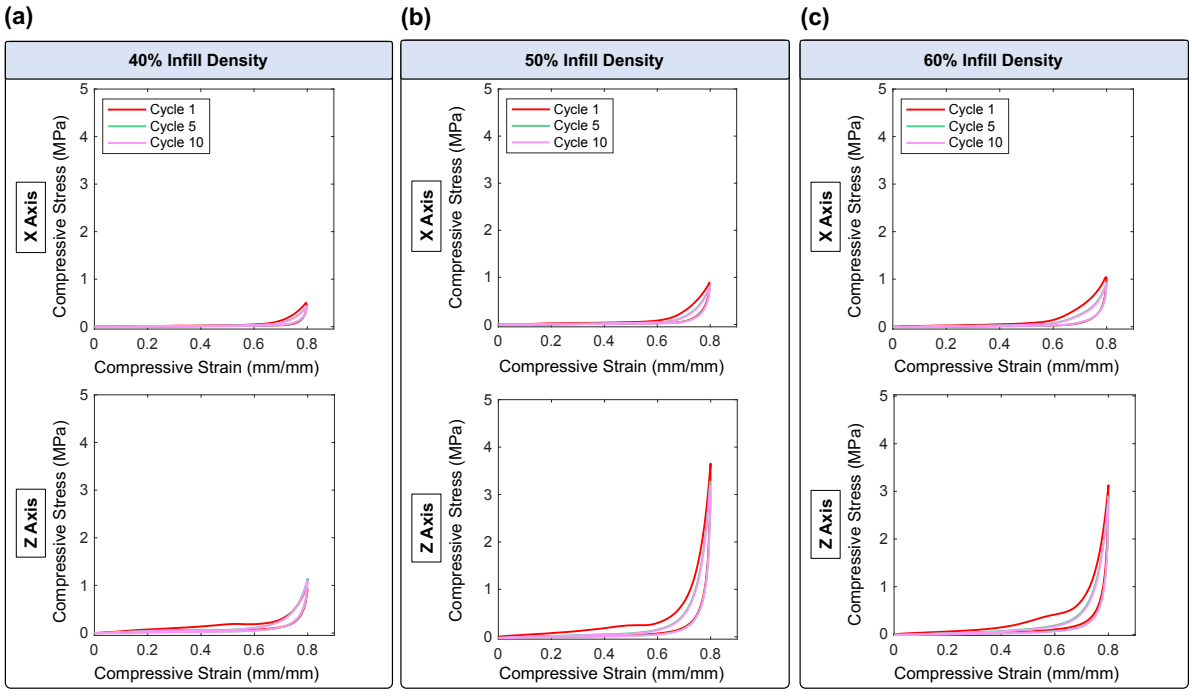


Figure 4-7. Representative compressive stress-strain curves of the 3DSMP foams fabricated with different infilldensities: (a) 40% (b) 50% (c) 60%.

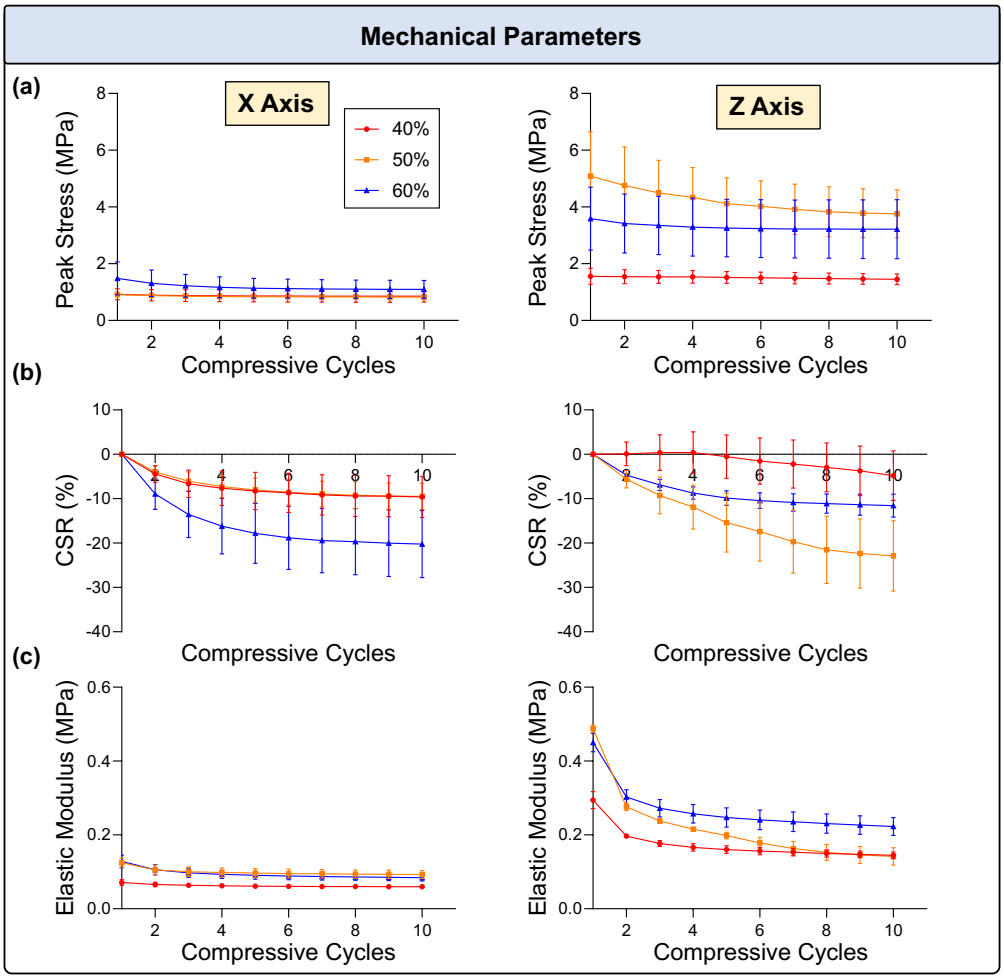


Figure 4-8. Mechanical parameters derived from the stress-stretch curves of 3DSMP foams: (a) Peak stress, (b) CSR and (c) Elastic Mudulus; obtained for the *X*- (*left*) and *Z*-axis (*right*).

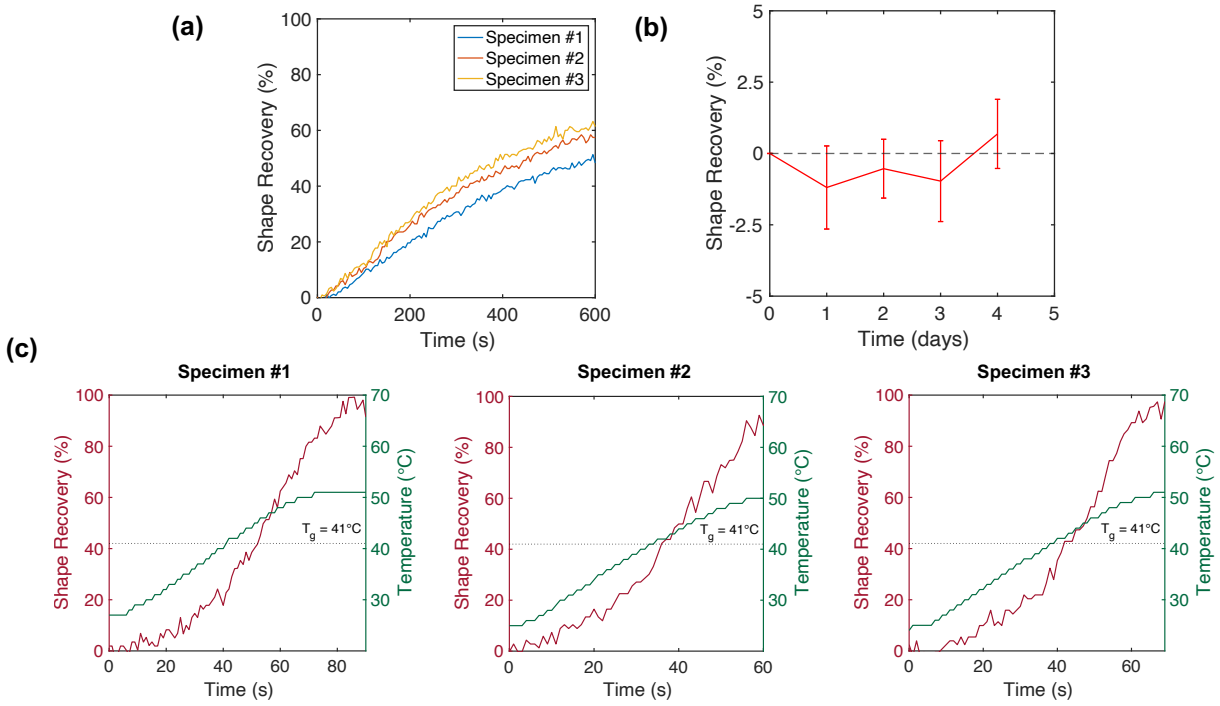


Figure 4-9. Shape recovery properties of the 3DSMP foams: Shape storage at (a) room temperature (T = 23 °C) and (b) T = –20 °C. (c) Shape recovery triggering using a heating ramp up to $T = T_g + 10$°C.

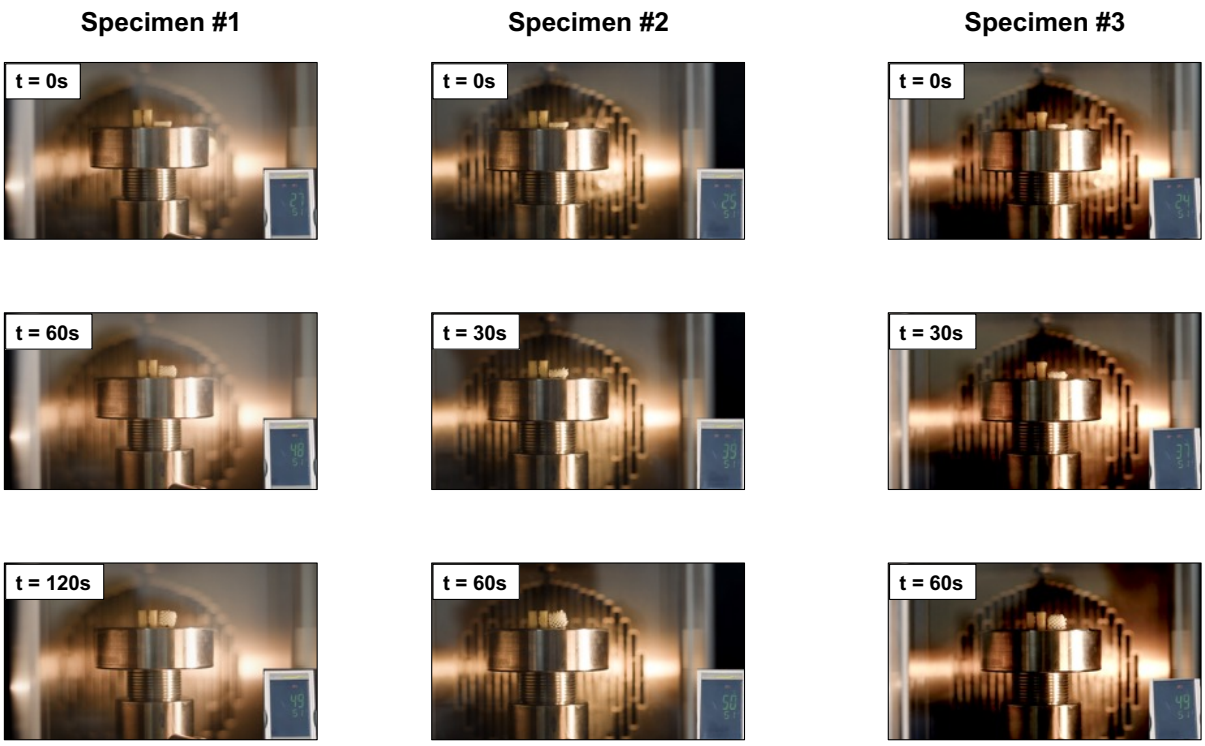


Figure 4-10. Snapshots at different time points of the shape recovery experiment of 3DSMP specimens in a heating chamber. Insets show the temperature inside the heating chamber at each time point.

4.2.6 Fabrication of Patient-Specific 3DSMP Foams: Demonstration of Image-Based Fabrication and Phantom Occlusion

To demonstrate the use of the indirect 3D-printing method to fabricate patient-specific 3DSMP foams, we fabricated aneurysm phantom models with geometries derived from patient CTA data. We fabricated aneurysm phantoms and 3DSMP foams using two different geometries (**Figure 4-11**). The phantoms were used to simulate the aneurysm space, which was occluded by the patient-specific foams. We observed that complete occlusion of the aneurysm models was achieved for both geometries. Aneurysm geometry #1 is a bifurcation aneurysm with an elongated geometry, which allowed a facile delivery and complete occlusion of the aneurysm

space and neck. On the other hand, aneurysm geometry #2 was a side-wall aneurysm with a "cherry-like" geometry. This aneurysm had a more spherical and irregular shape, which made delivery more difficult due to hanging portions of the foam that required repositioning of the foam during delivery. Overall, both aneurysm geometries were successfully occluded using our 3DSMP foam.

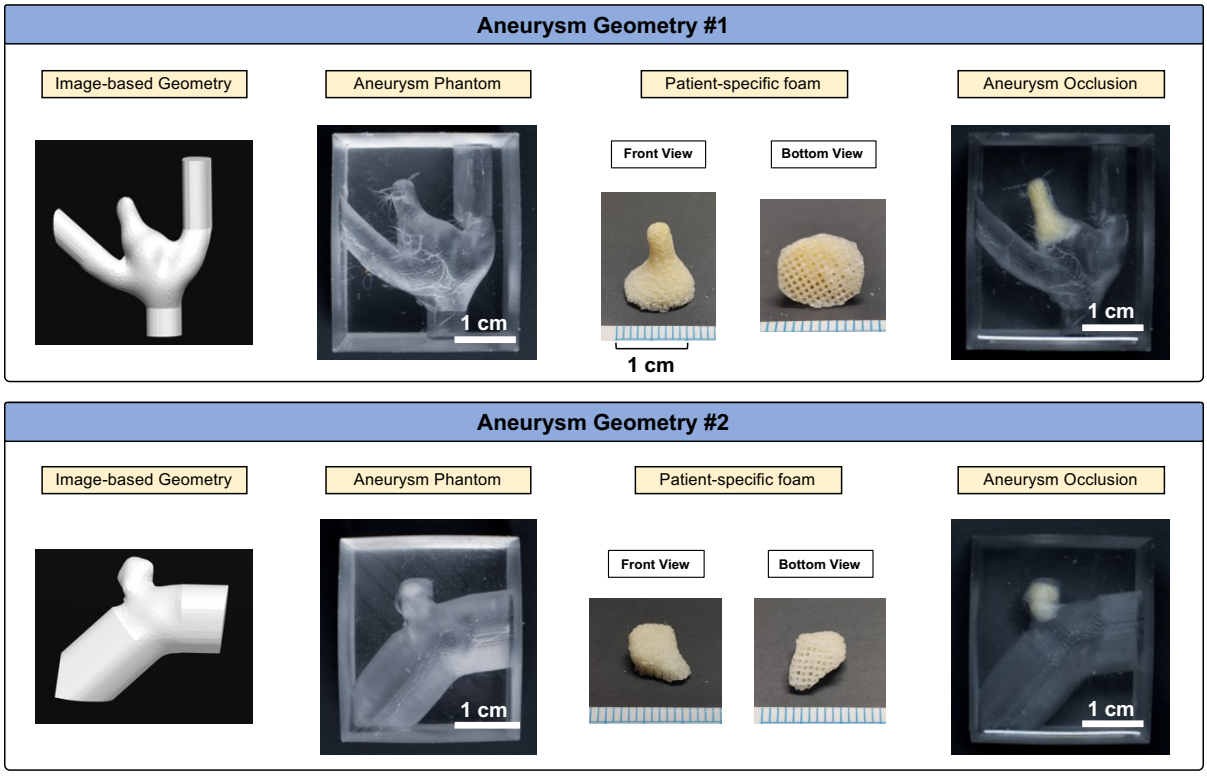


Figure 4-11. *Proof-of-concept* demonstration of the occlusion of aneurysm phantoms with patient-specific image-based geometries using 3DSMP foams. Aneurysm geometries were enlarged threefold to facilitate delivery of the foam.

4.3 Discussion

4.3.1 Overall Findings

In this study, we fabricated porous polyurethane 3D structures using a 3D-printing/leaching method, inspired by the method proposed by Hernández-Córdova *et al*. [159]. This method overcomes previous limitations related to the direct extrusion of our polyurethane formulation in a liquid state. Specifically, due to the use of TEA in our polyurethane formulation, our material presents a high degree of crosslinking, making traditional fused deposition modeling (FDM) methods not applicable for the fabrication of patient-specific foams. Therefore, this study provides a significant advance in our goal to fabricate novel endovascular devices with patient-specific geometries that can provide complete occlusion of ICAs. We found that combining PVA FDM 3D-printing combined with leaching provided a low-cost, facile technique for the fabrication of computer-aided design of SMPs. Overall, the comprehensive characterization of the 3DSMP foams led to the following findings:

1. The SMP solution is able to adhere to the PVA 3D-printed grid structure and, after curing, to create a sheath that surrounds the infill filament. After leaching, the 3DSMP foam accurately mimics the filament grid pattern and the overall 3D geometry of the PVA template (**Figure 4-2** and **Figure 4-3**).
2. The T_g of the resultant 3DSMP foams can be fine-tuned by judiciously adjusting the monomer molar ratios, as described previously (**Figure 4-5**) [60]. Also, 3DSMP foams exhibit a significantly lower T_g, than the solid SMP.
3. The FTIR spectra of the 3DSMP and solid SMP materials demonstrate the synthesis of highly crosslinked polyurethane. In addition, 3DSMP FTIR spectrum exhibits features that are more typical of linear polyurethane, which may arise from unwanted

PVA-HDI urethane linkage. The formation of these linear urethane links might explain the lower T_g, observed in DSC of the 3DSMP foams, due to higher polymer chain mobility.

4. The 3DSMP foams exhibit an anisotropic mechanical behavior where the *X*-axis of the grid-pattern prints is significantly more compliant than the *Z*-axis. This is due to the lower material density in this direction. Specifically, the grid design on the *X*-*Y* plane facilitates compression along these axes, while the short distance between lattices along the *Z* axis makes the material stiffer in this direction. This anisotropic behavior provides an opportunity for the design of compression patterns for the guided compression of the patient-specific endovascular devices. In addition, we also demonstrated the control of infill density (i.e., porosity) of the 3DSMP material, which led to subtle changes in the mechanical parameters of the material. Overall, the 3DSMP foams exhibit great compressibility along the *X*-*Y* plane with fine-tunable porosity.
5. Finally, we demonstrated the use of the 3D-printing/leaching method for the fabrication of patient-specific foams. The patient-specific 3DSMP foams were used to occlude aneurysm models with two patient-specific geometries from patient medical image data.

4.3.2 Study Limitations

This study, while advancing the development of individualized therapeutics for ICAs endovascular treatment, faces some limitations. First, SMP solution infiltration is uncontrolled and might lead to the formation of closed pores in the final 3DSMP foam due to non-

homogenous distribution of the solution. We recommend that infill densities higher than 60% are avoided to prevent this issue. In addition, the formation of the hollow channels, created by the PVA filament leaching, can also lead to regions prone to rupture after cyclic compression. Our experiments indicate that 10 cycles of compression do not induce significant damages to the polymeric structure, as the specimens are able to completely recover their original shape after compression (data not shown); however, for its future application, we will limit cyclic compression prior to delivery to the aneurysm to prevent rupture of the inner lattice structure.

Also, the SMP-X TEA molar ratio that was determined in our DSC experiments also utilizes a higher HPED ratio. During synthesis HPED is the most viscous monomer of our formulation, which in high concentrations can make monomer dissolution difficult and time consuming. Previously, we have reported our monomer mixing times as the time from initial contact between monomers to the change in solution transparency from a "hazy" consistency to a completely clear solution. We found later found that monomer mixing should be extended for monomer ratios containing high HPED concentrations, as this can lead to local variations in T_g, which can affect the overall thermomechanical behavior of the final product.

Further, our *proof-of-concept* occlusion of aneurysm models provided insight of the potential aneurysm geometries that can be treated with the 3DSMP devices. Aneurysm #1 had an elongated geometry with a wide neck and a narrow tip, which allowed for the printing of a template without hanging portions. These features yielded an easy-to-manipulate and smooth 3DSMP foam. On the other hand, aneurysm geometry #2 did exhibit some hanging portions, due to a very narrow neck, making foam delivery difficult and requiring adjusting its position

during delivery. In fact, we aimed at performing 3DSMP foam delivery to a giant aneurysm geometry (see the 3D model in **Figure 4-1b**) with a relatively narrow parent artery. However, occlusion of this geometry was not possible due to the yet unfeasible compression degree that would be required to transport the foam to the aneurysm. This limitation in compressibility also played a role in our decision to enlarge the aneurysm geometries to facilitate delivery. In addition, this geometry exhibited protrusions that, in a lattice-based structure, can be structurally unstable and lead to foam rupture.

Overall, this 3DSMP device exhibits remarkable potential for the treatment of saccular bifurcation aneurysms, such as in the aneurysm geometry #1; other geometries will require further improvement of the infill structure.

4.3.3 Future Directions

The application of the method presented in this study opens opportunities to test the potential of individualized therapies for ICAs. Using this technique, we plan to develop a closed flow loop for the *in vitro* demonstration of occlusion, and experimental flow dynamics characterization of treated and untreated aneurysms, similarly to the work performed by Baidya *et al* [160]. In addition, we will develop a triggering mechanism for shape recovery. In our previous work, we have used carbon nanotubes to induce Joule-heating of porous SMPs [62]; in Chapter 5, we present the use of polypyrrole to induce Joule-heating
behaviors on the 3DSMP foams.

Moreover, we plan to improve the infill structure presented in this study, based on the geometrical limitations discussed in Section 4.3.2. We plan to develop in-house algorithms for more structurally stable complex geometries, as well as infill patterns for guided compression. These developments will be based on *in silico* simulations of foam delivery.

Furthermore, we plan to translate this device from its current *in vitro* conditions, to an *in vivo* setting that provides information on key biological processes involved in aneurysm embolization. First, we will explore the capacity of this material to promote platelet aggregation, a fundamental process in the thrombogenesis that is characteristic of GDCs [2, 3]. We will also explore the interaction of the material with cell lines that will be neighboring the material *in vivo*, such as endothelial and smooth muscle cells. Finally, we plan to test the effectiveness of this individualized approach in animal models, such as the elastase-induced aneruysm model that will be presented in Chapter 6 of this dissertation [161].

4.4 Conclusions

In this study, we have developed polyurethane porous SMPs using an 3D-printing/leaching method. This approach allows for the fabrication of 3D structures using a grid infill pattern with anisotropic compressibility, tunable T_g, and with the capacity to occlude image-based aneurysm models. The 3DSMP foams provide a significant improvement to our previously characterized porous SMPs. Future investigations will combine 3DSMP foams with conductive materials to obtain a Joule-heating-triggered SMP with patient specific geometries, thus advancing the potential of endovascular therapy to obtain complete occlusion for ICA treatment.

CHAPTER 5 Design and Characterization of a Joule-Heating-Activated Patient-Specific SMP using Polypyrrole Coating

This chapter presents the application of the method described in Chapter 4 to develop a Joule-heating activated 3DSMP foam. Based on the limitations of the CNT-infiltration method described in Chapter 3, we explored an alternative method for the induction of electric conductivity on the porous foams. First, we present our approach for the coating of the 3DSMP foams with a conductive polymer: polypyrrole (PPy) (Sections 5.1.1-5.1.2). Then, we assess the topographical features of the PPy coating, its effects on the thermomechanical properties of the 3DSMP foams and the induced electric resistivity (Sections 5.2.1-5.2.5). Further, we demonstrate the Joule-heating behavior of the PPy-coated 3DSMP foams using direct current (DC), which was applied using an in-house electronic system for the controlled maximum temperature and heating rate of the foam. The chapter concludes with the demonstration of the Joule-heating induce shape recovery behavior of the PPy-coated 3DSMP foams in both cubic and patient-specific geometries.

5.1 Materials and Methods

5.1.1 Fabrication of 3DSMP Foams

Polyurethane SMP solution was synthesized using hexamethylene diisocyanate (HDI, ≥98.0%, Sigma-Aldrich), N,N,N0,N0-tetrakis (hydroxypropyl) ethylenediamine (HPED, ≥98.0%, Alfa Aesar), and Triethanolamine (TEA, ≥99.0%, Sigma-Aldrich), as described in Section 4.1.2. HDI, HPED and TEA were mixed at the SMP-X ratio described in **Table 4-1** following the procedure described in previous chapters and in APPENDIX B. Briefly, the

uncured polyurethane solution was poured onto 10×10×10 mm cubic PVA (Sigma-Aldrich) 3D-printed templates. SMP-coated PVA templates were stored at –20 °C in a vacuum container for 1 h to prevent curing and to allow complete infiltration of the solution into the template. Then, the specimens were cured at 70 °C for 1 h and 130 °C for an additional hour each under a nitrogen-rich environment using a vacuum oven (BOV-20, Being Instrument, USA). Cured blocks were immersed in a water bath (Branson 1800, Branson Ultrasonics Corporation, USA) and sonicated at 50 °C for 24 h to dissolve the PVA templates. Finally, the 3D foams (3DSMP) were dried out in a vacuum oven at 60 °C. The fabricated specimens were stored in a desiccator to preserve thermal properties of the material.

5.1.2 Polypyrrole coating of 3DSMP Foams

3DSMP foams were coated with polypyrrole, a conductive polymer, using a modification of the method proposed by Zhang *et al.* [56]. First, SMP foams were stored in a desiccator prior to coating to prevent moisture on the surface of the foams. Then, foams were immersed in a $FeCl_3$/isopropanol solution at different concentrations (5, 7.5 and 10%w/v) at room temperature in a laminar flow cabinet. After ten minutes, the foams were removed from the $FeCl_3$ solution and air dried inside of the cabinet for 30 min. Once dried, the foams were suspended over 2 mL of pyrrole (Sigma-Aldrich) using a sealed plastic cup and an in-house 3D-printed porous basket. Using this approach, the pyrrole fumes were deposited on the surface of the SMP foam, where polymerization was catalyzed by the $FeCl_3$ coating. This resulted in the formation of a polypyrrole (PPy) sheath surrounding the 3DSMP foam fibers, which gave the foams a black appearance that indicated successful polymerization. Finally, the foams were washed in DI water to remove $FeCl_3$ particles and stop polymerization. Time from

contact with pyrrole fumes to DI water wash was defined as polymerization time. Specimens were coated at different polymerization times: 30, 60 and 120 min. After washing, the PPy-coated 3DSMP foams were air-dried at room temperature overnight.

5.1.3 Microscopy of PPy-coated 3DSMP Foams

The PPy-coated 3DSMP foams were visually inspected utilizing an ultramicroscope (Keyence VHX-7000). The foams were inspected to determine the homogeneity of PPy-coating, its appearance, presence of lingering $FeCl_3$, and microstructural integrity after coating. SEM of PPy-3DSMP foams was performed in a ThermoFisher Quattro S scanning electron microscope using a 20kV accelerating voltage. Pristine 3DSMP foams were coated with iridium.

5.1.4 Attenuated Total Reflectance – Fourier Transform Infrared Spectroscopy

PPy-3DSMP foams were characterized with ATR-FTIR to assess the effect of PPy coating on the polyurethane chemical composition and to detect potential traces of $FeCl_3$. ATR-FTIR spectrum was obtained using a similar method as described in previous chapters: spectra were obtained using a spectrometer (Nicolet iS50R, Thermo Scientific, USA) with a *L*-alanine doped triglycine sulfate (DTGS) and mercury cadmium telluride (MCT) detector. Spectrum analysis was performed using an in-house MATLAB program (Mathworks, USA).

5.1.5 Differential Scanning Calorimetry

DSC was performed as described in Chapter 4. We used DSC to determine the effect of the PPy coating process in the T_g of the synthesized 3DSMP foams. Specimens ($n = 3$) at the SMPX (HDI:HPED:TEA = 1:0.32:0.22) and SMP9 (HDI:HPED:TEA = 1:0.15:0.46)

monomer ratio were coated using the method described in Section 5.1.2. using a $FeCl_3$ = 7.5% solution and 60 min of polymerization time. Experimental groups included: (i) coated and (ii) uncoated 3DMP specimens, and (iii) uncoated solid specimens at the specified ratios. Specimens were tested in a DSC device (DSC2500, TA Instruments, USA) with three heating/cooling cycles at a range of –20 °C to 120 °C at a 5 °C/min heating rate and 10 °C/min cooling rate. T_g was measured from the second heating cycle using the TA Instruments Trios software v5.1.1.45672. The obtained T_g measurements were used to obtain a linear fit (MATLAB R2022a) of the leached and solid specimens. Using the predicted values of the fit, a monomer ratio with $T_g \approx 41$ °C was formulated. The resultant SMP ratio was named SMP-ICA and tested in DSC to verify its T_g.

5.1.6 Volumetric Resistivity Assessment

The PPy-coated 3DSMP cubic specimens ($n = 6$, 10x10x10 mm) were placed in a parallel copper plate setup (**Figure 5-1**). Plates were connected to a multimeter to measure resistivity. Foam dimensions were measured using a caliper (resolution: 0.01 mm). Volumetric resistivity was calculated with:

$$\rho = \frac{RA}{L} \tag{5.1}$$

where R is the measured resistivity from the multimeter, A is the cross-sectional area of the specimen, and L is the distance between the plates of the setup. Comparisons in volumetric resistivity were performed between $FeCl_3$ concentration and polymerization time groups. All assessments were performed at room temperature (≈25 °C).

5.1.7 Assessment of Joule-Heating Behavior

The PPy-coated 3DSMP specimens tested in Section 5.1.6 were subjected to a thermal release analysis. Specimens were mounted in our parallel plate setup and DC voltage was applied using an electric DC source. Pulse width modulation (PWM) signals were applied to the foams using an Arduino Mega2560 (Arduino.cc, Italy) microcontroller unit (MCU) setup (**Figure 5-1a**). The duty cycle of the PWM signal was defined as:

$$Duty\ Cycle\ (\%) = \frac{t_{ON}}{t_{ON} + t_{OFF}} \times 100\ \% \tag{5.2}$$

where t_{ON} is the period when $V = 30\ V$ and t_{OFF} is the period when $V = 0\ V$. PWM signals with 25, 50, 75 and 100% duty cycles (**Figure 5-1b**) were applied to the foams at a frequency of 490 Hz for 10 s. Joule-heating of the PPy-coated 3DSMP foams was monitored using an IR thermal camera (FLIR ETS320, USA). Average surface temperature of the foam was compared among experimental groups and PWM duty cycles. All assessments were performed at room temperature (≈25 °C).

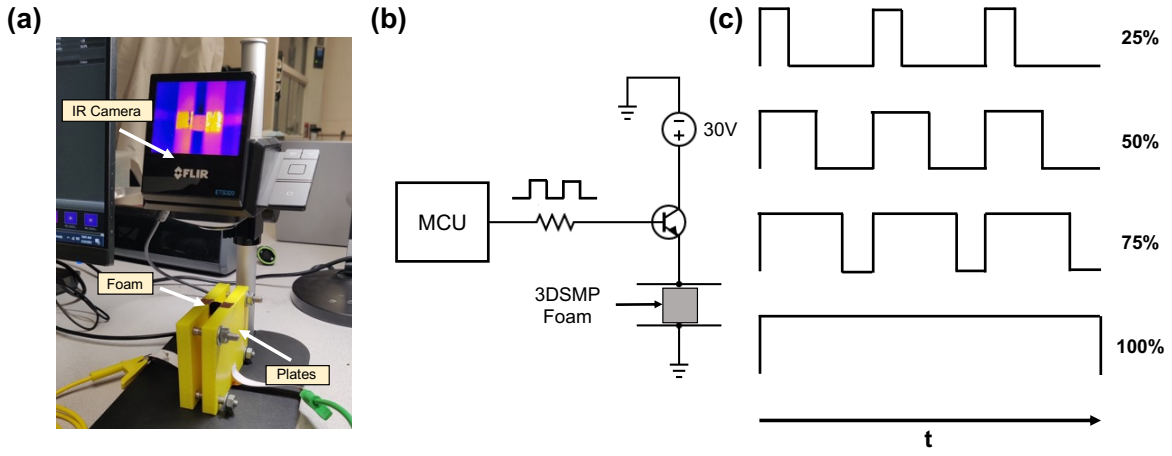


Figure 5-1. (a) Circuit diagram showing a microcontroller (MCU) sending a PWM signal to a transistor that controls electric flow through the PPy-coated 3DSMP foam. (b) Graphical

representation of PWM signals at different duty cycles.

5.1.8 Shape Recovery Analysis

PPy-coated 3DSMP specimens were subjected to a shape recovery analysis using Joule-heating as a triggering mechanism. First, PPy-coated 3DSMP foams, with an SMP ratio determined in Section 5.1.5 and coated with a 7.5%w/v FeCl3 solution and 60 min of polymerization time, were brought above their T_g in a vacuum oven. Length along the *X*-axis of the foam was measured and recorded before compression. Then, the foam was compressed to ~30% of their original height and were transported, while compressed, to a freezer (–20°C) to cool down and store the deformed configuration (**Figure 5-2a**). Finally, the compressed foam was placed between two copper plates to apply a 100% PWM 30VDC electric pulse using our MCU setup (**Figure 5-1b**). During shape recovery two assessments were performed: (i) topdown view of the thermal release of the foam during Joule-heating using an IR camera (FLIR ETS 320), and (ii) recording of the frontal view of the foam to track shape recovery using a digital camera (Nikon d5600 – 50 mm lens, Japan). Thermal data was processed and analyzed using an in-house MATLAB script and shape recovery images were processed using ImageJ to quantify shape recovery percentage using Equation 4.1. All assessments were performed at room temperature (≈25 °C).

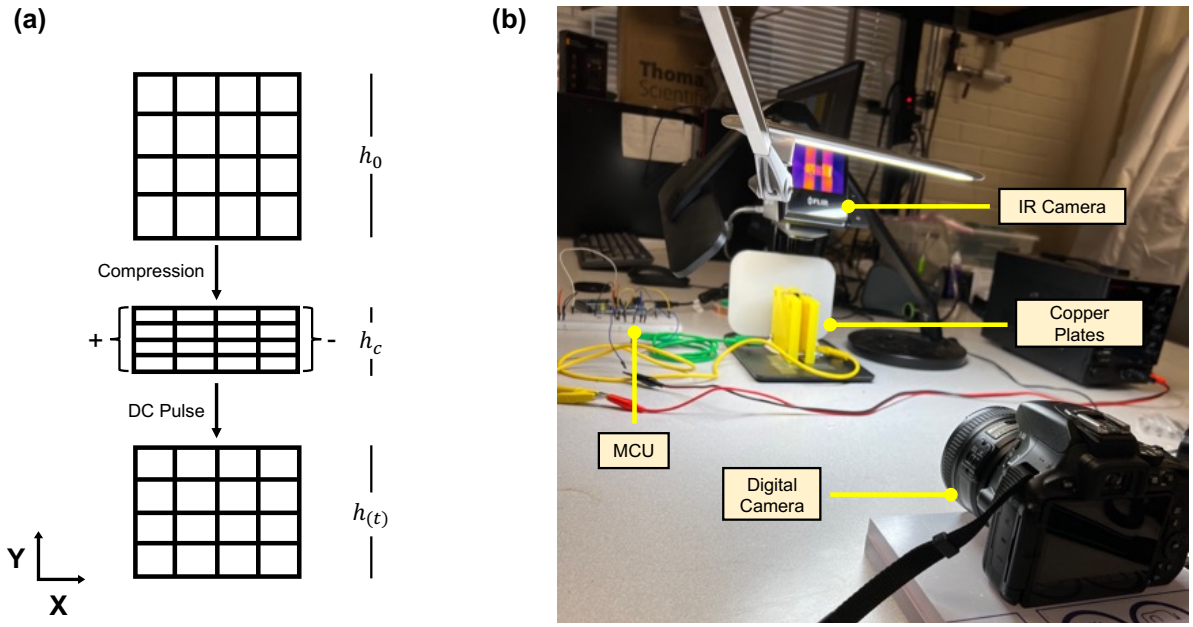


Figure 5-2. (a) Diagram representing the measured height of the foam during the shape recovery experiment. (b) Setup for the assessment of Joule-heating-induced shape recovery of the PPy-coated 3DSMP foams.

5.2 Results

5.2.1 Fabrication of PPy-coated 3DSMP Foams

The 3DSMP foams were fabricated using our method established in Chapter 4. For this study, we replaced the PVA filament used in Chapter 4 for a biocompatible version to reduce potential for cytotoxicity of the material [159, 162]. Pristine 3DSMP foams were successfully fabricated (**Figure 5-3** – *left*) using PVA templates with 50% infill density. After submerging the foams in $FeCl_3$ solutions, $FeCl_3$ coating was evidenced by an orange coloration (**Figure 5-3** – *middle*). Finally, PPy coating was successfully performed by suspending the $FeCl_3$-coated foams over the liquid pyrrole fumes. PPy polymerization was evidenced as a sudden blackening of the foam (**Figure 5-3** – *right*).

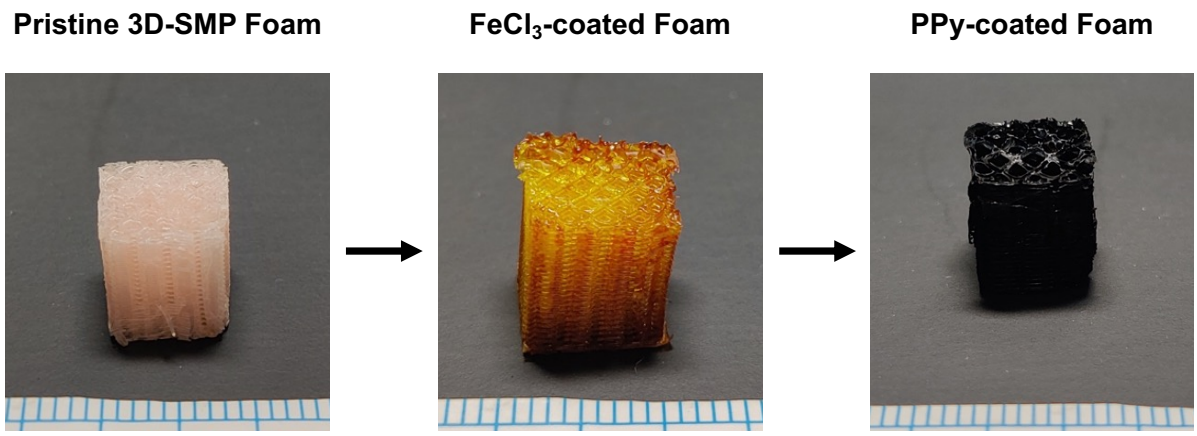


Figure 5-3. Representative photographs of the 3DSMP foams at different steps of the PPy-coating process: (*left*) pristine 3DSMP foam, (*center*) FeCl3-coated foam and (*right*) PPy-coated foam.

During polymerization, we shifted the position of the foams at intermediate intervals to ensure that the pyrrole fumes were deposited homogenously on the surface of the foam. In preliminary experiments, we found that this step is key for homogeneous PPy coating, as the core of the foam can be left uncoated and lead to inconsistent Joule-heating. In addition, we also tested submerging the $FeCl_3$-coated foams in pyrrole as an alternative method for coating. We found that this method causes uncontrolled PPy chain elongation that is evidenced by the swelling and overall structural deformation of the original pristine 3DSMP foam. The method presented here guarantees homogenous coating of the foam and maintaining its structural integrity.

5.2.2 Microstructure of PPy-Coated 3DSMP Foams

PPy-coated foams were imaged using two different microscopy techniques: (i) ultra-high resolution light microscopy and (ii) SEM. Photographs of the uncoated 3DSMP foams (**Figure 5-4a**) demonstrated features that were observed previously: (i) the SMP material creates a

sheath around the PVA filament, which after wash-out, leaves and hollow channel inside the SMP "fibers" that constitute the overall 3DSMO foam; (ii) overall microstructure of the PVA template is replicated with high precision; and, (iii) some pores become clogged by SMP solution excess in a random fashion (not shown). On the other hand, PPy-coated 3DSMP foams photographs demonstrated further details on the coating process. First, we observed that coating was homogenous on the surface of the foam, as evidenced in the black appearance of the material (**Figure 5-4b**) with an iridescent behavior. In addition, we also observed the absence of PPy coating on the edges of some of the foams, which was evidenced as a persistent orange coloration of the $FeCl_3$ coating. We found that these uncoated areas were those in contact with the container where PPy polymerization was performed, further indicating the necessity for rotating the foam during this step to allow homogeneous coating.

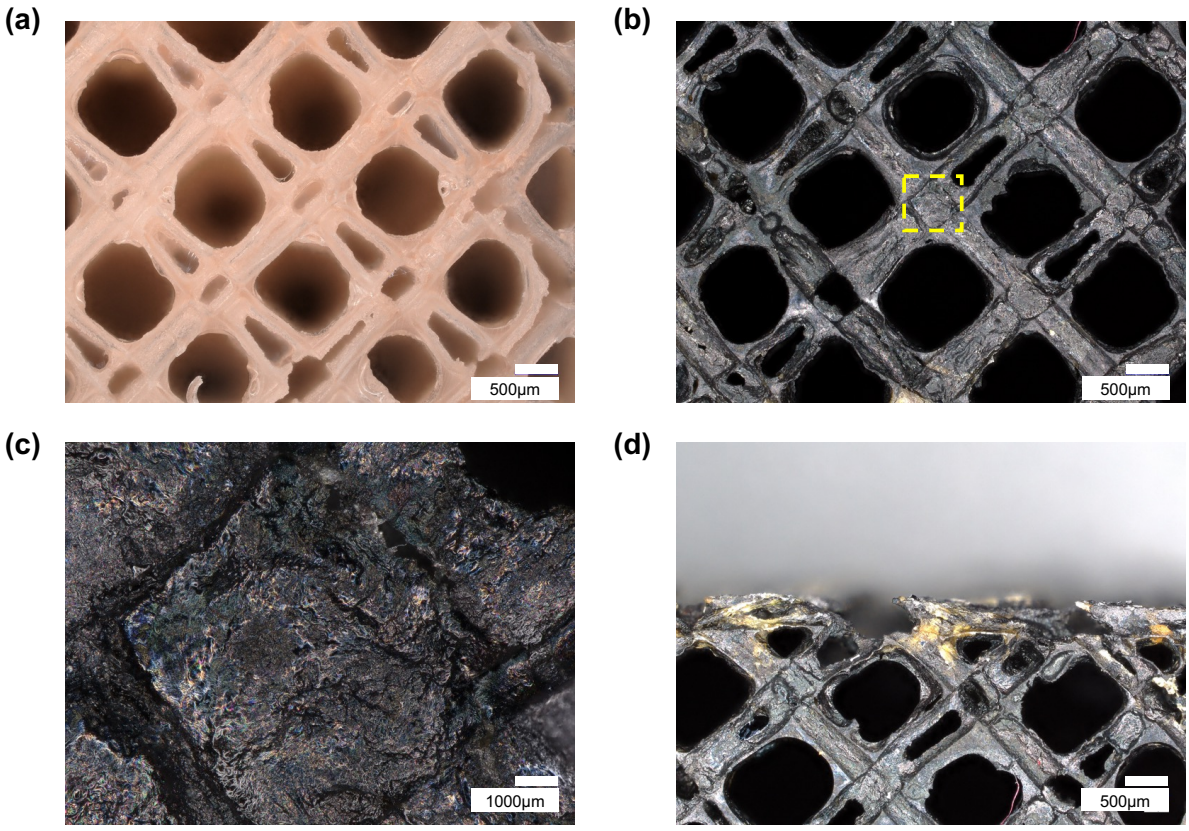


Figure 5-4. Ultramicroscope photographs of (a) pristine 3DSMP foams and (b) PPy-coated 3DSMP foams fabricated using 50% infill pattern densities. The yellow dashed box shows the area covered in (c) of the PPy-coated 3DSMP foams. (d) Edge of a PPy-coated foam demonstrating lack of PPy-coating at the contact areas with the container where polymerization was performed.

In SEM, we evidenced that the surface of pristine 3DSMP foams was smooth (**Figure 5-5a**) and replicated the geometry of the PVA filament. In addition, we observed that the synthesized PPy coating exhibited a rugged topography (**Figure 5-5b**). SEM also revealed the presence of persistent $FeCL_3$ on the edge of coated foams (**Figure 5-5c-d**), which produced electron charging in low magnification SEM micrographs. In high magnification, $FeCl_3$ crystals were visible and exhibited their characteristic hexagonal geometry [163].

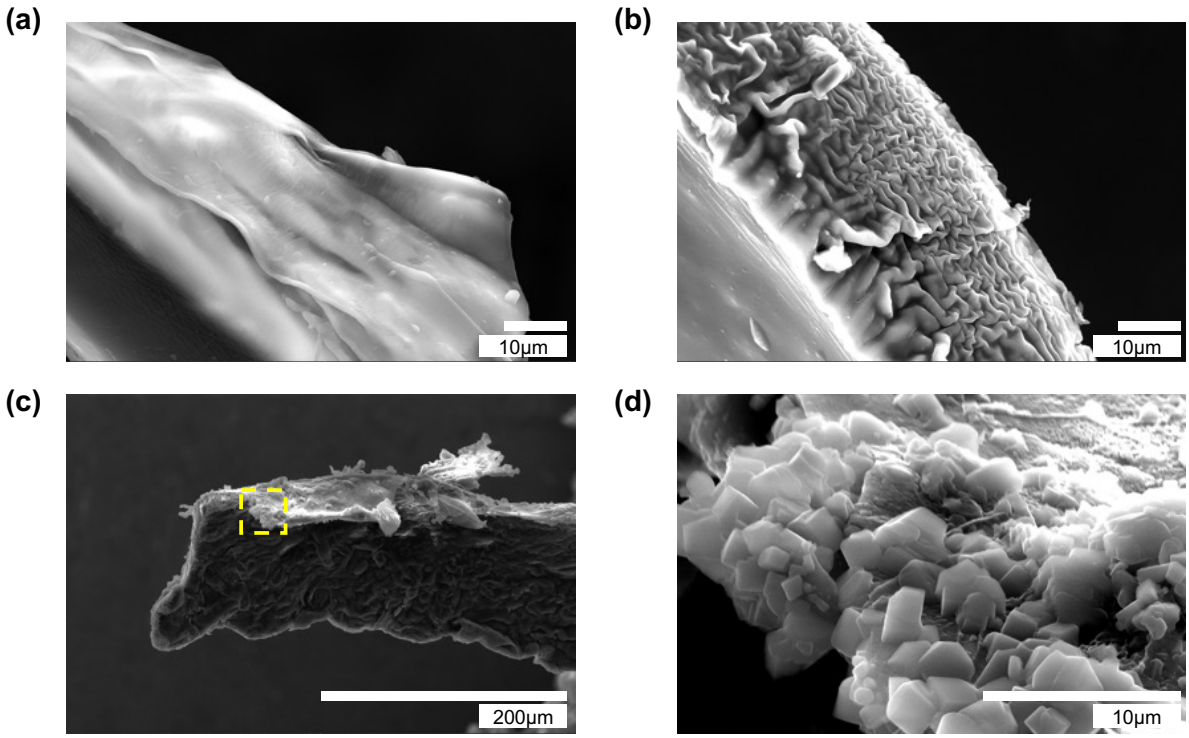


Figure 5-5. SEM micrographs of individual strands of 3DSMP foams: (a) Pristine 3DSMP and (b) PPy-coated 3DSMP foam. (c) Additional strand from the edge of a PPy-coated 3DSMP foam demonstrating charging (brighter edges), which is produced by (d) $FeCl_3$ crystals on the surface of the material.

Overall, microscopy techniques provided information on the topography of the coated and uncoated 3DSMP foams. In addition, microscopy aided in revealing the presence of areas with incomplete PPy polymerization.

5.2.3 Attenuated Total Reflectance – Fourier Transform Infrared Spectroscopy (ATR-FTIR) Characterization

FTIR spectra of the PPy-coated 3DSMP foams exhibited common features of polyurethane foams (**Figure 5-6**). As described in previous chapters, the main observed peaks were: (i) 1685 cm^{-1}, related to urethane carbonyl C=O stretching, (ii) 1522 cm^{-1}, associated with urethane C−N−H deformation vibrations, (iii) 1246 cm^{-1} related to C−N stretching vibrations, (iv) 1132 cm^{-1}, related to C−O−C stretching vibrations, and (v) 3323 cm^{-1}, corresponding to N-H stretching vibrations [134, 158]. Interestingly, the PPy-coated foams did not exhibit significant differences from the uncoated ones.

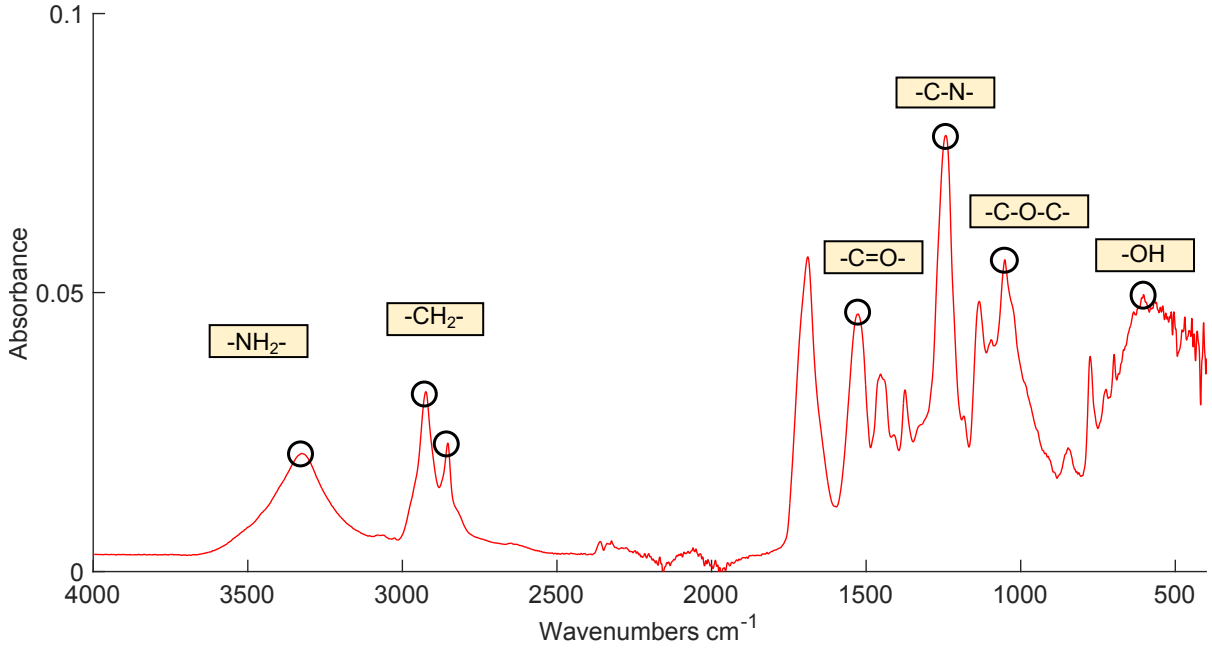


Figure 5-6. ATR-FTIR spectrum of a PPy-coated 3DSMP foam. Labels indicate the most relevant molecular structures of the PPy-coated polyurethane material.

The spectrum in **Figure 5-6** corresponds to a representative specimen that was coated using a 7.5%w/v $FeCl_3$ solution and 30min polymerization time. In addition, this specimen was evenly coated by rotating the foam position during polymerization. In our preliminary experiments, we observed that FTIR of foams exhibited common features of pure PPy (**Figure 5-7**): (i) an elevation in the 2000-3500cm^{-1} range that in pure PPy is featureless (i.e., no sharp or noticeable peaks in the signal), which displaced the absorbance of the polyurethane peaks upwards [164], and (ii) peaks at 1550 and 1460cm^{-1}, corresponding to the pyrrole ring vibration [165]. Other common features described in the literature can also be identified; however, these features overlap with several common chemical structures found in the polyurethane matrices. In these preliminary experiments, we did not rotate the foam during polymerization in our in-house setup, which could have led to the synthesis of a thicker PPy film that was detectable by FTIR.

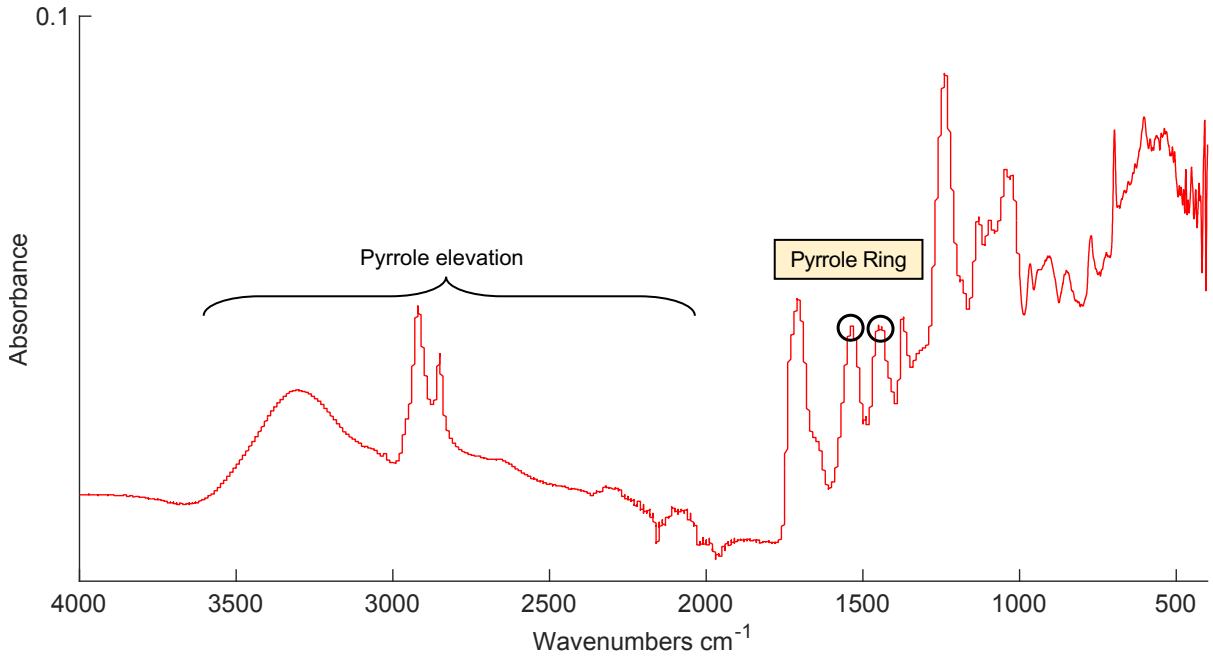


Figure 5-7. ATR-FTIR spectrum of a preliminary PPy-coated 3DSMP foam. Labels indicate the molecular structures of the PPy that were observed in preliminary 3DSMP polyurethane foams.

5.2.4 Differential Scanning Calorimetry

DSC of the PPy-coated SMP foams was performed to investigate the effect of PPy coating on the glass transition behavior of the SMP foam. We first tested the SMP-X monomer ratio (HDI:HPED:TEA = 1:0.32:0.22) that was designed in Chapter 4. We observed that the T_g of the pristine 3DSMP was similar to the solid SMP (**Figure 5-8**), differently to the 3DSMP foams that we characterized in Chapter 4, where the 3D foams had a significantly lower T_g than their solid counterparts. In this study, we 3D-printed our PVA templates using a biocompatible PVA filament, which could explain the non-modified polyurethane chemistry of the 3DSMP foams in this chapter. In addition, we also observed that there were no significant differences between the T_g of the PPy-coated and uncoated foams (68.52 ± 0.41 °C vs. 67.54 ± 0.49 °C, respectively).

Based on the observed T_g of the PPy-coated foams in this experiment, we re-designed the monomer ratio to obtain a $T_g \approx 41$ °C. We fabricated a 3DSMP batch of foams with the SMP9 ratio (HDI:HPED:TEA = 1:0.15:0.46) that had a $T_g \approx 45$°C by Kunkel *et al*. [60] to perform a linear fit to predict the TEA monomer ratio of the desired monomer ratio. We found that the uncoated 3DSMP foams with an SMP9 monomer ratio had an average T_g of 31.24 ± 1.02 °C, which was not significantly different to the PPy-coated foams (32.27 ± 0.73 °C). Using the T_g measurements of 3DSMP-X and the 3DSMP9 foams, we calculated a TEA monomer ratio of ≈0.40 to produce a PPy-coated 3DSMP foam with a $T_g \approx 41$ °C.

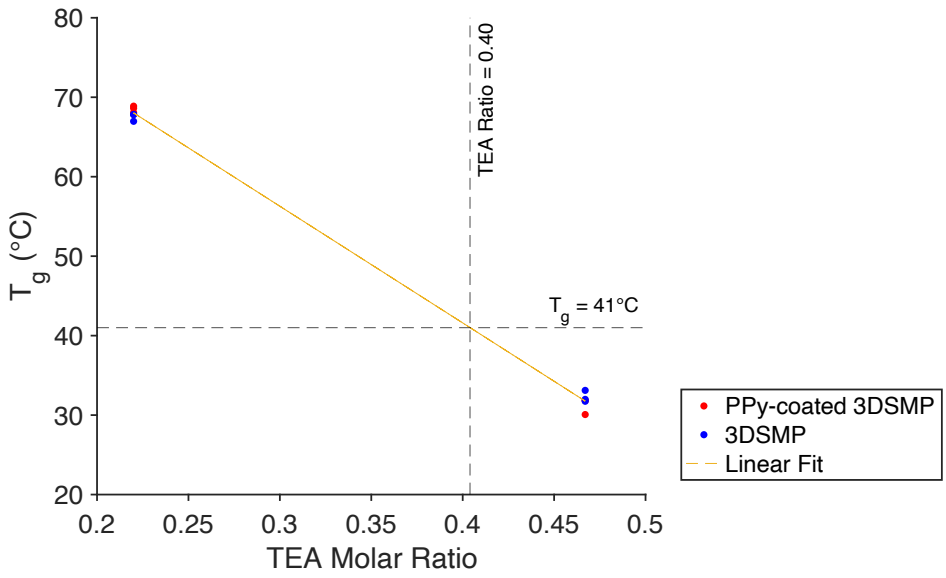


Figure 5-8. Experimental T_g of 3DSMP-X and SMP9 ratios. Dashed lines indicated the predicted monomer ratio that yielded a $T_g \sim 41$ °C.

5.2.5 Assessment of resistivity of PPy-Coated 3DSMP Foams

We coated 3DSMP foams using three different $FeCl_3$ solution concentrations (5, 7.5 and 10%w/v) and polymerization times (30, 60 and 120 min). These foams were subjected to a resistivity assessment to determine the effects of the PPy polymerization on the conductivity of the polyurethane foams. We found that PPy coating induced conductivity of the foams and that their resistivity was dependent on the $FeCl_3$ solution concentration. We observed that volumetric resistivity (see Eq. 5.1) decreased significantly with increased $FeCl_3$ solution concentration. Specifically, for the 30 min of polymerization time group, the 5%%w/v solution group had an average volumetric resistivity of 434.74 ± 291.98 kOhm·mm, which was significantly greater than the 7.5%%w/v solution (121.93 ± 83.60 kOhm·mm, $p < 0.05$), and not significantly greater than the 10%w/v group (308.57 ± 83.60 kOhm·mm, $p = 0.49$). These differences became more evident with increased polymerization time. In the 60 min

group, the 5%%w/v solution group had an average volumetric resistivity of 564.83 ± 404.59 kOhm·mm, which was significantly greater than the 7.5 and 10%w/v solution groups (79.01 ± 24.69 kOhm·mm and 73.73± 41.46 kOhm·mm, respectively; p<0.001). A similar behavior was observed in the 10%w/v solution group, although with marginal significance ($0.05 < p < 0.1$).

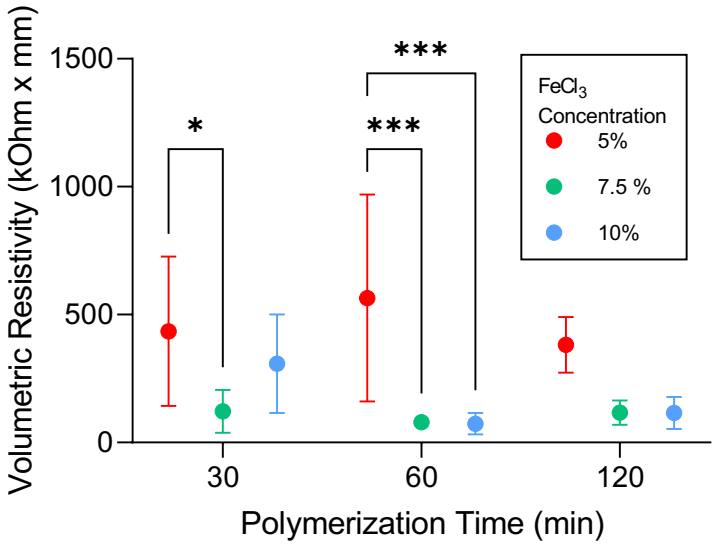


Figure 5-9. Volumetric resistivity measurements of PPy-coated 3DSMP foams coated with different $FeCl_3$ concentrations and polymerization time.

5.2.6 Evaluation of Joule-Heating Behaviors of PPy-Coated 3DSMP Foams

Joule-heating behavior of the PPy-coated was assessed using a parallel plate setup (**Figure 5-1a**). First, we assessed the thermal release of the material as a response to stimulation with a direct current signal of 30 V of amplitude. We observed that the foams rapidly released heat and reached temperatures above the designed T_g (41 °C). Specifically, we observed that some specimens reached average surface temperatures >50 °C, such as the representative specimen in **Figure 5-10**. In addition, we observed that the surface temperature of the PPy-coated foams

could reach temperatures as high as 85 °C in less than 10 s of electrical stimulation.

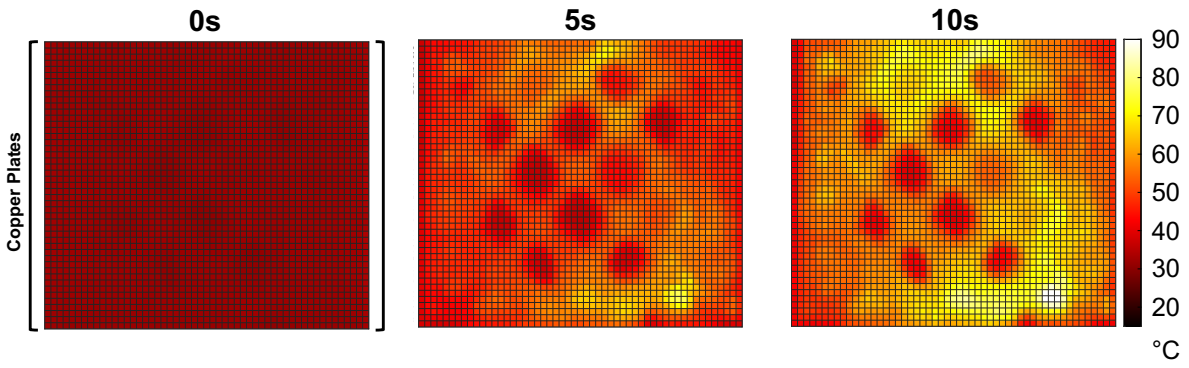


Figure 5-10. Representative heatmaps of a 3DSMP foam coated with PPy using a 5%w/v FeCl3 solution and 30min of polymerization time. Joule-heating was induced using a 30 VDC signal in a parallel plate setup. Thermal images were taken at different timepoints during electric stimulation. Square brackets indicate the position of the copper plates for all thermal images.

Based on these observations, we aimed at designing a method to control the maximum Joule-heating temperature emitted by the PPy-coated foams without altering the PPy synthesis conditions. To do this, we built a PWM system, where DC current was applied using a variable pulsed signal (**Figure 5-1a**), which allowed to control the maximum emitted temperature by the PPy-coated foams. For example, the representative specimen in **Figure 5-11** demonstrates the use of the PWM duty cycles to reduce the maximum temperature of the foam after 10 s of electrical stimulation. At 100% duty cycle, this specimen emitted an average of 65.7 $\pm$ 10.6 °C, which was reduced to 56.9 $\pm$ 7.7 °C, 48.5 $\pm$ 5.2 °C, and 40.5 $\pm$ 2.5 °C, when 75, 50 and 25% duty cycles were used.

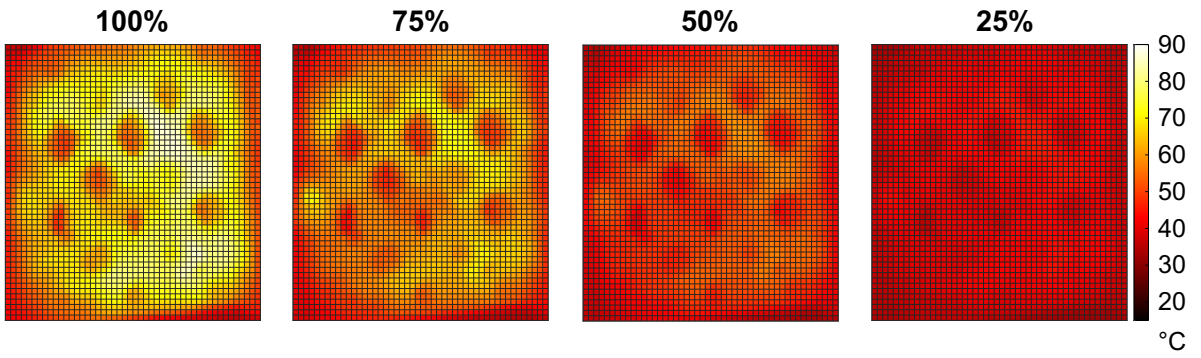


Figure 5-11. Representative heatmaps of a a 3DSMP foam coated with PPy using a 5%w/v FeCl3 solution and 60min of polymerization time. Joule-heating was induced using different duty cycles of a PWM 30 VDC signal at 490 Hz. Thermal images were taken after 10 s of stimulation with PWM signal.

The effect of PWM duty cycle was observed across all experimental groups, where the average temperature increase was proportional to the duty cycle applied to the PPy-coated foam (**Figure 5-12**) within each individual experimental group. However, we also observed that the average temperature increase was also dependent on the $FeCl_3$ solution concentration and polymerization time. In summary, we observed that:

1. In the 5%w/v $FeCl_3$ solution group, the average temperature increase was reduced with increased polymerization time and this reduction was exacerbated by the reduction of PWM duty cycle.
2. In the 7.5 w/v $FeCl_3$ solution group, the average temperature increase was directly proportional to the PWM duty cycle, but it was not dependent on the PPy polymerization time.
3. In the 10 w/v $FeCl_3$ solution group, the average temperature increase was directly proportional to the polymerization time, and inversely proportional to PWM duty cycle.

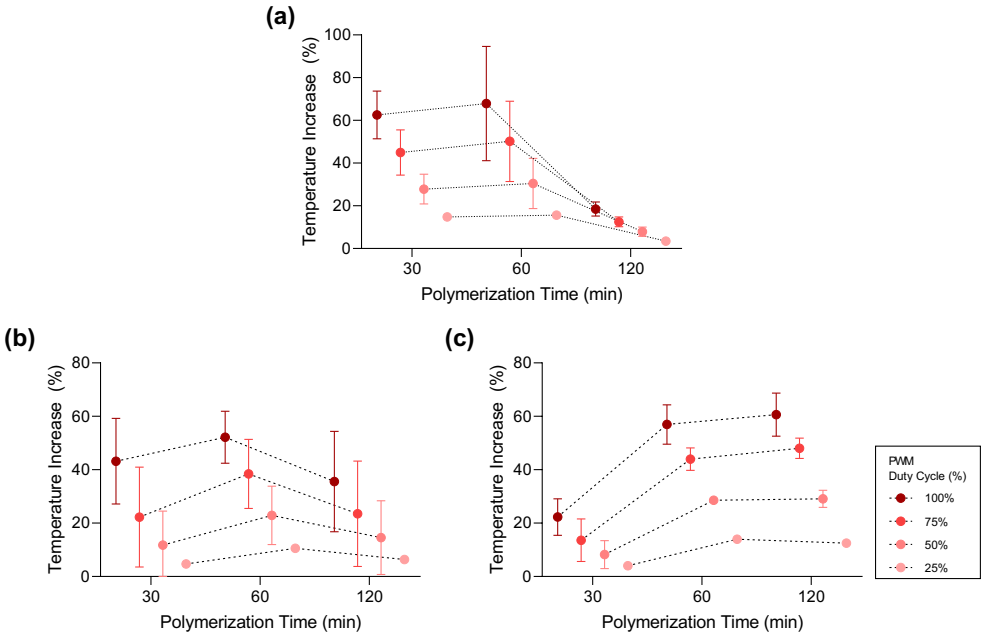


Figure 5-12. Average temperature increase of the PPy-coated SMP foams after stimulation with different PWM duty cycle signals for 10 s. Results are grouped by FeCl3%w/v solution concentration: (a) 5%w/v, (b) 7.5%w/v and (c) 10%w/v.

Based on these results, we also calculated the average heating rate of the PPy-coated foams **Figure 5-13**. Heating rate exhibited a similar behavior to average temperature increase. In this parameter, some of the differences were accentuated, especially in the 10%%w/v group. Nonetheless, differences across experimental groups were not significant for average temperature increase nor heating rate, only marginal ($0.05 < p < 0.1$) significance was observed across polymerization times.

Due to the consistency in heating rate across polymerization times, we decided to pursue further experiments for the PPy-coated 3DSMP using the 7.5%w/v $FeCl_3$ solution and 60 min of polymerization time (**Figure 5-12b** and **Figure 5-13b**). These PPy coating parameters were

used for shape recovery experiments using the SMP ratio calculated in Section 5.2.4.

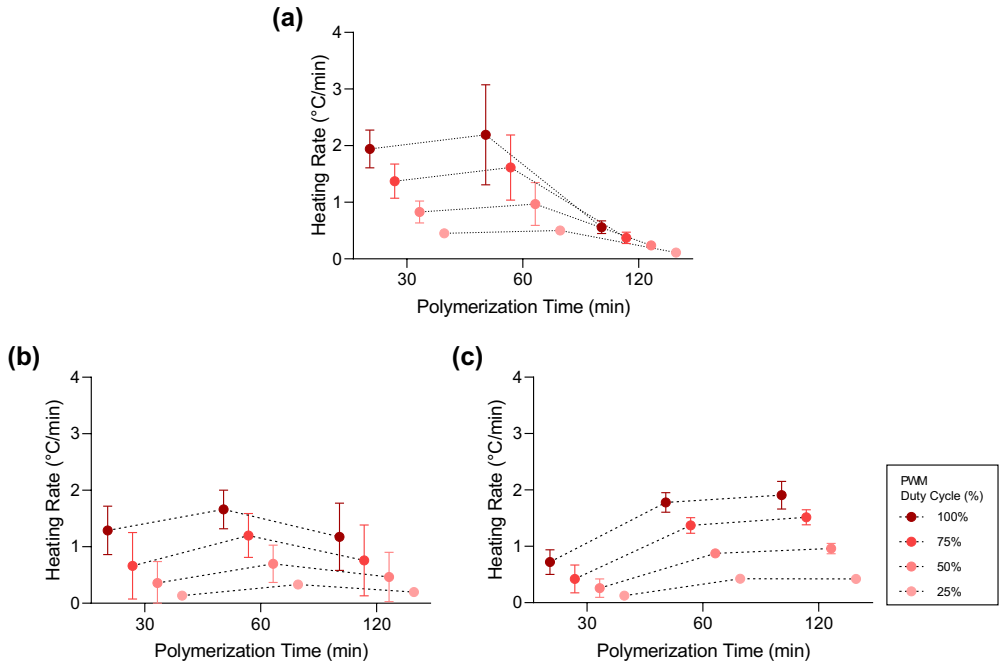


Figure 5-13. Heating rate of the PPy-coated SMP foams after stimulation with different PWM duty cycle signals for 10 s. Results are grouped by FeCl3%w/v solution concentration: (a) 5%w/v, (b) 7.5%w/v and (c) 10%w/v.

5.2.7 Shape Recovery using Joule-Heating

Shape recovery assessment was performed by placing the compressed PPy-coated 3DSMP foams between two copper plates and applying 30VDC with a 100% PWM cycle for 10s. We performed this assessment on three representative specimens with a cubic geometry with dimensions of approximately 10× 10 ×10 mm. Simultaneously to shape recovery assessment, we evaluated the heat release during this process. With this experiment, we observed the following:

1. The stimulation of PPy-coated 3DSMP foams with a 30V DC signal induced its shape recovery due to the observed Joule-heating behavior (**Figure 5-14** – *middle row*).
2. The shape recovery of three different specimens after 10 s electric of stimulation was 91.3%, 56%, 69%. Prior to electric stimulation, specimens exhibited a quantified shape recovery of ~20%, indicating residual stress release after the foam was removed from the plates (**Figure 5-15**).
3. The foams exhibited "hotspots" in specific areas of the foam, which corresponded to points where, SMP filaments crossed to form the lattice structure of the 3DSMP material (**Figure 5-14** – *top row*).
4. The foam exhibited rapid heating after stimulation, reaching temperatures >90 °C in less than 10 s (**Figure 5-14** – *top row*).
5. The average surface temperature curve of the foam during Joule-heating-induced shape recovery exhibited a positive (during heating) and negative exponential behavior (during cooling) (**Figure 5-14** – *bottom row*). This behavior was replicated across different specimens (**Figure 5-15**), where only one specimen exhibited a less "sharp" exponential behavior, cause by the physical displacement of the foam during recovery, yielding slight errors in temperature recording with the IR camera.
6. The MCU system provided a facile method for the application of PWM DC signals to 3DSMP foam for the triggering of its shape recovery.
7. No shape recovery was observed during the period prior to the application of the 30 V DC signal (**Figure 5-14** – *bottom row*).

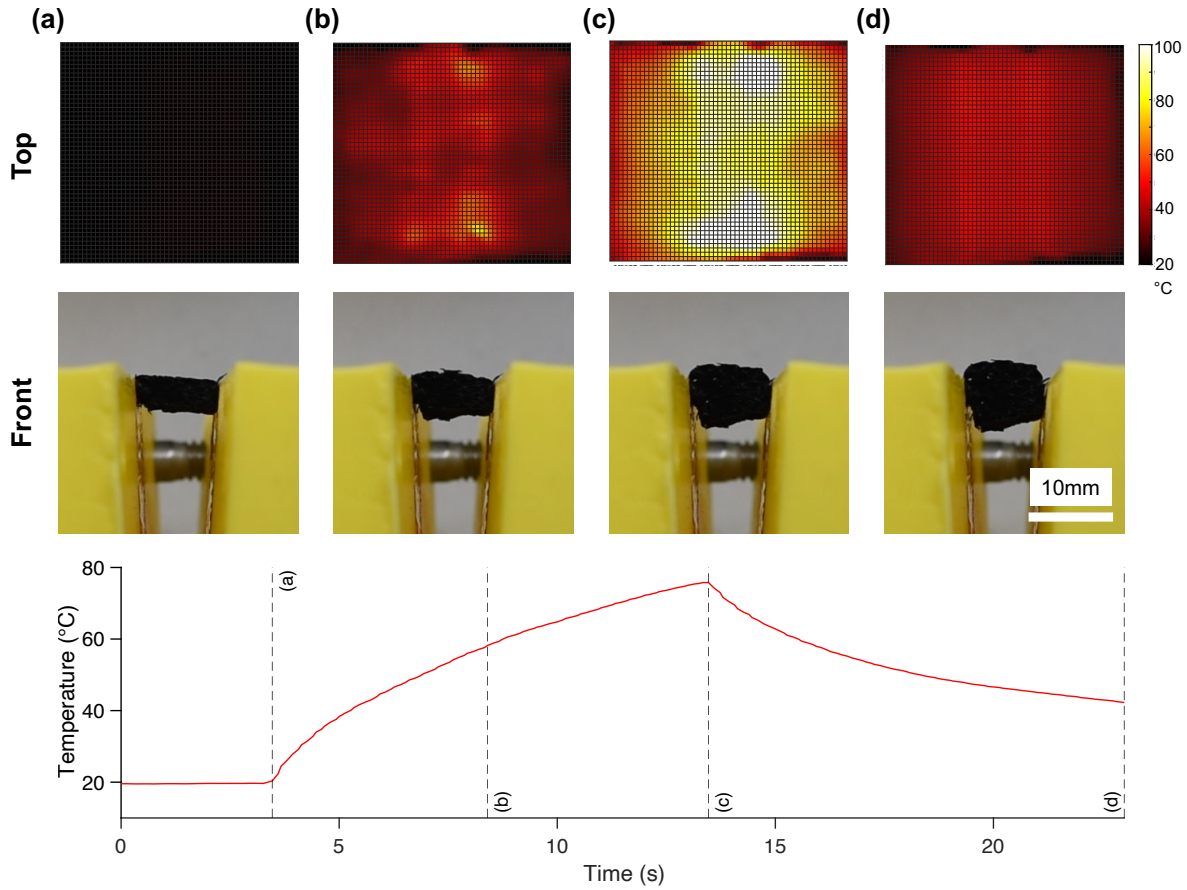


Figure 5-14. Representative results of the shaperecovery of a PPy-coated 3DSMP foam (SMP8, FeCl3 = 7.5% ,Polymerization time = 60min) using Joule-heating at different timepoints: (a) before applying a 30V pulse ($t = 0$s), (b) at the midpoint of the electrical pulse ($t = 5$s), (c) at the end of the pulse ($t = 10$s), and (d) cooling of the foam after the end of the pulse ($t = 20$s). (*Top row*) Top-down view of the surface temperature of the foam during shape recovery. (*Middle row*) Frontal view of the foam during shape recovery. (*Bottom row*) shows the average temperature of the foam during shape recovery.

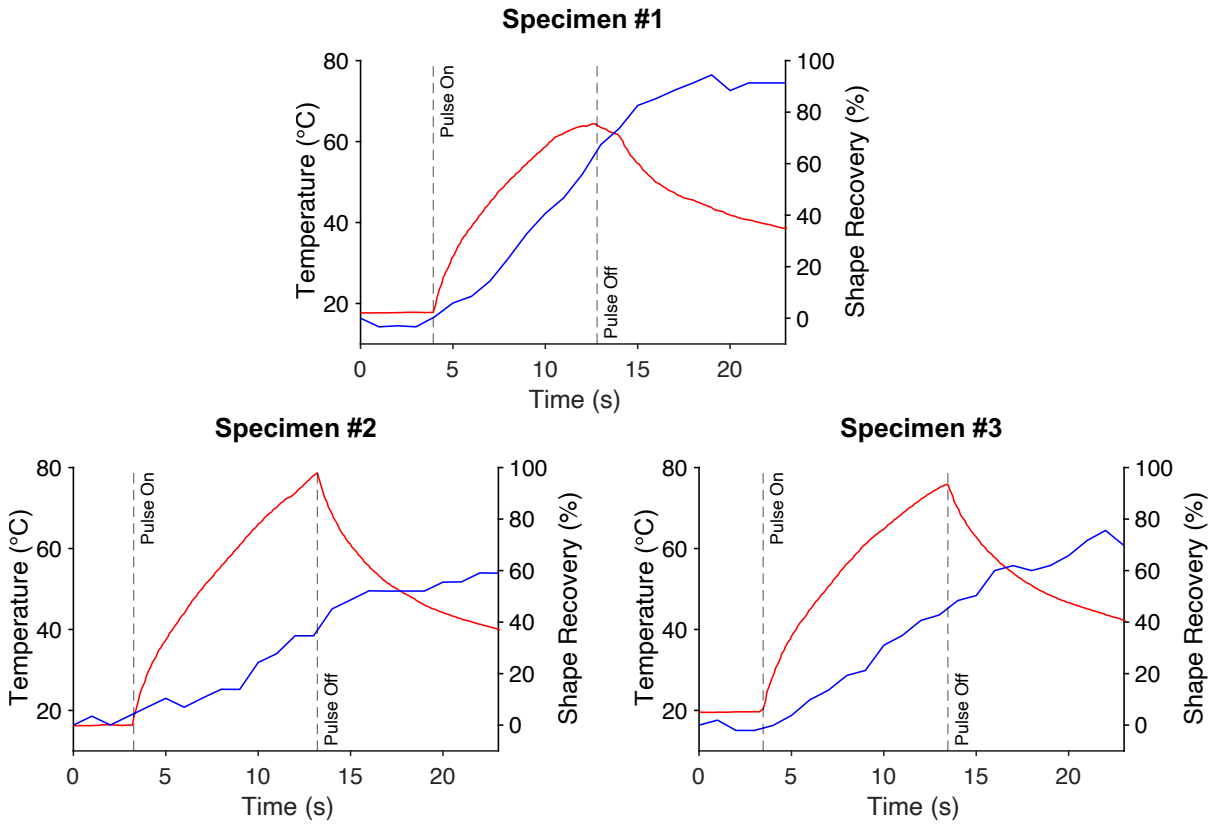


Figure 5-15. Shape recovery behavior of three PPy-coated 3DSMP specimens and their surface temperature during the Joule-heating activation.

5.3 Discussion

5.3.1 PPy Coating Method Selection

In this chapter, we investigated the use of PPy in the induction of conductivity in our 3DSMP polyurethane foams. Polyurethane is a not an electrically conductive material, which creates the necessity for additives such as PPy to use Joule-heating as a triggering mechanism of shape recovery. In this study, we modified the method proposed by Zhang *et al*. [56] for the *in situ* polymerization of PPy to coat biomaterials. In their study., this method was used to create core-shell nanostructures in polylactic acid (PLA) electrospun fibers. In contrast, we modeled the

coating process based on their results, where they reported that conductivity was stable when the material was washed in $FeCl_3$/isopropanol solutions for periods ≥8 min. Based on this we chose a constant washing time of 10 min, as described in Section 5.1.2. In addition, they found that polymerization times >2 h yielded non-significant differences in conductivity. Therefore, we aimed at testing the effect of polymerization times ≤2h in our foams. Lastly, they found that the conductivity of their PPy-coated PLA fibers significantly increased when polymerization was performed in the environments at temperatures ≤0 °C. However, our preliminary experiments did not exhibit any benefit in performing polymerization in freezing conditions, as we found that our foams exhibited low resistivities (<100 kOhm) using room temperature.

Other methods for PPy synthesis and deposition have been described in the literature. Kim *et al*. [166] used an electrochemical polymerization method to coat electrodes for batteries and biosensor applications. They enriched their polymerization solution using dopamine, which significantly improved mechanical and conductive properties of the material. Another method for PPy polymerization was described by Kim *et al*. [89], where commercial polyurethane fibers were immersed in a pyrrole/ammonium persulfate/2,6-naphthalenedisulfonic acid/disodium salt solution to induce PPy polymerization and coating. This method demonstrated to be useful for the fabrication of joint flexion sensors. Further, Sahoo *et al*. performed several investigations in the use of PPy in SMP-based applications. First, they studied the effect of immersing polyurethane (4,4'-methylene bis(phenylisocyanate) as hard segment, and polycaprolactonediol as soft segment) films in pyrrole prior to contact with $FeCl_3$ solutions [90]. This method used the same oxidative reaction that we used in our study, albeit

with a different exposure of the SMP to pyrrole solutions. They found that this method provided a homogeneous PPy coating of the material, similar to our results in **Figure 5-5**. However, they found that PPy-coated SMPs exhibited reduced tensile strength with increased PPy polymerization, indicating that PPy content should be minimized to obtain mechanically stable materials. In further studies, Sahoo *et al*. also studied the infiltration of CNTs in their SMP nanocomposites, with similar effects on the mechanical properties of the material with increased PPy content [87].

Overall, most PPy polymerization methods involve the direct contact of the material with pyrrole, which can be detrimental to mechanical stability. The method proposed by Zhang *et al*. and optimized by us for the coating of 3DSMP foams provided a facile approach to coat the 3DSMP fibers. This method minimized the contact of the foam with pyrrole, thus preventing detrimental effects on mechanical properties of the material. In fact, we observed in our preliminary experiments that when $FeCl_3$-coated 3DSMP foams were immersed in pyrrole, the foams would become deformed by the excessive PPy polymerization.

5.3.2 Overall Findings

In this study, we aimed at optimizing the *in situ* PPy polymerization method for the coating of 3DSMP foams. Our experiments yielded the following results:

1. The described *in situ* coating method yielded a homogeneous black layer on the surface of the 3DSMP foams (**Figure 5-4**). This coating appeared as a rugged surface in SEM micrographs (**Figure 5-5**).
2. Coating of the 3DSMP foam was improved by rotating the foam during

polymerization. This allowed the coating of the inner core of the 3DSMP foams.

3. ATR-FTIR demonstrated the presence of the synthesized PPy in preliminary foams (**Figure 5-7**). With the improved *in situ* poylmerization method, PPy FTIR features became less evident due to a more homogeneous and thinner PPy layer that was not detectable by the ATR-FTIR (**Figure 5-6**).
4. The presence of PPy on the surface of 3DSMP foams did not affect its overall thermal properties. The T_g of the PPy-coated foams did not exhibit significant differences when compared to uncoated 3DSMP foams (**Figure 5-8**).
5. We designed an HDI:HPED:TEA monomer ratio that yielded a $T_g \approx 41$ °C for the application of PPy-coated 3DSMP foams in ICA endovascular embolization.
6. The volumetric resistivity of the PPy-coated 3DSMP foams was inversely proportional to $FeCl_3$ solution concentration. No significant differences were observed across the polymerization time groups (**Figure 5-9**).
7. The PPy-coated 3DSMP foams demonstrated great conductivity and Joule-heating behaviors. We first induced Joule-heating of the PPy-coated 3DSMP foams using a 30 V DC signal for 10 s which produced rapid heat release from the foam, reaching local temperatures up >80 °C (**Figure 5-10**).
8. To control the rapid heat release of the PPy-coated 3DSMP foams, we designed. PWM circuit with variable duty cycles (100, 75, 50, and 25%). These pulsed signals provided control over the maximum temperature and heating rate of the PPy-coated 3DSMP foams undergoing Joule-heating (**Figure 5-11**, **Figure 5-12** and **Figure 5-13**).
9. The PPy-coated 3DSMP foams exhibited great Joule-heating-induced shape recovery behaviors. Joule-heating of the foams had a positive exponential behavior during

heating and negative exponential during cooling. Shape recovery percentages of 91.3, 58.9, and 69.7% were observed in three separate specimens after electric stimulation for 10 s (**Figure 5-14** and **Figure 5-15**).

Overall, our results demonstrate the great potential of our PPy-coated 3DSMP foams in their applications as embolic devices for ICA therapeutics. In this chapter, we have demonstrated a significant advance in inducing Joule-heating behaviors in our SMP formulation. In Chapter 3, we aimed at inducing these behaviors using CNTs that were infiltrated in the foam using a sugar-leaching method. As described in Section 3.3.2, CNTs induced detrimental effects in the mechanical properties of the material (foams became brittle and exhibited significant cumulative stress reduction as a response to cyclic deformation) and induced a reduction in the T_g of the material. In addition, resistivity levels of the CNT-infiltrated foams with low CNT concentrations (5%w/w CNT/POR) were >4 MOhm, requiring great current levels to induce Joule-heating behavior. In this study, we have combined our improved method for the fabrication of SMP foams (see Chapter 4) with the use of a conductive polymer to induce Joule-heating behaviors on the matrices and, thus, improve the observed limitations in Chapter 3.

5.3.3 Study Limitations

The current study is limited by a series of factors that can limit the translation potential of the PPy-coated 3DSMP material. First, the fabrication of the 3DSMP foams is still limited to the minimal dimensions that we can fabricate using our 3D-printing setup. For example, in this study we limited the PPy-coating to foams with a 50% infill density, which are designed to have cubic pores with a dimension of approximately 1 mm. Adding the wall thickness of

approximately 0.5 mm in Section 4.2.1 (**Figure 4-4**), tubules of 2 mm in length/width make up our 3DSMP foams. These factors limit the ultimate compressibility of our material and its potential to be transported along the human brain vessels that have inner diameters of 2-4 mm. Further, the proposed *in situ* polymerization of PPy on the surface of our 3DSMP foams suffers from the non-homogeneous coating of the foams.

In this study, we aimed at promoting the homogeneous deposition of pyrrole fumes on the surface of the foam by rotating the position of the 3DSMP foam during polymerization, thus guaranteeing similar exposure time to fumes. Despite this preventive measure, we still observed areas that were not coated with PPy, due to its contact with the container where polymerization was performed (**Figure 5-4**). This non-homogeneous coating of the foams led to the formation of hotspots on some specimens during the Joule-heating assessments. For example, **Figure 5-16** demonstrates two representative specimens that exhibited hotspots, which can be an indication of non-homogeneous PPy polymerization and lower resistivity gradients in these areas. It is of paramount importance to design methods that aim at preventing this issue.

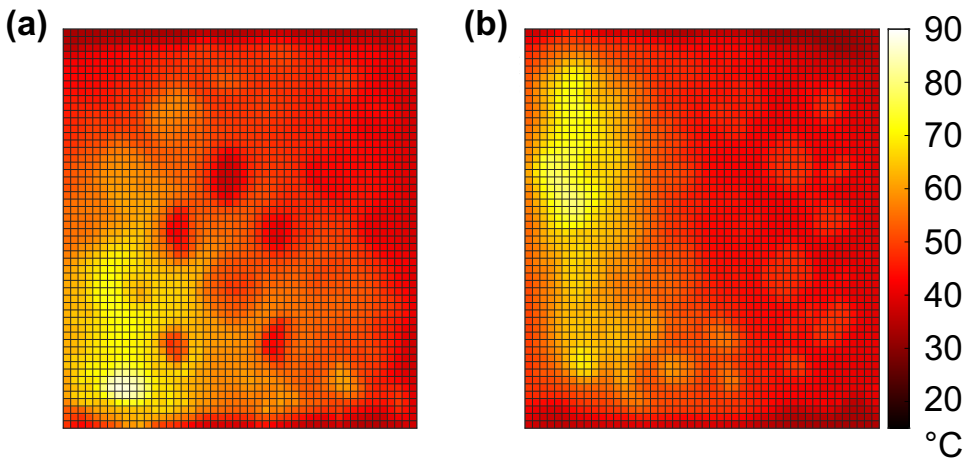


Figure 5-16. Representative thermographies of two PPy-coated 3DSMP foams with non-homogenous heating patterns: (a) exhibits a hotspot at one corner of the foam, and (b) exhibited a hotspot along the left side of the foam.

In our shape recovery experiments, we found several limitations related to our experimental setup. First, Joule-heating was performed using our parallel plate setup. In this setup, the foams maintain contact with the plate during the first seconds of the recovery, which induces friction between the foam and the plate. These forces can prevent full recovery of the foam and might explain the low recovery percentages of Specimens #2 and #3. In addition, we only performed stimulation of the foams for 10 s, which could have prematurely stopped complete share recovery. These factors together might amount to incomplete shape recovery. For future experiments, a novel setup that reduces potential forces being exerted on the foam might improve the accuracy of the shape recovery measurements. Also, testing the effect of different stimulation times might provide further information on how to control shape recovery behaviors. Further, we observed that Joule-heating in our shape recovery experiment led the foam to high temperatures that might not be safe *in vivo*. Future experiments should also

include the use of our PWM approach to reduce the maximum surface temperature of the foam, while promoting shape recovery.

Finally, we did not explore the biocompatibility of our PPy-coated 3DSMP foams. Other studies have previously demonstrated the biocompatibility of PPy as a coating for biomaterials. For example, Fahlgren *et al*. [167] studied the cell adhesion and gene expression of osteoblasts when cultured on the surface of PPy films fabricated with different dopants. They found that PPy films exhibited great cell adhesion and gene expression, and that dopants had different effects on select osteoblastic genes. Another study by Wang *et al*. [168] studied the PPy-induced systemic toxicity, hemolysis, allergic reactions, in ICR mice. They found that PPy did not induce any systemic or local toxicity when injected in the abdominal cavity of the mice. No allergic responses were observed and there was no evidence of hemolysis when blood was mixed with PPy solutions. Based on these studies, we expect the PPy on our foams to be biocompatible for endovascular embolization. However, we observed that some portions of our PPy-coated foams exhibited lingering $FeCl_3$ crystals, indicating that our washout process requires improvement to prevent $FeCl_3$-induced cytotoxicity. Future studies will be dedicated to study the biocompatibility of the PPy-coated 3DSMP foams, its cell adhesion potential and immunogenic behavior.

5.4 Conclusion

This study demonstrates the use of an *in situ* polymerization method for the coating of 3DSMP foams with a conductive polymer. PPy was synthesized on the surface of the 3DSMP foams, which induced electric conductivity on the polyurethane matrices. This coating also induced Joule-heating behaviors on the foams when DC voltage was applied. Here, we demonstrated the use of the PPy-coating to fabricate 3DSMP foams with the capacity to undergo shape recovery as a response to electric stimuli. This novel biomaterial exhibits great potential to be used as an embolic device for the endovascular treatment of ICAs.

CHAPTER 6 Translation of SMP-based Endovascular Devices: Elastase-induced Aneurysm Formation in New Zealand Rabbits for the Study of Pre-Clinical Effectiveness of Endovascular Devices

Parallel to the development of a conductive SMP material with Joule-heating properties and patient-specific geometries, this dissertation also established groundwork for the translation of the SMP-based device. In general, the development of biomedical devices requires thorough testing *in vitro* and *in vivo* before its translation to the clinic. Specifically, *in vivo* safety and efficacy testing of endovascular devices require *proof-of-concept* and efficacy assessments in animal models.

ICA animal models have been developed for pathological studies [169], drug testing [170] and device translation [171]. These models have included mice, rat, rabbit, dog, and pig models, where rabbit and rat carotid artery models are the most frequently used. ICA formation in these animal models can be performed via different methods, including parent artery ligation, elastase injection, among others [172]. These methods and their combinations are widely accepted for *in vivo* testing of endovascular devices (See refs. [21, 171, 173] for examples).

In this chapter, we aimed at establishing an ICA animal model for our research group and improving the execution of the elastase/RCCA-ligation method for the rabbit ICA models. First, we present our modified method for the creation of aneurysms in New Zealand rabbits using elastase injections in ligated CCAs (Section 6.1.1). Then, we present our assessments of

the formed aneurysms at different time points. We present histology and geometrical assessments of the created aneurysms, where we demonstrate the formation of stable aneurysms with degraded elastic lamellae. Lastly, we discuss our results and their implications for the development of our SMP-based device.

6.1 Materials and Methods

6.1.1 Aneurysm Formation

Experimental elastase aneurysms were formed in male New Zealand white rabbits (Charles River Laboratories, NY, USA) (weight: 3.0-4.0 kg). Rabbits were sedated with an intramuscular injection of Ketamine (50 mg/kg) and Xylazine (5 mg/kg). Sedation was maintained using 1-4% isofluorane inhalation. The RCCA was exposed by placing the anesthesized rabbit in supine position and making an incision between the medial edge of the sternocleidomastoid and the trachea. A clip was tightly secured around the RCCA, close to the brachiocephalic trunk. A silk tie was placed around the artery and tied securely at 1.5 cm above the aneurysm clip. A 1:2 mixture of elastase (BD Millipore) and saline was injected into the RCCA while maintaining the aneurysm clip secured. After 20 minutes the aneurysm clip was removed to restore flow (**Figure 6-1a**). Elastase solution enzymatically degraded the healthy elastic lamina (**Figure 6-1b.1** and **Figure 6-1b.2**) which debilitated the wall and induced ballooning of the arterial wall (**Figure 6-1b.3**). The incision was closed and covered with triple antibiotic ointment. The rabbit was then moved to a recovery chamber for recover and monitored daily for 7 days post-surgery.

6.1.2 Assessment of Aneurysm Formation

Rabbits were prepared for angiography at the end of 2, 4, and 6 weeks ($n = 4$, per group) periods using the same anesthetic procedures described previously. The left femoral artery was exposed and an aneurysm clip was placed proximally and the artery was tied about 2 cm distal to the clip. A small cut was performed, and the catheter and the guide wire were inserted. A C-arm angiography device (GE 9800 Omnipaque contrast) was used to confirm that the catheter reached the ascending aorta. Digitally subtracted angiography was then performed to demonstrate the aneurysm. Imaging was performed to assess aneurysm growth and maintenance. After aneurysm visualization, the catheter was positioned in the left ventricle and Euthasol (1 mL/4.5 kg) were injected. After confirmation of death, the original incision was re-opened to expose the RCCA and resect the aneurysm. The left common carotid artery was also resected as control. Tissues were stored in saline prior to further processing.

Angiographic images were processed to measure aneurysm length (AL) and aneurysm width (AW), using open-source software ImageJ [132]. Measurements were compared at the three imaging timepoints using a one-way ANOVA test. Differences were deemed significant if $p < 0.05$.

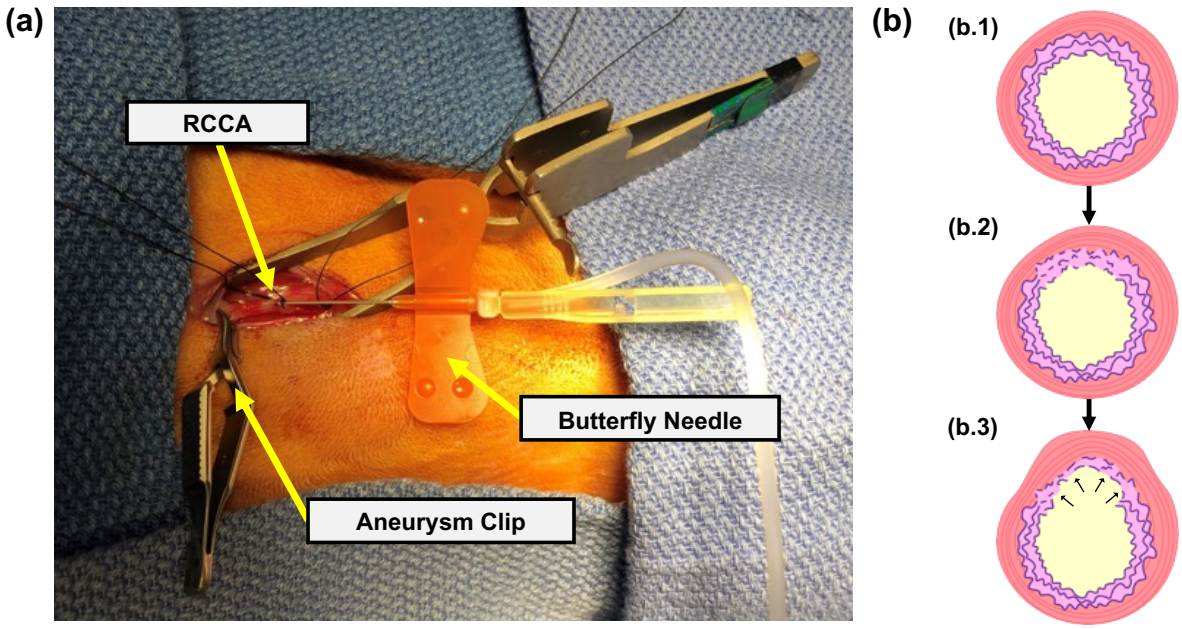


Figure 6-1. (a) Surgical setup for aneurysm formation, showing the use of the butterfly catheter. (b) Schematic of aneurysm formation via elastase injection: (b.1) healthy vascular wall with integral elastic lamina, (b.2) elastic lamina degradation induced by elastase injection and (b.3) focal dilation of the arterial wall caused by the breakdown of the elastic lamina.

6.1.3 Histology

Resected aneurysms tissues and controls were processed with routine histology methods. Briefly, tissues were fixed in 10% formalin and embedded in paraffin. Tissue sections of 5-7 μm of thickness were obtained using a microtome and stained with Verhoeff-elastic-Van Gieson stain. Tissue sections mounted on glass slides for light microscopy assessment. Digital histology images were obtained using a light microscope. Images were taken using a 4X objective and digitally merged using ImageJ (National Institutes of Health, USA) [132].

6.1.4 Statistical Analysis

All quantitative measurements are represented as mean $\pm$ standard deviation. Animal groups were compared using ANOVA test, where differences were deemed significant when $p < 0.05$. All statistical assessments were performed in SPSS (IBM Corp.).

6.2 Results

6.2.1 Aneurysm Formation

Male New Zealand white rabbits underwent successful aneurysm creation (n=12). Average aneurysm length was 4.0 ± 1.9 mm (range 2.2-8.4 mm) and an average width of 1.5 ± 0.4 mm (range: 1.0-2.3 mm). **Table 6-1** lists average aneurysm length and width at the investigated time points. ANOVA analysis returned no significant difference for length ($p = 0.983$) or width ($p = 0.401$). **Figure 6-2** shows representative angiographic assessment of aneurysm formation at the RCCA.

Table 6-1. Geometric dimensions of the elastase-induced aneurysms in New Zealand rabbits at different time points.

Timepoint	*AL (mm)*	*AW (mm)*
2 weeks	4.2 ± 2.8	1.3 ± 0.3
4 weeks	3.9 ± 1.0	1.4 ± 0.2
6 weeks	3.9 ± 1.8	1.7 ± 0.4

6.2.2 Histological Assessment

Histological sections were successfully obtained from the resected aneurysms. Tissue sections exhibited the classic structure for the arterial wall of the aneurysm. Specifically, Verhoeff-Van Gieson staining allowed the observation of the elastic fibers in the vascular wall, which were observed as the darker purple tone in **Figure 6-3**. Our results indicate a generalized deficiency of elastic fibers in the aneurysm wall, where we even observed regions sections with complete absence of these elastic structures. Additionally, we observed that the aneurysms of the 6-week group exhibited an evident lack of structure in the elastic fibers (**Figure 6-3c**), while the other two time points still exhibited some fragments of the elastic lamina (**Figure 6-3a-b**).

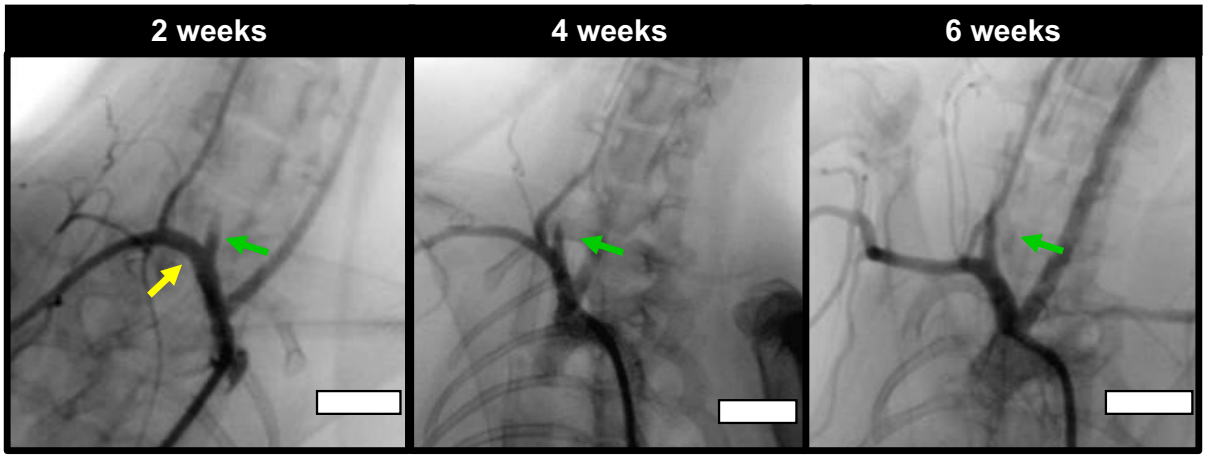


Figure 6-2. Representative angiograms of the created aneurysms. The green arrows point towards the created aneurysms and the yellow arrow indicates the RCCA. Scale bars = 10 mm).

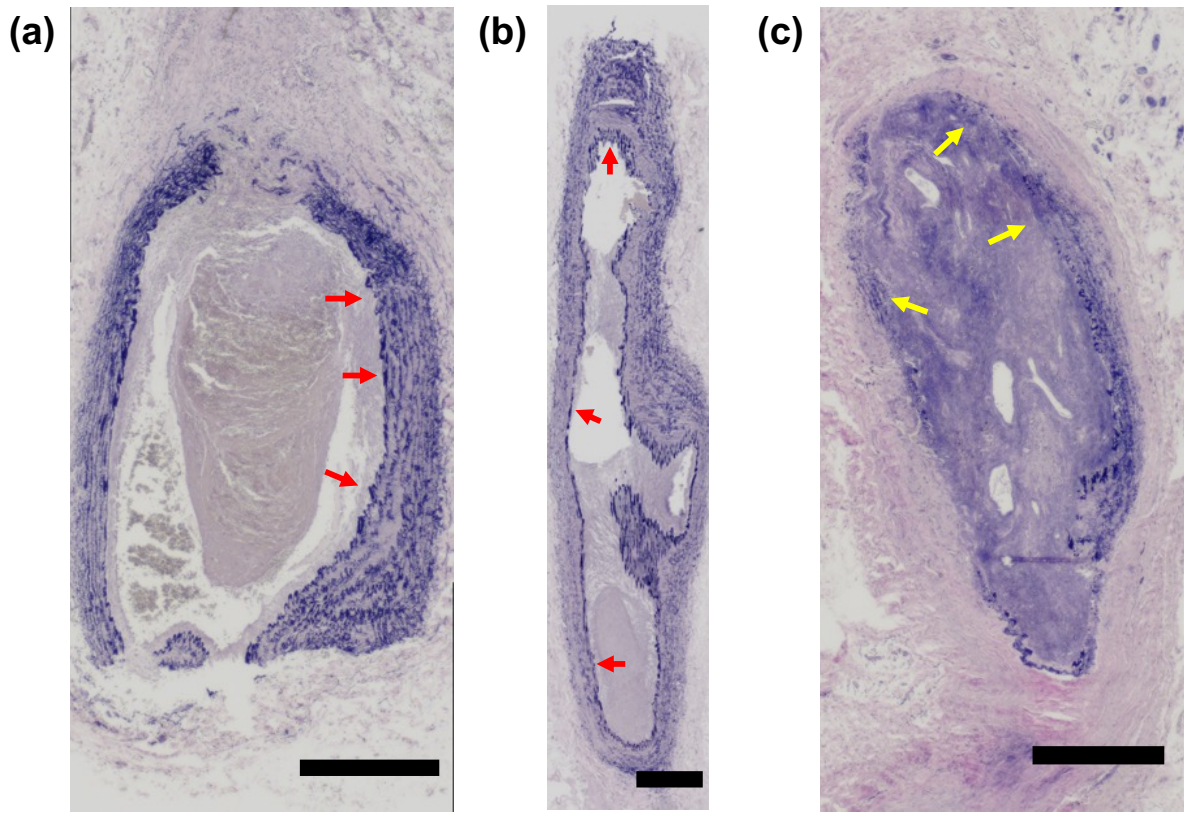


Figure 6-3. Histology slides of the created aneurysms depicting elastin degradation at (a) 2 weeks, (b) 4 weeks, and (c) 6 weeks. Red arrows indicate the portions of the non-degraded elastic lamina. Yellow arrows indicate the degradation of the elastic fibers. Scale bars = 0.5 mm.

6.3 Discussion

6.3.1 Our Approach

Technology for endovascular embolization of intracranial aneurysms has advanced significantly over the last thirty years since the development of GDCs. Further innovation in the field requires the development of pre-clinical models that allow testing of safety and efficacy of endovascular devices. To this end, animal models for saccular aneurysms have been developed and improved over the past six decades [174-176]. These models have been able to

accurately mimic the anatomy and hemodynamics of human aneurysms using different species, including mice, rats, rabbits, among several others. Specifically, the rabbit model has proved to be superior for the testing of endovascular devices, due to the docility of the animal, low maintenance cost, wide availability and appropriate size for the formation of aneurysms with similar geometry to the human [172].

Among the different aneurysm formation techniques in the rabbit model, elastase injection is described as a fast alternative for the formation of aneurysms prone to rupture [172]. In this procedure, successful elastase injection requires proximal and distal ligation of the common carotid artery (CCA), which is consistently described to include the dissection of the parent artery and the use of a silk tie for distal ligation of the CCA. Currently, two techniques for proximal ligation of the vessel are extensively applied: (i) the use of a Fogarty balloon [177], or (ii) use of a temporary aneurysm clip [178]. Based on our experience, we agreed with Hoh *et al.* about the potential damage to the CCA when using the Fogarty balloon. Therefore, we have adapted the method as described by Hoh *et al.* and aimed at its improvement.

Hoh *et al.* used an angiocatheter to inject elastase between the proximal and distal ligation sites and it was maintained in the intraluminal space for the 20-minute elastase injection time. We initially performed our aneurysm formation with the angiocatheter but we noticed that it had the potential to cause torque on the vessel. In addition, it was not only more difficult to insert the catheter into the CCA initially, but it placed unwanted pressure on the sides of the arterial wall. These complications during elastase injection might lead to unwanted vessel lesion and and remodeling processes on the artery, ultimately altering the native condition of the healthy

artery wall [179]. As a result, we have substituted the use of the angiocatheter for a butterfly catheter to reduce the potential application of torque. This modification of the protocol allowed the surgical team to step back from the table and inject elastase from the opposite end of the catheter without risk of vessel damage. As a result, we have been able to induce the formation of stable saccular aneurysms via elastic lamina degradation, as demonstrated in **Figure 6-2** and **Figure 6-3**. We believe that this modification to the aneurysm formation protocol can provide significant improvement to the ease-of-use of this animal model.

6.3.2 Applications for Endovascular Device Testing

Formation of saccular aneurysms for the testing of endovascular devices requires the maintenance of native properties in the parent artery, as off-target damages during elastase injection might lead to parent vessel rupture or reduce effectiveness of the model, in addition to animal fatalities. Damages to the vessel wall might also increase alterations in the vessel flow dynamics, limiting the accuracy of aneurysm computational flow dynamics research, which is of paramount importance for the development of endovascular devices [129].

Our findings in this modified protocol will be applied to the development of a novel coil-free endovascular device. We have developed a shape memory polymer (SMP) for endovascular embolization of patient-specific aneurysm geometries [60-62, 127], and we believe that this elastase-induced aneurysm formation protocol can aid in the translation of our material to the pre-clinical setting. We plan to test our material with a statistically powerful sample size, to determine the pre-clinical safety and effectiveness of our SMP device (measured using Raymond-Roy Occlusion Classification scale). We also plan on studying the microstructural

and mechanical properties of the aneurysms formed in this animal model, and compare them to our recent findings in the properties of a human aneurysm specimen [180]. Lastly, this animal model can also be used for training of surgical teams in the deployment of current marketable endovascular devices [181].

6.3.3 Study Limitations

The key advantage of this technique over similar techniques is the significant reduction in the torque on the artery. While this is not necessarily stated as an issue in the literature, we experienced vessel torsion while using an angiocatheter and injecting the elastase solution. To minimize the risk of injury, it was imperative that we substitute the angiocatheter, which was done by using a butterfly catheter. We also found that, while the balloon catheter method was effective, this step required more time than was necessary to achieve the same result. While we did not encounter any short-term complications from our procedure, or any post-operative complications with any of the animals, it would be advantageous to replicate this protocol with more samples and/or a longer study period.

6.4 Conclusions

In this study, we present a modification to traditional elastase-induced aneurysm models. We have substituted the use of an angiocatheter for elastase injection for a butterfly catheter, which reduced the applied torque on the artery, reducing the potential for parent vessel injury. This modification to the traditional elastase/RCCA-ligation method can further improve aneurysm modeling in rabbit animal models. This method improvement has important implications for the *in vivo* testing of endovascular devices and training for ICA embolization procedures.

CHAPTER 7 Translation of SMP-based Endovascular Devices: Meta-Analysis of the Occlusion Effectiveness of Modern Endovascular Technology

The design of pre-clinical studies for the evaluation of occlusion effectiveness of our SMP-based device requires a control group. For clinical trials for medical devices, the control group is typically designed as the "gold standard" (i.e., the best-performing device available in the market) for the treated indication. As discussed in previous chapters, the endovascular therapy for ICAs is going through a "golden era" where novel devices emerge frequently and extend the range of treatable aneurysms. For unruptured saccular aneurysms, the selected treatment depends on anatomical location, tortuosity of parent vessel, bifurcation or non-bifurcation, among several other criteria. We have proposed that our SMP-based device will be used to treat unruptured saccular aneurysms in general, and our animal model has been designed specifically for this indication. However, current available literature for the immediate and long-term efficacy for this general indication is abundant and few meta-analyses include the overall efficacy of a given device. Most available meta-analyses use few studies and, therefore, small patient populations.

In this chapter, we present a meta-analysis where we aimed at including studies that evaluated the immediate and long-term occlusion of modern endovascular devices for the treatment of unruptured saccular ICAs. First, we present the methods used for the systematic extraction of studies from scientific databases, and the criteria used for inclusion/exclusion (I/E) of studies

for final data extraction and analysis. Then, we present the meta-results of the included studies, where we present general demographic characteristics of the included population. Lastly, we present our analysis of the immediate and long-term efficacy of the included devices. Based on this analysis, we present our selection of a device as a control group for our future pre-clinical studies.

7.1 Materials and Methods

7.1.1 Literature Search

Literature search was conducted by following the recommendations of Tawfik *et al*. [182], the Preferred Reporting Items for Systematic Reviews and Meta-Analyses (PRISMA) statement [183] and the Cochrane Handbook for Systematic Reviews of Interventions [184]. A systematic literature search was performed using online databases available at our institution: PubMed, Cochrane, Web of Science and ClinicalTrials.gov. The search was conducted to obtain prospective and retrospective studies evaluating the occlusion efficacy of endovascular devices (including GDCs, hydrogel-coated coils, WEB, flow diverters and liquid embolic devices) for the treatment of unruptured saccular ICAs. Only peer-reviewed studies published between 2000-2022, with recruitment start date on or after 1999, were included in the screening process. A complete set of queries for the database search can be found in APPENDIX E.

7.1.2 Inclusion/Exclusion (I/E) Criteria for Study Screening

Screening of the search results was performed using a list of Inclusion/Exclusion (I/E) criteria; individual studies not adhering to the I/E criteria were rejected for data collection. Some key inclusion criteria were: (i) reporting of occlusion rates with Raymond-Roy Occlusion

Classification (RROC) or a translatable scale; (ii) in the case of including ruptured aneurysms, reporting of occlusion rates must be done separately per rupture status; (iii) reporting of long-term follow-up of ICA occlusion; (iv) endovascular treatment must be performed as the first line of treatment for the target aneurysm. Exclusion criteria included: (i) reviews; (ii) case studies; (iii) unrelated articles; (iv) animal studies; (v) studies including trauma-induced, mycotic, pathogen-induced aneurysms; (vi) studies that reported occlusion rates with no discrimination of saccular and non-saccular geometries (i.e. saccular geometries should be reported separately). A complete list of the I/E criteria can be found in Appendix E. The first stage for screening was performed by three independent reviewers using a spreadsheet containing the title and abstract of the search results after removing duplicates. A second stage of screening was performed by four reviewers by reading the full manuscript. All the studies included after both stages of screening were used for data collection.

7.1.3 Data Collection

Data collection was performed by two reviewers. Studies were distributed proportionally between reviewers and data was extracted using a standardized spreadsheet that was previously pilot tested. Data extracted for analysis included (i) basic study information (first author, country, publication date, sample size), (ii) patient demographics (age and sex), (iii) aneurysm dimensions (largest diameter and neck length), and location (see **Table 7-1**), and (iv) aneurysm occlusion effectiveness results (type of endovascular device, angiographic assessment time, follow-up time, number of aneurysms assessed, and RROC rates). After initial data collection, studies were re-distributed among the reviewers to perform a data verification step, to confirm correct data extraction.

Table 7-1. List of aneurysm locations at the Circle of Willis and their corresponding acronyms.

Circulation	Artery	Acronym	Portions
Anterior	Anterior Communicating Artery	ACommA	
	Anterior Cerebral Artery	ACA	A1,A2
	Middle Cerebral Artery	MCA	
	Internal Carotid Artery	ICaA	
	Anterior Choroidal Artery	AChA	
	Anteromedial Central Arteries	ACeA	
Posterior	Posterior Cerebral Artery	PCA	P1,P2
	Posterior Communicating Artery	PCommA	
	Posteromedial Central Arteries	PCeA	
	Superior Cerebral Artery	SCA	
	Pontine Arteries	PA	
	Basilar Artery	BA	Tip, Trunk
	Internal Auditory Artery	IAA	
	Anterior Spinal Artery	ASA	
	Anterior Inferior Cerebellar Artery	AICA	
	Posterior Inferior Cerebellar Artery	PICA	
	Vertebral Artery	VA	

7.1.4 Outcomes

The primary objective of this meta-analysis was to compare the immediate and long-term occlusion rate of modern endovascular devices for the treatment of ICAs. In addition, demographic information about the ICA size and location on the Circle of Willis was be collected and analyzed.

7.1.5 Statistical Analysis

Summary statistics reported in individual studies were transformed to obtain the mean ± standard deviation of each extracted metric. Proportions, averages and their respective 95% confidence interval (CI) were pooled across studies using a random-effects mixed model

meta-analysis. Heterogeneity was quantified using I^2 and τ^2. A logistic generalized linear mixed model (LGLMM) was used to compare the time-dependent complete occlusion rate between endovascular devices. All statistical analysis were performed in R v4.1.2 using the meta-package [185].

7.2 Results

7.2.1 Literature Search Results and Screening

Literature search was performed on November 7th, 2022, and yielded 5,227 results, which were included in the screening pipeline presented in **Figure 7-1**. A total of 80 studies were included for data extraction. A summary of the included studies can be found in Appendix E.

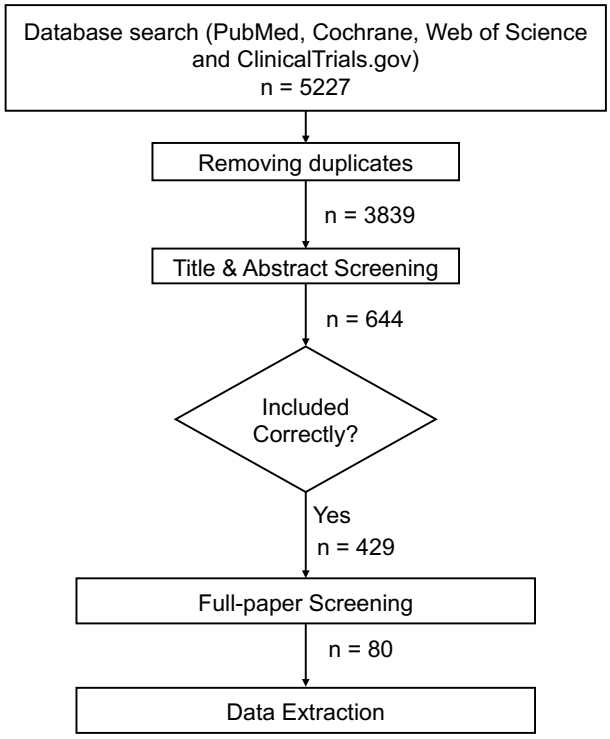


Figure 7-1. Flow diagram for the screening of obtained studies. *n* represents the number of studies that were included after each phase of the screening process.

7.2.2 Patient and Study Demographics

In total, the 80 studies used for data extraction included 21,331 patients that harbored 22,791 aneurysms from 15 countries (**Table 7-2**). Pooled female proportion was 72.54% (95% CI: 70.87-74.15). Pooled mean patient age was 58.17 (95% CI: 56.76-59.59, **Table 7-3**). Overall aneurysm maximum diameter average and neck size were 7.15 (95% CI: 6.50-7.81) and 4.35 (95% CI: 4.05-4.66), respectively (**Table 7-3**). Pooled proportions of aneurysm location are listed in **Table 7-4**. The pooled follow-up time in months was 13.01 (95% CI: 10.21-15.81).

Table 7-2. Country distribution of the studies included in the meta-analysis.

Country	***Study count - n (%)***
Austria	2 (2.5)
China	6 (7.5)
Denmark	1 (1.2)
Egypt	1 (1.2)
Finland	1 (1.2)
France	8 (10)
Germany	15 (19)
Italy	2 (2.5)
Japan	10 (12)
Korea	13 (16)
Poland	4 (5)
Russia	1 (1.2)
Taiwan	1 (1.2)
USA	14 (18)
International	1 (1.2)

Table 7-3. Patient demographics and meta-averages of aneurysm dimensions.

Patient Demographics	$\boldsymbol{n = 21331}$
Female	72.5 (70.8-74.1)
Age	58.1 (56.7-59.5)
ICA Geometry	**Mean (95% CI)**
Average maximum diameter (mm)	7.1 (6.5-7.8)
Average neck width (mm)	4.3 (4.0-4.6)

Table 7-4. Meta-proportions of ICA anatomic location on the circle of Willis.

ICA Anatomic Location	**% (95% CI)**
ACommA	26.4 (22.5-30.8)
ACA – A1	10.2 (6.1-16.8)
ACA – A2	7.4 (0.6-52.4)
MCA	24.5 (19.2-30.8)
ICaA	46.4 (41.9-50.9)
AChA	3.4 (3.1-3.8)
ACEA	1.8 (1.6-2.2)
PCA – P1	2.7 (1.3-5.5)
PCA – P2	0.8 (0.2-3.1)
PCommA	13.9 (12.2-15.7)
PCeA	1.6 (0.1-19.7)
SCA	4.2 (2.7-6.7)
BA – Tip	14.4 (11.3-18.3)
BA – Trunk	4.7 (2.2-9.8)
IAA	0.7 (0.2-2.3)
PICA	2.9 (1.7-5.0)
VA	3.0 (2.0-4.5)

Overall, 20,874 ICAs had angiographic occlusion rates reported immediately after treatment or at the earliest follow-up (for flow-diverters only). From this subset, 15713 (74.85%) were treated with coiling alone, 3206 (15.27%) with stent-assisted coiling (SAC), 782 (3.72%) with balloon-assisted coiling (BAC), 896 (4.26%) with flow diverters, 270 (1.2%) with the Woven-EndoBridge (WEB), and 158 (0.75%) with others (hydrogel-coated coils, Contour Neurovascular system, and Medina).

7.2.3 Occlusion Effectiveness

Occlusion effectiveness meta-analysis was performed in three parts: (i) pooled meta-proportion of immediate complete IAC occlusion (i.e., RROC-I rates), (ii) long-term occlusion effectiveness using a logistic generalized linear mixed models (LGLMM), and (iii) a comparison of the last available follow-up complete occlusion meta-proportion and predicted probability of complete occlusion at the average follow-up time based on the LGLMM. All analyses were performed with the extracted RROC-I rates for Coils (grouped as coiling-alone and assisted-coiling techniques), the WEB device and flow diverters. Other devices (hydrogel-coated coils, Contour Neurovascular system) were excluded from analysis due to low number of studies available but are discussed in Section 7.3.

7.2.3.1 Immediate Occlusion after Endovascular Treatment

Proportions for RROC-I rates immediately after endovascular therapy were obtained for each study. A proportion meta-analysis was performed to pool study proportions using a random effects model. A meta-proportion for each individual device is presented in **Table 7-5**. These proportions represent the global complete occlusion rate obtained in all study for each device

and its confidence interval. Flow diverters were not analyzed immediately after treatment due to the nature of its mechanism of action, where aneurysms become progressively occluded over time (i.e., theoretically, no occlusion occurs immediately after treatment).

Table 7-5. Pooled meta-proportions of RROC-I for modern endovascular devices, except flow diverters.

Device (k studies)	RROC-I Meta-Proportion % (CI 95%)	I^2 (%)
Coiling (29)	58.11 (53.42-62.66)	95
SAC(25)	55.95 (46.0-65.45)	94.2
BAC (6)	73.87 (65.0-81.15)	81.8
WEB (6)	27.75 (13.20-49.23)	77.1

Pooled meta-proportions exhibit a higher degree of immediate occlusion for BAC than other coiling techniques. The WEB device exhibited poor immediate occlusion degrees immediately after treatment.

7.2.3.2 Long-Term Occlusion Effectiveness of Endovascular Treatment

LGLMM models were fitted to the occlusion effectiveness data obtained from the 80 studies. Three models were obtained for probability of RROC-I for each individual device categories as a function of angiographic follow-up time: (i) all coiling techniques, (ii) the WEB device, and (iii) flow diverters. Models for other devices were not performed due to low number of available studies. An individual model for balloon-assisted coiling (BAC) was attempted; however, this was not possible the low availability of follow-up time points for this technique. Therefore, one model for all available coiling data was performed. Model parameters are summarized in **Table 7-6** and models fits are represented in **Figure 7-2**. In addition, traditional

fixed-effects logistic models (FELM) were compared to the LGLMM to demonstrate the effect of random effects induced by individual study variation.

Table 7-6. Model parameters for the LGLMM and FELM models of probability of RROC-I as a function of follow-up (FU) time for endovascular therapy techniques. OR: odds ratio.

Device	Parameter	LGLMM			FELM		
		OR	CI (95%)	p-value	OR	CI	p-value
Coiling	Intercept	2.50	1.51-4.15	<0.001	1.15	1.12-1.19	<0.001
	FU time	1.04	0.98-1.09	0.199	1.03	1.03-1.04	<0.001
WEB	Intercept	0.37	0.08-1.63	0.187	0.49	0.37–0.64	<0.001
	FU time	1.20	0.98-1.47	0.074	1.16	1.12–1.21	<0.001
Flow Diverters	Intercept	2.63	0.67–10.32	0.165	0.77	0.65–0.91	0.003
	FU time	1.05	0.92–1.19	0.452	1.09	1.07–1.10	<0.001

Fitted models in **Figure 7-2** demonstrate similar complete occlusion behaviors across the different endovascular therapy techniques. The WEB device exhibits a unique behavior, where the initial (FU time = 0 months) occlusion degree approximates the proportion described in **Table 7-5**, which then increases to similar levels of complete occlusion of coiling and flow diverters. Using the discrete predicted values of the models, we observed that the predicted probability of complete occlusion (i.e., RROC-I) at 6 months for coiling, WEB, and flow diverters was 0.76 (95% CI: 0.67-0.82), 0.53 (95% CI: 0.30-0.74) and 0.78 (95% CI: 0.60-0.90). At 11-12 months, the probability increased to 0.79 (95% CI: 0.69-0.86) for coils, 0.74 (0.40-0.92) for WEB, and 0.83 (0.65-0.92) for flow diverters. Finally, at the last available FU point the RROC-I probability was 0.91 (95% CI: 0.60-0.99) at 40 months for coiling, 0.91 (95% CI: 0.41-0.99) at 18 months for WEB, and 0.92 (95% CI: 0.37-1.00) for flow diverters. Overall, the long-term RROC-I probability was homogeneous across these studied

endovascular techniques.

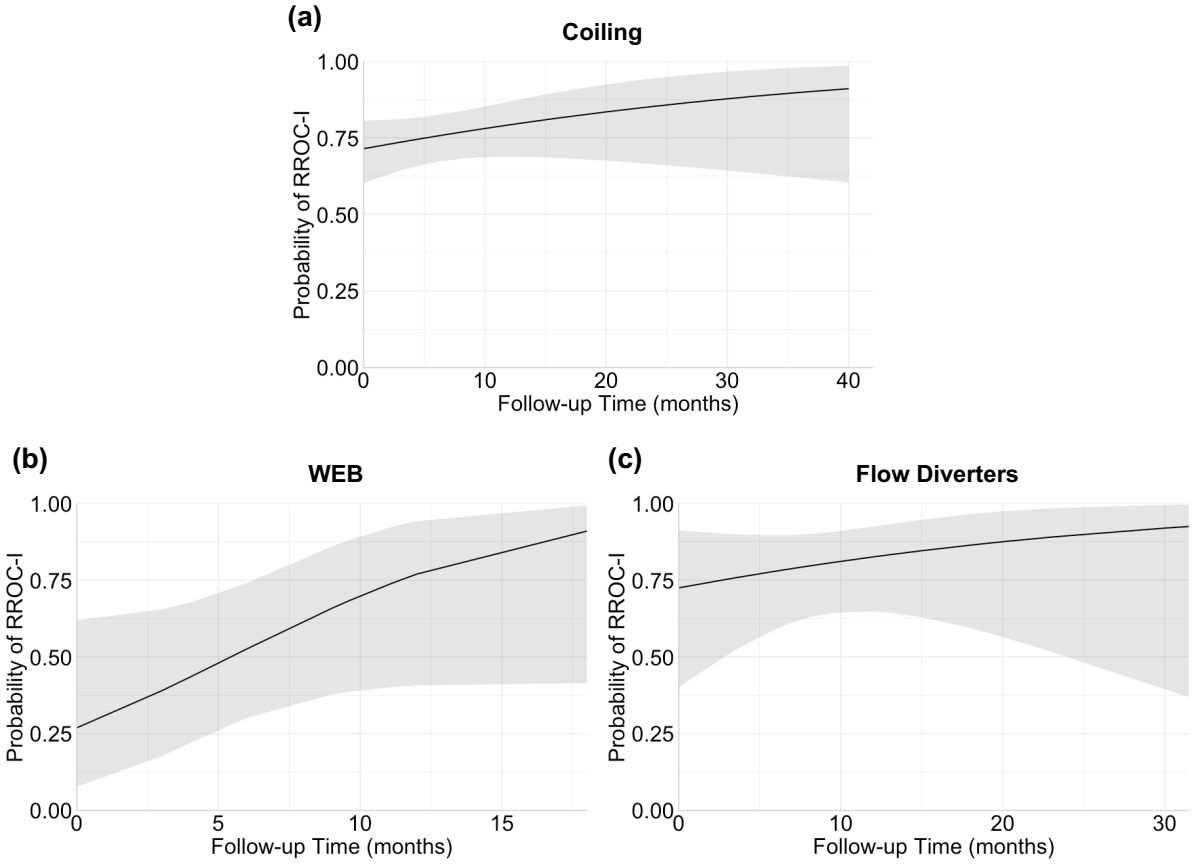


Figure 7-2. LGLMM model fits for probability of RROC-I as a funcion of follow-up time for the evaluated endovascular therapy techniques. Grey shading areas represent CI 95%.

7.3 Discussion

7.3.1 Overall Remarks and Occlusion Effectiveness

Endovascular therapies were first introduced in 1991 with Guglielmi's development of coils of ICA intrasaccular embolization [2, 3]. Ever since, coils have been the gold standard for endovascular therapy. In this study, 19751 aneurysms were treated with coil-based techniques in the 22-year span of the included studies. However, coiling exhibited limitations in its early

years related to procedural complications, such as aneurysm/parent vessel perforation, mass effect, parent vessel occlusion, and coil migration [186]. In addition, long-term efficacy of coiling is limited by potential coil compaction and/or aneurysm recurrence, thus leading to retreatment of the aneurysm. These limitations led to the development of assisting techniques for coil embolization. For example, BAC emerged as a safe alternative for ICAs with unfavorable dome-to-neck ratios, and SEC for more complex geometries (giant, fusiform) with difficult-to-treat locations, such as bifurcation ICAs. Nonetheless, overall coiling techniques suffer from aneurysm recurrence, difficulty to treat aneurysms with tortuous parent vessels, and high re-treatment rates [187].

Based on coiling limitations, flow diverters emerged as a great alternative for ICA embolization. Flow diverters are similar to stents in terms of fabrication methods and materials (both are tubular wire meshes) but differ in porosity and flexibility. Flow diverters decouple blood flow between the parent vessel and the aneurysm space, allowing progressive thrombus formation within the sac. In addition, the wire mesh acts as a scaffold for neo-endothelization, which can lead to complete parent vessel remodeling [188]. This approach has expanded the application of endovascular therapy to ICA geometries and locations that are not treatable with coiling techniques. Lastly, endosaccular flow diverters, like the WEB, have expanded flow diverting technology to bifurcation aneurysms.

In this study, we aimed at understanding the potential of these techniques for the treatment of saccular unruptured aneurysms, a broad ICA category that can be treated with most endovascular approaches. Due to the great effect of immediate complete occlusion in

recurrence rates and retreatment [4, 189], understanding the overall RROC-I rate of the most prominent endovascular therapies is of paramount importance for improved method selection and the development of novel endovascular technologies.

The results of this meta-analysis from 22,193 unruptured saccular ICAs shows several key differences and similarities between endovascular devices. We found that immediate ICA occlusion is improved in BAC, when compared to other coiling techniques (73.8% [95% CI: 65.0-81.1] vs 56.7 [95% CI: 52.5-60.8]), as described previously in the literature. These differences contribute to the debate on the differences between coiling techniques, where occlusion rates have been found to be similar for coiling alone, SAC and BAC [190-192]. In addition, our results validate previous results for RROC-I rates immediately after treatment; we found that RROC-I pooled proportion was 27.7 (95% CI: 13.2-49.2), similar to what Asnafi *et al*. found in their meta-analysis for the same device: 27.0% (95% CI: 15.0-39.0) [193].

In the long-term, our results indicate that endovascular therapies provide similar levels of RROC-I rates. In the last available follow-up point, coiling, WEB and flow diverters exhibited >90% occlusion (**Figure 7-2**). However, the WEB device reached these levels of occlusion in a shorter time (18 months), while coiling techniques and flow diverters required 40 and 31.5 months, respectively, to achieve the same probability of RROC-I. Quantitatively, this was observed in a greater odds ratios for the WEB GLMM model (**Table 7-6**). These findings could be applied to inform current guidelines for method selection for ICA endovascular therapy.

7.3.2 Occlusion Efficacy of Other Devices

In this study, we aimed at obtaining comprehensive information about modern endovascular devices using studies that fulfilled our I/E criteria. However, not all the included studies could be analyzed using a meta-analysis, due to a low number of available studies. Specifically, two devices from two separate studies that fulfilled our I/E criteria were not included in the analysis. The devices that were not analyzed were hydrogel-coated coils (HCC) and the Contour Neurovascular System (CNS).

The CNS is an intrasaccular flow diverter with a similar mechanism of action as the WEB device. However, their geometries differ from the WEB and make the CNS a separate field of study for this analysis. The CNS is a braided wire mesh that is designed specifically for wide-necked bifurcation aneurysms. It has an "upside-down-umbrella" geometry that resembles the original geometry of a bifurcation when deployed in the aneurysm [194]. The included study by Biondi *et al*. (2022) [195]is a retrospective single-arm study where the CNS was tested in 53 patients. Complete occlusion using the CNS was 16.7% immediately after treatment, 79.6% at 3 months follow-up, and 51.8% at 1 year follow-up. It is not common to see a reduction in complete occlusion when data is available for the whole cohort across follow-up times, and this reduction is not explained in the study discussion. Future research for the CNS should shed more light on the behavior observed in this study. Also, the authors indicate that the patient cohort included their "learning curve" period for the CNS, which can also yield to biased results. Overall, the CNS is a promising device that requires further and prospective research to be included in long-term meta-analysis studies.

On the other hand, HCC are an advancement of coil-based technology where the coil is coated with a polymeric sheath, which absorbs water and swells to occupy gaps between coils. This technology was developed to increase packing density of traditional coils. Several trials have been performed to study the advantage of HCC over traditional coiling, but no significant differences have been found in immediate complete occlusion rates [26, 28]. In our meta-analysis, only one study including HCC was accepted for inclusion. Poncyljusz *et al.* [196] performed a single-center controlled randomized trial to compare bare platinum coils (BPCs) and HCC, but with no significant difference in occlusion effectiveness. The HCC data from this study was not included in any of the meta-analyses due to being the only HCC data point.

7.3.3 Implications for the Development of SMP-based Endovascular Devices

Our learnings from this meta-analysis will be used to plan and design the translational stages of the SMP endovascular device presented in the previous chapters. We plan to execute *in vivo* studies using the New Zealand Rabbit model presented in Chapter 7. This study is planned to test the safety and efficacy of our SMP-based endovascular device in elastase-induced aneurysms and compare it with one of the endovascular devices presented in this meta-analysis. Currently, most novel endovascular devices are compared with GDCs in their pre-clinical and clinical trials. However, with the growth of flow diverting technology (both intra- an extrasaccular), we questioned the "gold standard" status of GDCs for unruptured aneurysms. Our results demonstrate that immediate occlusion of unruptured saccular ICAs is homogeneous across GDC technology, and that other devices do not offer an advantage over the use of GDCs for unruptured saccular ICAs. However, long-term complete occlusion of ICAs is more likely to occur after 18 months of treatment when WEB devices are used. These

findings will guide the clinical decisions made by our team to select an endovascular device that is better suited for the effectiveness evaluation of our SMP-based ICA endovascular embolization system.

7.3.4 Study Limitations

A meta-analysis is understood as the highest form of scientific evidence. However, most meta-analysis suffer from a high degree of heterogeneity between the studies used to perform them, in addition to very low availability of data that suffices I/E criteria in the literature. These factors played a significant role in our study. This heterogeneity can be induced by differences in study design, prospective or retrospective data generation and gathering, experience of neurosurgeons with a given endovascular device, use of internal or centralized assessment of angiographic outcomes, among several other factors. In this study, we aimed at reducing the chances of Type II error by including study-specific variability in the assessment of our data. To do this, all our meta-analyzed metrics (averages and proportions) were calculated using random effects models, which have the great advantage of providing homogeneous weights for all studies in the analysis. In addition, the long-term modeling of RROC-I probability as a function of follow-up time in months was performed using a logistic GLMM, which also accounts for the random effects associated with study-specific variability.

Another important limitation in our analysis is related to a low availability of angiographic outcomes in the long-term follow-up (>2 years) of ICAs treated with endovascular devices. This is related to different factors: (i) the WEB became available for clinical use in Europe in 2011 and later in other regions; long-term prospective trials have started to become available

recently, but more data is expected to be published in the coming decade; (ii) flow diverters can be applied to more ICA geometries than other endovascular devices, including fusiform and dissecting aneurysms; in this study, we aimed at including unruptured saccular aneurysms only, which led to the rejection of a relatively high number of studies that reported angiographic outcomes for all types of geometries together, which can be solved with an open availability of individual patient data; (iii) we intended to perform analysis of HGCs as individual endovascular devices; however, it is frequently applied as a "finishing" coil after occupying most of the aneurysm space with bare GDCs. The reporting of this type of procedure is inconsistent across literature, which led our protocol to be designed to only include studies where HGCs were used as the only type of coil in the aneurysm; (iv) novel devices, such as the Medina embolic device [197], the CNS, the LUNA embolization system [198], among other flow diverting devices are still "young" in the endovascular market, and their available data did not fulfill our I/E criteria.

7.4 Conclusions

Endovascular therapy for unruptured saccular ICAs has benefited from the emergence of novel technology in the last decade. Intra- and extrasaccular flow diverters are some of the most notable technologies for the treatment of a wide array of ICA geometries, rupture status, and anatomic location. However, GDCs, and the assisting technology used to improve its applicability, remains as a great tool for endovascular embolization. Immediate occlusion rates for GDCs are yet to be improved and future developments in endovascular devices for ICA therapeutics should aim at addressing this long-standing limitation to reduce aneurysm recurrence in the short- to mid-term. Nevertheless, the WEB device shows great promise in

reducing periods for progressive complete occlusion, as demonstrated in this meta-analysis. For the development of SMP-based endovascular devices, our learnings in this chapter will guide the translational strategy of our device, as it will provide key information on the selection of a device for effectiveness assessment in controlled randomized pre-clinical studies.

CHAPTER 8 Conclusions and Future Work

8.1 Summary of Results

The results presented in this dissertation can be divided in two major sections: (i) material science studies for the development of polyurethane SMP for the development of a coil-free endovascular device for ICA therapeutics (Chapters 3, 4 and 5), and (ii) strategies for the translation of our SMP-based endovascular embolization device (Chapters 6 and 7).

The first section presented our first strategy for the development of a Joule-heating activated porous SMP material, where we infiltrated CNTs in the polymeric matrix to induce conductivity. Our results demonstrated that CNT infiltration was an acceptable option for inducing conductivity in the polyurethane matrix. However, we found that CNT infiltration was detrimental to thermomechanical properties of the SMP. Specifically, we found that these materials were not suitable for further investigation due to their poor mechanical performance and reduction on the T_g of the SMP material. This investigation raised new research questions that drove the studies presented in the following chapters.

In Chapter 4, we focused on improving the manufacturing process of porous SMP foams. Before the study presented in this chapter, the fabrication of foams relied on a sugar leaching method. This method was effective for pore generation, but it led to inconsistent thermal behaviors on the material, which was reflected in a low reproducibility of the T_g across different batches of produced materials. In addition, the fabrication of patient specific using the sugar leaching method was difficult, due to the brittle nature of sugar crystals, which led

to inconsistent and mechanically unstable sugar templates. Based on these limitations, we were motivated to advance the development of a 3D-printing method for the fabrication of SMPs.

Our first approach to 3DSMP materials was the direct printing of the polyurethane solution with an in-house system developed by our group (see Robert Kunkel's thesis [199]). This approach demonstrated that the unique polymerization/curing of our polyurethane formulation made direct 3D-printing difficult, due to its fast curing at room temperatures, its high sensitivity of oxygen, and the difficult rheological properties of the fresh SMP solution. These failed efforts led us to combine leaching and 3D-printing.

The method presented in Chapter 4 provided a facile approach for the fabrication of SMP foams with complex 3D geometries and pore sizes. We demonstrated that the combination of FDM 3D-printing using PVA filaments and leaching produced highly accurate 3D patient-specific geometries. The findings of this study advanced our goal towards the fabrication of individualized embolic devices for ICA therapeutics. Nevertheless, we also found limitations in our method, including the capacity of our 3D-printing system to produce PVA templates with high resolution and the maximum compressibility degree of the resultant foams.

Based on the 3DSMP foams obtained in Chapter 4, we aimed at inducing conductivity on the foams. Since CNT infiltration exhibited great limitations for the development of Joule-heating activated SMPs, we introduced conductivity with an approach that did not depend on the infiltration of nanomaterials in the polymeric matrix. Specifically, we used PPy coating as the best available alternative for this purpose.

In Chapter 5, we presented the results of our study on PPy coating and its use to induce Joule-heating behaviors on 3DSMP foams. Our results demonstrate that our method for PPy coating induces the deposition of a thin conductive layer on the surface of 3DSMP foams. In addition, PPy coating did not induce any significant detrimental changes on the thermomechanical properties of the 3DSMP foam. These results produced, for the first time, Joule-heating activated 3DSMP foams with patient specific geometries, a fundamental milestone for our long-term goal of producing individualized embolic devices for ICA therapy. This major milestone finalized the first portion of this dissertation.

In the second portion of this dissertation (Chapters 6-7), we focused on the development of translational strategies for our ICA device. These strategies included the development of an aneurysm animal model (Chapter 6), which will be used in future studies to determine the *in vivo* occlusion effectiveness of our SMP-based device. This future study will compare the effectiveness of our device against a "gold standard" to evaluate if our coil-free approach has the potential to outperform modern endovascular ICA embolization techniques *in vivo*. In Chapter 7, we aimed at determining this "gold standard" using a meta-analysis of immediate and long-term occlusion of unruptured saccular ICAs treated with modern endovascular devices. This study, which analyzed the angiographic outcomes of 22,791 unruptured saccular ICAs, demonstrated that traditional coiling techniques (assisted and non-assisted) are still the most effective method for the treatment of this type of aneurysms, as demonstrated with a superior immediate complete occlusion probability, compared to the WEB device and flow diverters. In addition, we found that the long-term complete occlusion probability in the WEB device was >90% in 18months, indicating that the WEB device can provide superior long-term

angiographic outcomes. Therefore, we concluded that our animal studies should include control groups where saccular aneurysms are treated with coiling or WEB devices.

8.2 Future Directions

This dissertation presented the development of the functional properties of the SMP material, which has been designed to be activated using Joule-heating and to be fabricated with a leaching/3D-printing method. However, further developments are required to use the material for endovascular embolization in a blood-rich environment with the dimensional constraints of the brain vasculature. In the following sections, we present some of the next developments required for the translation of our SMP-based device.

8.2.1 Material Microstructural Design for Guided Compression

Our leaching/3D-printing method provided great control for the porosity of the resultant 3DSMP foams, as seen in Section 4.2.1. However, the porosity of the material is homogeneous across the *X*–*Y* axes, and significantly lower in the *Z*–axis. This type of design impedes compressibility of the foam along the *Z*–axis, as demonstrated in our mechanical testing experiments (See Section 4.2.4). In addition, the current compression method for the foam induces expansion of the foam along the orthogonal axis (Poisson effect, **Figure 8-1a**), which makes delivery of the foam difficult. In fact, this was observed in our *in vitro* delivery experiments (see Section 4.3). In addition, the complex geometry of the patient's aneurysm can also make compression along a single axis difficult for delivery, due to the presence of hanging portions. Therefore, it is of great importance that infill patterns are designed with features that allow the guided compression of the foam to obtain a compressed geometry that

allows transportation of the material with a catheter. For example, we propose that future research is focused on the development of 3D-printing technology with porosity gradients (i.e., non-constant distance between infill lines) that allow multi-axial compression of the foam to a rod-like geometry (**Figure 8-1b**). This potential research route would also involve the design of a multi-axial compression system.

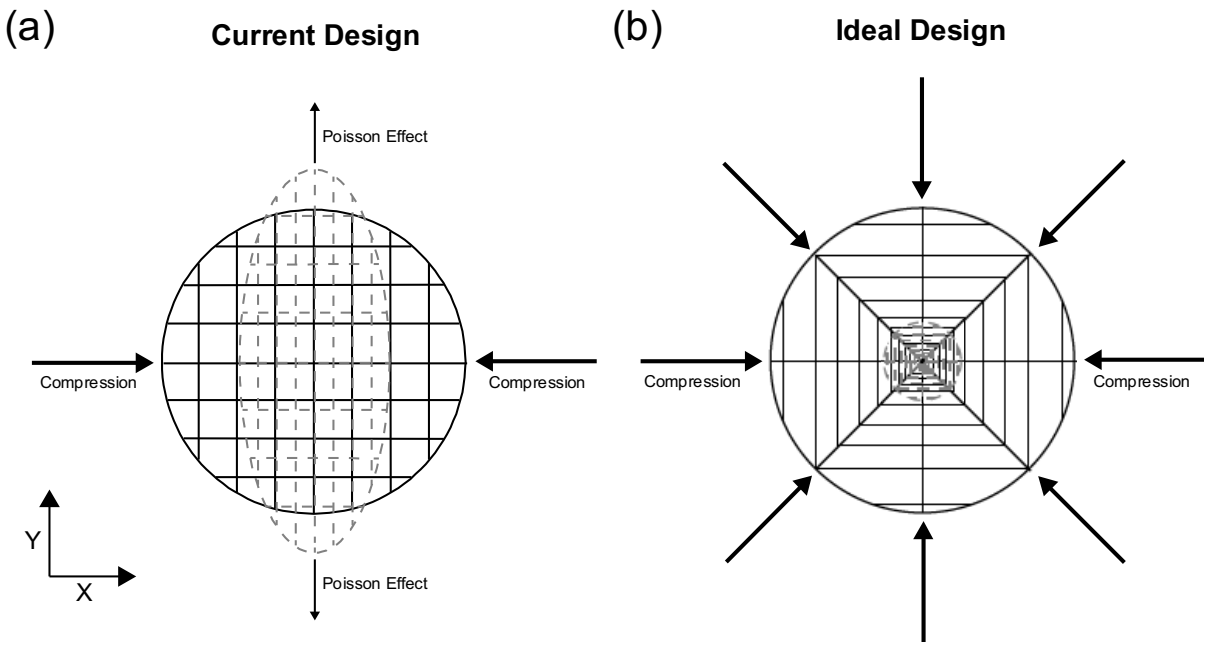


Figure 8-1. Compression patterns and their effects on the compressed foam geometry. Diagrams represent a cross-section of the 3DSMPs obtained using our leaching/3D-printing method. (a) represents the current infill design of the 3DSMP foams, and the dashed gray lines represent the compressed geometry exhibiting Poisson effect. (b) denotes an ideal design (not physically accurate) with a porosity gradient that allows compression to a circular cross sections (a rod-like geometry in 3D).

8.2.2 Biocompatibility and Immunogenicity of SMPs

Biocompatibility is a key property of biomaterial-based technology. Previously, other groups have demonstrated the biocompatibility of polyurethane with different formulations [49, 200-202]. However, in our group we have not tested the potential cytotoxicity of our pristine and/or PPy-coated 3DSMP foams. While our HDI:HPED:TEA formulation and PPy films have been demonstrated to be biocompatible with low immunogenicity [167, 202, 203], the combination of these two materials in our manufacturing process might induce potential cytotoxic behavior. Specifically, the results presented in Section 5.1.3 demonstrated that our current manufacturing process cannot get rid of $FeCl_3$ completely during the washout steps, which may induce unwanted cytotoxicity. In addition, preliminary experiments of cell culture with rat bone marrow stem cells (rBMSCs) have shown that our material has an acid behavior in cell media (observed as a yellow media coloration when cultured in phenol-red-rich media). Even with preconditioning of the material in phosphate-buffered saline (PBS) and in Dulbecco's Modified Eagle Medium (DMEM) for 24 h each, we observed a significant reduction in metabolic activity after 24 h using a PrestoBlue™ assay [204] (**Figure 8-2**). These preliminary results indicate a potential cytotoxicity induced by our pristine material and the manufacturing process. It is of paramount importance that future research is focused on investigating the surface chemistry of the material and its potential effects on cell viability.

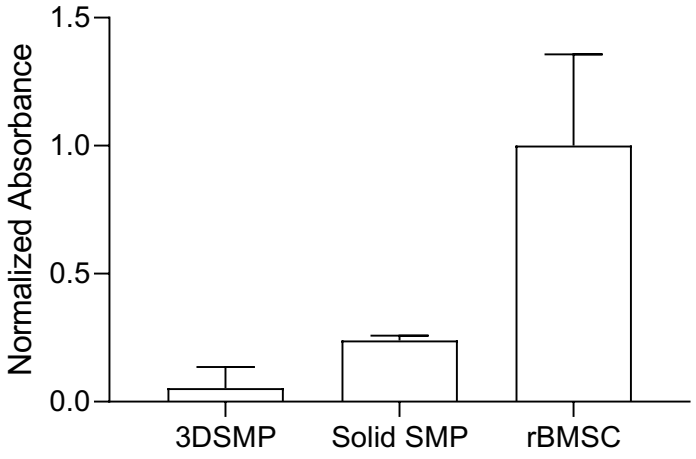


Figure 8-2. Comparison of the normalized absorbance of PrestoBlue assay on rBMSC cultured on 3DSMP, solid SMP or alone, as control ($n = 6$).

Further, traditional coiling techniques have also been designed to induce thrombogenesis using electrothrombosis (See Chapter 2). Induction of thrombogenesis using electrical currents has been described for centuries [205] and it is a fundamental feature of GDCs [3]. We also expect that the use of Joule-heating in our SMP-based device would induce the deposition of platelets and other blood cell populations on the surface of the material, especially with the voltage levels that our device utilizes, which are higher than the GDCs. However, modern endovascular devices do not aim at inducing electrothrombosis, as it has been described to not have a significant effect on complete occlusion rates [205]. Due to the great success of flow diverters inducing neoendothelization on the luminal surface of the device [188], exploring the potential of our SMP material to induce both electrothromboses and neoendothelization is a future route for research that should be addressed.

8.2.3 Mechanical & Microstructural Characterization of Arterial Tissues

The study of the mechanical properties of ICAs has been extensive over the years [206-208]. Our lab has also characterized the mechanics and load-dependent microstructural features of a human aneurysm [180] and developed methods for the characterization of regional mechanics of arterial tissues [209]. Learning about these features is paramount importance to build on the work performed by Ryan Bodlak [129] for the simulation of aneurysm hemodynamics and the simulation of foam delivery. For example, understanding the effect that elastin degradation on the microstructural and mechanical properties of the aneurysms obtained in our animal model could provide valuable information for the development of models that allow prediction of aneurysm stability/recurrence [210]. This type of assessment could be performed using the developed polarized spatial frequency domain (pSFDI) methods that have been described by our group [209, 211], in combination with multiphoton confocal microscopy (MPM) (**Figure 8-3**). See Appendix D for a method for the preparation of arterial tissues for MPM using optical clearing.

In addition, future simulation for foam delivery can also be informed by the mechanical characterizations of the forces that are exerted by the foam during shape recovery. For example, measurement of these forces has been characterized previously by Liu *et al*. [212] using dynamic mechanical analysis. These characterizations can be performed in future studies of our 3DSMP foams with custom infill designs and *patient-specific* geometries. By understanding these forces, the mechanical interactions between the 3DSMP foam and the arterial wall could be simulated and used as a method to predict potential device-induced aneurysm rupture or mass effect.

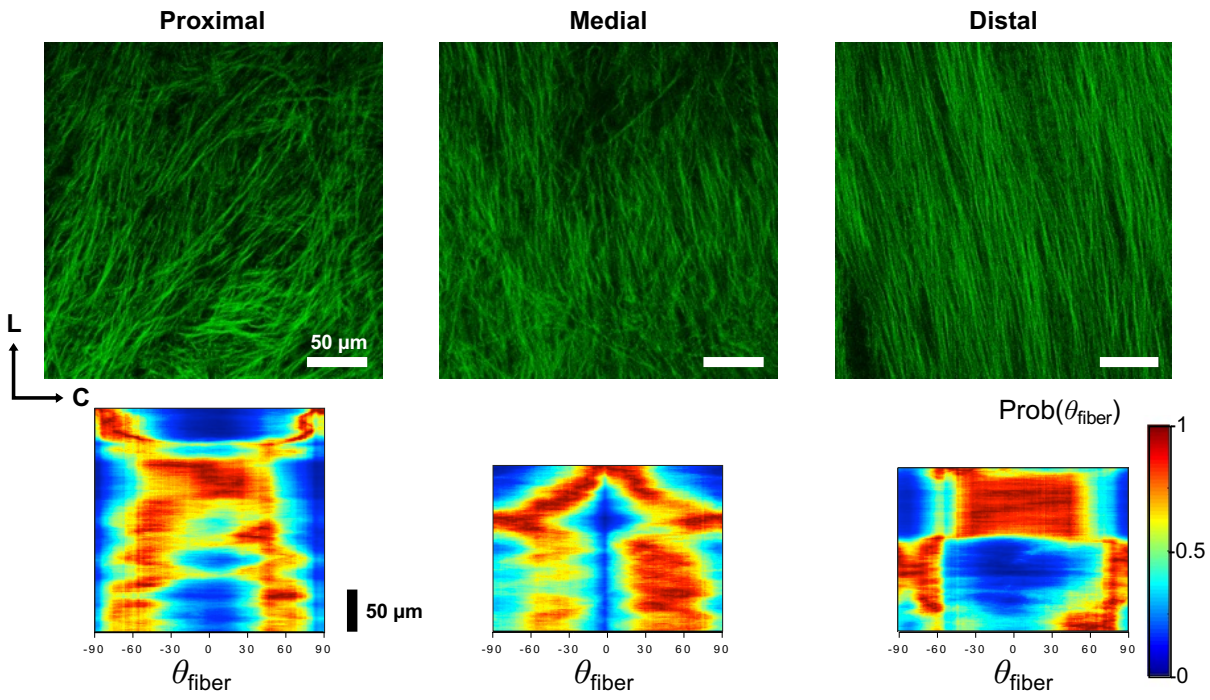


Figure 8-3. Representative specimens of our MPM microstructural assesssments of coronary artery tissues. Each representative autofluorescence micrograph represents a region of the left anterior descending artery and its collagen fiber architecture at the tunica adventitia. The arrows represent the longitudinal (L) and circumferential (C) directions of the tissue. Heatmaps represent the tissue-thickness-dependent fiber orientation probability. See Pineda-Castillo *et al*. [209] for more details on this study.

8.2.4 Scaling of SMP-based Endovascular Device Production

Having addressed the limitations and future directions presented in this chapter, we will be able to determine the time from aneurysm diagnosis to SMP-based endovascular device fabrication. With this information, we will be able to undergo optimization processes that reduce the fabrication time of our endovascular device, as well as determining the overall timeline for the application of the device. It is of paramount importance that future research is

performed on the optimization of our 3D-printing/leaching method to reduce synthesis times, the sterilization of the biomaterial and its preconditioning for implantation.

8.2.5 Pre-Clinical Studies

Finally, the animal model developed in Chapter 6 will be used to perform *in vivo* testing of our SMP-based device for two purposes: (i) assessment of *in vivo* toxicity/immunogenicity and overall safety, and (ii) evaluation of immediate complete occlusion effectiveness. These pre-clinical studies will provide fundamental information for the potential translation of the SMP-based device to the clinical setting.

APPENDIX A Nomenclature

Table A-1. List of abbreviations used throughout the dissertation.

Abbreviation	Definition
3D	Three dimensional
3DSMP	Three-dimensional shape memory polymer
ACA	Anterior cerebral artery
ACeA	Anteromedial central arteries
AChA	Anterior choroidal artery
ACommA	Anterior communicating artery
AICA	Anterior inferior cerebellar artery
ANOVA	Analysis of variance
ASA	Anterior spinal artery
ATR-FTIR	Attenuated total reflectance – Fourier transform IR spectroscopy
β–CDAlg	β–cyclodextrin–modified alginate
BA	Butylacrylate
BA	Basilar artery
BAC	Balloon-assisted coiling
BPC	Bare platinum coils
C4	Fourth cervical vertebra
CAD	Computer-aided design
CNS	Contour neurovascular system
CNT	carbon nanotubes
CSR	Cumulative stress reduction
CTA	Computerized tomography angiography
DETA-Alg	diethylenetriamine-modified alginate
DMSO	Dimethyl sulfoxide
DSC	Differential scanning calorimetry
DTGS	Doped triglycine sulfate
ECA	External carotid atery
FDA	Food and drug administration
FDM	Fused deposition modeling
FELM	Fixed effects logistic model
FRED	Flow-redirection endoluminal device
FU	Follow-up
GDCs	Guglielmi detachable coils
GREAT	German-French randomized endovascular aneurysm trial

Table A-1. (*continued*) List of abbreviations used throughout the dissertation.

HDI	Hexamethylene diisocyanate
HELPS	HydroCoil endovascular aneurysm occlusion and packing study
HPED	N,N,N0,N0-tetrakis (hydroxypropyl) ethylenediamine
IAA	Internal auditory artery
ICA	Intracranial aneurysm
ICaA	Internal carotid artery
I/E	Inclusion/exclusion
IR	Infrared
IRB	Institutional Review Board
ISAT	International Subarachnoid Aneurysm Trial
LCCA	Left common carotid artery
LGLMM	Logistic generalized linear mixed model
MCA	Middle cerebral artery
MCT	Mercury cadmium telluride
MCU	Microcontroller
OR	Odds ratio
PA	Pontine arteries
PCA	Posterior cerebral artery
PCeA	Posteromedial central arteries
PCL	Polycaprolactone
PCO	Polycyclooctene
PCommA	Posterior communicating artery
PEG	Polyethylene glycol
PEGDMA	Polyethylene glycol dimethacrylate
PICA	Posterior inferior cerebellar artery
PLA	Polylactic acid
POR	Porogen
PPy	Polypyrrole
PRET	Prone to recurrence after endovascular treatment trial
PRISMA	Preferred reporting items for systematic reviews and meta-analyses
PU	Polyurethane
PVA	polyvinyl alcohol
PWM	Pulse width modulation
RCCA	Right common carotid artery
RROC	Raymond-Roy occlusion classification
SAC	Stent-assisted coiling

Table A-1. (*continued*) List of abbreviations used throughout the dissertation.

SAH	Subarachnoid hemorrhage
SCA	Superior cerebral artery
SEM	Scanning electron microscopy
SMP	Shape memory polymer
T	Temperature
T_g	Glass transition temperature
T_{trans}	Transition temperature
TEA	Triethanolamine
UV	Ultraviolet
VA	Vertebral arteries
VA	Vertebral artery
WEB	Woven EndoBridge
WNBIA	Wide-necked bifurcation intracranial aneurysm

APPENDIX B Synthesis of Patient-Specific Shape Memory Polymers Using a Leaching/3D-Printing Method

Goal: To fabricate porous 3D-printed SMP foams with geometries that can be used for material characterization experiments and patient-specific embolization. A method for the fabrication of patient-specific aneurysm models is also described.

Materials:

3D-Printing of Templates

- Polyvinyl alcohol (PVA) Filament (Sigma Aldrich AtlasSupport #901034)
- .STL file with custom geometry
- Desiccator

SMP Foam Synthesis

- Monomers:
    - Hexamethylene diisocyanate (HDI)
    - Triethanolamine
    - N,N,N0,N0-tetrakis (hydroxypropyl) ethylenediamine (HPED)
- Plastic cup
- Beaker
- Magnetic bar
- Pipette controller
- Pasteur pipette
- Sonicator
- Vacuum container

- Vacuum pump for vacuum container
- Paper towels
- Glass bar
- Weigh boat
- Plastic dropper pipette
- Kimwipes
- Pocket scale
- Freezer (–20°C)

Patient-Specific Phantom Fabrication:

- PVA Filament
- .STL file with aneurysm geometry
- Sylgard 184 kit (Polydimethylsiloxane – PDMS).
- Balance
- Weigh boat
- Stirring rod

Procedure:

3D-Printing of Templates

1. Remove the microSD card from the printer and insert into a slicing computer.
2. Slice the CAD geometry to be printed using Cura. In most cases, the "material characterization mold" (i.e., a standardized cube) will be used for PVA 3D-printing. Make sure to use the most current version of the printing profile ("Sigma Calibration Mech Molds_12-5-22").

3. Save the resulting GCode to the microSD card from the printer.
4. Insert the microSD card into the printer (Creality CR-10s). Turn the printer on. Preheat the hot end and build plate. On the printer interface screen:
    a. Select Control > Nozzle Temperature > 200°C.
    b. Select Control > Build Plate Temperature -> 60°C.
5. Alternatively:
    a. Select Prepare > Preheat PLA (same preset temperatures as in step 4).
6. Insert the filament end into the extruder.
    a. Cut the filament end at an angle for an easier insertion.
7. Print the GCode. On the printer interface screen:
    a. Select print from SD card > Select filename.
8. Once the print is complete, remove the filament from the extruder and place the filament back into a vacuum container for storage.[1]
    a. Do this before the hot end cools down so no filament is left in the nozzle.

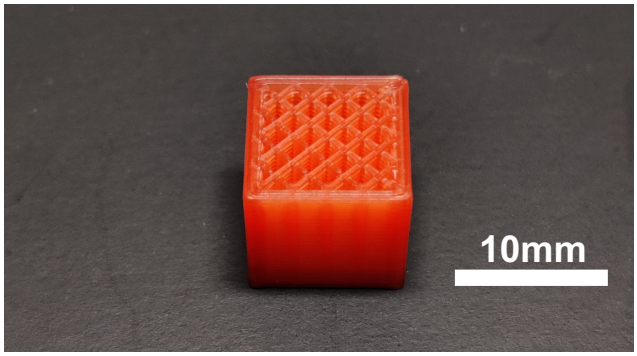


Figure B-1. Photograph of a PVA template with a 50% grid infill density.

9. Wait for the build plate to cool down. Use the scrapper to gently remove the printed

[1] PVA filaments are moisture sensitive and improper storage can lead to unstable and inconsistent prints.

model from the build plate.

a. The PVA may still stick to the build plate after cooling but be careful to not damage the print during removal.

10. Turn off the printer.
11. Store print in the desiccator.

SMP Solution Synthesis

12. Wear a respirator with filters for solvents.[2] Follow manufacturer instructions for the safe use of the respirator. Wear nitrile gloves.
13. Prepare workspace:
    a. Prepare the vacuum container by placing a paper towel inside. Place open container next to the vacuum pump.
    b. Place the 3D printed templates in a weigh boat next to the vacuum container.
    c. If preparing a solid specimen for DSC, place it next to the weigh boat.
    d. Check that there is enough space in the -20°C freezer to store the vacuum container.
    e. Open vacuum bags containing the three monomers and place the bottles inside of the glovebox.
    f. Place the following elements in the glovebox: plastic cup, pipette controller with a Pasteur pipette on, beaker, magnetic bar, glass bar, plastic dropper pipette. Kimwipes, pocket scale and magnetic stirrer should be always stored inside of the glovebox. Close the glovebox.
    g. Check that nitrogen tank is not empty. Close the oven valve, open the glovebox

[2] It is recommended to use a 3M respirator and 3M P100 Respirator Cartridge/Filter 60926.

valve

h. Double check that all tools are ready to be used, and organize tools.

14. Start nitrogen flow by opening the tank valve and regulator. Low nitrogen pressures (<5 psi) are enough for proper synthesis.
15. The following steps will describe monomer mixture. Follow monomer weighing order as instructed to prevent unwanted polymerization:
    a. Place the glass beaker containing the magnetic bar on the pocket scale.
    b. Turn on the pocket scale and tare using the glass bar.
    c. Pour HPED directly from the bottle to the beaker. HPED is very viscous and pours slowly. Make sure to pour directly to the bottom of the beaker and not on the beaker walls, as this can make mass measurements inaccurate and prevent HPED from getting in good contact with the other monomers. Due to its high viscosity, it can be hard to stop pouring HPED to the beaker timely. To help this, keep the glass bar at hand to cut the HPED filament.
    d. Use Kimwipes to clean the glass bar and bottle when finished.
    e. Set the beaker aside.
    f. Place the plastic cup on the scale. Tare.
    g. Open the HDI bottle and prepare the pipette controller and Pasteur pipette.
    h. HDI has a viscosity similar to water, so it can be pipetted easily; be careful not to pipette above the pipette constriction to prevent HDI from entering the controller and blocking the filter. Pipette the required amount of HDI into the plastic cup. When finished, unused HDI in the pipette must be thrown out and not returned to the bottle. Use an additional plastic cup to contain it. Throw

away the Pasteur pipette.

i. Place the plastic cup aside. Keep HDI and HPED apart from each other.

j. Return the beaker to scale. Tare.

k. TEA has a viscosity similar to glycerin, which can make the use of the pipette controller difficult. Use plastic dropper pipette to transport TEA into beaker with HPED. Due to the viscosity of TEA, pouring from the bottle should be avoided as it is easy to go over the required amount.

l. Place the beaker containing HPED and TEA (catalyzer and soft segment) on the magnetic stirrer.

m. Prepare a timer.

n. Prepare to turn on the magnetic stirrer. Pour HDI (hard segment) from the plastic cup to the beaker and start stirring.

o. Start the timer.

p. Watch the HDI, HPED and TEA mixing together. The solution will have a milky appearance at first. When TEA is exhausted, the solution will become completely transparent.

q. Stop the timer when solution becomes transparent. Polymerization time will depend on the TEA concentration, as well as the glass transition temperature (See Kunkel *et al*. 2018). For solutions with a higher concentration of HPED, it is a good practice to leave solution on magnetic stirrer for a longer period to help HPED to mix homogenously. Keep the solution stirring and decrease and increase rotational speed of the magnetic bar cyclically to break down clogs of HPED. Once the solution appears completely transparent and HPED is

completely dissolved, move to the next step.

r. Keep the solution stirring. Close nitrogen tank and open glove box.

16. Remove the SMP solution from the glove box and transport to the fume hood.
17. Pour the SMP solution over template. For solid specimens, pour a few drops of the solution in a rectangular silicon rubber mold. For 3DSMP foams, pour the solution over the PVA templates (make sure they are contained in a weigh boat).

Curing of Solid Specimens

18. Transport the silicon rubber mold to the vacuum oven immediately.
19. Close the glove box nitrogen valve and open the vacuum oven valve. Open the nitrogen tank and regulator. Nitrogen should NOT flow continuously, as the oven should be airtight and the purge valve should be closed.
20. Open the vacuum pump valve of the vacuum oven.
21. Turn on the vacuum pump. Allow negative pressure to reach roughly –0.8psi.
22. Turn off the vacuum pump. Then, close the vacuum pump valve of the vacuum oven.[3]
23. Wait for 2 min.
24. Open the purge valve to let nitrogen flow into the chamber. You should hear nitrogen hissing. Close purge valve when pressure reaches about –0.2psi.
25. Wait for 2 min.
26. Open the vacuum pump valve and turn on vacuum pump. Allow negative pressure to reach –0.8psi.
27. Turn off the vacuum pump. Then, close the vacuum pump valve of the vacuum oven.

[3] NEVER start vacuum pump without opening the vacuum pump valve. This could damage the pump and/or the oven.

28. Wait for 2 min.
29. Repeat steps 13 to 17 at least three times at room temperature.
30. Start a curing program that follows these thermal steps sequentially:
    a. 3 hours at 45°C.[4]
    b. 1 hour at 70°C.
    c. 1 hour at 100°C.

Curing of 3DSMP specimens (starting from step 6)

31. Place the weigh boat containing the 3D printed PVA templates and liquid SMP solution in the vacuum container.
32. Close the vacuum container and use the vacuum pump to remove air from the container. Bubble on the lid should flip upside down to indicate adequate negative pressure.
33. Transport the vacuum container to –20 °C freezer.
34. Wait for at least 1 h to allow full infiltration of SMP solution into the PVA templates. The templates and uncured solution can stay in the freezer for up to 24 h (low temperatures slow down polymerization). Do not leave in the freezer for longer than 24 h.
35. Take the vacuum container out of the freezer. Press the purging button to allow pressure regulation inside of the container. Remove the lid and take the weigh boat out of the container.
36. The solution should be viscous and clear. Solidification of the solution can be an indicator of unwanted curing due to the presence of oxygen in the container.
37. Move the PVA templates to a sheet of aluminum foil. Pour the SMP solution over the

[4] During this time, vacuuming and purging steps (13-17) can be repeated in case bubbles emerge.

templates to maximize use of the solution.

38. Move the sheet of foil to the oven.
39. Start a curing program that follows these thermal steps sequentially:
    a. 3 hours at 45°C.
    b. 1 hour at 70°C.
    c. 1 hour at 100°C.
40. Remove the foil from the oven. The cured SMP should form a transparent film on the foil and a "mushroom" on top of the PVA templates:

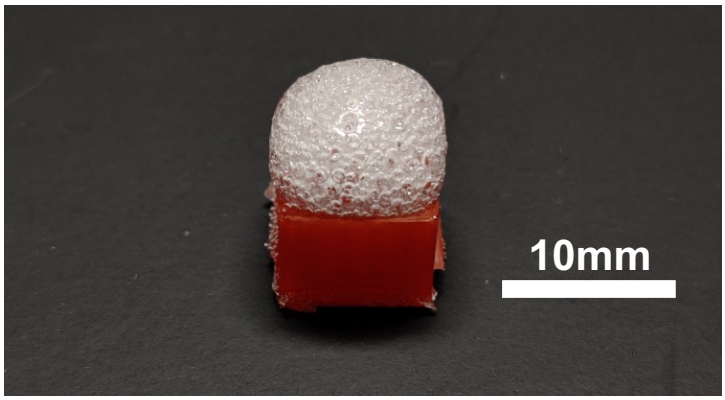


Figure B-2. Photograph of a representative specimen of a PVA template infiltrated with cured SMP solution. The bulging of the SMP on the top surface (referred to as "SMP mushroom" internally) of the PVA template demonstrates proper curing.

41. Remove the solid SMP surrounding the template. When using SMP monomer ratios with a higher T_g (>45 °C), the SMP film on the surface of the foil can be hard to break. Use pliers and/or wire cutters to remove the SMP. Make sure that everyone in the lab wears goggles, as pieces of solid SMP can fly away from the templates and cause eye damage.
42. Place the 3DSMP/PVA product in a plastic cup and fill with DI water.

43. Fill the sonicator tank up to the fill line using DI water. Place the plastic cup with a lid on in the tank.
44. Press the "*Sonic*" button on the sonicator screen. Ultrasonic waves will promote PVA dissolution.
45. Press the "*Heat*" on the sonicator screen. Heat will facilitate PVA dissolution. Make sure that heating temperature is set to the maximum provided by the device (59 °C).
46. Change water in the cup every hour until the solution remains transparent after sonication. A batch of 5 foams per cup should take from 12-24 h to be completely washout of PVA.
47. Dry the foams using paper towels.
48. Place foams on aluminum foil and dry in the vacuum oven at 60°C for 12 h. Vacuum up to -0.4psi and purge with nitrogen during drying.
49. Place the foams on a Ziplock bag with a label that allows to identify monomer ratio, synthesis date, infill density, and other important information.
50. Place the bag containing foams in a desiccator to preserve shape memory properties.

Fabrication of Patient-Specific Aneurysm Phantoms

1. Print the aneurysm geometry using PVA filaments.
2. Prepare PDMS solution:
    a. Place the weigh boat on the scale. Tare.
    b. Pour the uncured PDMS solution on the weigh boat. Use as much PDMS as needed to fill the PVA aneurysm template.
    c. Record total PDMS weight.

d. Tare.

e. Add PDMS catalyst to the solution in a 1:10 ratio (i.e. 10% of total weight of step 2.c).

3. Remove weigh boat containing the PDMS solution from the balance. Mix vigorously.
4. Place the weigh boat in the vacuum oven.
5. Make sure that nitrogen tanks are closed.
6. Open the glove box and vacuum oven valves.
7. Open the vacuum pump valve.
8. Turn on the vacuum pump. Allow negative pressure to reach –0.8psi.
9. Turn off the vacuum pump. Then, close the vacuum pump valve of the vacuum oven.[5]
10. Wait for 2 min.
11. Open the purge valve to let air flow into the chamber. Close the purge valve when pressure reaches –0.2psi.
12. Wait for 2 min.
13. Repeat steps 7-12 three times. In the last repetition, let the chamber reach ambient pressure and open the oven.
14. Remove the weigh boat for the oven. The PDMS solution should be covered in bubbles. Mechanically burst all the bubbles using tweezers or a metal rod.
15. Return the weigh boat to the vacuum oven.
16. Repeat steps 7-15 as many times as needed until the solution is completely clear and bubble-free. Typically, 3-5 repetitions are required, but this number can vary depending on the amount of solution being synthesized.

[5] NEVER start vacuum pump without opening the vacuum pump valve. This could damage the pump and/or the oven.

17. Pour the PDMS solution on the PVA template.
18. Place the PVA template filled with PDMS solution in the oven. Repeat steps 7-15 if bubbles have emerged.
19. Cure PDMS at 70°C for 1 h.
20. Take the cured PDMS models from the oven and place them in a plastic cup. Place the cup in the sonicator.
21. Press the “sonic” and “heat” buttons on the sonicator screen to start PVA dissolution. Change water periodically until PVA is completely dissolved. The walls of the PVA template will dissolve fast, but the aneurysm geometry typically requires several water changes. The number of water changes will depend on the geometry and size of the PVA template.
22. Once all PVA is dissolved, dry the PDMS phantoms in the oven at 60°C.

APPENDIX C PPy-Coating

Goal: To obtain conductive SMP foams by coating with Polypyrrole. This procedure uses *in situ* polymerization of pyrrole.

Materials:

- Reagents:
    - Pyrrole (Sigma Aldrich #31709)
    - Ferric chloride (Sigma Aldrich #157740)
    - Isopropanol (Sigma Aldrich # 190764)
- 3DSMP foams ready for testing
- Plastic cup with a lid
- Beakers
- Strainer 3D-printed piece
- Respirator with filters for organic solvents
- Goggles
- White coat

Procedure:

Adaptation of the method by Zhang *et al*. [56]:

1. Wear a respirator, a white coat, and goggles for the complete duration of this procedure.
2. While in the fume hood, prepare $FeCL_3$ solution by weighing $FeCl_3$ to reach a concentration of 5-15% w/v in isopropanol.
3. Immerse the 3DSMP foam specimens in $FeCl_3$ solution for 10 min.
4. Air dry the specimens at room temperature for 30 min.

5. Place the specimen above a beaker containing pyrrole (do not immerse).
    a. Perform this procedure for the established time on each side of the specimen (films, two faces; cubic foams, 6 faces).
    b. Let the pyrrole evaporate and complete polymerization at -20°C or room temperature for 2 h.
6. Rinse the specimens in deionized water for 1 min to remove $FeCl_3$.
7. Air dry the specimen and keep in desiccator with silica gel.

APPENDIX D Label-Free Microstructural Characterization of Arterial Tissues Using Optical Clearing and Multiphoton Microscopy

Goal: To obtain optically clear/transparent soft tissues for confocal microscopy or advanced microscopy techniques, such as multiphoton and second-harmonic generation microscopy.

Materials:

- Soft tissue: typically, this will be a tissue that has been biaxially tested or another tissue of interest (i.e. heart valves, arteries, etc.)
- Reagents:
    - Ethanol
    - PBS
    - Formalin (check paraformaldehyde concentration: this is for fixing. Typically, we fix tissues for histology, we have observed better results for imaging using autofluorescence when tissue is not fixed)
    - Benzyl benzoate (Sigma Aldrich #B6630)
    - Benzyl alcohol (Sigma Aldrich #402834)
- Plastic cup
- Pipette controller
- Pasteur pipette

Procedure:

Ethanol dehydration

1. Prepare tissue by using dissecting protocols. This procedure uses a coronary artery as an example. For a dissecting method description refer to Pineda-Castillo *et al*. (2022) [209].

2. Prepare a complete coronary artery tissue in its original tubular geometry.
3. Optional: if the fixing[6] of the tissue is necessary, follow these steps:
    a. Use a blunt needle to go inside the artery. Slide it the artery along the needle until the complete artery covers the needle.
    b. Immerse the specimen in formalin for 30 min.
    c. Remove tissue from formalin and slide it off from the needle.
4. Immerse the prepared tissue in PBS for 3 h. This step is fundamental for proper imaging.
5. Prepare a series of solutions of ethanol in PBS in different containers:
    a. 50% v/v Ethanol/PBS
    b. 75% v/v Ethanol/PBS
    c. 100% Ethanol.
    d. 100% Ethanol.
6. Immerse the tissue for 30 min in each ethanol solution sequentially from step 5a to 5d.
7. Tissues can be stored in 100% ethanol before starting step 8.

Tissue Clearing

8. Prepare a 1:2 benzyl alcohol (BA) to benzyl benzoate (BB) solution. This solution will be referred to as 100% BABB.
9. Prepare the following solutions and immerse the tissue for 30 min in each:
    a. 1:1 ethanol:BABB.
    b. 1:1 ethanol:BABB.
    c. 100% BABB.

[6] Only perform if needed for study design.

d. 100% BABB.

10. The specimen will become completely cleared during the last solution of step 9, as seen in **Figure D-1**.

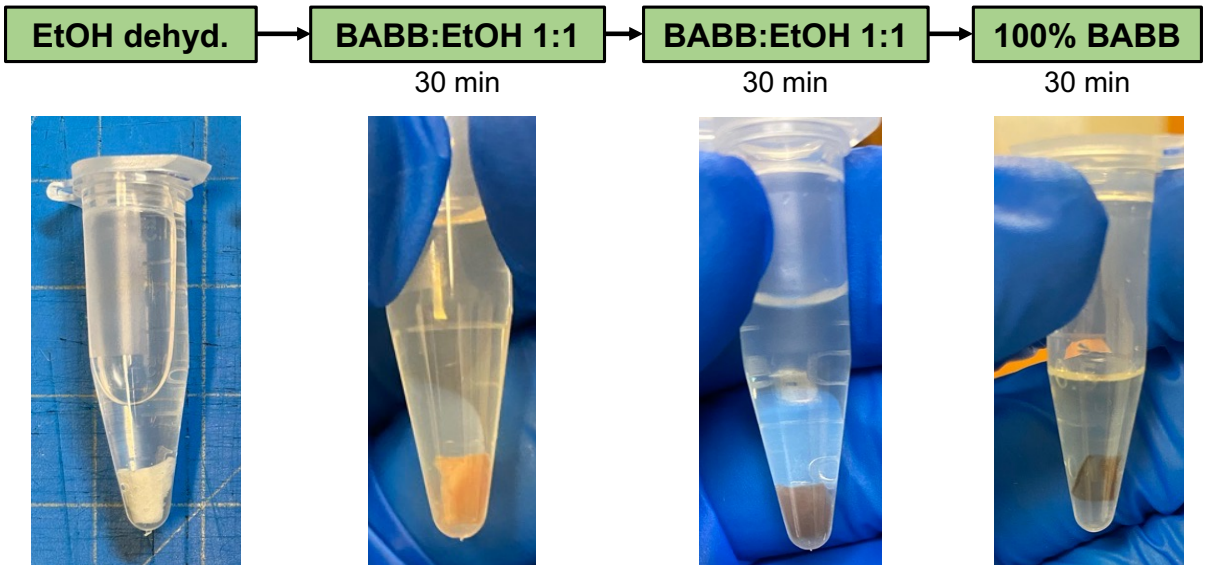


Figure D-1. Photographs of coronary artery tissues in a falcon tube containing the clearining solutions and their effect in the resultant optically-cleared tissue.

11. Mount the specimen on a glass slide using double sided tape:
    a. Place the strips of double-sided tape, one over the other, on a cutting board.
    b. Cut a small square at the center of the double-sided tape stack and remove it to create a “window”.
    c. Remove the tape stack from the cutting board and place it on a clean glass slide.
    d. Make sure that the stack is bubble free and that there is no space between the glass slide and the stack. Any unwanted channels will lead to BABB leakage, washout of the glue on the tape and ultimate unmounting of the tissue. This is also a risk for BABB dripping on the platform of the microscope.

e. Place the cleared tissue in the created reservoir (**Figure D–1a**). For arterial tissues, place the tissue with the adventitia facing down (i.e. in contact with the glass slide).

f. Pour 1-2 drops of BABB in the created reservoir, over the tissue. 1-2 drops should create a bigger drop over the tissue that is maintained within the boundaries of the reservoir by the surface tension of the solution.

g. Use the coverslip to seal the reservoir. Do this step in a swift manner to prevent leakage of the BBAB solution. Hold the coverslip and press against the tape firmly but avoiding the edges or center of the slip to prevent it from breaking. This step is fundamental to maintain BABB solution inside the reservoir. If sealed properly, the specimen can be preserved in the slide for up to two weeks.

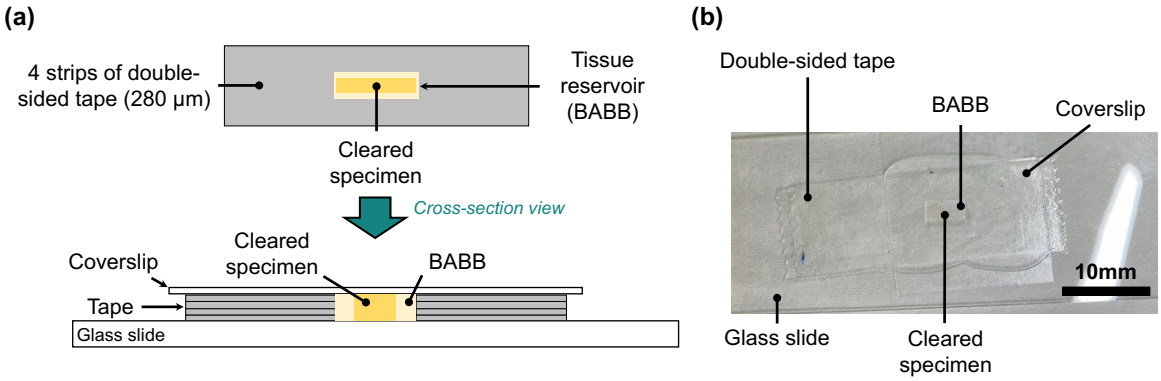


Figure D-2. (a) Diagram representing the top and cross-sectional view of the mounting of a cleared specimen on a glass slide using double sided tape to build a BABB reservoir. (b) Photograph of a cleared specimen mounted on a glass slide.

APPENDIX E Meta-Analysis Protocol

This document documents all applicable information required for the design of the meta-analysis. It includes documents required for the planning and design of the study, research questions, keywords for systematic search, plan for paper screening, plan for data collection, analysis, etc.

Reading Material for Guidance on Meta-Analysis Design

"*A Step-By-Step Guide for Conducting A Systematic Review and Meta-Analysis with Simulation Data"* by Tawfik *et al*. (2019). [182]

"*Cochrane Handbook for Systematic Reviews of Interventions*" by Cochrane (2008). [184]

"*Preferred Reporting Items for Systematic Reviews and Meta-Analyses: The PRISMA Statement*" by Moher *et al*. (2009). [183]

Steps of the Meta-Analysis

1. Formulate research question, intervention and stablish target population/characteristics.
2. Perform preliminary search to ensure that the study has not been performed previously.
3. Design inclusion/exclusion (I/E) criteria.
4. Design search strategy (queries, databases to be used).
5. Plan data extraction and analysis pipeline.
6. Review research question and I/E criteria with PI and collaborators.
7. Update/write protocol for the study.
8. Perform study search (following the plan designed in step 4).
9. Report number of extracted studies.
10. Title & Abstract screening (2-3 reviewers, trained undergraduate researchers, in our

case).

11. Report the number of texts selected for full reading.
12. Download and screen the full texts.
13. Manually search and include studies that might be relevant but did not come up in the search.
14. Data extraction.
15. Data check.
16. Statistical analysis.
17. Manuscript writing.

Research Question

Research questions should be formulated using the PICO (Population, Intervention, Comparison, Outcome) tool. Example: "*How is the safety and immunogenicity of Ebola vaccine in human?"*

Question: What is the long-term effectiveness and aneurysm recurrence risk of modern endovascular therapy devices in the occlusion of intracranial bifurcation saccular aneurysms?

Population: humans with intracranial bifurcation saccular aneurysms.

Intervention: endovascular therapy.

Comparison: endovascular device occlusion effectiveness.

Outcome: long-term occlusion rates – Raymond-Roy Occlusion Classification (RROC).

I/E Criteria

Inclusion:

1. Date range: 2000-2022.
2. Clinical trials testing the occlusion effectiveness of endovascular devices (concentric coils, flow diverters, hydrogel-coated coils, WEB device, balloons, liquid embolic device) for the first line of treatment for unruptured intracranial saccular aneurysms.
3. At least 10 patients of 18 years of age and older.
4. Report of rupture status of treated aneurysm.
5. Report of risk factors (smoking habits, hypertension).
6. Report of region (Americas, Asia, Europe, Africa, etc).
7. Report of patient demographics (sex, age, etc.).
8. Report of aneurysms characteristics (size, shape, location, parent artery).
9. Report of a post-operatory follow-up (longitudinal designs) reporting occlusion degree, fatality, reoperation.
10. Report of recurrence rates.
11. Include crude or adjusted effect estimates with corresponding 95% CIs or mean +/- SD for risk factors of clinical complications available or retrievable from the data.

Exclusion:

1. Language different to: English, Spanish, Italian, French, German, Dutch, Portuguese.
2. Duplicates.
3. Unrelated articles.
4. Abstract-only OR clinical protocol papers.
5. Case studies.

6. Unavailable papers.
7. Animal studies.
8. Studies where the occlusion degree of aneurysms is not measured OR it is measured with classifications that cannot be translated to RROC.
9. Studies where target aneurysms are trauma-induced, or pseudoaneurysms.
10. Studies where target aneurysms are mycotic or pathogen-induced aneurysms.
11. Studies where target aneurysms are of fusiform, lobular (sac within main sac), dissecting OR other non-saccular geometries.
12. Studies with target aneurysms associated with arterial malformations (such as collagen disorders, Moyamoya disease or syndrome, dwarfism, or autoimmune disorders).
13. Studies where the reported outcome (RROC) is not distinguished between ruptured and unruptured aneurysms, OR the study targets ruptured-only aneurysms.

Search Strategy

Database search will be performed in PubMed first with the following search conditions:

- ("aneurysm"[TiAb] OR “intracranial aneurysm”[MeSH] OR "aneurysms"[TiAb])
- AND ("unruptured"[TiAb] OR "incidental"[TiAb])
- AND ("endovascular"[TiAb] OR "surgically "[TiAb] OR "surgical"[TiAb] OR "treatment"[TiAb] OR "treated"[TiAb] OR "management"[TiAb] OR "repair"[TiAb] OR "coiling"[TiAb] OR “endovascular procedure”[MeSH] OR “neurosurgical procedure”[MeSH] OR "coil"[TiAb] OR "coils"[TiAb] OR "flow-diverter"[TiAb] OR "embolization"[TiAb] OR "occlusion"[TiAb] OR "surgery"[TiAb] OR "preventive"[TiAb] OR "prevention"[TiAb] OR "procedure"[TiAb] OR "hydrogel"[TiAb] OR "liquid"[TiAb] OR "liquid-embolic"[TiAb] OR "WEB"[TiAb]

OR "Woven EndoBridge"[TiAb] OR "GDC"[TiAb])

- AND ("risk"[TiAb] OR "outcome"[TiAb] OR "Raymond-Roy"[TiAb] OR "degree"[TiAb])
- Then, search will be performed in Cochrane with the following search conditions:
- ("aneurysm" OR “intracranial aneurysm” OR "aneurysms") AND ("unruptured" OR "incidental") AND ("endovascular" OR "surgically " OR "surgical" OR "treatment" OR "treated" OR "management" OR "repair" OR "coiling" OR “endovascular procedure” OR “neurosurgical procedure” OR "coil" OR "coils" OR "flow-diverter" OR "embolization" OR "occlusion" OR "surgery" OR "preventive" OR "prevention" OR "procedure" OR "hydrogel" OR "liquid" OR "liquid-embolic" OR "WEB" OR "Woven EndoBridge" OR "GDC") AND ("risk" OR "outcome" OR "Raymond-Roy" OR "degree").

This conditional query covers all applicable key words we expect to observe in the selected studies.

Then, search will be complemented with 3 additional databases:

- Cochrane.
- ClinicalTrials.gov.
- Web of Science.

Search results will be stored in an EndNote library that will be designated for this study only. EndNote will be used to remove duplicates from PubMed results. Results will be exported to an Excel sheet.

Title and Abstract Screening

Reviewers will use the Excel Sheet obtained during search to screen titles and abstracts. They will decide if studies should be included or not in the analysis based on the previously defined I/E criteria. This process will be performed independently by 2-3 reviewers, who will not discuss their inclusion/exclusion decisions amongst each other. If there are doubts in the inclusion/exclusion of a study, consultation should be made with the head reviewer (PhD candidate, in our group). The head reviewer will train reviewers to build their judgement on study selection; however, head reviewer will not perform title/abstract screening. Once title/abstract screening is finalized by all reviewers, they will submit their Excel sheets to the head reviewer.

Full-text Downloading

Screening Excel sheets will be summarized by the head reviewer to download ALL included studies by ALL reviewers. Articles will be downloaded through OU Libraries system. The head reviewer will use I/E criteria to verify that selected articles by the reviewers can be included in the analysis. Once screened, full texts will be stored in a shared folder. Then, a manual search of studies that fulfill I/E criteria will be performed to ensure that all applicable studies are included and reduce bias.

Data Extraction

Data will be extracted by the head reviewer using the Extraction Spreadsheet. The extracted data will be listed for each study and will include:

- Enrollment period (start and end of study).
- Study population size (n number).
- Follow-up period(s).

- Outcome assessment (RROC or other equivalent scale).
- Patient demographics (mean/median age cohorts, sex distribution,).
- Aneurysm characteristics (size [maximum dome diameter], location/parent artery).
- Treatment characteristics (endovascular device, assisting devices)

APPENDIX F Meta-Analysis: List of Included Studies

Table F-1. List of the studies included in the meta-analysis after the screening process.

First Author Last Name	Year	Journal	Title
Abdelkhalek	2022	Neurological Sciences	Predictors of flow diverter stent in large and giant unruptured intracranial aneurysms, single-center experience
Aguilar-Salinas	2019	Cureus	Safety and efficacy of stent-assisted coiling in the treatment of unruptured widenecked intracranial aneurysms: A single center experience
Al-Schameri	2021	Acta Neurochirurgica	Microsurgical and endovascular treatment of unruptured cerebral aneurysms by European hybrid neurosurgeons to balance surgical skills and medical staff management
Baek	2019	British Journal of Neurosurgery	Initial multicentre experience using the neuroform atlas stent for the treatment of un-ruptured saccular cerebral aneurysms
Bhogal	2017	Journal of Neurointerventional Surgery	Use of flow diverters in the treatment of unruptured saccular aneurysms of the anterior cerebral artery
Bhogal	2019	Clinical Neurodiology	Treatment of unruptured, tandem aneurysms of the ICA with a single flow diverter
Bhogal	2018	World Neurosurgery	The use of flow diversion in vessels 2.5 mm in diameter: A single-center experience
Bhogal	2018	Clinical Neuroradiology	Management of unruptured saccular aneurysms of the M1 segment with flow diversion
Biondi	2022	Journal of Neurointerventional Surgery	Endosaccular flow disruption with the contour neurovascular system: angiographic and clinical results in a single-center study of 60 unruptured intracranial aneurysms
Cagnazzo	2020	Journal of Neurointerventional Surgery	Flow modification on the internal carotid artery bifurcation region and A1 segment after M1-internal carotid artery flow diverter deployment
Celik	2022	Nature Scientific Reports	Comparison of angiographic outcomes and complication rates of WEB embolization and coiling for treatment of unruptured basilar tip aneurysms
Chalouhi	2014	Stroke	Extending the indications of flow diversion to small, unruptured, saccular aneurysms of the anterior circulation
Chalouhi	2013	Stroke	Comparison of flow diversion and coiling in large unruptured intracranial saccular aneurysms
Cho	2014	Clinical Neuroradiology	Single-stage coil embolization of multiple intracranial aneurysms: Technical feasibility and clinical outcomes
Chung	2015	Journal of Neurosurgery	Preliminary experience with self-expanding closed-cell stent placement in small arteries less than 2 mm in diameter for the treatment of intracranial aneurysms
Consoli	2014	Journal of Neurointerventional Surgery	Assisted coiling of saccular wide-necked unruptured intracranial aneurysms: Stent versus balloon

Table F-1. (*continued*) List of the studies included in the meta-analysis after the screening process.

First Author Last Name	Year	Journal	Title
D'Urso	2012	American Journal of Neuroradiology	Coiling for paraclinoid aneurysms: time to make way for flow diverters?
Dammann	2014	Neurosurgical Review	Outcome for unruptured middle cerebral artery aneurysm treatment: surgical and endovascular approach in a single center
De Leacy	2018	Journal of Neurointerventional Surgery	Wide-neck bifurcation aneurysms of the middle cerebral artery and basilar apex treated by endovascular techniques: A multicentre, core lab adjudicated study evaluating safety and durability of occlusion (BRANCH)
Di	2020	Journal of Clinical Neuroscience	Clinical and angiographic outcomes of stent-assisted coiling of paraclinoid aneurysms: Comparison of LVIS and Neuroform stents
DiMaria	2015	American Journal of Neuroradiology	Flow diversion versus standard endovascular techniques for the treatment of unruptured carotid-ophthalmic aneurysms
Diaz	2012	World Neurosurgery	Middle cerebral artery aneurysms: A single-center series comparing endovascular and surgical treatment
Feng	2022	Journal of the Chinese Medical Association	Flow-diverter stent to manage intracranial aneurysms: A single center experience
Fields	2011	Journal of Neurointerventional Surgery	Stent assisted coil embolization of unruptured middle cerebral artery aneurysms
Ge	2017	Interventional Neuroradiology	The role of endovascular treatment in unruptured basilar tip aneurysms
Ge	2022	Frontiers in Neurology	Endovascular treatment of large or giant basilar artery aneurysms using the pipeline embolization device: Complications and outcomes
Gerlach	2006	Journal of Neurology, Neurosurgery & Psychiatry	Treatment related morbidity of unruptured intracranial aneurysms: Results of a prospective single centre series with an interdisciplinary approach over a 6-year period
Sturiale	2022	Neurosurgical Review	Clipping versus coiling for treatment of middle cerebral artery aneurysms: A retrospective Italian multicenter experience
Suzuki	2022	Neurology Medical Chir	Comparison of pipeline embolization and coil embolization for the treatment of large unruptured paraclinoid aneurysms
Teranishi	2022	Neurology Medical Chir	Preliminary experience of the surpass streamline flow diverter for large and giant unruptured internal carotid artery aneurysms
Yan	2020	Interventional Neuroradiology	The use of single low-profile visualized intraluminal support stent-assisted coiling in the treatment of middle cerebral artery bifurcation unruptured wide-necked aneurysm
Gherasin	2015	Department of Interventional Neuroradiology	Endovascular treatment of wide-neck anterior communicating artery aneurysms using WEB-DL and WEB-SL: Short-term results in a multicenter study

Table F-1. (*continued*) List of the studies included in the meta-analysis after the screening process.

First Author Last Name	Year	Journal	Title
Goertz	2021	Neurosurgery	Woven Endobridge embolization versus microsurgical clipping for unruptured anterior circulation aneurysms: A propensity score analysis
Goertz	2019	World Neurosurgery	Extending the indication of Woven Endobridge (WEB) embolization to internal carotid artery aneurysms: A multicenter safety and feasibility study
Gordham	2011	Neurological Research	Stent-assisted aneurysm coil embolization: Safety and efficacy at a low-volume center
Greve	2021	Clinical Neuroradiology	Initial Raymond-Roy occlusion classification but not packing density defines risk for recurrence after aneurysm coiling
Haeren	2022	World Neurosurgery	Fast transition from open surgery to endovascular treatment of unruptured anterior communicating artery aneurysms – A retrospective analysis of 128 patients
Heo	2019	Korean Neurosurgery	Selective temporary stent-assisted coil embolization for intracranial wide-necked small aneurysms using solitaire AB retrievable stent
Hetts	2014	American Society of Neuroradiology	Stent-assisted coiling versus coiling alone in unruptured intracranial aneurysms in the matrix and platinum science trial: Safety, efficacy, and mid-term outcomes
Huang	2019	World Neurosurgery	Clipping versus coiling in the management of unruptured aneurysms with multiple risk factors
Hwang	2011	Journal of Neuroradiology	Endovascular treatment for unruptured intracranial aneurysms in elderly patients: Single-center report
Kabbasch	2019	Clin Neuroradiol	The barrel vascular reconstruction device: A retrospective, observational multicentric study
Kabbasch	2019	World Neurosurgery	Comparison of WEB embolization and coiling in unruptured intracranial aneurysms: Safety and efficacy based on a propensity score analysis
Khalid	2019	Acta Neurochirugica	Efficiency and complications of Woven Endobridge (WEB) devices for treatment of larger, complex intracranial aneurysms: A single-center experience
Kim	2022	Jounal of Cerebrovascular and Endovascular Neurosurgery	Y-stent-assisted coiling with Neuroform Atlas stents for wide-necked intracranial bifurcation aneurysms: A preliminary report
Kim	2021	Journal of Neuroradiology	Safety and efficacy of stent-assisted coiling of unruptured intracranial aneurysms using low-profile stents in small parent arteries
Kim	2016	British Medical Journal	Endovascular treatment of unruptured ophthalmic artery aneurysms: Clinical usefulness of the balloon occlusion test in predicting vision outcomes after coil embolization
Kocur	2019	Polish Journal of Radiology	Endovascular treatment of small (<5 mm) unruptured middle cerebral artery aneurysms
Kuhn	2018	Interventional Neuroradiology	Flow-diverter stents for endovascular management of non-fetal posterior communicating artery aneurysms-analysis on aneurysm occlusion, vessel patency, and patient outcome

Table F-1. (*continued*) List of the studies included in the meta-analysis after the screening process.

First Author Last Name	Year	Journal	Title
Kuhn	2016	British Medical Journal	Stent-assisted coil embolization of aneurysms with small parent vessels: Safety and efficacy analysis
Kumar	2019	World Neurosurgery	A retrospective analysis of treatment outcomes of 40 incidental cavernous carotid aneurysms
Kunert	2021	Nature Portfolio	Flow-diverting devices in the treatment of unruptured ophthalmic segment aneurysms at a mean clinical follow-up of 5 years
Kwon	2014	Acta Neurochirurgica	Endovascular coil embolization of unruptured intracranial aneurysms: A Korean multicenter study
Lee	2020	Journal of Cerebrovascular and Endovascular Neurosurgery	Endovascular coil embolization for unruptured intracranial aneurysms in patients over 80 years of age
Liu	2018	Journal of Neuroradiology	Parent artery reconstruction for large or giant cerebral aneurysms using the Tubridge flow diverter: A multicenter, randomized, controlled clinical trial (PARAT)
Lubicz	2013	Journal of Neuroradiology	WEB device for endovascular treatment of wide-neck bifurcation aneurysms
Lylyk	2019	Clinical Neuroradiology	Treatment of wide-necked bifurcation aneurysms: Initial results with the pCANvas neck bridging device
Moon	2020	Journal of Cerebrovascular and Endovascular Neurosurgery	Result of coiling versus clipping of unruptured anterior communicating artery aneurysms treated by a hybrid vascular neurosurgeon
Oh	2015	Clinical Neurology	Management strategy of surgical and endovascular treatment of unruptured paraclinoid aneurysms based on the location of aneurysms
Oishi	2015	Journal of Neurointerventional Surgery	Treatment results of endosaccular coil embolization of asymptomatic unruptured intracranial aneurysms in elderly patients
Oishi	2020	Journal of Clinical Neuroscience	Stent-assisted coil embolization of unruptured middle cerebral artery aneurysms using LVIS Jr. Stents
Oishi	2012	Journal of Neuroradiology	Endovascular therapy of 500 small asymptomatic unruptured intracranial aneurysms
Ozpeynirci	2019	Acta Neurochirugica	WEB-only treatment of ruptured and unruptured intracranial aneurysms: A retrospective analysis of 47 aneurysms
Park	2021	Korean Society of Radiology	Single center experience of the balloon-stent technique for the treatment of unruptured distal internal carotid artery aneurysms: Sharing a simple and reliable tip to use Scepter-Atlas combination
Petr	2016	Journal of Neuroradiology	Current trends and results of endovascular treatment of unruptured intracranial aneurysms at a single institution in the flow-diverter era

Table F-1. (*continued*) List of the studies included in the meta-analysis after the screening process.

First Author	Year	Journal	Title
Petrov	2021	Interventional Neuroradiology	Initial experience with the novel p64mw HPC flow diverter from a cohort study in unruptured anterior circulation aneurysms under dual antiplatelet medication
Pierot	2008	Americal Heart Association	Immediate clinical outcome of patients harboring unruptured intracranial aneurysms treated by endovascular approach – Results of the ATENA study
Pierot	2010	Americal Heart Association	Endovascular treatment of very small unruptured aneurysms: Rate of procedural complications, clinical outcome, and anatomical results
Pierot	2009	Radiology	Endovascular treatment of unruptured intracranial aneurysms: Comparison of safety of remodeling technique and standard treatment with coils
Poncyljusz	2020	Journal of Clinical Medicine	Stent-assisted coiling of unruptured MCA aneurysms using the LVIS Jr. device: A multicenter registry
Poncyljusz	2015	European Journal of Radiology	Bare platinum coils vs. Hydrocoil in the treatment of unruptured intracranial aneurysms – A single center randomized controlled study
Pop	2020	Interventional Neuroradiology	Balloon-assisted coiling of intracranial aneurysms using the Eclipse 2L double lumen balloon
Popielscki	2018	Journal of Neuroradiology	Two-center experience in the endovascular treatment of ruptured and unruptured intracranial aneurysms using the WEB device: a retrospective analysis
Raslan	2011	Neurosurgery	Neuroform stent-assisted embolization of incidental anterior communicating artery aneurysms: Long-term clinical and angiographic follow-up
Samaniego	2018	Interventional Neurology	LVIS Jr device for Y-stent-assisted coil embolization of wide-neck intracranial aneurysms: A multicenter experience
Sato	2021	Turkish Neurosurgery	Comparison of stent-assisted coiling for unruptured internal carotid artery aneurysms between LVIS or LVIS Jr. and Enterprise VRD: A retrospective and single-center analysis
Satow	2020	Japan Neurosurgical Society	Coil embolization for unruptured intracranial aneurysms at the dawn of stent era: Results of the Japanese registry of neuroendovascular therapy (JR-NET)
Sedat	2018	Neuroradiology	Stent-assisted coiling of intracranial aneurysms using LEO stents: Long-term follow-up in 153 patients
Shigematsu	2013	Stroke	Endovascular therapy for asymptomatic unruptured intracranial aneurysms: JR-NET and JR-NET2 findings
Shimizu	2016	Journal of Neuroradiology	Endovascular treatment of unruptured paraclinoid aneurysms: Single-center experience with 400 cases and literature review

References

1. Dott, N.M., “Intracranial Aneurysms: Cerebral Arterio-Radiography: Surgical Treatment”. *Edinburgh Medical Journal*, 1933. 40(12): pp. T219-T240.
2. Guglielmi, G., Viñuela, F., Dion, J., and Duckwiler, G., “Electrothrombosis of saccular aneurysms via endovascular approach: Part 2: Preliminary clinical experience”. *Journal of Neurosurgery*, 1991. 75(1): pp. 8-14.
3. Guglielmi, G., Vinuela, F., Sepetka, I., and Macellari, V., “Electrothrombosis of saccular aneurysms via endovascular approach. Part 1: Electrochemical basis, technique, and experimental results”. *Journal of Neurosurgery*, 1991. 75(1): pp. 1-7.
4. Sadato, A., Hayakawa, M., Adachi, K., Nakahara, I., and Hirose, Y., “Large residual volume, not low packing density, is the most influential risk factor for recanalization after coil embolization of cerebral aneurysms”. *PloS ONE*, 2016. 11(5): p. e0155062.
5. Charlick, M. and J, M.D., *Anatomy, Head and Neck, Internal Carotid Arteries*, in *StatPearls*. 2022: Treasure Island (FL).
6. Schievink, W.I., “Intracranial aneurysms”. *New England Journal of Medicine*, 1997. 336(1): pp. 28-40.
7. Frösen, J., Tulamo, R., Paetau, A., Laaksamo, E., Korja, M., Laakso, A., Niemelä, M., and Hernesniemi, J., “Saccular intracranial aneurysm: pathology and mechanisms”. *Acta Neuropathologica*, 2012. 123(6): pp. 773-786.
8. Kim, C., Cervós-Navarro, J., Kikuchi, H., Hashimoto, N., and Hazama, F., “Degenerative changes in the internal elastic lamina relating to the development of saccular cerebral aneurysms in rats”. *Acta Neurochirgica*, 1993. 121(1-2): pp. 76-81.
9. Jamous, M.A., Nagahiro, S., Kitazato, K.T., Tamura, T., Aziz, H.A., Shono, M., and

Satoh, K., “Endothelial injury and inflammatory response induced by hemodynamic changes preceding intracranial aneurysm formation: experimental study in rats”. *Journal of Neurosurgery*, 2007. 107(2): pp. 405-411.

10. Toth, G. and Cerejo, R., “Intracranial aneurysms: Review of current science and management”. *Vascular Medicine*, 2018. 23(3): pp. 276-288.
11. Keedy, A., “An overview of intracranial aneurysms”. *McGill Journal of Medicine*, 2006. 9(2): pp. 141-146.
12. Etminan, N. and Rinkel, G.J., “Unruptured intracranial aneurysms: development, rupture and preventive management”. *Nature Reviews Neurology*, 2016. 12(12): pp. 699-713.
13. Greving, J.P., Wermer, M.J., Brown, R.D., Jr., Morita, A., Juvela, S., Yonekura, M., Ishibashi, T., Torner, J.C., Nakayama, T., Rinkel, G.J., and Algra, A., “Development of the PHASES score for prediction of risk of rupture of intracranial aneurysms: a pooled analysis of six prospective cohort studies”. *Lancet Neurology*, 2014. 13(1): pp. 59-66.
14. Claiborne, J.S., Wilson, C.B., Halbach, V.V., Higashida, R.T., Dowd, C.F., McDermott, M.W., Applebury, C.B., Farley, T.L., and Gress, D.R., “Endovascular and surgical treatment of unruptured cerebral aneurysms: Comparison of risks”. *Annals of Neurology*, 2000. 48(1): pp. 11-19.
15. Johnston, S.C., Dudley, R.A., Gress, D.R., and Ono, L., “Surgical and endovascular treatment of unruptured cerebral aneurysms at university hospitals”. *Neurology*, 1999. 52(9): pp. 1799-1805.
16. Johnston, S.C., Zhao, S., Dudley, R.A., Berman, M.F., and Gress, D.R., “Treatment of

unruptured cerebral aneurysms in California". *Stroke*, 2001. 32(3): pp. 597-605.

17. Molyneux, A.J., Kerr, R.S., Yu, L.-M., Clarke, M., Sneade, M., Yarnold, J.A., Sandercock, P., and Group, I.S.A.T.C., "International subarachnoid aneurysm trial (ISAT) of neurosurgical clipping versus endovascular coiling in 2143 patients with ruptured intracranial aneurysms: a randomised comparison of effects on survival, dependency, seizures, rebleeding, subgroups, and aneurysm occlusion". *Lancet*, 2005. 366(9488): pp. 809-817.

18. Guglielmi, G., "Guglielmi detachable coils". *Journal of Neurointerventional Surgery*, 2018. 10(4): p. e5.

19. Tahtinen, O.I., Vanninen, R.L., Manninen, H.I., Rautio, R., Haapanen, A., Niskakangas, T., Rinne, J., and Keski-Nisula, L., "Wide-necked intracranial aneurysms: treatment with stent-assisted coil embolization during acute (<72 hours) subarachnoid hemorrhage--experience in 61 consecutive patients". *Radiology*, 2009. 253(1): pp. 199-208.

20. Bendok, B.R., Abi-Aad, K.R., Ward, J.D., Kniss, J.F., Kwasny, M.J., Rahme, R.J., Aoun, S.G., El Ahmadieh, T.Y., El Tecle, N.E., Zammar, S.G., Aoun, R.J.N., Patra, D.P., Ansari, S.A., Raymond, J., Woo, H.H., Fiorella, D., Dabus, G., Milot, G., Delgado Almandoz, J.E., Scott, J.A., DeNardo, A.J., Dashti, S.R., and Investigators, H.S., "The hydrogel endovascular aneurysm treatment trial (HEAT): A randomized controlled trial of the second-generation hydrogel coil". *Neurosurgery*, 2020. 86(5): pp. 615-624.

21. Herting, S.M., Ding, Y., Boyle, A.J., Dai, D., Nash, L.D., Asnafi, S., Jakaitis, D.R., Johnson, C.R., Graul, L.M., and Yeh, C., "*In vivo* comparison of shape memory

polymer foam-coated and bare metal coils for aneurysm occlusion in the rabbit elastase model". *Journal of Biomedical Materials Research Part B: Applied Biomaterials*, 2019. 107(8): pp. 2466-2475.

22. Chueh, J.Y., Vedantham, S., Wakhloo, A.K., Carniato, S.L., Puri, A.S., Bzura, C., Coffin, S., Bogdanov, A.A., Jr., and Gounis, M.J., "Aneurysm permeability following coil embolization: packing density and coil distribution". *Journal of Neurointerventional Surgery*, 2015. 7(9): pp. 676-681.

23. White, P.M., Lewis, S.C., Gholkar, A., Sellar, R.J., Nahser, H., Cognard, C., Forrester, L., and Wardlaw, J.M., "Hydrogel-coated coils versus bare platinum coils for the endovascular treatment of intracranial aneurysms (HELPS): A randomised controlled trial". *Lancet*, 2011. 377(9778): pp. 1655-1662.

24. Williams, A., Millar, J., Ditchfield, A., Vundavalli, S., and Barker, S., "Use of Hydrocoil in small aneurysms: Procedural safety, treatment efficacy and factors predicting complete occlusion". *Interventional Neuroradiology*, 2014. 20(1): pp. 37-44.

25. Guo, X.B., Fan, Y.M., and Zhang, J.N., "HydroSoft coil versus HydroCoil for endovascular aneurysm occlusion study: A single center experience". *European Journal of Radiology*, 2011. 79(2): pp. e42-e46.

26. Taschner, C.A., Chapot, R., Costalat, V., Machi, P., Courtheoux, P., Barreau, X., Berge, J., Pierot, L., Kadziolka, K., Jean, B., Blanc, R., Biondi, A., Brunel, H., Gallas, S., Berlis, A., Herbreteau, D., Berkefeld, J., Urbach, H., Elsheikh, S., Fiehler, J., Desal, H., Graf, E., and Bonafe, A., "Second-generation hydrogel coils for the endovascular treatment of intracranial aneurysms: A randomized controlled trial". *Stroke*, 2018.

49(3): pp. 667-674.

27. Raymond, J., Klink, R., Chagnon, M., Barnwell, S.L., Evans, A.J., Mocco, J., Hoh, B.H., Turk, A.S., Turner, R.D., Desal, H., Fiorella, D., Bracard, S., Weill, A., Guilbert, F., Lanthier, S., Fox, A.J., Darsaut, T.E., White, P.M., and Roy, D., "Hydrogel versus bare platinum coils in patients with large or recurrent aneurysms prone to recurrence after endovascular treatment: A randomized controlled trial". *American Journal of Neuroradiology*, 2017. 38(3): pp. 432-441.

28. Xue, T., Chen, Z., Lin, W., Xu, J., Shen, X., and Wang, Z., "Hydrogel coils versus bare platinum coils for the endovascular treatment of intracranial aneurysms: A meta-analysis of randomized controlled trials". *BMC Neurology*, 2018. 18(167).

29. Poupart, O., Conti, R., Schmocker, A., Pancaldi, L., Moser, C., Nuss, K.M., Sakar, M.S., Dobrocky, T., Grützmacher, H., Mosimann, P.J., and Pioletti, D.P., "Pulsatile flow-induced fatigue-resistant photopolymerizable hydrogels for the treatment of intracranial aneurysms". *Frontiers in Bioengineering and Biotechnology*, 2021. 8(1567): p. 619858.

30. Poupart, O., Schmocker, A., Conti, R., Moser, C., Nuss, K.M., Grutzmacher, H., Mosimann, P.J., and Pioletti, D.P., "*In vitro* implementation of photopolymerizable hydrogels as a potential treatment of intracranial aneurysms". *Frontiers in Bioengineering and Biotechnology*, 2020. 8: p. 261.

31. Murayama, Y., Viñuela, F., Tateshima, S., Viñuela, F., Jr., and Akiba, Y., "Endovascular treatment of experimental aneurysms by use of a combination of liquid embolic agents and protective devices". *American Journal of Neuroradiology*, 2000. 21(9): pp. 1726-1735.

32. Tevah, J., Senf, R., Cruz, J., and Fava, M., "Endovascular treatment of complex cerebral aneurysms with Onyx HD-500® in 38 patients". *Journal of Neuroradiology*, 2011. 38(5): pp. 283-290.

33. Chalouhi, N., Tjoumakaris, S., Gonzalez, L.F., Hasan, D., Alkhalili, K., Dumont, A.S., Rosenwasser, R., and Jabbour, P., "Endovascular treatment of distal intracranial aneurysms with Onyx 18/34". *Clinical Neurology and Neurosurgery*, 2013. 115(12): pp. 2528-2532.

34. Klisch, J., Sychra, V., Strasilla, C., Liebig, T., and Fiorella, D., "The Woven EndoBridge cerebral aneurysm embolization device (WEB II): Initial clinical experience". *Neuroradiology*, 2011. 53(8): pp. 599-607.

35. Pierot, L., Liebig, T., Sychra, V., Kadziolka, K., Dorn, F., Strasilla, C., Kabbasch, C., and Klisch, J., "Intrasaccular flow-disruption treatment of intracranial aneurysms: Preliminary results of a multicenter clinical study". *American Journal of Neuroradiology*, 2012. 33(7): pp. 1232-1238.

36. Caroff, J., Mihalea, C., Klisch, J., Strasilla, C., Berlis, A., Patankar, T., Weber, W., Behme, D., Jacobsen, E.A., Liebig, T., Prothmann, S., Cognard, C., Finkenzeller, T., Moret, J., and Spelle, L., "Single-layer WEBs: Intrasaccular flow disrupters for aneurysm treatment—Feasibility results from a European study". *American Journal of Neuroradiology*, 2015. 36(10): pp. 1942-1946.

37. Lubicz, B., Klisch, J., Gauvrit, J.Y., Szikora, I., Leonardi, M., Liebig, T., Nuzzi, N.P., Boccardi, E., Paola, F.D., Holtmannspötter, M., Weber, W., Calgliari, E., Sychra, V., Mine, B., and Pierot, L., "WEB-DL endovascular treatment of wide-neck bifurcation aneurysms: short- and midterm results in a European study". *American Journal of*

Neuroradiology, 2014. 35(3): pp. 432-438.

38. Caroff, J., Mihalea, C., Dargento, F., Neki, H., Ikka, L., Benachour, N., Moret, J., and Spelle, L., "Woven Endobridge (WEB) device for endovascular treatment of ruptured intracranial wide-neck aneurysms: a single-center experience". *Neuroradiology*, 2014. 56(9): pp. 755-761.

39. Clajus, C., Strasilla, C., Fiebig, T., Sychra, V., Fiorella, D., and Klisch, J., "Initial and mid-term results from 108 consecutive patients with cerebral aneurysms treated with the WEB device". *Journal of Neurointerventional Surgery*, 2017. 9(4): pp. 411-417.

40. Arthur, A.S., Molyneux, A., Coon, A.L., Saatci, I., Szikora, I., Baltacioglu, F., Sultan, A., Hoit, D., Delgado Almandoz, J.E., Elijovich, L., Cekirge, S., Byrne, J.V., Fiorella, D., and investigators, W.-I.S., "The safety and effectiveness of the Woven EndoBridge (WEB) system for the treatment of wide-necked bifurcation aneurysms: Final 12-month results of the pivotal WEB intrasaccular therapy (WEB-IT) study". *Journal of Neurointerventional Surgery*, 2019. 11(9): pp. 924-930.

41. Maragkos, G.A., Dmytriw, A.A., Salem, M.M., Tutino, V.M., Meng, H., Cognard, C., Machi, P., Krings, T., and Mendes Pereira, V., "Overview of different flow diverters and flow dynamics". *Neurosurgery*, 2020. 86(Suppl 1): pp. S21-S34.

42. Martínez-Galdámez, M., Lamin, S.M., Lagios, K.G., Liebig, T., Ciceri, E.F., Chapot, R., Stockx, L., Chavda, S., Kabbasch, C., Faragò, G., Nordmeyer, H., Boulanger, T., Piano, M., and Boccardi, E.P., "Treatment of intracranial aneurysms using the pipeline flex embolization device with shield technology: angiographic and safety outcomes at 1-year follow-up". *Journal of Neurointerventional Surgery*, 2019. 11(4): pp. 396-399.

43. Trivelato, F.P., Wajnberg, E., Rezende, M.T.S., Ulhôa, A.C., Piske, R.L., Abud, T.G.,

de Castro-Afonso, L.H., Abath, C.G.C., Nakiri, G.S., Araújo, J.F.S., Silva, J.L.J., Tosello, R.T., Vanzin, J.R., Manzato, L.B., Baccin, C.E., da Mota, B.A.A., and Abud, D.G., "Safety and effectiveness of the pipeline flex embolization device with shield technology for the treatment of intracranial aneurysms: midterm results from a multicenter study". *Neurosurgery*, 2020. 87(1): pp. 104-111.

44. Li, L., Gao, B.L., Wu, Q.W., Shao, Q.J., Wang, Z.L., Zhang, K., and Li, T.X., "Pipeline flex embolization device for the treatment of large unruptured posterior circulation aneurysms: Single-center experience". *Journal of Clinical Neuroscience*, 2022. 96: pp. 127-132.

45. Killer-Oberpfalzer, M., Kocer, N., Griessenauer, C.J., Janssen, H., Engelhorn, T., Holtmannspötter, M., Buhk, J.H., Finkenzeller, T., Fesl, G., Trenkler, J., Reith, W., Berlis, A., Hausegger, K., Augustin, M., Islak, C., Minnich, B., and Möhlenbruch, M., "European multicenter study for the evaluation of a dual-layer flow-diverting stent for treatment of wide-neck intracranial aneurysms: The European flow-redirection intraluminal device study". *American Journal of Neuroradiology*, 2018. 39(5): pp. 841-847.

46. Liu, J.M., Zhou, Y., Li, Y., Li, T., Leng, B., Zhang, P., Liang, G., Huang, Q., Yang, P.F., Shi, H., Zhang, J., Wan, J., He, W., Liang, C., Zhu, G., Xu, Y., Hong, B., Yang, X., Bai, W., Tian, Y., Zhang, H., Li, Z., Li, Q., Zhao, R., Fang, Y., and Zhao, K., "Parent artery reconstruction for large or giant cerebral aneurysms using the Tubridge flow diverter: A multicenter, randomized, controlled clinical trial (PARAT)". *American Journal of Neuroradiology*, 2018. 39(5): pp. 807-816.

47. Zhang, Y., Huang, Q.-H., Fang, Y., Yang, P., Xu, Y., Hong, B., and Liu, J., "A novel

flow diverter (Tubridge) for the treatment of recurrent aneurysms: A single-center experience". *Korean Journal of Radiology*, 2017. 18(5): pp. 852-859.

48. De Beule, T., Boulanger, T., Heye, S., van Rooij, W.J., van Zwam, W.H., and Stockx, L., "p64 flow diverter: Results in 108 patients from a single center". *Interventional Neuroradiology*, 2021. 27(1): pp. 51-59.

49. Singhal, P., Rodriguez, J.N., Small, W., Eagleston, S., Van de Water, J., Maitland, D.J., and Wilson, T.S., "Ultra low density and highly crosslinked biocompatible shape memory polyurethane foams". *Journal of Polymer Science Part B: Polymer Physics*, 2012. 50(10): pp. 724-737.

50. Horn, J., Hwang, W., Jessen, S.L., Keller, B.K., Miller, M.W., Tuzun, E., Hartman, J., Clubb Jr, F.J., and Maitland, D.J., "Comparison of shape memory polymer foam versus bare metal coil treatments in an *in vivo* porcine sidewall aneurysm model". *Journal of Biomedical Materials Research Part B: Applied Biomaterials*, 2017. 105(7): pp. 1892-1905.

51. Jessen, S.L., Friedemann, M.C., Mullen, A.E., Ginn-Hedman, A.M., Herting, S.M., Maitland, D.J., and Clubb Jr, F.J., "Micro-CT and histopathology methods to assess host response of aneurysms treated with shape memory polymer foam-coated coils versus bare metal coil occlusion devices". *Journal of Biomedical Materials Research Part B: Applied Biomaterials*, 2020. 108(5): pp. 2238-2249.

52. Echeverría, D., Rivera, R., Giacaman, P., Sordo, J.G., Einersen, M., and Badilla, L., "A novel self-expanding shape memory polymer coil for intracranial aneurysm embolization: 1 year follow-up in Chile". *Journal of NeuroInterventional Surgery*, 2022: pp. 1-6.

53. Lendlein, A., Behl, M., Hiebl, B., and Wischke, C., "Shape-memory polymers as a technology platform for biomedical applications". *Expert Review of Medical Devices*, 2010. 7(3): pp. 357-379.

54. Rousseau, I.A., "Challenges of shape memory polymers: A review of the progress toward overcoming SMP's limitations". *Polymer Engineering & Science*, 2008. 48(11): pp. 2075-2089.

55. Xiao, M., Zhang, N., Zhuang, J., Sun, Y., Ren, F., Zhang, W., and Hou, Z., "Degradable poly(ether-ester-urethane)s based on well-defined aliphatic diurethane diisocyanate with excellent shape recovery properties at body temperature for biomedical application". *Polymers*, 2019. 11(6): p. 1002.

56. Zhang, F., Xia, Y., Wang, L., Liu, L., Liu, Y., and Leng, J., "Conductive shape memory microfiber membranes with core–shell structures and electroactive performance". *ACS Applied Materials & Interfaces*, 2018. 10(41): pp. 35526-35532.

57. Julich-Gruner, K.K., Löwenberg, C., Neffe, A.T., Behl, M., and Lendlein, A., "Recent trends in the chemistry of shape-memory polymers". *Macromolecular Chemistry and Physics*, 2013. 214(5): pp. 527-536.

58. Hu, J., Chen, W., Fan, P., Gao, J., Fang, G., Cao, Z., and Peng, F., "Epoxy shape memory polymer (SMP): Material preparation, uniaxial tensile tests and dynamic mechanical analysis". *Polymer Testing*, 2017. 62: pp. 335-341.

59. Kaloshkin, S., Maksimkin, A., Kaloshkina, M., Zadorozhnyy, M., and Churyukanova, M., "Shape memory behavior of ultra-high molecular weight polyethylene". *MRS Online Proceedings Library*, 2012. 1403(1): pp. 207-213.

60. Kunkel, R.P., Laurence, D.W., Wang, J., Robinson, D.O., Scherrer, J.H., Wu, Y.,

Bohnstedt, B.N., Chien, A., Liu, Y., and Lee, C.-H., "Synthesis and characterization of bio-compatible shape memory polymers with potential applications to endovascular embolization of intracranial aneurysms". *Journal of the Mechanical Behavior of Biomedical Materials*, 2018. 88: pp. 422-430.

61. Wang, J., Luo, J., Kunkel, R., Saha, M., Bohnstedt, B.N., Lee, C.-H., and Liu, Y., "Development of shape memory polymer nanocomposite foam for treatment of intracranial aneurysms". *Materials Letters*, 2019. 250: pp. 38-41.

62. Pineda-Castillo, S.A., Luo, J., Lee, H., Bohnstedt, B.N., Liu, Y., and Lee, C.-H., "Effects of carbon nanotube infiltration on a shape memory polymer-based device for brain aneurysm therapeutics: Design and characterization of a Joule-heating triggering mechanism". *Advanced Engineering Materials*, 2021. 23(6): p. 2100322.

63. Wypych, G., *3 – Mechanisms of Action of Blowing Agents*, in *Handbook of Foaming and Blowing Agents*, G. Wypych, Editor. 2017, ChemTec Publishing. pp. 29-43.

64. Drenckhan, W. and Saint-Jalmes, A., "The science of foaming". *Advances in Colloid and Interface Science*, 2015. 222: pp. 228-259.

65. Singhal, P., Small, W., Cosgriff-Hernandez, E., Maitland, D.J., and Wilson, T.S., "Low density biodegradable shape memory polyurethane foams for embolic biomedical applications". *Acta Biomaterialia*, 2014. 10(1): pp. 67-76.

66. Hasan, S.M., Fletcher, G.K., Monroe, M.B.B., Wierzbicki, M.A., Nash, L.D., and Maitland, D.J., "Shape memory polymer foams synthesized using glycerol and hexanetriol for enhanced degradation resistance". *Polymers*, 2020. 12(10): p. 2290.

67. Petryk, N.M., Haas, G., Vakil, A.U., and Monroe, M.B.B., "Shape memory polymer foams with tunable interconnectivity using off-the-shelf foaming components".

Journal of Biomedical Materials Research Part A, 2022. 110(8): pp. 1422-1434.

68. Song, J.J., Srivastava, I., and Naguib, H.E., "Development of multifunctional shape memory polymer foams". *AIP Conference Proceedings*, 2015. 1664(1): p. 040005.

69. Vakil, A.U., Petryk, N.M., Shepherd, E., and Monroe, M.B.B., "Biostable Shape Memory Polymer Foams for Smart Biomaterial Applications". *Polymers*, 2021. 13(23): p. 4048.

70. Zhang, F., Zhou, T., Liu, Y., and Leng, J., "Microwave synthesis and actuation of shape memory polycaprolactone foams with high speed". *Scientific Reports*, 2015. 5(1): p. 11152.

71. De Nardo, L., Bertoldi, S., Tanzi, M.C., Haugen, H., and Fare, S., "Shape memory polymer cellular solid design for medical applications". *Smart Materials and Structures*, 2011. 20(3): p. 035004.

72. Zhang, D., Petersen, K.M., and Grunlan, M.A., "Inorganic–organic shape memory polymer (SMP) foams with highly tunable properties". *ACS Applied Materials & Interfaces*, 2013. 5(1): pp. 186-191.

73. De Nardo, L., Bertoldi, S., Cigada, A., Tanzi, M.C., Haugen, H.J., and Farè, S., "Preparation and characterization of shape memory polymer scaffolds via solvent casting/particulate leaching". *Journal of Applied Biomaterials & Functional Materials*, 2012. 10(2): pp. 119-126.

74. Langford, T., Mohammed, A., Essa, K., Elshaer, A., and Hassanin, H., "4D printing of origami structures for minimally invasive surgeries using functional scaffold". *Applied Sciences*, 2021. 11(1): p. 332.

75. Mehrpouya, M., Gisario, A., Azizi, A., and Barletta, M., "Investigation on shape

recovery of 3D printed honeycomb sandwich structure". *Polymers for Advanced Technologies*, 2020. 31(12): pp. 3361-3365.

76. Jia, H., Gu, S.-Y., and Chang, K., "3D printed self-expandable vascular stents from biodegradable shape memory polymer". *Advances in Polymer Technology*, 2018. 37(8): pp. 3222-3228.

77. Nguyen, T.T. and Kim, J., "4D-printing - Fused deposition modeling printing and polyJet printing with shape memory polymers composite". *Fibers and Polymers*, 2020. 21(10): pp. 2364-2372.

78. Cersoli, T., Cresanto, A., Herberger, C., MacDonald, E., and Cortes, P., "3D printed shape memory polymers produced via direct pellet extrusion". *Micromachines*, 2021. 12(1): p. 87.

79. Chen, Y., Garces, I.T., Tang, T., and Ayranci, C., "Cellulose nanocrystals reinforced shape memory polymer cardiovascular stent". *Rapid Prototyping Journal*, 2021. 27(1): pp. 37-44.

80. Liu, J., Zhao, L., Guo, Y., Zhang, H., and Zhang, Z., "Multi-responsive shape memory polymer printed by fused deposition modeling technique". *Express Polymer Letters*, 2020. 14: pp. 348-357.

81. Melocchi, A., Uboldi, M., Inverardi, N., Briatico-Vangosa, F., Baldi, F., Pandini, S., Scalet, G., Auricchio, F., Cerea, M., Foppoli, A., Maroni, A., Zema, L., and Gazzaniga, A., "Expandable drug delivery system for gastric retention based on shape memory polymers: Development via 4D-printing and extrusion". *International Journal of Pharmaceutics*, 2019. 571: p. 118700.

82. Ehrmann, G. and Ehrmann, A., "3D printing of shape memory polymers". *Journal of*

Applied Polymer Science, 2021. 138(34): p. 50847.

83. Han, X.J., Dong, Z.Q., Fan, M.M., Liu, Y., li, J.H., Wang, Y.F., Yuan, Q.J., Li, B.J., and Zhang, S., "pH-induced shape-memory polymers". *Macromolecular Rapid Communications*, 2012. 33(12): pp. 1055-1060.

84. Sun, L. and Huang, W.M., "Thermo/moisture responsive shape-memory polymer for possible surgery/operation inside living cells in future". *Materials & Design*, 2010. 31(5): pp. 2684-2689.

85. Baer, G.M., Small, W., Wilson, T.S., Benett, W.J., Matthews, D.L., Hartman, J., and Maitland, D.J., "Fabrication and *in vitro* deployment of a laser-activated shape memory polymer vascular stent". *Biomedical Engineering Online*, 2007. 6(1): p. 43.

86. Xia, S., Li, X., Wang, Y., Pan, Y., Zheng, Z., Ding, X., and Peng, Y., "A remote-activated shape memory polymer network employing vinyl-capped Fe_3O_4 nanoparticles as netpoints for durable performance". *Smart Materials and Structures*, 2014. 23(8): p. 085005.

87. Sahoo, N.G., Jung, Y.C., Yoo, H.J., and Cho, J.W., "Influence of carbon nanotubes and polypyrrole on the thermal, mechanical and electroactive shape-memory properties of polyurethane nanocomposites". *Composites Science and Technology*, 2007. 67(9): pp. 1920-1929.

88. Meng, H. and Li, G.Q., "A review of stimuli-responsive shape memory polymer composites". *Polymer*, 2013. 54(9): pp. 2199-2221.

89. Kim, I. and Cho, G., "Polyurethane nanofiber strain sensors via *in situ* polymerization of polypyrrole and application to monitoring joint flexion". *Smart Materials and Structures*, 2018. 27(7): p. 075006.

90. Sahoo, N.G., Jung, Y.C., Goo, N.S., and Cho, J.W., "Conducting shape memory polyurethane-polypyrrole composites for an electroactive actuator". *Macromolecular Materials and Engineering*, 2005. 290(11): pp. 1049-1055.

91. Leng, J., Zhang, D., Liu, Y., Yu, K., and Lan, X., "Study on the activation of styrene-based shape memory polymer by medium-infrared laser light". *Applied Physics Letters*, 2010. 96(11): p. 111905.

92. Schmidt, A.M., "Electromagnetic activation of shape memory polymer networks containing magnetic nanoparticles". *Macromolecular Rapid Communications*, 2006. 27(14): pp. 1168-1172.

93. Liu, Y., Lv, H., Lan, X., Leng, J., and Du, S., "Review of electro-active shape-memory polymer composite". *Composites Science and Technology*, 2009. 69(13): pp. 2064-2068.

94. Yu, K., Liu, Y., and Leng, J., "Shape memory polymer/CNT composites and their microwave induced shape memory behaviors". *RSC Advances*, 2014. 4(6): pp. 2961-2968.

95. Meng, H., Zheng, J., Wen, X., Cai, Z., Zhang, J., and Chen, T., "pH- and sugar-induced shape memory hydrogel based on reversible phenylboronic acid-diol ester bonds". *Macromolecular Rapid Communications*, 2015. 36(6): pp. 533-537.

96. Lu, L., Tian, T., Wu, S., Xiang, T., and Zhou, S., "A pH-induced self-healable shape memory hydrogel with metal-coordination cross-links". *Polymer Chemistry*, 2019. 10(15): pp. 1920-1929.

97. Huang, W., Yang, B., An, L., Li, C., and Chan, Y., "Water-driven programmable polyurethane shape memory polymer: demonstration and mechanism". *Applied*

Physics Letters, 2005. 86(11): p. 114105.

98. Chae Jung, Y., Hwa So, H., and Whan Cho, J., "Water-responsive shape memory polyurethane block copolymer modified with polyhedral oligomeric silsesquioxane". *Journal of Macromolecular Science, Part B*, 2006. 45(4): pp. 453-461.

99. Zhang, H., Wang, H., Zhong, W., and Du, Q., "A novel type of shape memory polymer blend and the shape memory mechanism". *Polymer*, 2009. 50(6): pp. 1596-1601.

100. DiOrio, A.M., Luo, X., Lee, K.M., and Mather, P.T., "A functionally graded shape memory polymer". *Soft Matter*, 2011. 7(1): pp. 68-74.

101. Xu, J. and Song, J., "High performance shape memory polymer networks based on rigid nanoparticle cores". *Proceedings of the National Academy of Sciences*, 2010. 107(17): pp. 7652-7657.

102. Xie, T., "Tunable polymer multi-shape memory effect". *Nature*, 2010. 464: pp. 267-270.

103. Yang, B., Huang, W.M., Li, C., and Chor, J.H., "Effects of moisture on the glass transition temperature of polyurethane shape memory polymer filled with nano-carbon powder". *European Polymer Journal*, 2005. 41(5): pp. 1123-1128.

104. Yang, B., Huang, W., Li, C., Li, L., and Chor, J., "Qualitative separation of the effects of carbon nano-powder and moisture on the glass transition temperature of polyurethane shape memory polymer". *Scripta Materialia*, 2005. 53(1): pp. 105-107.

105. Guo, B., Chen, Y., Lei, Y., Zhang, L., Zhou, W.Y., Rabie, A.B.M., and Zhao, J., "Biobased poly (propylene sebacate) as shape memory polymer with tunable switching temperature for potential biomedical applications". *Biomacromolecules*, 2011. 12(4): pp. 1312-1321.

106. Bai, Y., Zhang, X., Wang, Q., and Wang, T., "A tough shape memory polymer with triple-shape memory and two-way shape memory properties". *Journal of Materials Chemistry A*, 2014. 2(13): pp. 4771-4778.

107. Min, C., Cui, W., Bei, J., and Wang, S., "Biodegradable shape-memory polymer - polylactide-co-poly (glycolide-co-caprolactone) multiblock copolymer". *Polymers for Advanced Technologies*, 2005. 16(8): pp. 608-615.

108. Liu, G., Ding, X., Cao, Y., Zheng, Z., and Peng, Y., "Novel shape-memory polymer with two transition temperatures". *Macromolecular Rapid Communications*, 2005. 26(8): pp. 649-652.

109. Nji, J. and Li, G., "A self-healing 3D woven fabric reinforced shape memory polymer composite for impact mitigation". *Smart Materials and Structures*, 2010. 19(3): p. 035007.

110. Nji, J. and Li, G., "A biomimic shape memory polymer based self-healing particulate composite". *Polymer*, 2010. 51(25): pp. 6021-6029.

111. Boyle, A.J., Wierzbicki, M.A., Herting, S., Weems, A.C., Nathan, A., Hwang, W., and Maitland, D.J., "*In vitro* performance of a shape memory polymer foam-coated coil embolization device". *Medical Engineering and Physics*, 2017. 49: pp. 56-62.

112. Small, W., Buckley, P.R., Wilson, T.S., Benett, W.J., Hartman, J., Saloner, D., and Maitland, D.J., "Shape memory polymer stent with expandable foam: A new concept for endovascular embolization of fusiform aneurysms". *IEEE Transactions on Biomedical Engineering*, 2007. 54(6): pp. 1157-1160.

113. Imai, S. and Sakurai, K., "An actuator of two-way behavior by using two kinds of shape memory polymers with different T_g's". *Precision Engineering*, 2013. 37(3): pp. 572-

579.

114. Wilson, T., Bearinger, J., Herberg, J., Marion, J., Wright, W., Evans, C., and Maitland, D., "Shape memory polymers based on uniform aliphatic urethane networks". *Journal of Applied Polymer Science*, 2007. 106(1): pp. 540-551.

115. Gu, S., Yan, B., Liu, L., and Ren, J., "Carbon nanotube–polyurethane shape memory nanocomposites with low trigger temperature". *European Polymer Journal*, 2013. 49(12): pp. 3867-3877.

116. Zheng, N., Hou, J., Xu, Y., Fang, Z., Zou, W., Zhao, Q., and Xie, T., "Catalyst-free thermoset polyurethane with permanent shape reconfigurability and highly tunable triple-shape memory performance". *ACS Macro Letters*, 2017. 6(4): pp. 326-330.

117. Yu, Z., Zhang, Q., Li, L., Chen, Q., Niu, X., Liu, J., and Pei, Q., "Highly flexible silver nanowire electrodes for shape-memory polymer light-emitting diodes". *Advanced Materials*, 2011. 23(5): pp. 664-668.

118. Zhang, Y., Wang, Q., Wang, C., and Wang, T., "High-strain shape memory polymer networks crosslinked by SiO 2". *Journal of Materials Chemistry*, 2011. 21(25): pp. 9073-9078.

119. Choong, Y.Y.C., Maleksaeedi, S., Eng, H., Wei, J., and Su, P.-C., "4D printing of high performance shape memory polymer using stereolithography". *Materials & Design*, 2017. 126: pp. 219-225.

120. Uchiyama, N., Kida, S., Nomura, M., Hasegawa, M., Yamashima, T., Yamashita, J., and Matsui, O., "Significance of volume embolization ratio as a predictor of recanalization on endovascular treatment of cerebral aneurysms with Guglielmi detachable coils". *Interventional Neuroradiology*, 2000. 6(1_suppl): pp. 59-63.

121. Tamatani, S., Ito, Y., Abe, H., Koike, T., Takeuchi, S., and Tanaka, R., "Evaluation of the stability of aneurysms after embolization using detachable coils: Correlation between stability of aneurysms and embolized volume of aneurysms". *American Journal of Neuroradiology*, 2002. 23(5): pp. 762-767.

122. Yang, B., Huang, W.M., Li, C., Lee, C.M., and Li, L., "On the effects of moisture in a polyurethane shape memory polymer". *Smart Materials and Structures*, 2003. 13(1): pp. 191-195.

123. Yang, B., Huang, W.M., Li, C., and Li, L., "Effects of moisture on the thermomechanical properties of a polyurethane shape memory polymer". *Polymer*, 2006. 47(4): pp. 1348-1356.

124. Tey, S., Huang, W., and Sokolowski, W., "Influence of long-term storage in cold hibernation on strain recovery and recovery stress of polyurethane shape memory polymer foam". *Smart Materials and Structures*, 2001. 10: p. 321.

125. De Nardo, L., Alberti, R., Cigada, A., Tanzi, M.C., and Farè, S., "Shape memory polymer foams for cerebral aneurysm reparation: Effects of plasma sterilization on physical properties and cytocompatibility". *Acta Biomaterialia*, 2009. 5(5): pp. 1508-1518.

126. De Nardo, L., Moscatelli, M., Silvi, F., Tanzi, M.C., Yahia, L.H., and Farè, S., "Chemico-physical modifications induced by plasma and ozone sterilizations on shape memory polyurethane foams". *Journal of Materials Science: Materials in Medicine*, 2010. 21(7): pp. 2067-2078.

127. Fisher, H., Woolard, P., Ross, C., Kunkel, R., Bohnstedt, B.N., Liu, Y., and Lee, C.H., "Thermomechanical data of polyurethane shape memory polymer: Considering

varying compositions". *Data in Brief*, 2020. 32: p. 106294.

128. Wang, J., Kunkel, R., Luo, J., Li, Y., Liu, H., Bohnstedt, B.N., Liu, Y., and Lee, C.-H., "Shape memory polyurethane with porous architectures for potential applications in intracranial aneurysm treatment". *Polymers*, 2019. 11(4): p. 631.

129. Bodlak, R.A., "*Computational Investigations of A Shape-Memory Polymer Foam Embolization Device for Intracranial Aneurysms"*. 2021: University of Oklahoma.

130. Leng, J.S., Lan, X., Liu, Y.J., Du, S.Y., Huang, W.M., Liu, N., Phee, S.J., and Yuan, Q., "Electrical conductivity of thermoresponsive shape-memory polymer with embedded micron sized Ni powder chains". *Applied Physics Letters*, 2008. 92(1): p. 014104.

131. Stefani, M.A., Schneider, F.L., Marrone, A.C., Severino, A.G., Jackowski, A.P., and Wallace, M.C., "Anatomic variations of anterior cerebral artery cortical branches". *Clinical Anatomy*, 2000. 13(4): pp. 231-236.

132. Schindelin, J., Arganda-Carreras, I., Frise, E., Kaynig, V., Longair, M., Pietzsch, T., Preibisch, S., Rueden, C., Saalfeld, S., Schmid, B., Tinevez, J.-Y., White, D.J., Hartenstein, V., Eliceiri, K., Tomancak, P., and Cardona, A., "Fiji: an open-source platform for biological-image analysis". *Nature Methods*, 2012. 9(7): pp. 676-682.

133. Wang, J., Chowdhury, S., Liu, Y., Bohnstedt, B.N., and Lee, C.-H. "*Development of thermally-activated shape memory polymers and nanocomposites for biomedical devices"*. in *ASME 2017 International Mechanical Engineering Congress and Exposition*. 2017. American Society of Mechanical Engineers.

134. Coates, J., *Interpretation of Infrared Spectra: A Practical Approach*, in *Encyclopedia of Analytical Chemistry*.

135. Asefnejad, A., Khorasani, M.T., Behnamghader, A., Farsadzadeh, B., and Bonakdar, S., "Manufacturing of biodegradable polyurethane scaffolds based on polycaprolactone using a phase separation method: Physical properties and in vitro assay". *International Journal of Nanomedicine*, 2011. 6: pp. 2375-2384.

136. Zhang, S., Ren, Z., He, S., Zhu, Y., and Zhu, C., "FTIR spectroscopic characterization of polyurethane-urea model hard segments (PUUMHS) based on three diamine chain extenders". *Spectrochimica Acta A: Molecular and Biomolecular Spectroscopy*, 2007. 66(1): pp. 188-193.

137. Zhao, P., Wang, Y., Zhu, J., Hua, X., and Wen, Q., "Characterization of graded polyurethane elastomer by FTIR". *Science in China Series B: Chemistry*, 2008. 51(1): pp. 58-61.

138. Askari, F., Barikani, M., Barmar, M., and Shokrollahi, P., "Polyurethane/amino-grafted multiwalled carbon nanotube nanocomposites: Microstructure, thermal, mechanical, and rheological properties". *Journal of Applied Polymer Science*, 2017. 134(4): p. 44411.

139. Ross, K.A., Campanella, O.H., and Okos, M.R., "The effect of porosity on glass transition measurement". *International Journal of Food Properties*, 2002. 5(3): pp. 611-628.

140. Xia, H. and Song, M., "Preparation and characterization of polyurethane–carbon nanotube composites". *Soft Matter*, 2005. 1(5): pp. 386-394.

141. Lu, H., Zhu, S., Yang, Y., Huang, W.M., Leng, J., and Du, S., "Surface grafting of carbon fibers with artificial silver-nanoparticle-decorated graphene oxide for high-speed electrical actuation of shape-memory polymers". *Journal of Applied Polymer*

Science, 2015. 132(12): p. 41673.

142. Tobushi, H., Okumura, K., Endo, M., and Hayashi, S., "Thermomechanical properties of polyurethane-shape memory polymer foam". *Journal of Intelligent Material Systems and Structures*, 2001. 12(4): pp. 283-287.

143. Giannitelli, S.M., Basoli, F., Mozetic, P., Piva, P., Bartuli, F.N., Luciani, F., Arcuri, C., Trombetta, M., Rainer, A., and Licoccia, S., "Graded porous polyurethane foam: A potential scaffold for oro-maxillary bone regeneration". *Materials Science and Engineering: C*, 2015. 51: pp. 329-335.

144. Chen, W., Lu, F., and Winfree, N., "High-strain-rate compressive behavior of a rigid polyurethane foam with various densities". *Experimental Mechanics*, 2002. 42(1): pp. 65-73.

145. Shatri, J., Bexheti, D., Bexheti, S., Kabashi, S., Krasniqi, S., Ahmetgjekaj, I., and Zhjeqi, V., "Influence of gender and age on average dimensions of arteries forming the circle of Willis: Study by magnetic resonance angiography on Kosovo's population". *Open Access Macedonian Journal of Medical Sciences*, 2017. 5(6): pp. 714-719.

146. Gawlitza, M., Soize, S., Barbe, C., le Clainche, A., White, P., Spelle, L., and Pierot, L., "Aneurysm characteristics, study population, and endovascular techniques for the treatment of intracranial aneurysms in a large, prospective, multicenter cohort: Results of the analysis of recanalization after endovascular treatment of intracranial aneurysm study". *American Journal of Neuroradiology*, 2019. 40(3): pp. 517-523.

147. Rahman, M., Smietana, J., Hauck, E., Hoh, B., Hopkins, N., Siddiqui, A., Levy, E.I., Meng, H., and Mocco, J., "Size ratio correlates with intracranial aneurysm rupture status: A prospective study". *Stroke*, 2010. 41(5): pp. 916-920.

148. Xie, X.-L., Mai, Y.-W., and Zhou, X.-P., "Dispersion and alignment of carbon nanotubes in polymer matrix: A review". *Materials Science and Engineering: R: Reports*, 2005. 49(4): pp. 89-112.

149. Mut, F., Chung, B.J., Chudyk, J., Lylyk, P., Kadirvel, R., Kallmes, D.F., and Cebral, J.R., "Image-based modeling of blood flow in cerebral aneurysms treated with intrasaccular flow diverting devices". *International Journal of Numerical Methods in Biomedical Engineering*, 2019. 35(6): p. e3202.

150. Berg, P., Saalfeld, S., Voß, S., Redel, T., Preim, B., Janiga, G., and Beuing, O., "Does the DSA reconstruction kernel affect hemodynamic predictions in intracranial aneurysms? An analysis of geometry and blood flow variations". *Journal of NeuroInterventional Surgery*, 2018. 10(3): pp. 290-296.

151. Amili, O., Schiavazzi, D., Moen, S., Jagadeesan, B., Van de Moortele, P.F., and Coletti, F., "Hemodynamics in a giant intracranial aneurysm characterized by *in vitro* 4D flow MRI". *PLoS ONE*, 2018. 13(1): p. e0188323.

152. Medero, R., Ruedinger, K., Rutkowski, D., Johnson, K., and Roldán-Alzate, A., "*In vitro* assessment of flow variability in an intracranial aneurysm model using 4D flow MRI and tomographic PIV". *Annals of Biomedical Engineering*, 2020. 48(10): pp. 2484-2493.

153. Ahamed, T., Peattie, R.A., Dorfmann, L., and Cherry Kemmerling, E.M., "Pulsatile flow measurements and wall stress distribution in a patient specific abdominal aortic aneurysm phantom". *Journal of Applied Mathematics and Mechanics*, 2018. 98(12): pp. 2258-2274.

154. Padolecchia, R., Guglielmi, G., Puglioli, M., Castagna, M., Nardini, V., Collavoli, P.L.,

Guidetti, G., Dazzi, M., Zucchi, V., and Narducci, P., "Role of electrothrombosis in aneurysm treatment with Guglielmi detachable coils: an in vitro scanning electron microscopic study". *American Journal of Neuroradiology*, 2001. 22(9): pp. 1757-1760.

155. Smart, S.K., Cassady, A.I., Lu, G.Q., and Martin, D.J., "The biocompatibility of carbon nanotubes". *Carbon*, 2006. 44(6): pp. 1034-1047.

156. Zhang, X., Zeng, G., Tian, J., Wan, Q., Huang, Q., Wang, K., Zhang, Q., Liu, M., Deng, F., and Wei, Y., "PEGylation of carbon nanotubes via mussel inspired chemistry: Preparation, characterization and biocompatibility evaluation". *Applied Surface Science*, 2015. 351: pp. 425-432.

157. Wobbrock, J.O., Findlater, L., Gergle, D., and Higgins, J.J. "*The aligned rank transform for nonparametric factorial analyses using only ANOVA procedures"*. in *Proceedings of the SIGCHI Conference on Human Factors in Computing Systems*. 2011.

158. Stern, T., "Conclusive chemical deciphering of the consistently occurring double-peak carbonyl-stretching FTIR absorbance in polyurethanes". *Polymers for Advanced Technologies*, 2019. 30(3): pp. 675-687.

159. Hernandez-Cordova, R., Mathew, D.A., Balint, R., Carrillo-Escalante, H.J., Cervantes-Uc, J.M., Hidalgo-Bastida, L.A., and Hernandez-Sanchez, F., "Indirect three-dimensional printing: A method for fabricating polyurethane-urea based cardiac scaffolds". *Journal of Biomedical Materials Research A*, 2016. 104(8): pp. 1912-1921.

160. Baidya, A., Haghniaz, R., Tom, G., Edalati, M., Kaneko, N., Alizadeh, P., Tavafoghi, M., Khademhosseini, A., and Sheikhi, A., "A cohesive shear-thinning biomaterial for catheter-based minimally invasive therapeutics". *ACS Applied Materials & Interfaces*,

2022. 14(38): pp. 42852-42863.

161. Pineda-Castillo, S.A., Laurence, K.A., Homburg, H., Fung, K.-M., Bohnstedt, B.N., and Lee, C.-H., "A protocol for the reduction of applied torque on parent vessel during elastase-induced aneurysm formation using rabbit animal models". *bioRxiv*, 2021: p. 2021.10.08.463749.

162. Li, S., Liu, Y.-Y., Liu, L.-J., and Hu, Q.-X., "A versatile method for fabricating tissue engineering scaffolds with a three-dimensional channel for prevasculature networks". *ACS Applied Materials & Interfaces*, 2016. 8(38): pp. 25096-25103.

163. Wooster, N., "The Crystal Structure of Ferric Chloride $FeCl_3$". *Zeitschrift für Kristallographie - Crystalline Materials*, 1932. 83(1-6): pp. 35-41.

164. Fu, Y., Su, Y.-S., and Manthiram, A., "Sulfur-Polypyrrole Composite Cathodes for Lithium-Sulfur Batteries". *Journal of The Electrochemical Society*, 2012. 159(9): p. A1420.

165. Liang, X., Wen, Z., Liu, Y., Wang, X., Zhang, H., and Huang, M.W.L., "Preparation and characterization of sulfur–polypyrrole composites with controlled morphology as high capacity cathode for lithium batteries". *Solid State Ionics*, 2011. 192(1): pp. 347-350.

166. Kim, S., Jang, L.K., Park, H.S., and Lee, J.Y., "Electrochemical deposition of conductive and adhesive polypyrrole-dopamine films". *Scientific Reports*, 2016. 6: p. 30475.

167. Fahlgren, A., Bratengeier, C., Gelmi, A., Semeins, C.M., Klein-Nulend, J., Jager, E.W., and Bakker, A.D., "Biocompatibility of polypyrrole with human primary osteoblasts and the effect of dopants". *PLoS ONE*, 2015. 10(7): p. e0134023.

168. Wang, X., Gu, X., Yuan, C., Chen, S., Zhang, P., Zhang, T., Yao, J., Chen, F., and Chen, G., "Evaluation of biocompatibility of polypyrrole in vitro and in vivo". *Journal of Biomedical Materials Research A*, 2004. 68(3): pp. 411-422.

169. Tutino, V.M., Mandelbaum, M., Takahashi, A., Pope, L.C., Siddiqui, A., Kolega, J., and Meng, H., "Hypertension and estrogen deficiency augment aneurysmal remodeling in the rabbit circle of Willis in response to carotid ligation". *The Anatomical Record*, 2015. 298(11): pp. 1903-10.

170. Ikedo, T., Minami, M., Kataoka, H., Hayashi, K., Nagata, M., Fujikawa, R., Higuchi, S., Yasui, M., Aoki, T., Fukuda, M., Yokode, M., and Miyamoto, S., "Dipeptidyl peptidase-4 inhibitor anagliptin prevents intracranial aneurysm growth by suppressing macrophage infiltration and activation". *Journal of the American Heart Association*, 2017. 6(6): p. e004777.

171. Killer, M., Kallmes, D., Jones, R., Ding, Y., Vestal, M., Hauser, T., Virmani, R., and Cruise, G., "Long-term angiographic and histological results of a new hydrogel-containing filling coil in experimental rabbit aneurysms". *Minimally Invasive Neurosurgery*, 2010. 53(3): pp. 97-105.

172. Strange, F., Gruter, B.E., Fandino, J., and Marbacher, S., "Preclinical intracranial aneurysm models: A systematic review". *Brain Sciences*, 2020. 10(3): p. 134.

173. Ding, Y.-H., Dai, D., Schroeder, D., Kadirvel, R., and Kallmes, D.F., "Experimental testing of the dual-layer Woven EndoBridge device using an elastase-induced aneurysm model in rabbits". *Interventional Neuroradiology*, 2016. 22(3): pp. 299-303.

174. German, W.J. and Black, S.P.W., "Experimental production of carotid aneurysms". *New England Journal of Medicine*, 1954. 250(3): pp. 104-106.

175. Brinjikji, W., Ding, Y.H., Kallmes, D.F., and Kadirvel, R., "From bench to bedside: Utility of the rabbit elastase aneurysm model in preclinical studies of intracranial aneurysm treatment". *Journal of Neurointerventional Surgery*, 2016. 8(5): pp. 521-525.

176. Cloft, H.J., Altes, T.A., Marx, W.F., Raible, R.J., Hudson, S.B., Helm, G.A., Mandell, J.W., Jensen, M.E., Dion, J.E., and Kallmes, D.F., "Endovascular creation of an in vivo bifurcation aneurysm model in rabbits". *Radiology*, 1999. 213(1): pp. 223-228.

177. Ding, Y., Dai, D., Kadirvel, R., Lewis, D.A., and Kallmes, D.F., "Five-year follow-up in elastase-induced aneurysms in rabbits". *American Journal of Neuroradiology*, 2010. 31(7): pp. 1236-1239.

178. Hoh, B., Rabinov, J., Pryor, J., and Ogilvy, C., "A modified technique for using elastase to create saccular aneurysms in animals that histologically and hemodynamically resemble aneurysms in human". *Acta Neurochirurgica*, 2004. 146(7): pp. 705-711.

179. Han, H.C., Liu, Q., and Jiang, Z.L., "Mechanical behavior and wall remodeling of blood vessels under axial twist". *Yi Yong Sheng Wu Li Xue*, 2016. 31(4): pp. 319-326.

180. Laurence, D.W., Homburg, H., Yan, F., Tang, Q., Fung, K.-M., Bohnstedt, B.N., Holzapfel, G.A., and Lee, C.-H., "A pilot study on biaxial mechanical, collagen microstructural, and morphological characterizations of a resected human intracranial aneurysm tissue". *Scientific Reports*, 2021. 11(1): p. 3525.

181. Spetzger, U., von Schilling, A., Brombach, T., and Winkler, G., "Training models for vascular microneurosurgery". *Acta Neurochirurgica Supplementum*, 2011. 112: pp. 115-119.

182. Tawfik, G.M., Dila, K.A.S., Mohamed, M.Y.F., Tam, D.N.H., Kien, N.D., Ahmed, A.M., and Huy, N.T., "A step by step guide for conducting a systematic review and

meta-analysis with simulation data". *Tropical Medicine and Health*, 2019. 47: p. 46.

183. Moher, D., Liberati, A., Tetzlaff, J., Altman, D.G., and Group, P., "Preferred reporting items for systematic reviews and meta-analyses: the PRISMA statement". *Journal of Clinical Epidemiology*, 2009. 62(10): pp. 1006-1012.

184. McKenzie, J.E., Brennan, S.E., Ryan, R.E., Thomson, H.J., Johnston, R.V., and Thomas, J., *Defining the Criteria for Including Studies and How They Will Be Grouped for the Synthesis*, in *Cochrane Handbook for Systematic Reviews of Interventions*. 2019. pp. 33-65.

185. Balduzzi, S., Rücker, G., and Schwarzer, G., "How to perform a meta-analysis with R: a practical tutorial". *Evidence Based Mental Health*, 2019. 22(4): pp. 153-160.

186. Murayama, Y., Nien, Y.L., Duckwiler, G., Gobin, Y.P., Jahan, R., Frazee, J., Martin, N., and Viñuela, F., "Guglielmi detachable coil embolization of cerebral aneurysms: 11 years' experience". *Journal of Neurosurgery*, 2003. 98(5): pp. 959-966.

187. Lee, K.S., Zhang, J.J.Y., Nguyen, V., Han, J., Johnson, J.N., Kirollos, R., and Teo, M., "The evolution of intracranial aneurysm treatment techniques and future directions". *Neurosurgical Review*, 2022. 45(1): pp. 1-25.

188. Ravindran, K., Salem, M.M., Alturki, A.Y., Thomas, A.J., Ogilvy, C.S., and Moore, J.M., "Endothelialization following flow diversion for intracranial aneurysms: A systematic review". *American Journal of Neuroradiology*, 2019. 40(2): pp. 295-301.

189. Grunwald, I.Q., Papanagiotou, P., Struffert, T., Politi, M., Krick, C., Gül, G., and Reith, W., "Recanalization after endovascular treatment of intracerebral aneurysms". *Neuroradiology*, 2007. 49(1): pp. 41-47.

190. Vivanco-Suarez, J., Wallace, A.N., Dandapat, S., Lopez, G.V., Mendez-Ruiz, A.,

Kayan, Y., Copelan, A.Z., Dajles, A., Zevallos, C.B., Quispe-Orozco, D., Mendez-Ruiz, A., Galecio-Castillo, M., Samaniego, E.A., Farooqui, M., Delgado, J.E., and Ortega-Gutierrez, S., "Stent-assisted coiling versus balloon-assisted coiling for the treatment of ruptured wide-necked aneurysms: A 2-center experience". *Stroke: Vascular and Interventional Neurology*, 2023. 3(1): p. e000456.

191. Waldeck, S., Chapot, R., von Falck, C., Froelich, M.F., Brockmann, M., and Overhoff, D., "A comparative evaluation of standard and balloon-assisted coiling of intracranial aneurysms based on neurophysiological monitoring". *Journal of Clinical Medicine*, 2022. 11(3): p. 677.

192. Chalouhi, N., Starke, R.M., Koltz, M.T., Jabbour, P.M., Tjoumakaris, S.I., Dumont, A.S., Rosenwasser, R.H., Singhal, S., and Gonzalez, L.F., "Stent-assisted coiling versus balloon remodeling of wide-neck aneurysms: comparison of angiographic outcomes". *American Journal of Neuroradiology*, 2013. 34(10): pp. 1987-1992.

193. Asnafi, S., Rouchaud, A., Pierot, L., Brinjikji, W., Murad, M.H., and Kallmes, D.F., "Efficacy and safety of the Woven EndoBridge (WEB) device for the treatment of intracranial aneurysms: A systematic review and Meta-analysis". *American Journal of Neuroradiology*, 2016. 37(12): pp. 2287-2292.

194. Akhunbay-Fudge, C.Y., Deniz, K., Tyagi, A.K., and Patankar, T., "Endovascular treatment of wide-necked intracranial aneurysms using the novel Contour Neurovascular System: A single-center safety and feasibility study". *Journal of NeuroInterventional Surgery*, 2020. 12(10): p. 987.

195. Biondi, A., Primikiris, P., Vitale, G., and Charbonnier, G., "Endosaccular flow disruption with the Contour Neurovascular System: Angiographic and clinical results

in a single-center study of 60 unruptured intracranial aneurysms". *Journal of NeuroInterventional Surgery*, 2022.

196. Poncyljusz, W., Zarzycki, A., Zwarzany, Ł., and Burke, T.H., "Bare platinum coils vs. HydroCoil in the treatment of unruptured intracranial aneurysms: A single center randomized controlled study". *European Journal of Radiology*, 2015. 84(2): pp. 261-265.

197. Aguilar Perez, M., Bhogal, P., Martinez Moreno, R., Bazner, H., Ganslandt, O., and Henkes, H., "The Medina embolic device: Early clinical experience from a single center". *Journal of Neurointerventional Surgery*, 2017. 9(1): pp. 77-87.

198. Piotin, M., Biondi, A., Sourour, N., Mounayer, C., Jaworski, M., Mangiafico, S., Andersson, T., Soderman, M., Goffette, P., Anxionnat, R., and Blanc, R., "The LUNA aneurysm embolization system for intracranial aneurysm treatment: short-term, mid-term and long-term clinical and angiographic results". *Journal of Neurointerventional Surgery*, 2018. 10(12): p. e34.

199. Kunkel, R., *Investigation of Polyurethane Shape Memory Polymer for Potential Applications in Brain Aneurysm Treatment*. 2019, The University of Oklahoma.

200. Yang, J., Chen, H., Yuan, Y., Sarkar, D., and Zheng, J., "Synthesis and characterization of biocompatible polyurethanes for controlled release of hydrophobic and hydrophilic drugs". *Frontiers of Chemical Science and Engineering*, 2014. 8(4): pp. 498-510.

201. Cabanlit, M., Maitland, D., Wilson, T., Simon, S., Wun, T., Gershwin, M.E., and Van de Water, J., "Polyurethane shape-memory polymers demonstrate functional biocompatibility *in vitro*". *Macromolecular Bioscience*, 2007. 7(1): pp. 48-55.

202. Weems, A.C., Wacker, K.T., Carrow, J.K., Boyle, A.J., and Maitland, D.J., "Shape

memory polyurethanes with oxidation-induced degradation: *In vivo* and *in vitro* correlations for endovascular material applications". *Acta Biomaterialia*, 2017. 59: pp. 33-44.

203. Fonner, J.M., Forciniti, L., Nguyen, H., Byrne, J.D., Kou, Y.F., Syeda-Nawaz, J., and Schmidt, C.E., "Biocompatibility implications of polypyrrole synthesis techniques". *Biomedical Materials*, 2008. 3(3): p. 034124.

204. Xu, M., McCanna, D.J., and Sivak, J.G., "Use of the viability reagent PrestoBlue in comparison with alamarBlue and MTT to assess the viability of human corneal epithelial cells". *Journal of Pharmacological Toxicological Methods*, 2015. 71: pp. 1-7.

205. Henkes, H., Brew, S., Miloslavski, E., Fischer, S., Tavrovski, I., and Kuhne, D., "The underlying mechanisms of endovascular exclusion of intracranial aneurysms by coils. How important is electrothrombosis?". *Interventional Neuroradiology*, 2003. 9(2): pp. 127-140.

206. Cebral, J.R., Duan, X., Chung, B.J., Putman, C., Aziz, K., and Robertson, A., "Wall mechanical properties and hemodynamics of unruptured intracranial aneurysms". *American Journal of Neuroradiology*, 2015. 36(9): pp. 1695-1703.

207. Humphrey, J. and Canham, P., "Structure, mechanical properties, and mechanics of intracranial saccular aneurysms". *Journal of Elasticity and the Physical Science of Solids*, 2000. 61(1): pp. 49-81.

208. Signorelli, F., Pailler-Mattei, C., Gory, B., Larquet, P., Robinson, P., Vargiolu, R., Zahouani, H., Labeyrie, P.-E., Guyotat, J., and Pelissou-Guyotat, I., "Biomechanical characterization of intracranial aneurysm wall: A multiscale study". *World*

Neurosurgery, 2018. 119: pp. e882-e889.

209. Pineda-Castillo, S.A., Aparicio-Ruiz, S., Burns, M.M., Laurence, D.W., Bradshaw, E., Gu, T., Holzapfel, G.A., and Lee, C.-H., "Linking the region-specific tissue microstructure to the biaxial mechanical properties of the porcine left anterior descending artery". *Acta Biomaterialia*, 2022. 150: pp. 295-309.

210. Umeda, Y., Ishida, F., Tsuji, M., Furukawa, K., Shiba, M., Yasuda, R., Toma, N., Sakaida, H., and Suzuki, H., "Computational fluid dynamics (CFD) using porous media modeling predicts recurrence after coiling of cerebral aneurysms". *PLoS One*, 2017. 12(12): p. e0190222.

211. Jett, S.V., Hudson, L.T., Baumwart, R., Bohnstedt, B.N., Mir, A., Burkhart, H.M., Holzapfel, G.A., Wu, Y., and Lee, C.-H., "Integration of polarized spatial frequency domain imaging (pSFDI) with a biaxial mechanical testing system for quantification of load-dependent collagen architecture in soft collagenous tissues". *Acta Biomaterialia*, 2020. 102: pp. 149-168.

212. Liu, Y., Zhang, W., Zhang, F., Lan, X., Leng, J., Liu, S., Jia, X., Cotton, C., Sun, B., Gu, B., and Chou, T.-W., "Shape memory behavior and recovery force of 4D printed laminated Miura-origami structures subjected to compressive loading". *Composites Part B: Engineering*, 2018. 153: pp. 233-242.